



HAL
open science

Innovative Calibration Strategies for Large Adaptive Telescopes with Pyramid Wave-Front Sensors

Cedric Taïssir Heritier

► **To cite this version:**

Cedric Taïssir Heritier. Innovative Calibration Strategies for Large Adaptive Telescopes with Pyramid Wave-Front Sensors. Instrumentation and Methods for Astrophysic [astro-ph.IM]. Aix Marseille Université, 2019. English. NNT: . tel-02390861v1

HAL Id: tel-02390861

<https://theses.hal.science/tel-02390861v1>

Submitted on 3 Dec 2019 (v1), last revised 13 Jan 2020 (v3)

HAL is a multi-disciplinary open access archive for the deposit and dissemination of scientific research documents, whether they are published or not. The documents may come from teaching and research institutions in France or abroad, or from public or private research centers.

L'archive ouverte pluridisciplinaire **HAL**, est destinée au dépôt et à la diffusion de documents scientifiques de niveau recherche, publiés ou non, émanant des établissements d'enseignement et de recherche français ou étrangers, des laboratoires publics ou privés.

AIX-MARSEILLE UNIVERSITÉ

ECOLE DOCTORALE 352

UFR Sciences

Laboratoire d'Astrophysique De Marseille/ Groupe R&D Optique et Instrumentation

Thèse présentée pour obtenir le grade universitaire de docteur

Discipline : Physique et Sciences de la Matière. Spécialité : Instrumentation

Cedric Taïssir HERITIER-SALAMA

Innovative Calibration Strategies for Large Adaptive Telescopes with Pyramid Wave-Front Sensors

Soutenue le 07/11/2019 devant le jury composé de :

Jean Luc BEUZIT	LAM	Président du Jury
Jean Pierre VERAN	NRC Herzberg Astronomy and Astrophysics	Rapporteur
Gérard ROUSSET	LESIA - Observatoire de Paris	Rapporteur
Simone ESPOSITO	INAF - Arcetri	Examineur
Charlotte BOND	Institut For Astronomy - Hawaii	Examineur
Thierry FUSCO	ONERA/LAM	Directeur de thèse
Benoit NEICHEL	LAM	Encadrant
Sylvain OBERTI	European Southern Observatory	Encadrant

Numéro national de thèse/suffixe local : 2019AIXM0371/060ED352

Abstract

The new generation of Extremely Large Telescopes (ELT) will provide an optical resolution never achieved before for ground-based observation. However, in order to fully benefit from the potential of these telescopes, the scientific instruments will rely on complex Adaptive Optics Systems (AO) to correct for the optical aberrations due to the atmospheric turbulence. These AO instruments will all include Pyramid Wave-Front Sensor (PWFS) in their design as these WFS provide a gain in sensitivity with respect to the historical Shack-Hartmann WFS (SH). The cost of this gain in sensitivity comes with a higher operational complexity as the sensor exhibits a modal linearity and sensitivity that depends on both the seeing conditions and level of AO correction itself, the so-called optical gains of the PWFS.

Coupled to this very first technical challenge, the future ELT will provide a constrained environment for the AO calibration with a large number of degrees of freedom, that will have to be calibrated often without any external calibration source and unprecedented distances between Deformable Mirror (DM) and AO instruments. This will induce differential motions and thus opto-mechanical conjugation errors between WFS and DM. Regular evolution of these so-called mis-registrations are then to be expected during the observations. They have to be monitored and compensated as they will highly affect the AO performance or lead to loop instability that will jeopardize the scientific observations.

To address these operational constraints, we propose to consider a pseudo synthetic approach where calibration data are generated from a synthetic model, identifying the model parameters from experimental inputs. Such strategy is already used at the Adaptive Optics Facility working with SH-WFS. For PWFS, synthetic-based calibration have already been performed on several existing systems but a tracking of the mis-registration parameters during the operation is still to be investigated.

As part of my PhD studies, I first developed a pseudo-synthetic model of the AO system of the Large Binocular Telescope that included the modelling of a PWFS and Adaptive Secondary Mirror. The purpose of this model was to generate a pseudo synthetic Interaction Matrix that could be used on the real system and identify the key-ingredients to efficiently model the PWFS. The model has been experimentally validated at the telescope and provided the same level of AO performances as a measured interaction matrix, demonstrating the high accuracy of the model. For this experiment, to tune the parameters of the model, we had access to a full interaction matrix measured at the telescope which will not be the case of the future ELT.

The second part of my PhD was focused on optimizing the identification of the mis-registration parameters to allow a regular tracking of the parameters during the operation. We identified two strategies to provide an online tracking of the parameter. The first one is invasive and consists in dithering well selected signals with a low amplitude on the DM during the operations. This method appears to be robust to the different observing conditions and we demonstrated that the perturbation can

be reduced to a few signals only, selected to maximize the sensitivity to the mis-registrations. This method has to be applied with the constraints of minimizing the impact on the scientific path that has to be carefully evaluated.

Another strategy consists in accumulating enough telemetry data to retrieve a noisy interaction matrix that is used to give an estimation of the mis-registration parameters. This non invasive method appears to be attractive as no perturbation on the scientific path is required. The purpose of our research was to understand the physics that underpin the estimation of this noisy interaction matrix to identify the domain of validity of the method depending on the observing conditions, especially when considering its application with a PWFS.

Keywords: Adaptive Optics, Pyramid WFS, Calibration, Large Adaptive Telescopes

Résumé

Les futurs Télescopes Géants (ELT) auront une résolution jamais atteinte avec des télescopes terrestres. Cependant, pour exploiter pleinement leur potentiel scientifique, il sera nécessaire de les équiper de systèmes d'Optique Adaptative (AO) complexes pour corriger les aberrations optiques dues à la turbulence atmosphérique. Ces instruments posséderont tous un Analyseurs de Surface d'Onde (ASO) de type Pyramide (PWFS) qui permet d'obtenir un gain en sensibilité vis-à-vis de l'ASO Shack-Hartmann (SH). Ce gain a toutefois un prix en terme de complexité opérationnelle. Les PWFS présentent en effet une linéarité et une sensibilité modales qui dépendent à la fois des conditions d'observations et du niveau de correction de la boucle d'AO elle-même. Le design des futurs ELT imposera de nombreuses contraintes pour l'étalonnage des système d'OA avec un grand nombre de degrés de libertés à étalonner, souvent sans source d'étalonnage externe, et avec une très grande distance séparant le miroir déformable (DM) et l'ASO. Cette distance provoquera l'apparition d'erreurs de conjugaison opto-mécanique entre ASO et DM: les mis-registrations. Ces mis-registrations évolueront régulièrement pendant les observations ce qui impactera les performances du système d'OA ou provoquer des instabilités de la boucle. Un système de suivi et de compensation de ces mis-registrations sera nécessaire pour ne pas compromettre le bon déroulement des observations scientifiques. Pour répondre à ces problématiques, nous proposons de considérer une approche pseudo synthétique où les données d'étalonnages sont générées depuis un modèle qui requiert l'identification de quelques paramètres grâce à des données expérimentales. De telles stratégies ont déjà été développées pour des ASO de type SH. Dans le cas des PWFS, des étalonnages basés sur des modèles synthétiques ont déjà été développés mais il reste à étudier la possibilité de faire un suivi de ces paramètres durant les observations. Durant la première partie de ma thèse, j'ai développé un modèle Pseudo Synthétique des OA du Large Binocular Telescope (LBT) qui incluait la modélisation d'un PWFS et d'un miroir secondaire adaptatif. Le but de ce travail était de générer une matrice d'interaction pseudo synthétique qui puisse fonctionner au télescope et d'identifier les éléments clés pour effectuer une modélisation précise du PWFS. Ce modèle a été validé expérimentalement au LBT, obtenant le même niveau de performance qu'une matrice d'interaction mesurée au télescope ce qui a démontré la haute précision du modèle. Dans le cadre de cette expérience, nous avons accès à une matrice d'interaction mesurée au télescope pour paramétrer le modèle, ce qui ne sera pas le cas des futures ELT. La seconde partie de ma thèse était donc orientée pour optimiser les stratégies d'identifications de ces paramètres et ainsi permettre un suivi durant les observations. Une première stratégie, dite invasive, consiste à appliquer des perturbations à faible amplitude sur le DM pendant les opérations. Cette méthode apparait comme robuste aux différentes conditions d'observations et nous avons démontré que la perturbation appliquée sur le miroir pouvait être réduite à quelques signaux bien choisis pour maximiser la sensibilité aux mis-registrations.

L'application de cette méthode est cependant soumise à la contrainte de minimiser l'impact sur les observations scientifiques. Une autre stratégie consiste à accumuler suffisamment de données de la boucle pour retrouver une estimation bruitée de la matrice d'interaction qui est utilisée pour estimer les paramètres du modèle. Cette méthode, non invasive, apparaît comme séduisante car elle n'a aucun impact sur la voie scientifique. Le but de notre recherche était de comprendre la physique derrière l'estimation de cette matrice d'interaction bruitée pour identifier le domaine de validité de la méthode en fonction des conditions d'observations, en particulier en considérant son application avec le PWFS.

Mots clés: Optique Adaptative, ASO Pyramide, Etalonnage, Grands Télescopes Adaptatifs

Aknowledgments/Remerciements

Le sprint final de la rédaction est terminé, il est maintenant temps de regarder en arrière. Il faut dire que cette thèse s'est déroulée de manière assez particulière dans trois villes aux environnements bien différents. Tout a commencé avec le soleil et la mer de Marseille puis s'en sont suivies les lumières de Toscane à Florence pour enfin se retrouver au grand air dans les montagnes à Munich. Autant de lieux qu'il aura fallu découvrir, s'approprier mais finalement quitter. En premier lieu, je souhaite donc remercier les différents organismes qui ont financé cette thèse et qui m'ont accueilli pour mener ma recherche dans de parfaites conditions: l'ONERA, le LAM, l'ESO et l'INAF. Je souhaite également remercier mon jury de thèse, d'abord G. Rousset et J.-P. Véran d'avoir accepté d'être mes rapporteurs, C. Bond d'avoir accepté d'être mon examinatrice et enfin, le président du jury J.-L. Beuzit.

Il convient ensuite de remercier les personnes qui ont suivi mon travail au plus près tout au long de ces trois dernières années. Je souhaite donc remercier mon directeur de thèse, Thierry, dont le regard avisé aura toujours permis d'améliorer de manière significative la qualité de mes travaux. Merci en particulier pour ta disponibilité pendant ces durs derniers mois de rédaction. Je souhaite également remercier Benoit qui s'est toujours montré très disponible et encourageant tout au long de la thèse ! Ce fut un plaisir d'échanger régulièrement avec toi. Merci à Simone dont l'expérience au LBT avec l'ASO Pyramide aura été précieuse pour développer mon modèle synthétique. Enfin, je souhaite particulièrement remercier Sylvain pour ta disponibilité et ta gentillesse. Ce fut un réel plaisir de travailler avec toi, j'ai appris énormément de choses et si mon séjour en Allemagne s'est aussi bien déroulé sache que tu en es pour beaucoup !

Durant ces trois années de dur labeur et de déménagements successifs, j'ai eu la chance d'être entouré de nombreuses personnes qui m'auront permis de garder le cap aussi bien au niveau professionnel qu'au niveau personnel. Je souhaite ici les remercier pour leur soutien et pour tous ces moments de détente qui ont été indispensables au bon déroulement de cette thèse. Au risque d'être un peu long, j'ai choisi de me remémorer ces trois années de manière chronologique.

Ma thèse a donc démarré sur les bords de la Méditerranée, et le moins que l'on puisse dire, c'est qu'il ne m'aura pas fallu longtemps pour m'adapter au doux climat Phocéén et au rythme de vie marseillais. Cette intégration facile est à mettre au crédit de l'accueil que j'ai reçu en arrivant au LAM ! Merci donc au membres du GRD qui m'ont permis de débiter ma thèse dans de parfaites conditions, Manu, Kacem, Léo, Nohah, Arthur, Fred. En particulier, je souhaite remercier Carlos et Jeff' qui n'ont cessé de répondre à mes questions sur l'outil OOMAO ou sur l'état de forme des serveurs de calculs du labo. Merci également pour toutes les discussions très enrichissantes sur la modélisation de systèmes d'OA de manière générale !

Lors de cette première année j'ai eu la chance de faire partie de cette joyeuse équipe qui m'a tout de suite intégré (il n'aura pas fallu longtemps pour qu'on m'amène dans le virage sud du Vélodrome...contre mon gré !). Il y avait Nico, Thibault, Romain, Wilfried, Amandine, Guillaume, Simona, Yannick. Je tiens à dire que j'ai beaucoup apprécié la compagnie de mes deux collègues de bureau Charlotte et Lucie. Lulu, on pourra dire que les déroulements de nos thèses auront été bien similaires... jusqu'au bout du bout ! J'espère que tu garderas toujours cette énergie débordante et cette bonne humeur !

En particulier, Mich', je ne compte plus le nombre de fois où je suis venu t'embêter pour me faire un café dans ton labo, mais au moins ça me permettait de prendre 5 minutes pour discuter avec toi et d'apprendre des choses sur les techniques de polissage ! Et puis merci pour toutes les fois où tu m'auras prêté ton matériel de plongée...tout est si simple avec toi, ne change rien !

Et puis il y a Jean-Sabri, toujours dans les bons coups, toujours les bons tuyaux, une curiosité à toute épreuve, des jeux de mots dans tous les sens et quelle énergie sur un terrain de foot...enfin au moins pour 10 minutes ! J'ai vraiment apprécié ta compagnie dans le fameux bureau du Tarpin Large Telescope ! Merci d'avoir supporté sans broncher mes différentes phases musicales durant la rédaction du manuscrit, j'en avais besoin ! En tout cas merci de m'avoir fait découvrir tant de choses à Marseille, je te souhaite bon courage pour la dernière ligne droite et je t'attends à Munich pour fêter ça... avec Robbie bien sûr !

Ensuite, il y a Anaïs bien sûr ! La gentillesse incarnée. Je m'en rappelle encore, c'est toi qui était venue me chercher pour m'inviter à venir déjeuner avec vous lors de mon premier jour. Une chose était certaine, j'étais bien tombé dans cette équipe ! Merci pour tout Nan', les parties de contrées, les soirées pizza, les restos improvisés et le soutien psychologique lors de ces derniers mois, sans compter toutes les fois où vous m'aurez accueilli avec Val...que ce soit sur un bateau ou sur un sofa dans le salon !

Mélanie, là aussi, je me rappelle bien de ton arrivée: pleine d'énergie ! En particulier, merci pour le soutien durant les derniers mois de la thèse ! Les petites soirées contrée avec salade et croûtons à l'appart ou bien les pique-niques dans les calanques me faisaient vraiment prendre un bol d'air !

Enfin, vient le tour du frère. Oliv', je ne saurai pas par où commencer. Sans doute par te remercier de m'avoir pris sous ton aile pour me faire découvrir les bords et les fonds de la Méditerranée mais aussi ce fameux analyseur Pyramide ! J'en aurais appris des choses passionnantes ! Et puis, bien sûr, merci de m'avoir accueilli si souvent comme un roi sur ce bijou qu'est la presque île de Giens. Quelle fierté de me dire qu'on aura exploré (quasi) tous les fonds et crapahuté sur tous les bords de l'île tous les deux ! Nul doute que ces longs week-ends peinarde me manqueront et m'auront toujours fait un bien fou. Malgré tes choix de supporterisme douteux et quelques approximations culinaires (personne n'est parfait) tu m'auras toujours fait me sentir comme à la maison et crois moi, dans la rude période de rédaction, ce fut vraiment appréciable. En tout cas, je te souhaite le meilleur pour ton arrivée chez les bretons, mais j'ai le sentiment que ça va plutôt bien se passer pour toi. Prépare le canap', je ne vais pas traîner à venir te rendre visite. Ah oui, un dernier truc. Tu le dis souvent des autres, mais n'oublie jamais, c'est toi le meilleur.

Cette première étape maritime a été suivie de mon année italienne à l'observatoire d'Arcetri et la découverte de la belle ville de Florence, notamment grâce à la vue depuis l'observatoire ! Vorrei ringraziare tutte le persone del gruppo di ottica adattiva dell'Osservatorio di Arcetri che mi hanno accolto per un' anno tra di loro. Devo dire che tra tutti i posti in qui sono stato il vostro caffè era quello migliore, senza dubbio ! Grazie quindi a Fabio, Paolo (in particolare per avermi fatto entrare nel gruppo di calcetto), Lorenzo, Tommaso, Marco B, Alessio (anche per la giornata con le pizze a casa tua !) Marco X, Armando, Marina e Beatrice per le numerose conversazioni durante le pause pranzo. Grazie anche ad Elena per i numerosi passaggi in macchina per raggiungere l'osservatorio ! In particolare, vorrei ringraziare Guido, Alfio, Enrico e Runa per la vostra disponibilità. Mi avete aiutato molto a sviluppare il mio modello di FLAO e realizzare la dimostrazione sperimentale ad LBT. È stato un piacere lavorare con voi ed ho imparato molto durante quest'anno ! Durant cette deuxième année, j'ai également pu échanger avec Serge et Cyril du DOTA de l'ONERA, merci à vous pour ces discussions très intéressantes sur l'optimisation de l'étalonnage d'un système d'OA ! Enfin, il me semble juste de finir avec le deuxième Cédric, avec qui j'ai partagé mon bureau, cet îlot français à l'observatoire ! Merci pour ton aide précieuse sur mes simulations (en particulier sur la syntaxe d'IDL !) et pour ta bonne humeur inébranlable (même si j'ai quand même réussi à te faire craquer une ou deux fois !).

This European tour was then followed by a step in Germany where I could join back the ESO Adaptive Optics Group. I would like to thank all of you for your kindness and availability. These bi-weekly PhD progress-meetings were extremely useful to me and I am really grateful that you attended them so frequently. Thanks then to Markus (in particular for giving me the opportunity to work a bit with the Pyramid of the HOT bench), Jérôme (qui aura donc suivi mon travail depuis 2016 avec mon stage dans le groupe AO... Merci de m'avoir si bien préparé, c'était juste un échauffement en quelques sortes !), Miska, Christophe (en particulier, merci pour ton aide concernant mes projets post-doctorat !), Pierre, Elise, Stefan and by extension Rob and Pavel that were often joining us for the 16:00 break. Enfin, je souhaite particulièrement remercier Pierre-Yves qui n'a cessé d'être de bon conseil et qui a fait beaucoup pour que ma thèse se déroule dans les meilleures conditions. Merci pour ton accueil, ta gentillesse et ta confiance.

In fact, my year at ESO was extremely rich in terms of encounters and it will be hard not to forget anyone... So if I had to start with someone, I guess I would start with my dear office-mates. Kelly, quelle énergie ! Toujours partante pour organiser quelque-chose: du beach-volley à la soirée raclette ou bien boire un verre tout simplement ! Il n'aura pas fallu longtemps pour savoir qu'on s'entendrait bien et paf, ça n'a pas loupé ! C'était super de te retrouver à Marseille et tu vas me manquer mais je sais que tu viendras bientôt nous saluer à l'ESO ! De toute façon tu vas continuer à suivre mes traces non?

Then comes Prashant. We had fun. It was a real pleasure to tease you so often, but also to discuss on a daily basis about what was going on with our work or our life. I miss that ! And what should I say about the food? Your Indian dinners were always amazing. I hope that you will teach me how to do that some day ! However, now that you have experienced what a real pizza tastes like, I hope that you will cancel

your membership at Domino's Pizza !

Then come Nelly and Pablo, my dearest Chilean friends. Thank you for your hospitality and kindness, you really made me feel like I was at home anytime I would visit you ! I remember all the nice activities we did together, from volleyball to paintball including nice board-games evenings during the cold winter in Garching ! No wonder why I had such a nice time during this year at ESO ! And now that a new boy has joined the family, I can't wait to see him growing up !

In fact, I was lucky to arrive at ESO at the greatest hours of the "Freetime in Garching" group, and I could really appreciate my free-time during the summer in Bavaria by playing volleyball, swimming at the lakes, playing board games or just having drinks at the Biergarten ! So thank you all, Kateryna, Fabrice, Serban, Benoit, Stephen, Barnabas and of course the ones that joined the group later Jens, Byron ! These were good times, no doubt about it and i'm looking forward to see you all again !

Of course, I also have to mention the large Italian community that was always here to share some amazing products from Italy and always ready to organize nice dinners ! Thank you then to Sara (in particolare per i pomodorri !), Chiara, Giuliana, Eleonora (Eh si ci siamo ritrovati ad'ESO dopo la Sapienza !), Edo, Anita (in particolare per il caffè !), but also to the non Italians, Dinko, Prashin and Remco !

Of course, I will not forget one of the proudest citizen of Trento ! Thank you Carlo for all these nice days doing all kind of activities and in particular, these skiing trips ! We had some nice time in the mountains with my other skiing fellow Tereza. I am looking forward to go again with you, especially if this includes listening to the finest après-ski music (dear Mamma Lauda) !

Talking about skiing, I now think about one of the greatest skier of Scotland: Calum. I can't wait to make fun of your english accent in French ! I will definitely miss you in Garching but I am sure that you will visit some time to go to Jocky's Treff. Talking about Jocky's Treff, I am thinking about Adriano ! We did not have much time to get to know each other but I am coming back ! And maybe this time we will get to play football together !

Finally, I have to thank my dearest housemate Silvia. Grazie per tutto Silvia, per la tua gentilezza, e per tutte le volte che mi hai portato un pò di cibo da Roma ! Mi mancano le serate a cucinare, lamentarsi della vita o del lavoro ed apprezzare un buon Amaro nel bellissimo appartamento di Steiningerweg 3 ! Senza dubbio, il tuo supporto durante la stesura della tesi mi ha tirato sù...la qualità di questa tesi non sarebbe stata la stessa senza il tuo "approvvigionamento" da Castroni ! Grazie davvero, e come dici sempre tu... Daje !

Enfin, j'attaque la dernière étape de mon voyage, le retour à Marseille pour la rédaction du manuscrit de thèse. Là encore, malgré un emploi du temps un peu chargé, j'ai pu compter sur le soutien d'une belle bande pour aller m'occuper et me changer les idées ! Merci donc à Romain, Steven, Elder, Sandy, Axel, Sergio, Pierre, Elena, Alessia pour ces nombreuses parties de beach-volley sur la plage du Prado ou bien les parties de foot du midi, ça m'aura vraiment servi pour décompresser dans cette partie intense de la thèse ! Merci également à Mona, la dernière arrivée qui n'a pas mis longtemps à s'intégrer et j'espère que tu vas t'éclater à Marseille ! J'en profite aussi pour remercier Alexis d'avoir pris le temps de relire un chapitre de ma thèse et

d'avoir pris des nouvelles si régulièrement. Depuis le temps que je dois venir te voir, je n'ai vraiment plus aucune excuse maintenant que j'ai un peu plus de temps !

Et puis bien sûr Vincent, là aussi, quelle énergie et quelle curiosité ! Toujours partant pour tout type d'activité et toujours disponible pour discuter de la Pyramide et bien sûr des gains optiques... merci pour ton aide, tu m'auras fait comprendre plein de choses, et ta bonne humeur est contagieuse ! Comme tu le dis si souvent, t'es en bombe !

Enfin Yoann... ça m'a fait plaisir de passer autant de temps avec toi. Toujours là pour les copains ! C'est génial qu'on ait réussi à faire ce petit périple italien, et ça m'a encore plus fait plaisir de voir à quel point tu l'as apprécié ! à quand le prochain? quand tu auras acheté ta méthode d'italien !

Le dernier paragraphe de cette (longue?) section de remerciements est bien évidemment dédié à ma famille qui m'aura soutenu sans faille du début à la fin.

Merci donc à Violaine pour ses nombreux petits gestes et lettres tout au long de ces trois ans, j'ai particulièrement apprécié le petit paquet d'Egypte durant la phase de rédaction ! Il y avait tout ce qu'il fallait dedans pour me faire sentir comme à la maison !

Magda, le pigeon voyageur qui sera venue me rendre visite dans toutes les villes où j'ai habité ! J'espère que ça continuera ! En particulier, merci pour avoir toujours été là dans les moments faciles et un peu moins faciles.

Nayra, ça m'a fait plaisir de te montrer Marseille, et j'espère que tu auras apprécié ! En tout cas, merci mille fois d'avoir relu l'anglais de mon manuscrit ! Je peux t'assurer que dans ce moment de stress intense, c'était quand même super de savoir que je pouvais compter sur toi ! Merci également à Myriam d'avoir relu certaines parties de la thèse, cela m'a vraiment aidé à en voir le bout !

Enfin, je remercie mes parents de m'avoir toujours accompagné et soutenu tout au long de mes études, depuis ma première aventure romaine jusqu'au jour de ma soutenance où vous aurez été d'une aide précieuse. Quelques lignes ne suffiraient pas pour exprimer toute ma gratitude, mais sachez que si j'en suis arrivé là, vous en êtes pour beaucoup.

Contents

Abstract	3
Résumé	5
Aknowledgments/Remerciements	10
Contents	11
Introduction	18
1 The Context of the Large Adaptive Telescopes	19
1.1 Imaging through the atmospheric turbulence	20
1.1.1 Modal representation of the phase	20
1.1.2 Statistical properties of the turbulence	21
1.1.3 Modelling the atmospheric turbulence	23
1.2 The concept of Adaptive Optics	23
1.2.1 Principle of an Adaptive Optics system	23
1.3 Wave-Front Sensors	24
1.3.1 Shack Hartman WFS	25
1.3.2 The Pyramid WFS	27
1.3.2.1 Principle of a PWFS	28
1.3.2.2 Post-Processing of the PWFS signals	30
1.3.2.3 The PWFS in operation: a trade-off between Sensitivity and Linearity	32
1.3.2.4 Optical Gains of the PWFS	34
1.4 Deformable Mirrors	36
1.5 Control of an Adaptive Optics System	39
1.5.1 Interaction Matrix	39
1.5.2 Modal Interaction Matrix	40
1.5.3 Dynamic control of an AO loop	41
1.6 Calibration of an AO system	44
1.6.1 Measurement of the Interaction Matrix	44
1.6.2 Impact of a mis-registration	45
1.7 Adaptive Telescopes	46
1.7.1 AO Calibration for Large Adaptive Telescopes	47
1.7.1.1 On-sky calibration	48
1.7.1.2 Synthetic-Based calibration	49
1.7.2 The Large Binocular Telescope	50
1.7.3 The Adaptive Optics Facility at the Very Large Telescope	53
1.7.4 The Extremely Large Telescope	55

1.7.5	AO Calibration in the VLT/ELT context	57
2	Synthetic Based Calibration with Pyramid WFS	59
2.1	Mis-registrations and mis-alignments	60
2.1.1	Definition	60
2.1.2	Sensitivity to a mis-registration	62
2.2	Modelling of the key components of the AO System for the computation of the synthetic interaction matrix	63
2.2.1	Modelling of the Deformable Mirror	63
2.2.1.1	Experimental Influence Functions	63
2.2.1.2	Synthetic Influence Functions	64
2.2.2	Modelling of the Pyramid WFS	66
2.2.2.1	Pyramid Phase Mask	66
2.2.2.2	Selection of the valid pixels	68
2.3	Experimental Validation: MNRAS article	70
2.4	Complementary Analysis: Fully Synthetic DM	85
2.4.1	Model Validation	85
2.4.2	Influence Functions	86
2.4.3	Model mis-registration parameters identification	87
2.5	Optimizing the Mis-Registration Identification Algorithm	91
2.5.1	Principle	91
2.5.2	Linearity of the mis-registration parameters estimation	93
2.5.3	Coupling between the parameters	96
2.5.4	Identification of large amplitude mis-registrations	98
2.5.5	Sensitivity to a modal scaling	99
3	Online Identification of Mis-Registration Parameters: The Invasive Ap- proach	103
3.1	Definition of the model	105
3.2	On-sky acquisition of reference signals	105
3.3	Maximizing the sensitivity to a mis-registration	106
3.3.1	Defining the sensitivity to a mis-registration	106
3.3.2	An Optimal Modal Basis for the Mis-Registration Identification?	107
3.3.3	Impact on the scientific observations	115
3.4	Application: Mis-Registration Identification using on-sky signals	118
3.4.1	Impact of the SNR on the parameters identification	120
3.4.2	Impact of the wind on the parameters identification	123
3.4.3	Ramps of mis-registrations	124
3.4.3.1	Ramp of rotation	125
3.4.3.2	Ramp of shift X	127
3.4.3.3	Ramp of shift Y	129
3.4.4	Dynamic case with various mis-registrations	131
4	Online Identification of Mis-Registration Parameters: The Non-Invasive Approach	133
4.1	Estimation of the interaction matrix from closed loop data	133
4.1.1	AO equations	133

4.1.2	Estimation of the interaction matrix from incremental closed loop data	134
4.1.3	Analysis of the composition of the signals of interest	136
4.2	Validation of the method	139
4.3	Challenging the validity of the hypothesis: limitations of the method	144
4.3.1	Centered System	145
4.3.2	Mis-registered System	155
4.3.3	Analysis of the spatio-temporal correlations	155
4.3.3.1	Impact of the loop gain	155
4.3.3.2	Focusing on the structures due to the spatio-temporal correlations	159
4.3.4	Ramp of mis-registrations	161
4.3.4.1	Ramp of Rotation	162
4.3.4.2	Ramp of Shift Y	164
4.3.4.3	Ramp of Shift X	165
4.4	Application with the Pyramid WFS	167
4.4.1	Nominal Case	168
4.4.2	Impact of the loop gain	171
4.4.3	Limit cases	172
4.5	Discussion	175
Conclusion and Perspectives		178
6 Résumé Long		182
Résumé Long		182
6.1	Introduction et Contexte	182
6.1.1	L'Optique Adaptative	182
6.1.1.1	Principe	182
6.1.1.2	Étalonnage d'un système d'OA	182
6.1.2	Le contexte des futurs grands télescopes adaptatifs	184
6.2	Modélisation de système d'OA avec ASO Pyramide: le cas du Large Binocular Telescope	185
6.2.1	Développement du modèle et principaux objectifs	185
6.2.2	Validation du modèle	187
6.3	Identification des paramètres du modèle sur ciel: l'approche perturbatrice	188
6.4	Identification des paramètres du modèle sur ciel: l'approche non-perturbatrice	191
APPENDIX		197
A AO Modelling of the High Order Test-Bench		197
B Complementary Analysis of the PCA Modes		201
C AO4ELT5 Conference Proceeding: Overview of the AO Calibration Strategies in the ELT context.		208

D SPIE Conference Proceeding: Analysis of AO modelling for Pseudo-Synthetic Interaction Matrix at the LBT.	220
Bibliography	231
List of Figures	239
List of Tables	250

List of Abbreviations

AO	Adaptive Optics
AOF	Adaptive Optics Facility
ASM	Adaptive Secondary Mirror
CL	Closed-Loop
CoG	Center of Gravity
DSM	Deformable Secondary Mirror
ELT	Extremely Large Telescope
ESO	European Southern Observatory
FEA	Finite Element Analysis
FLAO	First Light Adaptive Optics
GLAO	Ground Layer Adaptive Optics
GMT	Giant Magellan Telescope
HOT	High Order Test-bench
KL	Kharunen-Loève
LBT	Large Binocular Telescope
LGS	Lase Guide Star
LTAO	Laser Tomography Adaptive Optics
MCAO	Multi Conjugate Adaptive Optics
MMT	Multi Mirror Telescope
NCPA	Non Common Path Aberrations
OL	Open-Loop
OOMAO	Object Oriented Matlab Adaptive Optics
PCA	Principal Component Analysis
PSD	Power Spectral Density
PSF	Point Spread Function
PSIM	Pseudo Synthetic Interaction Matrix
PWFS	Pyramid Wave-Front Sensor
RMS	Root Mean Square
RMSE	Root Mean Square Error
RTC	Real Time Computer
RTF	Rejection Transfer Function
SCAO	Single Conjugate Adaptive Optics
SH	Shack-Hartmann
SNR	Signal to Noise Ratio
SVD	Singular Value Decomposition
TCog	Thresholded Center of Gravity
TMT	Thirty Meter Telescope
VLT	Very Large Telescope
WCoG	Weighted Center of Gravity
WFE	Wave-Front Error
WFS	Wave-Front Sensor

Introduction

Today's Astronomy observations rely on state-of-the-art instrumentation and facilities. As the observation of extremely distant objects is the only source of information, the gain in higher sensitivity, better image quality, and wider field of view allows for a more detailed understanding of the Universe. The resolution provided by a telescope is defined as the smallest angular separation between two distinguishable objects. The ultimate resolution is limited by the diffraction. In this case, it is equal to the ratio between the observing wavelength λ and the diameter of the telescope D . With the development of the technological capacities, it appeared judicious to develop new telescopes with larger diameters to improve the optical resolution of the observations and increase the collecting area. This eventually led to considering segmented telescopes with the Multiple Mirror Telescope (MMT) (Hege et al. 1985) and the Keck Observatory (J. E. Nelson et al. 1985) to overcome the technological challenge of building large monolithic mirrors.

However, λ/D defines the **optimal** angular separation of the telescope when operating at the diffraction limit, assuming a perfectly plane wave-front. For ground-based astronomical observation, this hypothesis is no longer true since the light coming from the celestial objects has to go through the earth's atmosphere. The non homogeneities of the different structures of the atmosphere (temperature, humidity) create variations of the refractive index of the air that distort the wave-front and impact the quality of the observation on a fast temporal scale. The strength of the turbulence can be characterized using the Fried diameter $r_0(\lambda)$ (D. Fried 1965) that defines the typical area over which the turbulent wave-front can be considered as "flat" (wave-front variance inferior to 1 rad²). This parameter is used to define the seeing s of the atmosphere as the ratio between λ and r_0 ¹. The seeing corresponds to the effective angular separation of the telescope in presence of atmospheric turbulence. In other words, for a telescope with a diameter larger than r_0 the effective angular resolution at the wavelength λ is no longer λ/D but is instead λ/r_0 : the telescope is not diffraction-limited anymore but **seeing-limited**. Values of r_0 in the visible (550 nm) typically go from 7 cm under bad seeing conditions to 25 cm in the best conditions. This means that even in extremely good conditions, the angular separation of a telescope in the visible, with infinite diameter, would be the same as a telescope with a 25 cm diameter. Fortunately, the development of Adaptive Optics (AO) (Babcock 1953) for Astronomy (Rousset et al. 1990) in the 1990's allowed to overcome these observational challenges.

This technology is now commonly spread on large aperture optical telescope facilities to compensate in real time the variations of optical index in the atmosphere and retrieve the full angular resolution of the telescope. The principle of a typical AO system is the following: a Wave-Front Sensor (WFS) measures a signal relative to the wave-front and sends it to a Real Time Computer (RTC) that computes the

1. More exactly $s = 0.976 \frac{\lambda}{r_0}$

corresponding commands to apply on a Deformable Mirror (DM). This system is usually operated in a feedback-loop at a higher frequency than the temporal evolution of the turbulence (typically, a few hundred Hz). However, to provide a good correction (*i.e.* to be able to apply the correct shape on the DM at the right time), the AO loop has to be properly calibrated before the operations. This is notably achieved by measuring the **interaction matrix** of the system which consists in recording the WFS signals corresponding to a specific command of the DM actuators. If this calibration is imperfect, the AO system may not be responding as expected, and the resulting AO performance will be affected.

Within a decade, there will be a new generation of telescopes with diameters up to 39m, called the Extremely Large Telescopes. These giants will address fundamental astrophysical science cases as for instance the direct imaging and characterization of rocky exoplanets located close to their orbiting star or the study of bulk and evolution of the first galaxies. The scientific potential of these new telescopes relies on challenging new AO concepts such as Deformable Mirrors integrated inside the telescope itself, turning them from Active to Adaptive Telescopes.

The colossal size of these Large Adaptive Telescopes and the complexity of the scientific instruments compel us to a complete rethinking, in order to improve the overall performance, but more specifically the sensitivity and the robustness of the AO systems, and thus to maximize the astrophysical returns of AO-assisted instruments. The Extremely Large Telescope (ELT) (Gilmozzi et al. 2007), in particular, will provide a challenging environment for the AO systems. First of all, the calibration of a large number of degrees of freedom (around 5000 actuators) with no external calibration source will be required. Moreover, the DM will be located directly in the telescope, far from the AO instruments with moving elements in the optical path. Regular evolution of the DM-WFS registration (Rotation, shifts or higher order of pupil distortion of the DM actuators grid with respect to the WFS subapertures) are therefore to be expected during the observations. These so-called mis-registrations have to be monitored and compensated as they will highly affect the AO performance or lead to loop instabilities that will jeopardise the scientific observations.

In addition, all the future Single Conjugate Adaptive Optics instruments of the ELT will be equipped with Pyramid Wave-Front Sensors (PWFS) (Ragazzoni 1996). This type of WFS has achieved impressive on-sky performance in various facilities and provides a higher sensitivity than Shack Hartmann WFS with a lower propagation of aliasing errors. However, this gain in performance comes with a cost in terms of operational complexity. The PWFS appears indeed to be highly non-linear with a response that depends on the level of AO correction itself, the so-called optical gains. These challenges are currently under active investigation by the AO community to make AO systems more robust to these non-linear effects and benefit from the full potential of the high sensitivity of PWFS.

To overcome these operational challenges, optimizing the calibration strategies of the AO systems is required, especially working with PWFS. This thesis is organized as follows: a first chapter is dedicated to the presentation of the context of this research and introduces the principle and properties of an AO system. Particular attention is given to the specificities of PWFS. In addition, we give a summary of the technical challenges of existing and future Large Adaptive Telescopes, focusing on the aspects of AO calibration.

The second chapter addresses the-key elements to develop a pseudo-synthetic model for an AO system equipped with Pyramid WFS. The purpose of the model, developed in the OOMAO simulator (R. Conan et al. 2014), is to generate pseudo-synthetic interaction matrices that can be used on a real system. We present the numerical and experimental validation of a pseudo-synthetic model for the AO systems FLAO of the Large Binocular Telescope. The successful results of this experiment were published in the article Heritier et al. 2018 where we reported the closed-loop performance achieved at the telescope using an interaction matrix generated from the model.

In the following chapters, we investigate two different strategies to identify the mis-registration parameters during the scientific observations. Chapter 3 analyzes the possibility to track the mis-registration parameters by applying small disturbances on the DM. We present how this **invasive approach** can be optimized by identifying the most sensitive modes to a given mis-registration and by reducing the number of signals required.

Finally, chapter 4 provides a thorough analysis of an existing method that consists in using only telemetry data to estimate a noisy interaction matrix of the system and extracting the corresponding mis-registration parameters. The developments achieved to characterize this **non invasive** approach allowed us to understand the underlying physics behind the estimation of the noisy interaction matrix and to identify the domain of validity and limitation of the method. These results will be presented in a second article that is still in preparation (Heritier et al. [in prep](#)).

1. The Context of the Large Adaptive Telescopes

1.1. Imaging through the atmospheric turbulence

We mentioned in the introduction that the non homogeneities of the different structures of the atmosphere (temperature, humidity) create variations of the refractive index n of the air that distort the wave-front and impact the quality of the observation on a fast temporal scale. In this section we will introduce a few key-properties of the atmospheric turbulence that will be required to introduce some of the problematics of this research¹. Defining $\vec{\rho}$ as the position vector and h as the altitude, the fluctuations $\delta n(\vec{\rho}, h)$ are given by the Kolmogorov spectrum:

$$\Phi_n(\vec{k}) = 0.033 (2\pi)^{-2/3} C_n^2(h) |\vec{k}|^{-11/3} \quad (1.1)$$

where $C_n^2(h)$ is the index structure constant and \vec{k} the spatial frequencies vector. This expression exhibits the asymptotic law in $|\vec{k}|^{-11/3}$ that is characteristic of the turbulence. In practice, the Kolmogorov spectrum will diverge for the low spatial frequencies. The Von-Kalman spectrum gives then a more accurate representation of the turbulence spectrum:

$$\Phi_n(\vec{k}) = 0.033 (2\pi)^{-2/3} C_n^2(h) \left[|\vec{k}|^2 + \left(\frac{1}{L_0} \right)^2 \right]^{-11/6} e^{-(|\vec{k}|l_0)^2} \quad (1.2)$$

where L_0 is defined as the outer-scale (where the largest eddies are formed) and l_0 as the inner-scale (where the turbulent energy is dissipated). In practice, the turbulence is distributed in layers, characterized by the value of $C_n^2(h)$ at the altitude h . Most of the turbulence is contained in the low-altitude layers (under 20 km).

The strength of the turbulence can be characterized using the Fried diameter $r_0(\lambda)$ (D. Fried 1965):

$$r_0(\lambda) = \left[0.423 \left(\frac{2\pi}{\lambda} \right) \int_0^\infty C_n^2(z) dz \right]^{-3/5} \quad (1.3)$$

The Fried diameter defines the typical area over which the turbulent wave-front can be considered as "flat" (wave-front variance inferior to 1 rad²).

1.1.1. Modal representation of the phase

To study the properties of the atmospheric turbulence, it is often more convenient to consider a modal representation of the phase. A modal basis \mathbf{Z} can be used to decompose a given phase ϕ as a linear combination of the different modes \mathbf{z}_i that constitute the basis \mathbf{Z} :

$$\phi = \sum_{i=1}^{\infty} a_i \cdot \mathbf{z}_i \quad (1.4)$$

where the a_i are scalars defined as the **modal coefficients** of the phase ϕ . The modal basis is usually chosen to be orthonormal:

$$\langle \mathbf{z}_i | \mathbf{z}_j \rangle = \delta_{i,j} \quad (1.5)$$

1. For a more detailed analysis of the atmospheric turbulence properties the reader can refer to Roddier 1999

where the scalar product is defined with respect to the Frobenius Norm and $\delta_{i,j}$ is the Kronecker symbol. This property ensures to have a unique representation of a given phase by the modal basis.

The most common modal basis used to describe the properties of the atmosphere consists of the Zernike polynomials (Zernike 1934). They have an analytical expression using the polar coordinates $\vec{\rho} = (\rho, \theta)$. We define a Zernike mode Z_i as:

$$\begin{aligned} Z_i &= \sqrt{n+1} \mathbf{R}_n^m(r) \sqrt{2} \cos(m\theta) & \text{for } m \neq 0 \text{ and } i \text{ even} \\ Z_i &= \sqrt{n+1} \mathbf{R}_n^m(r) \sqrt{2} \sin(m\theta) & \text{for } m \neq 0 \text{ and } i \text{ odd} \\ Z_i &= \sqrt{n+1} \mathbf{R}_n^0(r) & \text{for } m=0 \end{aligned} \quad (1.6)$$

where

$$\mathbf{R}_n^m(r) = \sum_{s=0}^{(n-m)/2} \frac{(-1)^s (n-s)!}{s! [(n+m)/2 - s]! [(n-m)/2 - s]!} r^{n-2s} \quad (1.7)$$

The modes are ordered according to their radial order n and to the azimuthal order m which correspond to sorting them in terms of spatial frequencies. By construction, the Zernike modes are orthonormal on a circular pupil. The 16 first Zernike modes are illustrated in Figure 1.1.

1.1.2. Statistical properties of the turbulence

The properties of the Zernike polynomials are particularly useful to achieve a statistical analysis of the turbulence. Figure 1.1 gives the decomposition of the phase variance of the turbulence on the Zernike Polynomials (Noll 1976) which informs on the **spatial properties of the turbulence**. This result indicates that most of the energy of the turbulence is contained in the low-order modes. In addition, since the Zernike polynomials are sorted in terms of spatial frequencies, we retrieve the asymptotic law in $(n+1)^{-11/3}$ from the Kolmogorov spectrum.

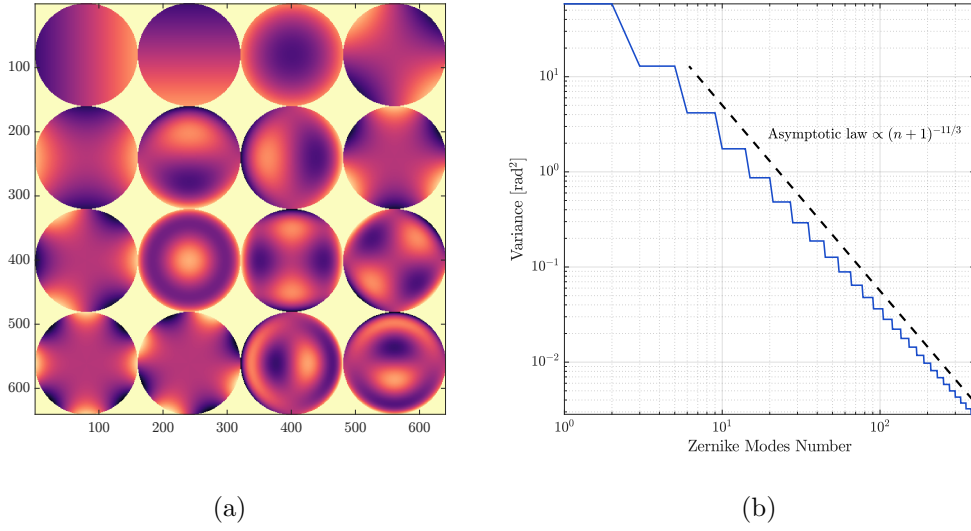


Figure 1.1. – 2D representation of the 16 first Zernike Polynomials (a) and decomposition of the turbulence variance on the 400 first Zernike polynomials (b).

Using this modal decomposition of the atmosphere, it is possible to determine analytically the **temporal properties of the atmosphere** and to compute analytically (J.-M. Conan 1994) the temporal Power Spectrum Density (PSD) of the modal coefficients a_i :

$$PSD_i = \langle |\mathcal{F}[a_i(t)](f)|^2 \rangle \quad (1.8)$$

where $\mathcal{F}[\bullet]$ is the Fourier transform of \bullet and f is the temporal frequency.

Figure 1.2 gives the temporal PSD of the first and 300th Zernike Polynomial using the phase-screens generated in the simulator OOMAO (R. Conan et al. 2014). They exhibit a different cut-off frequency, for the first (≈ 10 Hz) and for the 300th Zernike mode (≈ 100 Hz). These results are in agreement with the theoretical cut-off frequency given in J.-M. Conan 1994:

$$f_c = 0.3(n+1) \frac{\vec{v}}{D} \quad (1.9)$$

where \vec{v} is the wind speed and D the telescope diameter.

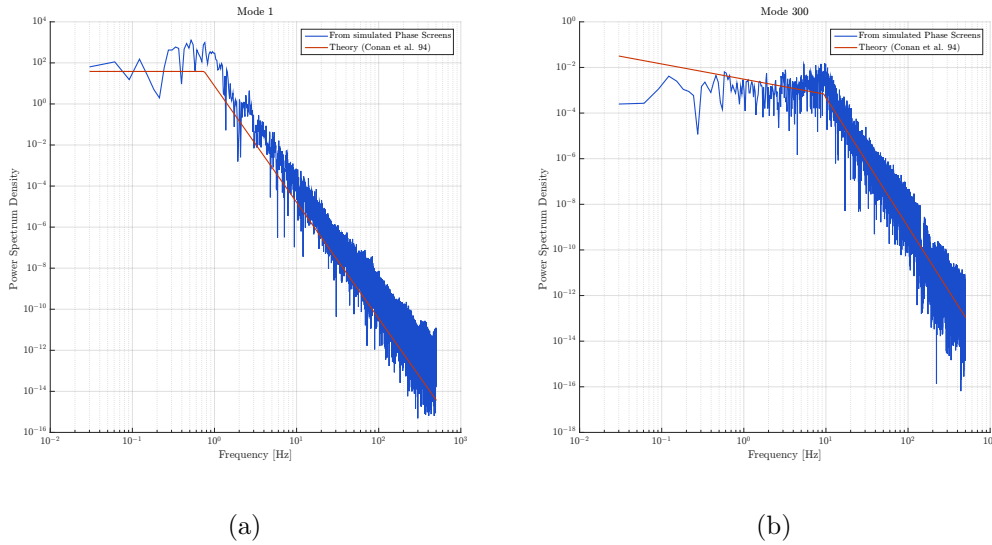


Figure 1.2. – Temporal PSD of the first (a) and 300th Zernike Polynomial (b). The red curves correspond to the theoretical PSD determined in J.-M. Conan 1994. We considered a wind-speed of 15 m/s and an 8-meter telescope.

Figure 1.2 illustrates the fact that small spatial frequencies evolve on a slower scale than high spatial frequencies. The temporal spectrum is characterized by an asymptotic law in $f^{-17/3}$.

1.1.3. Modelling the atmospheric turbulence

In practice, to model the different layers of the atmosphere, we often assume that the atmosphere is a superposition of independent layers in uniform translation. The evolution of the phase screens depends only on the wind direction and speed $\vec{v}(h)$, where h is the altitude of the layer. This hypothesis is called the **Frozen Flow** hypothesis (Taylor 1938). In the following of this thesis, we will call an atmosphere composed of a single layer with constant wind speed a **Frozen Flow atmosphere** and an atmosphere composed of several layers with different wind directions and speed a **Boiling atmosphere**. In OOMAO (R. Conan et al. 2014), which is the simulator tool used during this research, the phase screens are generated using the method introduced in Assémat et al. 2006 to generate infinite sequences of turbulent phase-screens. A more detailed section describing the numerical tool OOMAO is provided in chapter 2 and the different simulation parameters detailed in the different sections.

1.2. The concept of Adaptive Optics

1.2.1. Principle of an Adaptive Optics system

This technology was initially developed for military purposes (Babcock 1953) but has been applied to Astronomy for the first time with the COME-ON experiment (Rousset et al. 1990), providing the first diffraction-limited astronomical images from

the ground using meter class telescopes. The principle of Adaptive Optics consists in estimating the optical aberrations present in the wave-front using a **Wave-Front Sensor** (WFS) and in compensating for them almost in real time using a corrective device, usually a **Deformable Mirror** (DM). The principle of an Adaptive Optics System is presented in Figure 1.3.

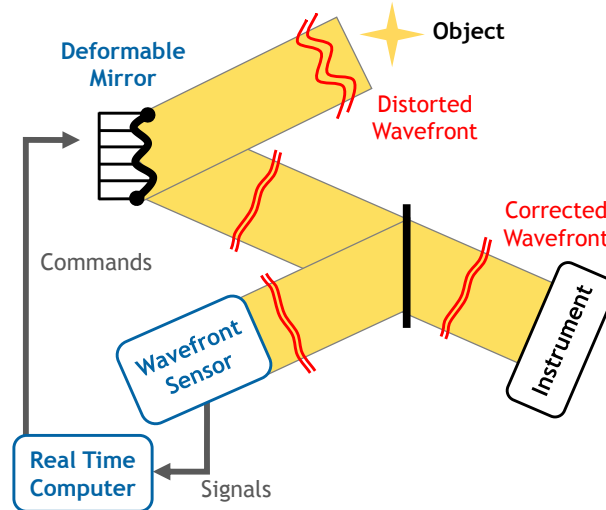


Figure 1.3. – Principle of an Adaptive Optics System.

An AO System requires the light coming from a guide star (natural or artificial bright object, close to the science object on sky) to illuminate a deformable mirror that can modify its shape to compensate for the optical paths and cancel the optical aberrations. On its way to a scientific detector, a fraction of the light (usually an interval of wavelength that has no scientific interest) is sent to the WFS that measures a signal related to the incoming wave-front. These measurements are input to a **Real Time Computer** (RTC) that reconstructs the wave-front and determines the appropriate commands for the DM. This process is operated in a feedback loop running at least ten times faster than the rate of changes in the atmosphere, typically at 1 kHz.

In this section we introduce the three main components of an AO system, focusing first on the WFS that will be investigated in this manuscript, the Shack Hartmann and Pyramid WFS. We then introduce the concept of deformable mirrors, investigating the different technologies that are of interest for our research. At last, we will introduce the core of the AO system, the control system that allows to determine the DM commands from the WFS measurements and operate the AO system in a feedback-loop.

1.3. Wave-Front Sensors

The purpose of a Wave-Front Sensor is to estimate the wave-front shape of the incoming light with the required spatial and temporal sampling. It typically requires indirect methods to convert phase-related information into signals that can be measured. In practice, the amplitude of the phase that can be well measured by the WFS is limited. We define the **linearity** of a WFS as the range of amplitude for which the sensor response is linear. We define the **sensitivity** of the WFS as the slope of the

sensor's response in the linear regime. These notions are illustrated in Figure 1.4 that gives the typical linearity curve of a WFS with a sensitivity of 1. For a phase amplitude of more than 40 nm RMS, the WFS measurements start to become saturated.

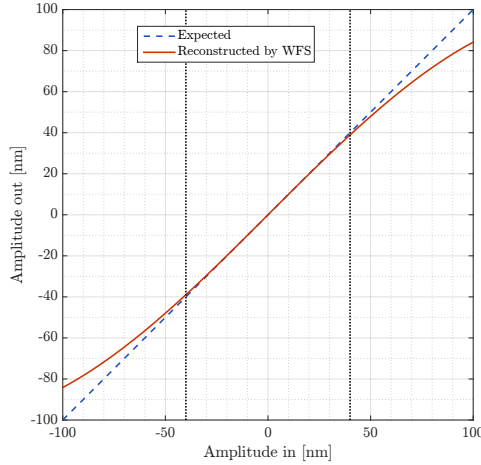


Figure 1.4. – Linearity curve of a WFS characterized by a sensitivity of 1. It exhibits the linear regime (within the two dotted lines) and the saturation of the WFS outside of the linear regime (absolute amplitude > 40 nm RMS).

In the linear regime, a WFS measurement y corresponding to a phase ϕ can then be written as:

$$y = M_{\text{WFS}} \cdot \phi \quad (1.10)$$

where M_{WFS} is a matrix that represents the WFS model measurement (light propagation and post-processing of the signals). Let us now introduce the properties of the two most common WFS, the Shack Hartmann and Pyramid WFS.

1.3.1. Shack Hartman WFS

We present here the principle of the Shack-Hartmann WFS (Hartmann 1900, Shack 1971) which has been the main WFS used for the development of Adaptive Optics. The principle of the SH-WFS consists in measuring the slopes of the wave-front of an incident light beam by imaging the light source through an array of lenslets, typically conjugated to the pupil plane. Each subaperture will image the source creating a spot on the detector. By measuring the spots position (over a reference), the local Tip/Tilt of the wave-front can be estimated, as illustrated in Figure 1.5.

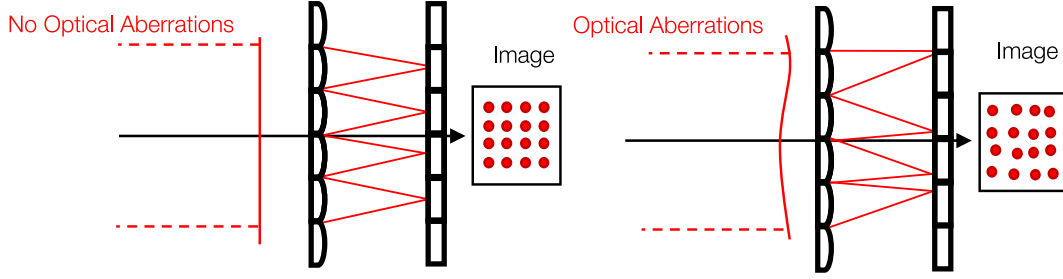


Figure 1.5. – Principle of the Shack Hartmann WFS: the movements of the spots on the detector indicate the presence of local Tip/Tilt at the level of the lenslet array.

To measure the spots position, different **centroiding algorithm** can be considered. Typically, the coordinates (x_P, y_P) of the Center of Gravity (CoG) P of a spot image are given by:

$$x_P = \frac{\sum_{i=1, j=1}^{n_{Pix}} I(i, j) x_{i,j}}{\sum_{i=1, j=1}^{n_{Pix}} I(i, j)} \quad y_P = \frac{\sum_{i=1, j=1}^{n_{Pix}} I(i, j) \cdot y_{i,j}}{\sum_{i=1, j=1}^{n_{Pix}} I(i, j)} \quad (1.11)$$

where $I(i, j)$ stands for the value of the pixel considered with coordinates $(x_{i,j}, y_{i,j})$. To provide a better robustness to the noise, it is also possible to consider other centroiding algorithm such as a Thresholded Center of Gravity (TCoG), where the pixel intensities under a given threshold are not considered, or a Weighted Center of Gravity (WCog), where a given function is used as a weighting function of the input spot image (typically a 2D Gaussian function). These algorithm are however impacting the linearity of the spot position estimation. The choice of centroiding algorithm results from a trade-off analysis between sensitivity and linearity that is system-dependant.

In addition, the linearity of the SH-WFS also depends on its **pixel-scale** that defines the portion of sky (in angle) seen by a pixel of the detector. The pixel-scale depends on the design of the SH: size and number of pixels per subaperture, interval of wavelength considered and lenslets properties (dimension and focal length).

An illustration of SH-WFS measurements is given in Figure 1.6. In that case, we consider a design with 20 by 20 subapertures for an 8-meter telescope, using 8 pixels per subaperture and a pixel scale of 0.22".

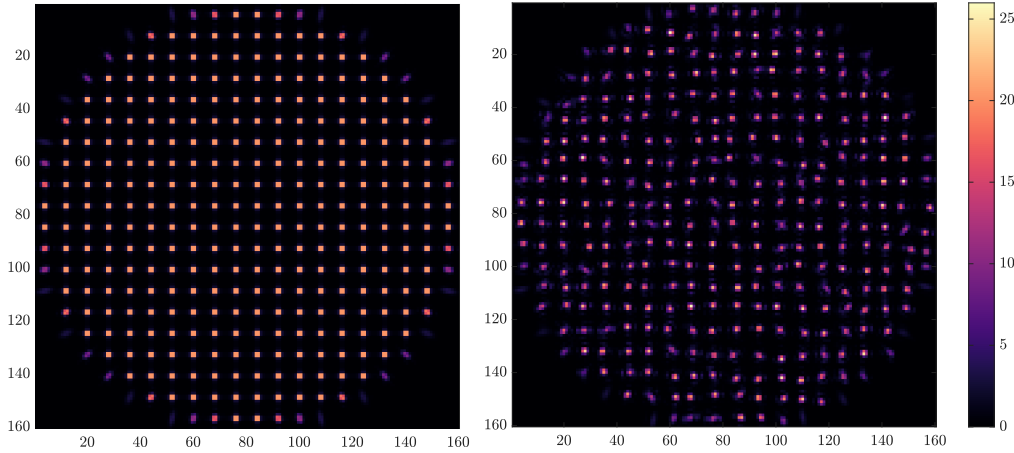


Figure 1.6. – SH-WFS measurements corresponding to a non-aberrated wave-front (left) and with aberrations (right).

By optimizing these parameters, the design of a Shack-Hartmann allows to maximize the dynamical range, *i.e.* the turbulence strength that can be linearly sensed by the sensor. The linearity will depend on several parameters including the spot dimension, the pixel size (sufficiently small to sample the spot properly), the subaperture Field of View (sufficiently large to avoid truncation), the level of noise and the choice of centroiding algorithm. The linear behavior of the SH-WFS makes it particularly suited for the AO modes operating with Laser Guide Stars (LGS).

1.3.2. The Pyramid WFS

The current development of the future AO System of the Extremely Large Telescopes revealed the limitation of the Shack Hartmann WFS to reach the ultimate AO performance. This WFS allowed to achieve the first milestones of the application of Adaptive Optics in Astronomy (Rousset et al. 1990) but it appears not to be suited to reach the performance required for the future AO systems of the ELT, especially in terms of AO correction and sensitivity. Since then, the AO community has been actively investigating new types of WFS to comply with these challenging requirements. The most promising system appears to be the Pyramid WFS (Ragazzoni 1996) that achieved impressive on-sky performance in various facilities (Esposito et al. 2012, Close et al. 2013, Jovanovic et al. 2015) and provides a higher sensitivity with respect to the Shack Hartmann (Ragazzoni et al. 1999, Esposito et al. 2001, Vérinaud 2004) and a lower propagation of aliasing (Vérinaud 2004). This gain in sensitivity is illustrated in Figure 1.7 that provides the comparison of AO performance between a PWFS and a SH-WFS as a function of the number of photons per subapertures.

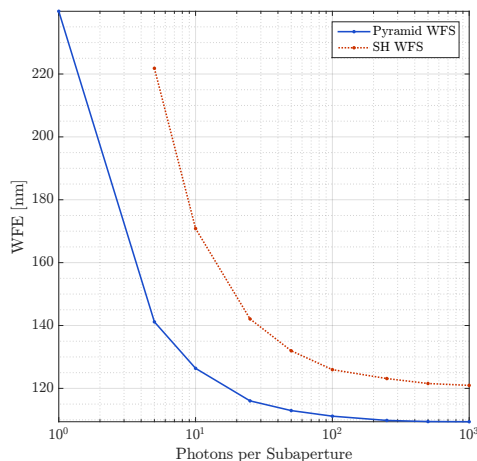


Figure 1.7. – Wave Front Error (WFE) as function of the number of photons per subaperture for a PWFS and a SH WFS.

In addition, the compact design of the PWFS offers a compression of the information on fewer pixels. This allows to relax the constraints on the design of the AO systems, in particular for the fast detectors with sub-electron noise (Feautrier et al. 2011). These promising results led all the first light instruments of the ELT to consider a PWFS for their Single Conjugate AO mode (Neichel et al. 2016, Clénet et al. 2016, Brandl et al. 2016) as well as the GMT (Pinna et al. 2014) and TMT instruments (Véran et al. 2015). However, this gain in performance comes with a cost in terms of operational complexity. The PWFS appears indeed to be highly **non-linear** with a response that depends on the level of AO correction itself, the so called **optical gains** (OG) of the Pyramid WFS (Korkiakoski et al. 2008, Esposito et al. 2015). These problematics are currently actively investigated by the AO community (Bond et al. 2018b, Deo et al. 2018a, Deo et al. 2019, Fauvarque et al. 2017, Fauvarque et al. 2019, Chambouleyron et al. *in prep*) to make the AO systems more robust to these non-linear effects and to benefit from the full potential of the high sensitivity of the PWFS.

1.3.2.1. Principle of a PWFS

The Pyramid WFS is a Fourier Filtering type of WFS (Fauvarque et al. 2017). It can also be seen as a generalization of the Foucault knife edge test as a pupil plane WFS. Its original design was proposed by Ragazzoni (Ragazzoni 1996) for its application in adaptive optics. A layout representing the PWFS is provided in Figure 1.8.

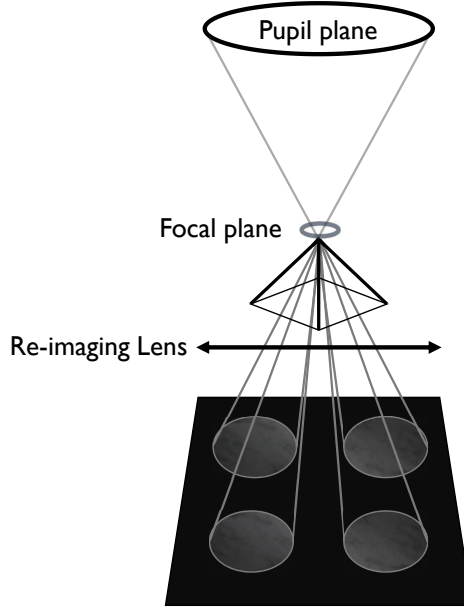


Figure 1.8. – Layout of the Pyramid WFS.

Optically, the PWFS consists of a transparent pyramid located at the focal plane of an optical system and acts as a spatial Fourier filter (Fauvarque 2017). This concept is illustrated in Figure 1.9.

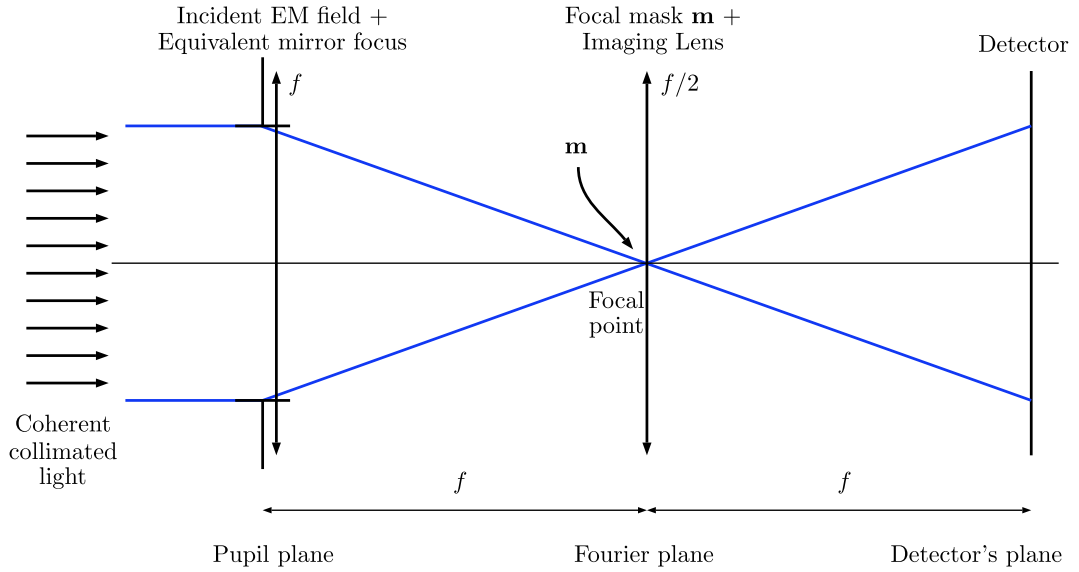


Figure 1.9. – Illustration of the concept of Fourier Filtering optical System (courtesy of O. Fauvarque, taken from Fauvarque et al. 2017)

Using the formalism developed in Fauvarque et al. 2017, the incoming electromagnetic field ψ coming on the pyramid can be written:

$$\psi(\phi^{turb}, n) = \sqrt{n} \cdot I_P \cdot \exp(i\phi^{turb}) \quad (1.12)$$

where n is the spatially averaged flux, I_P is the indicative function of the entrance pupil and ϕ^{turb} the turbulent phase at the observing wavelength λ . The Fourier mask

defined by the transparent pyramid can be fully characterized using its transparency function m :

$$m = \exp\left(\frac{2i\pi}{\lambda} OS\right) \quad (1.13)$$

where OS is the optical shape of the mask that depends on the number of faces of the pyramid and corresponding faces angle. In the case of the classical 4-sided PWFS with a phase angle of $\pi/2$, the mask m is represented in Figure 1.10. The angle of the faces will reject the light in different directions applying thus the operation of filtering.

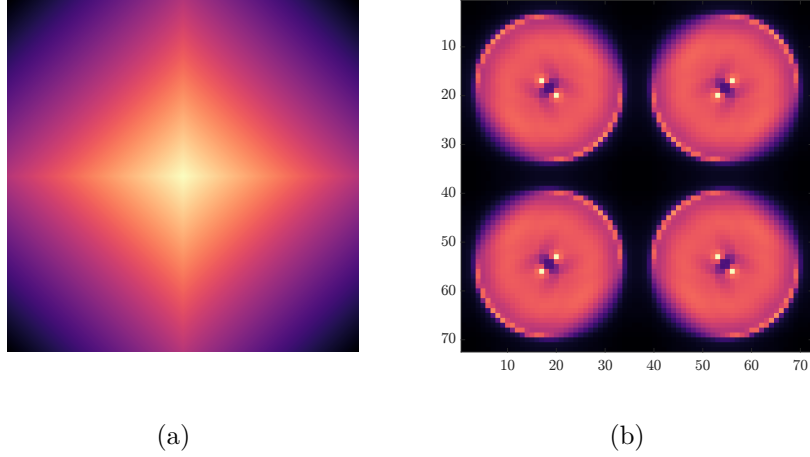


Figure 1.10. – Illustration of the argument of the mask m (a) of a classical Pyramid WFS and corresponding Pyramid Pupils (b) when I_P is circular with a central obstruction.

Using the wave optics formalism (diffraction theory) and the Fraunhofer approximation, it is possible to deduce the intensity on the detector:

$$I(\phi^{turb}, n) = \left| \psi(\phi^{turb}, n) * \mathcal{F}[m] \right|^2 \quad (1.14)$$

where the $\mathcal{F}[m]$ is the 2D Fourier transform of the mask and $*$ represents the convolution operator. This expression exhibits the dependency of I on the phase ϕ^{turb} and enable us to understand how the aberrations present in the focal plane can be coded in variation of pixels intensity on the detector.

1.3.2.2. Post-Processing of the PWFS signals

The post-processing of the PWFS signals has been evolving over the years. For the sake of clarity, we define the notation for the different quantities in Figure 1.11.

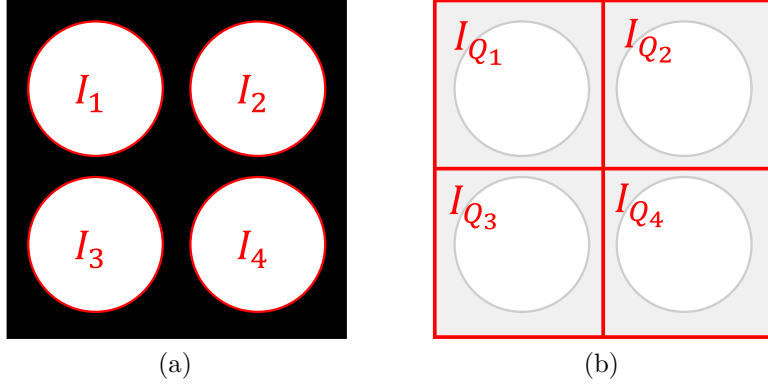


Figure 1.11. – Definition of the PWFS Pupils I_i (a) and Quadrants I_{Q_i} (b)

Initially, in Ragazzoni 1996, the post-processing proposed consisted in a quad-cell approach to compute the slopes maps, normalizing the signals by the total intensity in the selected PWFS pupils. Using the definition of Figure 1.11 for the different quadrants, the slopes $[S_X^{loc}, S_Y^{loc}]$ are defined as:

$$S_X(x, y)^{loc} = \frac{I_1(x, y) - I_2(x, y) + I_4(x, y) - I_3(x, y)}{I_{loc}(x, y)} \quad (1.15)$$

$$S_Y(x, y)^{loc} = \frac{I_1(x, y) - I_4(x, y) + I_2(x, y) - I_3(x, y)}{I_{loc}(x, y)} \quad (1.16)$$

where

$$I_{loc}(x, y) = I_1(x, y) + I_2(x, y) + I_3(x, y) + I_4(x, y) \quad (1.17)$$

The notation *loc* denotes the fact that the pixel values are normalized **locally** with the sum of the 4 pixels considered. In V erinaud 2004, a **global** normalization using the spatially averaged intensity has been introduced and widely adopted by the community. Using the definition of Figure 1.11 for the different quadrants, the slopes $[S_X^{glob}, S_Y^{glob}]$ are defined as:

$$S_X(x, y)^{glob} = \frac{I_1(x, y) - I_2(x, y) + I_4(x, y) - I_3(x, y)}{I_{glob}} \quad (1.18)$$

$$S_Y(x, y)^{glob} = \frac{I_1(x, y) - I_4(x, y) + I_2(x, y) - I_3(x, y)}{I_{glob}} \quad (1.19)$$

where I_{glob} is defined as

$$I_{glob} = \frac{1}{N_S} \sum_{x,y} I_1(x, y) + I_2(x, y) + I_3(x, y) + I_4(x, y) \quad (1.20)$$

where N_S is the total number of valid subapertures. However, another approach suggests to consider all the valid pixels (Clergeon 2014) instead of the quad-cell approach. It is currently becoming quite popular in the community as it offers a better robustness to the PWFS defects such as prism defects and mis-alignments (Deo et al. 2018b). In the following of the manuscript, the post-processing of the PWFS signals is achieved using the quad-cell approach with a global normalization $[S_X^{glob}, S_Y^{glob}]$.

1.3.2.3. The PWFS in operation: a trade-off between Sensitivity and Linearity

The particularity of the Pyramid WFS is that it exhibits a much smaller linear range than the SH-WFS. This can become problematic in the presence of a large residual phase. To overcome this difficulty, a solution proposed in Ragazzoni 1996 consists in artificially increasing the size of the PSF imaged on the top of the pyramid using spatial oscillations in the focal plane. Such spatial modulation is usually achieved using a circular Tip-Tilt modulation as introduced in Esposito et al. 2001 and allows the PWFS to be flexible to the different observing conditions. Figure 1.12 shows how the illumination of the pyramid signals evolves depending on the modulation radius: using a large modulation radius allows the light to fall back in the pyramid pupils, limiting the diffracting effects. An example of a few aberrations seen by a modulated PWFS are given in Figure 1.13.

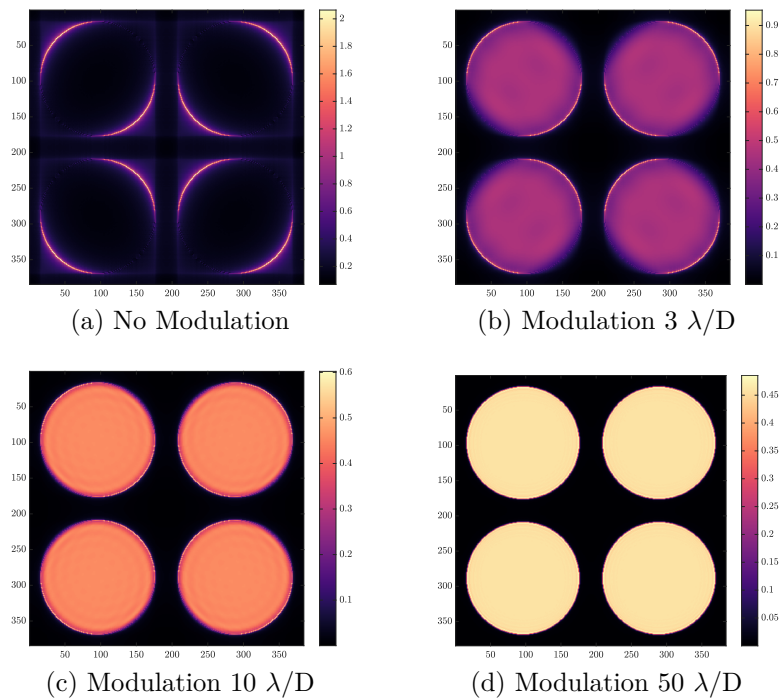


Figure 1.12. – Illustration of the Pyramid Pupils for different modulations.

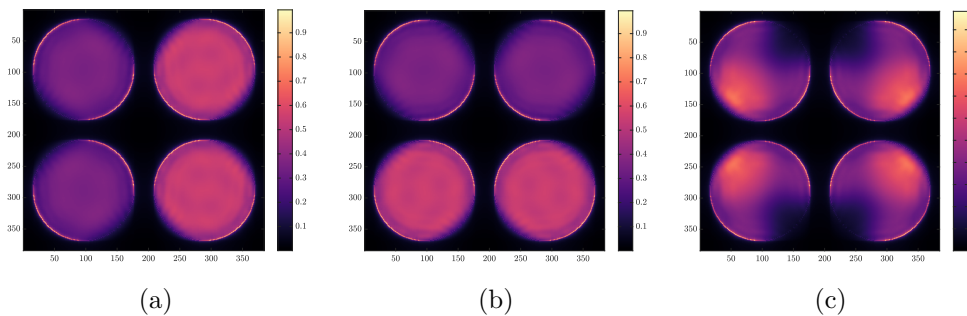


Figure 1.13. – Illustration of the PWFS signals corresponding to a Tip (a), a Tilt (b) and a Focus (c) aberration for a modulation of $3\lambda/D$

Modulating the PWFS to improve the linearity of the sensor has however a cost in terms of sensitivity. The analysis of sensitivity of a modulated PWFS provided in Fauvarque 2017 exhibits two different regimes: the sensitivity is first increasing linearly with the spatial frequencies while it remains constant for the high spatial frequencies. In addition, the cut-off frequency between the different regimes appears to be proportional to the modulation radius (Ragazzoni et al. 1999, Esposito et al. 2001, V erinaud 2004 Fauvarque 2017). In Figure 1.14, we reproduce these results using our simulator. We retrieve the same behavior with the two regimes depending on the modulation radius. In this case we also witness that the curves are not flat. This is due to the sampling of the PWFS. To obtain flat curves, the PWFS pupils should be sampled using the same sampling as the phase (Bond et al. 2018a).

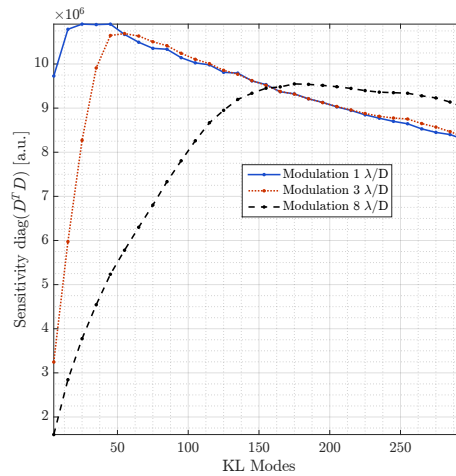


Figure 1.14. – Sensitivity Curves of the PWFS with respect to the KL Modal Basis (see section 1.5.2). The results are given for different modulation radius.

In addition, the corresponding linearity curves are given in Figure 1.15. To estimate the linearity, we apply a ramp of amplitude of a given mode and, using the reconstructor, we compare the amplitude of the modes reconstructed.

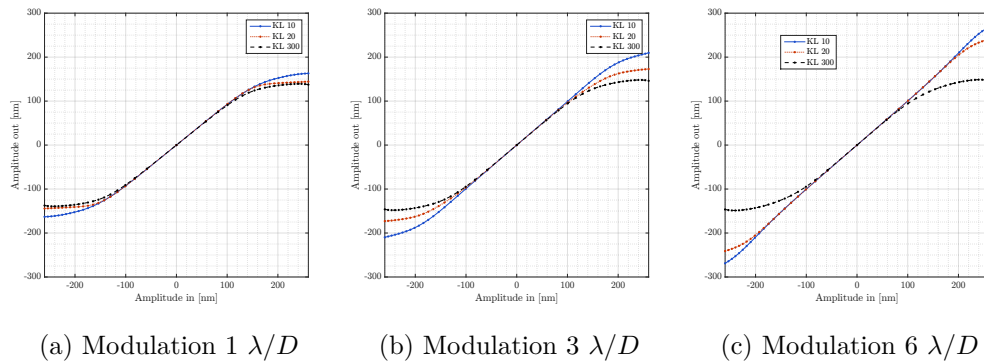


Figure 1.15. – Linearity curves for different modulation radius for different KL modes (see section 1.5.2).

These results exhibit the **modal sensitivity** and **linearity** of the PWFS that will depend on the modulation radius. This choice must then result from a trade-off between sensitivity and linearity that will depend on the observing conditions.

1.3.2.4. Optical Gains of the PWFS

In addition, the PWFS provides a particularly non-linear behavior when operating around a non-null working point. In presence of a residual phase, the size and shape of the PSF imaged on the top of the pyramid is modified and alter the sensor sensitivity.

We define the PWFS sensitivity $S(\phi)^{\phi^{res}}$ to a given phase ϕ in presence of a residual phase ϕ^{res} as:

$$S(\phi)^{\phi^{res}} = \frac{M_{WFS} \cdot (\varepsilon\phi + \phi^{res}) - M_{WFS} \cdot (-\varepsilon\phi + \phi^{res})}{2\varepsilon} \quad (1.21)$$

where ε represents a small amplitude. Due to the non linearities of the pyramid, the sensitivity $S(\phi)^{\phi^{res}}$ of the PWFS will not be the same as $S(\phi)^{\phi^{res}=0}$:

$$S(\phi)^{\phi^{res}} = G^{\phi^{res}} \cdot S(\phi)^{\phi^{res}=0} \quad (1.22)$$

where the matrix $G^{\phi^{res}}$ characterizes the non linear response of the Pyramid WFS in presence of ϕ^{res} and defines the **optical gains** (OG) of the PWFS. This matrix is often assumed to be diagonal and its coefficients are also called **modal gains** of the PWFS (Korkiakoski et al. 2008, Deo et al. 2018a).

The OG describe then a difference in sensitivity between different working points. This is typically the case between the calibration operated with a diffraction limited PSF and the closed loop operations operated around a residual phase ϕ^{res} . In this situation, an interaction matrix $D^{\phi^{res}}$ measured around ϕ^{res} will be more adapted to the closed loop conditions than the interaction matrix $D^{\phi^{res}=0}$ measured in diffraction limited conditions, and will provide better AO performance (Deo et al. 2018a).

The effect of these optical gains is illustrated in Figure 1.16 where we show the typical attenuation occurring in the reconstruction of a given KL mode (see section 1.5.2) measured over a 100 nm residual.

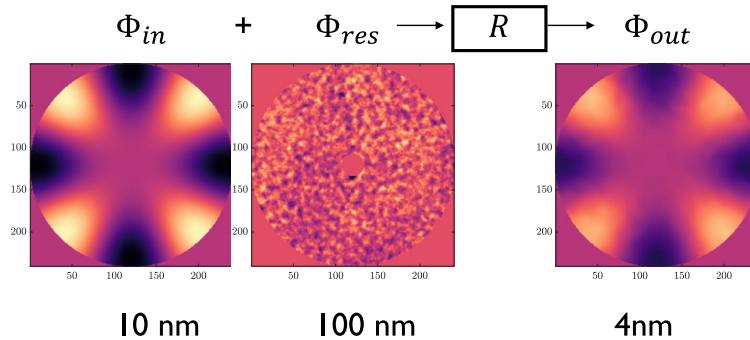


Figure 1.16. – Illustration of the impact of residual phase on the push pull measurement of the KL mode 20 (see section 1.5.2) using a Pyramid WFS.

In addition, Figure 1.17 provides an estimation of the diagonal of $G^{\phi^{res}}$ for differ-

ent r_0 in the case of an LBT-like system. To compute the optical gains displayed in this Figure, we consider the definition used in Deo et al. 2018a and we reproduce the results presented in the paper.

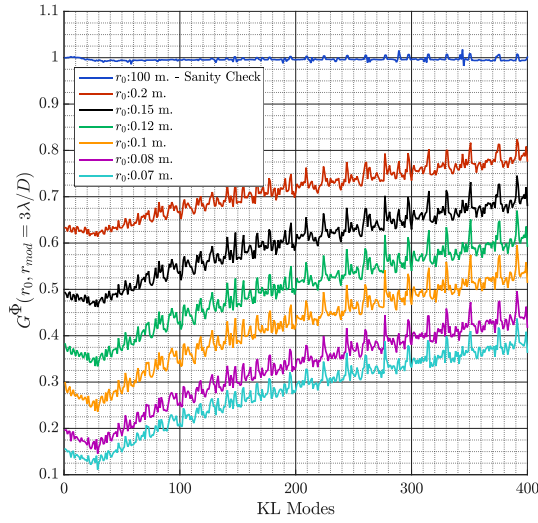


Figure 1.17. – Illustration of the Optical Gains of the PWFS as a function of the Fried Parameter r_0 . This plot reproduces the results presented in Deo et al. 2018a.

Figure 1.17 shows that the attenuation of the PWFS OG is inferior to 0.5 for most of the configurations considered which suggests that by compensating for these gain variations, the AO loop performance could be optimized.

Different strategies have been identified to handle the OG during the operations. A first idea consisted in adjusting the integrator gain to compensate for the Tip/Tilt sensitivity (Esposito et al. 2015) while other strategies proposed to dither different modes corresponding to well selected spatial frequencies to estimate the corresponding reduction of sensitivity (Viotto et al. 2016).

Other approaches suggest to consider linearization of the PWFS signals around the AO residuals to identify the **modal gains** that depend on the observing conditions and provide a significant improvement of the AO performance by compensating for the OG (Korkiakoski et al. 2008, Deo et al. 2018a, Deo et al. 2019). In the framework of the Fourier-Filtering WFS (Fauvarque et al. 2016, Fauvarque et al. 2019), a convolutionnal model of the PWFS has been developed to provide an analytic estimation of the OG, assuming the knowledge of a few parameters of the residual phase (Chambouleyron et al. in prep).

At last, the problem of the OG is particularly critical for the handling of the Non-Common Path Aberrations² (NCPA) that are usually compensated by applying offsets to the reference slopes of the PWFS. This point is currently actively investigated by the AO community (Esposito et al. 2015, Bond et al. 2018b).

2. Optical aberrations located between the WFS and the scientific instrument that can not be seen by the AO system.

1.4. Deformable Mirrors

In this section we introduce the concept of deformable mirrors. For a more complete description of the different DM technologies the reader can refer to Madec in Roddier 1999 and Madec 2012. A deformable mirror is an optical device which surface can be controlled to compensate for optical aberrations present in an optical system. It often has many degrees of freedom that can be associated to **actuators**, located under the surface of the DM and allow to control the shape of the mirror. The deformations corresponding to the actuation of a single actuator define the **influence functions** of the mirror. They inform on the **location** and **mechanical coupling** between the different actuators.

For a post-focal AO system, the DM is located on the same bench as the WFS, in a stable environment that will slowly evolve in time. In this situation, the DM geometry can be coupled with the Cartesian sampling of the WFS (lenslet array for a SH-WFS and detectors pixels for a PWFS). To maximize the sensitivity of the AO system, the optimal configuration consists in the Fried geometry (David L Fried 1977) where the actuator falls at the corner of 4 subapertures as illustrated in Figure 1.18.

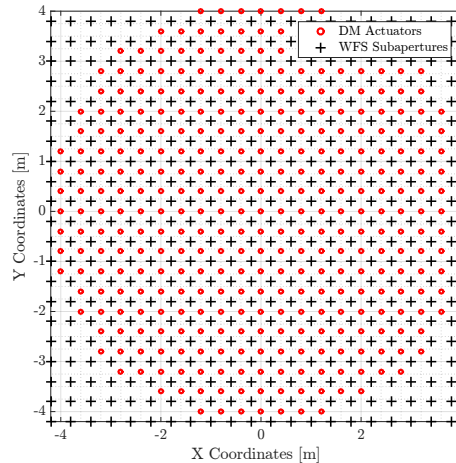


Figure 1.18. – Illustration of an AO system in the Fried Geometry.

To be in Fried Geometry, the number of actuators N_{DM}^D in a diameter is often linked to the number of subapertures N_{WFS}^D ³ in a diameter as:

$$N_{DM}^D = N_{WFS}^D + 1 \quad (1.23)$$

The number of subapertures is driven by the level of performance required by the AO system and requires a long design study that will not be presented here.

The deformable mirror has to be located in a pupil plane of the AO system. Depending on the optical system design, this will constrain the **diameter** and **actuator pitch** of the mirror that defines the distance between two actuators centers.

3. except in the case of curvature sensors where $N_{DM} = N_{WFS}$ but this type of WFS is not considered here.

The **mechanical stroke** of the DM is defined as the maximum possible actuator displacement. It is driven by the strength of turbulence that will be sensed by the AO system. Since this phenomenon is highly unpredictable, a worst case scenario is often selected to identify the specifications of the mirror in terms of mechanical stroke. For instance, the compensation of the atmospheric Tip/Tilt requires such a high mechanical stroke that the DM technology often does not allow to reach the required stroke while providing high order correction at the same time. It is thus common to develop a dedicated mirror for the Tip/Tilt correction and to couple it with a high order DM. Finally, the **temporal response** of the deformable mirror is defined as the time required by the mirror to converge to the requested shape. This property is driven by the AO loop frequency requirements.

From these considerations, different DM technologies allow to develop DM that meet the requirements of an AO system. Describing all the different DM technologies is beyond the scope of this manuscript but an overview is presented in Madec 2012 and introduces the stacked array DM, bimorph DM, voice-coil actuators DM or Micro Electro-Mechanical System DM. More information about these technologies can be found in Sauvage et al. 2010, Biasi et al. 2010, Cornelissen et al. 2010.

Let us however focus on the technology used to provide Deformable Secondary Mirrors. To reduce the number of optical surfaces and increase the number of photons available for the scientific instruments, it is possible to locate the DM directly in the telescope optical train. This has a cost in terms of technology developments, especially if we consider the size of the mirrors, typically from 1 m at the LBT & VLT to 2.6 m at the ELT (Riccardi et al. 2010, Arsenault et al. 2006, Vernet et al. 2012).

So far, the only technology considered for Large Adaptive Secondary Mirrors is based on voice-coil actuators. It consists in using a thin optical shell, "floating" on a magnetic field created by an array of voice-coil actuators, gluing permanent magnets on the rear face of the thin shell. By sending a current to the actuators, the shell surface is locally deformed by the magnetic field generated by the voice-coil actuators. These DM are controlled in position, associating capacitive sensors to each actuator that allow to measure the position of the thin shell using an internal loop running typically at 80 kHz. An illustration of the Deformable Secondary Mirror of the Very Large Telescope is provided in Figure 1.19 and illustrates some of the components previously introduced.

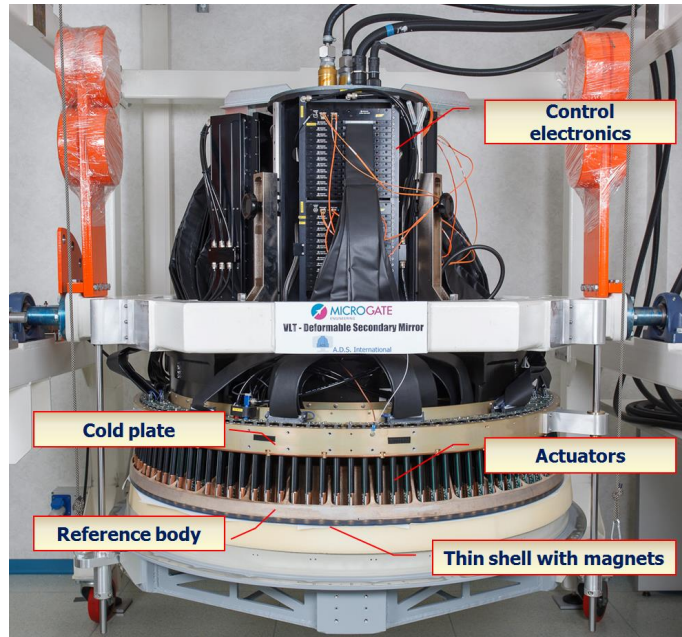


Figure 1.19. – Image of the DSM indicating the main components of the mirror. Image taken from Biasi et al. 2012

For such devices, the opto-mechanical coupling between DM and WFS becomes more complex due to the large distance separating the two elements. First of all, due to technological constraints, the geometry of these mirrors is often not Cartesian anymore (Riccardi et al. 2010, Arsenault et al. 2006, Vernet et al. 2012), preventing them from operating in a Fried-Geometry. This is well illustrated in Figure 1.20 that provides the location of the actuators of the Adaptive Secondary Mirror (ASM) (Riccardi et al. 2010) of the Large Binocular Telescope with respect to the FLAO WFS (Esposito et al. 2010a).

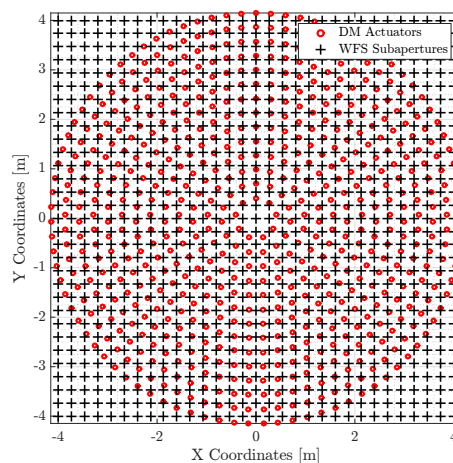


Figure 1.20. – Position of the ASM actuators with respect to the FLAO WFS subapertures.

In addition, the large distance between the two systems may lead to an evolution

of the opto-mechanical link between DM and WFS . This specificity of the adaptive secondary mirror is studied more in detail in section 1.7.1.

1.5. Control of an Adaptive Optics System

The control of an AO loop has to take in consideration the **spatial** aspect (wave-front reconstruction) and the **temporal** aspect (loop delay due to the detectors read-out and DM commands computation) to maximize the rejection of the turbulence.

1.5.1. Interaction Matrix

We first consider the spatial reconstruction of the phase. The determination of the WFS measurement y knowing the distorted wave-front ϕ^{turb} corresponds to a direct problem. What is required by the AO loop is to estimate the distorted wave-front ϕ^{turb} from the WFS measurements y and to project it on the DM by determining the commands c . To solve the inverse problem it is required to estimate the **interaction matrix** D of the system that is defined as the mapping matrix between the DM and the WFS space. In other words, the interaction matrix represents how each actuator's influence function is seen by the WFS subapertures:

$$D = M_{WFS} \cdot M_{DM} \quad (1.24)$$

where M_{DM} is the DM optical deformation matrix corresponding to each actuator (the influence functions of the DM) and M_{WFS} the corresponding WFS measurement model. That way, the WFS measurements Y are linked to a set of DM actuation C by the interaction matrix of the system D :

$$Y = D \cdot C \quad (1.25)$$

where we understand that inverting equation 1.25 provides a way to estimate the commands C from the WFS measurement Y defining the reconstructor⁴ R of the system that would be the inverse of the interaction matrix :

$$C = R \cdot Y \quad (1.26)$$

However, the matrix D is often non invertible. The most common inversion method consists then in using a Truncated Singular Values Decomposition (TSVD), filtering the modes badly seen by the WFS⁵ to improve the stability of the loop (Boyer et al. 1990):

$$R = D^\dagger = (D^T \cdot D)^\dagger \cdot D^T \quad (1.27)$$

where \dagger corresponds to the pseudo-inverse of the matrix D . Some research have shown that using a Generalized SVD, adding priors on the noise and turbulence statistics, provides a gain in the reconstruction (Wallner 1983, Fusco et al. 2001, Gilles 2005).

4. also called command matrix in the community.

5. Typically a Waffle mode in the case of a Shack Hartmann WFS

1.5.2. Modal Interaction Matrix

For various reasons, it is often more convenient to consider different modes defined in the phase space instead of the zonal actuation of the DM. For instance, we saw that the Zernike Polynomials are particularly well suited to describe the optical aberrations commonly seen in optics and in the atmosphere (see 1.1). Moreover, since they are sorted in terms of spatial frequencies, it creates a hierarchy in the modal basis, offering the possibility of limiting the modal basis to a number of modes inferior to the total number of degrees of freedom of the deformable mirror. Another advantage is that the modal approach provides a clear metric to compare the performance of different AO systems with different designs. In practice, the number of spatial frequencies that can be seen by the AO system or achieved by the DM is not infinite. It is limited by the number of degrees of freedom of either the DM or the WFS. The modal basis considered is then limited to a given number N_Z of modes that depends on the AO system definition:

$$\phi = \sum_{i=1}^{N_Z} a_i \cdot \mathbf{z}_i + \sum_{i=1+N_Z}^{\infty} a_i \cdot \mathbf{z}_i \quad (1.28)$$

where the right term contains the spatial frequencies that can not be seen by the AO system (and thus not corrected) and is defined as the fitting error $\phi_{fitting}$:

$$\phi_{fitting} = \sum_{i=1+N_Z}^{\infty} a_i \cdot \mathbf{z}_i \quad (1.29)$$

As briefly mentioned earlier, the choice of the modal basis can be dictated by different needs that are system dependant. In the context of Adaptive Optics, Gendron 1995 demonstrated that to optimize the correction of the aberration due to the atmosphere, an optimal basis can be obtained taking in consideration the statistics of the atmosphere and the DM influence functions properties. The principle consists in diagonalizing the covariance matrix of the atmospheric turbulence to identify the modes of the atmosphere that contain the most turbulent energy. In a second step, these modes have to be re-orthogonalized in the DM space by projecting them on the influence functions of the mirror. This double orthogonalization ensures to generate an orthonormal basis in the DM space that will contain the maximum of turbulent energy for a given number of modes considered. In the community, this modal basis is called **Kharunen-Loève** (KL) modes as it consists in applying a transformation of Kharunen-Loève⁶. An illustration of a few Zernike Polynomial and KL modes for a 20 by 20 Cartesian DM is given in 1.21.

6. although this transformation could be applied to diagonalize another criterion than the covariance matrix of the atmosphere

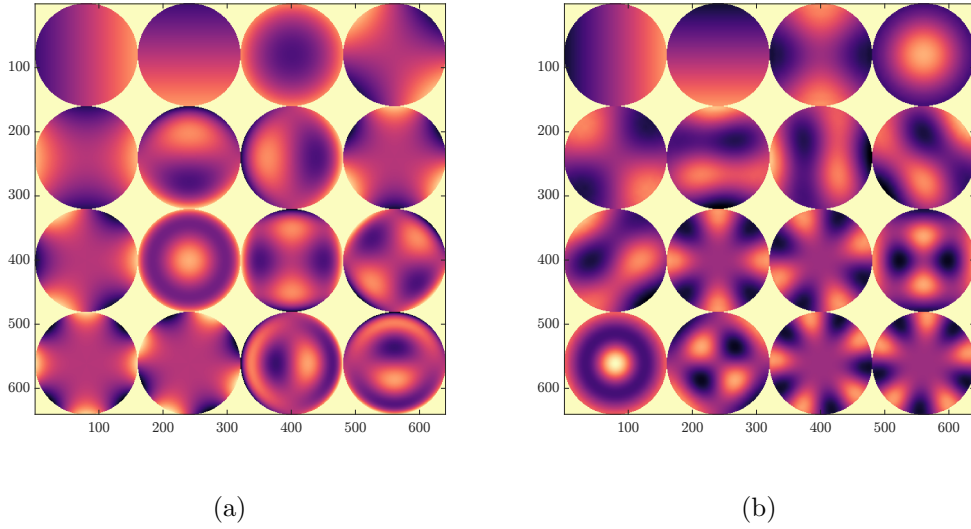


Figure 1.21. – Illustration of the Zernike Polynomials (Left) and KL modes (Right) defined for an atmosphere characterized with $r_0 = 11cm$

The WFS measurements \mathbf{Y}^Z corresponding to the calibration pattern \mathbf{C}^Z where \mathbf{Z} refers to a given modal basis is often called **modal interaction matrix**. The corresponding modal reconstructor \mathbf{R}^Z is obtained by inverting the modal interaction matrix directly, without estimating the interaction matrix \mathbf{D} .

This provides advantages in terms of control as the inversion of the interaction matrix is often more stable when the modes badly seen by the WFS are initially removed from the modal basis.

1.5.3. Dynamic control of an AO loop

In the previous section, we introduced the aspect of **spatial reconstruction** of the phase but we did not take in consideration the **temporal aspect** of the loop. The control of an AO system is dynamic to allow real time compensation of the turbulence. As we introduced in section 1.2.1 the AO system is typically operated in closed loop with the DM located upstream of the WFS to provide feed-backs after the applied correction. However a fundamental aspect of an AO loop is that a delay is involved between the WFS measurement and the time when the corresponding commands are applied to the DM. In the meantime, the turbulence evolves and generates errors in the correction. Typically, we can model the delays of an AO system as illustrated in Figure 1.22 with a full frame required for the WFS readout and a second frame required for the command computation and application.

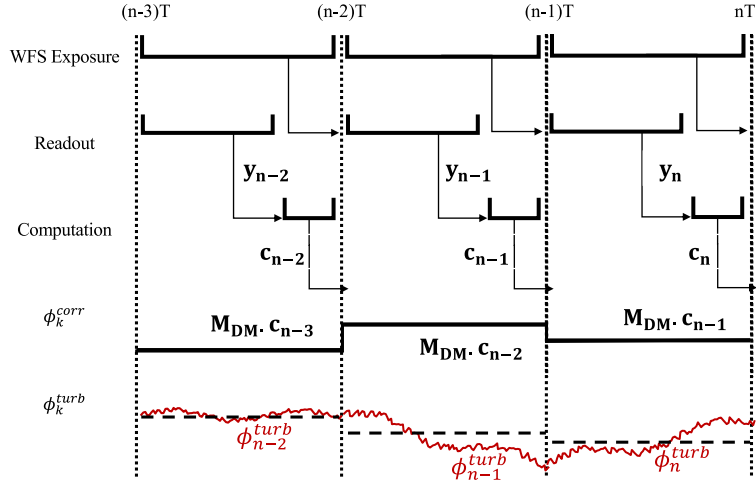


Figure 1.22. – Chronogram of an AO system characterized by a total of 2 frames delay. T represents the duration of a frame.

This Figure exhibits a global delay of two frames between the correction applied by the DM and the evolution of the turbulence. This delay impacts the performance of the system and has to be taken into account with an appropriate **control law**. The most common law used in Adaptive Optics is the integrator parametrized by an integral gain or loop gain g :

$$c_k = c_{k+1} + g\delta c_k \quad (1.30)$$

where δc_k is the DM commands determined by using equation 1.26. This control law provides a high attenuation of the low temporal frequencies and the value of g must be selected to optimize the AO performance while ensuring the good stability of the system. The block-diagram of a closed loop AO system is given in Figure 1.23. In closed loop, the WFS sees only the residual phase $\phi^{res}(t)$ corresponding to the difference between the turbulent phase $\phi^{turb}(t)$ and the correction phase $\phi^{corr}(t)$ of the DM.

$$\phi^{res}(t) = \phi^{turb}(t) - \phi^{corr}(t) \quad (1.31)$$

Using $\mathcal{L}[\bullet]$ to define the Laplace transform, we get :

$$\mathcal{L}[\phi^{corr}](f) = \mathcal{L}[\phi^{res}](f) \cdot G(f) \quad (1.32)$$

where $G(f)$ is the open-loop transfer function and f the temporal frequency (see Figure 1.23).

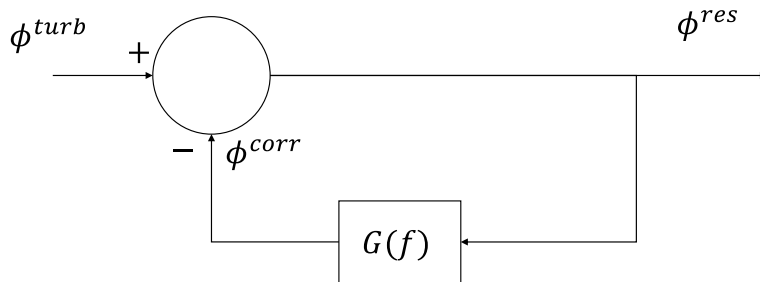


Figure 1.23. – Block diagram of a Closed Loop Adaptive System where $G(f)$ is the open loop transfer function.

We define the Rejection Transfer Function (RTF) $RTF(f)$ of the system as:

$$RTF(f) = \frac{\mathcal{L}[\phi^{res}](f)}{\mathcal{L}[\phi^{turb}](f)} \quad (1.33)$$

that we can express using equation 1.32 and taking the Laplace transform of equation 1.31:

$$RTF(f) = \frac{1}{1 + G(f)} \quad (1.34)$$

For instance, we give the theoretical RTF of an AO system with an integrator running at 1 kHz with two frames delay in Figure 1.24. In the same figure, we give the RTF obtained in end-to-end simulation, for a system in the same configuration. In this second case, the RTF_i of the mode i is obtained by computing the ratio of the Power Spectral Density (PSD) of the Closed Loop (CL) and Open Loop (OL) reconstruction of a mode \mathbf{z}_i :

$$RTF_i(f) = \frac{|\mathcal{F}[\mathbf{z}_i^{CL}](f)|^2}{|\mathcal{F}[\mathbf{z}_i^{OL}](f)|^2} \quad (1.35)$$

Figure 1.24 indicates that the bandwidth of the system increases with the loop gain g but it also amplifies the high temporal frequencies (overshoot). Depending on the system and observing conditions, different levels of noise are propagated in loop and the value of g has to be constrained to ensure the stability of the loop.

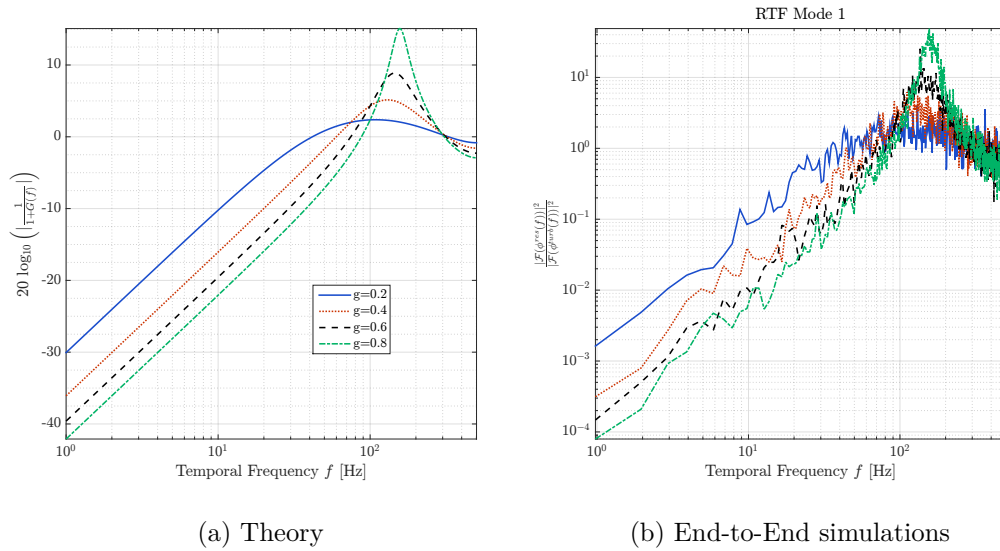


Figure 1.24. – Rejection Transfer Function of an AO loop running at 1 kHz for different loop gains. **Left:** Theoretical, **Right:** End-to-end simulation.

In practice, the performance of the AO system will be characterized by the product between the RTF (see Figure 1.24) and the temporal PSD of the atmosphere (see Figure 1.2). The control law has to be optimized with respect to the noise level. In this introduction, we narrowed down the analysis to the case of the simple integrator but other control laws can be considered. For instance, the modal integrator where

the gains of each mode has to be optimized (Gendron et al. 1994), predictive control laws that aim to minimize the temporal error (Roddir 1999, Kulcsár et al. 2006, Cyril Petit et al. 2008, Correia et al. 2014).

1.6. Calibration of an AO system

In the previous section, we introduced the theoretical aspects of an AO system operating in closed loop. We highlighted the importance of the interaction matrix that allows to reconstruct the phase from the WFS measurements and to determine the correct commands to apply to the deformable mirror. In this section we present the typical procedure to estimate the interaction matrix. In a second step, we investigate the impact of an evolution of the opto-mechanical link between the DM and WFS on the AO performance.

1.6.1. Measurement of the Interaction Matrix

A way to determine the interaction matrix of the system consists in measuring it experimentally. The measurement is achieved by recording the WFS signals \mathbf{Y} corresponding to a given set of actuation patterns \mathbf{C} . These measurements are impacted by two sources of disturbance, the WFS measurement noise $\boldsymbol{\eta}$ and the local turbulence ϕ^{turb} at the time of the measurements.

$$\mathbf{Y} = \mathbf{D} \cdot \mathbf{C} + \boldsymbol{\eta} + \mathbf{M}_{\text{WFS}} \cdot \phi^{turb} \quad (1.36)$$

Multiplying (1.36) by the pseudo inverse of the calibration pattern \mathbf{C}^\dagger provides the estimation of the interaction matrix \mathbf{D}^* .

$$\mathbf{D}^* = \mathbf{Y} \cdot \mathbf{C}^\dagger \quad (1.37)$$

Assuming that the calibration pattern is chosen to be full rank (for instance a zonal actuation or a modal basis such as DM stiffness modes) to calibrate all the degrees of freedom of the DM, the calibration pattern \mathbf{C} verifies $\mathbf{C} \cdot \mathbf{C}^\dagger = \text{Id}$. That way, we can define the calibration error $\Delta \mathbf{D}$ as:

$$\Delta \mathbf{D} = \mathbf{D} - \mathbf{D}^* = -(\boldsymbol{\eta} + \mathbf{M}_{\text{WFS}} \cdot \phi^{turb}) \cdot \mathbf{C}^\dagger \quad (1.38)$$

This equation consists of two independent terms, $\boldsymbol{\eta}$ the disturbance related to the WFS and $\mathbf{M}_{\text{WFS}} \cdot \phi^{turb}$ the disturbance related to the local turbulence and drifts, both multiplied by the pseudo inverse of the calibration pattern \mathbf{C}^\dagger .

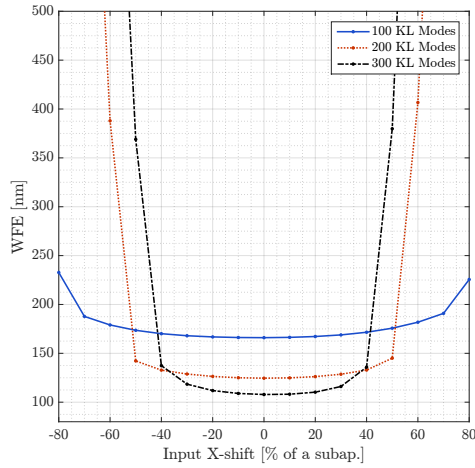
In the optimal case, both contributions can be minimized using a bright artificial calibration source to reduce the contribution of $\boldsymbol{\eta}$ and ϕ^{turb} can be reduced to the local turbulence of the optical bench, often static and that can be easily cancelled out by achieving push-pull measurements. In a high SNR regime, the choice of the calibration patterns becomes thus arbitrary. However, if these contributions become too important, and if the system has a large number of actuators, it is necessary to optimize the choice of calibration patterns to maximize the SNR and speed up the measurements. Such optimizations were investigated in Oberti et al. 2004, Kasper

et al. 2004 and Meimon et al. 2015 showing that using system modes or Hadamard patterns to maximize the signal provides a consistent gain in calibration time.

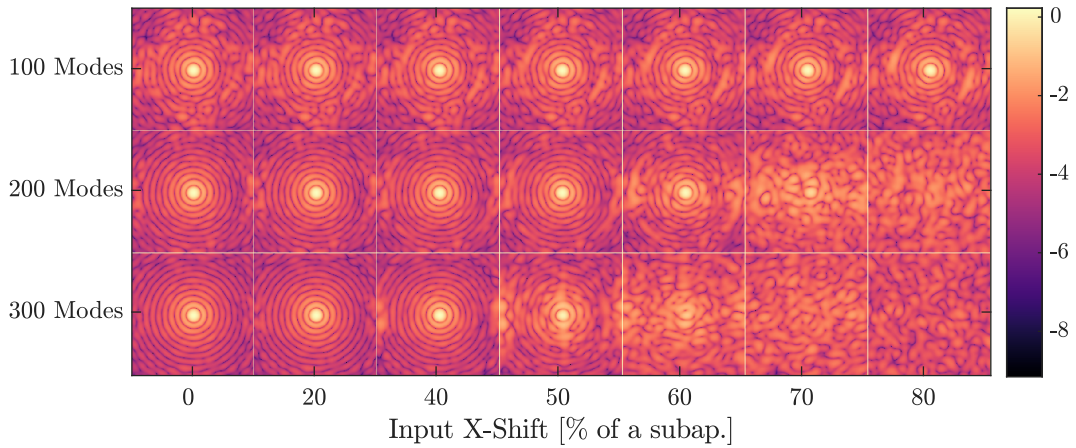
In any case, quantifying the quality of an interaction matrix remains an open question. Some metrics were investigated in Meimon et al. 2015 and Oberti et al. 2004 but no clear criteria have been identified yet. The only way to validate the accuracy of an interaction matrix is therefore to try to use it to close the loop of the AO system.

1.6.2. Impact of a mis-registration

In practice, the interaction matrix of the system \mathbf{D} is only valid at the time of the interaction matrix measurement and as long as the alignment of the system remains the same, in particular regarding the DM/WFS opto-mechanical conjugation. For various reasons, this alignment could evolve with time and lead to **mis-registrations** that consist of any shift, rotation, anamorphosis or higher order of pupil distortion of the DM actuator grid with respect to the WFS subapertures. In this section we propose to illustrate the impact of such mis-registrations in a simple case. The AO system is composed of a 20 by 20 subapertures Pyramid WFS and a Cartesian DM in the Fried geometry (David L Fried 1977) using a simple integrator controlling different number of modes in the interaction matrix. We consider a system operating in high flux regime, so that the WFS noise is negligible. The Wave-Front Error as a function of a shift X is given in Figure 1.25 and shows that the AO system is extremely sensitive to mis-registration errors. The system controlling the highest number of modes provides the best performance when the system is well centered but becomes unstable for a smaller value of shift (40% of a subaperture shift) than the systems controlling less modes. This illustrates how high orders AO systems will be more impacted by the mis-registrations. By contrast, low-orders systems can handle quite large mis-registrations. Figure 1.25 displays the corresponding long exposure H-Band Point Spread Functions (PSF) for different values of shift and exhibits the same trend.



(a)



(b)

Figure 1.25. – (a) Wave-Front Error as a function of the input X-Shift for the different number of modes considered. (b) H-Band PSF (log-scale) versus shift X mis-registration for different numbers of modes controlled in the interaction matrix. The sub-images are $0.5''$ across.

These results provide the first element to quantify the sensitivity of an AO system to a given mis-registration. They highlight that the accuracy required for the AO calibration depends on the number of modes controlled. In other words, this means that a high order AO system will require more frequent updates of its reconstructor R and with a highest precision than an AO system controlling less modes. This problem was already investigated in Dessenne et al. 1998, where it is shown that the AO system should remain under a shift of less than 10% of a subaperture to ensure a high quality of the AO correction.

1.7. Adaptive Telescopes

As briefly introduced in section 1.4, recent developments in telescopes designs and DM technologies have led to consider DM located directly into the telescope (turning

them from active to adaptive telescopes) to reduce the number of optical elements, increasing the number of photons available for the instruments and to minimize the thermal emission (Salinari et al. 1994, Martin et al. 1996, Madec 2012). This concept was first validated on the MMT (Wildi et al. 2003) and is now used on some of the largest ground based optical telescopes, at the Large Binocular Telescope (LBT), at the Very Large Telescope (VLT) and at the Magellan Telescope (Riccardi et al. 2010, Arsenault et al. 2008 Close et al. 2013).

The next generation adaptive telescopes, the Extremely Large Telescope (ELT) (Gilmozzi et al. 2007) and Giant Magellan Telescope (GMT) (Johns 2006), will also include large adaptive mirrors in their design with respectively 4356 and 4702 actuators (Vernet et al. 2012, P. M. Hinz et al. 2010) while this design is also considered for the Thirty Meter Telescope (TMT) (Boyer 2018).

These numbers shed light on the very first challenges for the calibration of the future large adaptive telescopes. These problematics constitute the core of our research : how much of (precious) telescope time will be required to provide a satisfying calibration of the AO systems and how could we maintain its accuracy during the operation?

In this section, we will first introduce the specificities of adaptive telescopes in terms of AO calibration and present the different calibration strategies that have been identified by the community to overcome these operational challenges. In a second step, we will focus on two existing adaptive telescopes facilities, the AOF at the VLT and the LBT to provide a comparison with the future ELT.

1.7.1. AO Calibration for Large Adaptive Telescopes

The problematics of calibrating AO systems with large DM were already addressed in Oberti et al. 2006 in which a summary of the main technical challenge is provided: large number of actuators and regular update of the calibration with often no external source illuminating the DM. Indeed, such telescopes usually do not provide any access to an intermediate focal plane ahead of the DM, and thus to any artificial calibration source. This specificity requires to completely rethink the way of acquiring the interaction matrix of the system. However, even in presence of such an artificial calibration source, the large distance between the DM and the WFS may frequently affect the registration between both systems (due to gravity or moving elements in the optical path). These mis-registrations, affect the performance of the AO correction, especially for high order systems which are extremely sensitive to these mis-alignments and require a high accuracy calibration (see section 1.6.2). Such calibration errors impact the performance of the scientific instruments and can lead to instabilities of the AO loop, disturbing telescope observations. With the future Large Adaptive Telescopes these constraints will reach another level. The first challenge in terms of telescope operations will be to calibrate a large number of actuators with no access to a calibration source. Moreover, the calibration will require regular updates during the operations due to the unprecedented distance between the DM and the WFS with moving optics between them.

It is then crucial to optimize and develop new calibration strategies to overcome these constraints and minimize the telescope time required. Some methods have already been identified to obtain these measurements. The first approach consists

in measuring the interaction matrix on-sky (Wildi et al. 2004, Esposito et al. 2006, Oberti et al. 2006, Pieralli et al. 2008, Pinna et al. 2012, Kellerer et al. 2012) while the second idea is to generate it synthetically using an AO simulator, injecting experimental inputs (Oberti et al. 2006, Kolb et al. 2012b, Kolb et al. 2012a). The community seems to be converging towards the second approach, working on synthetic models of the AO systems in which some mis-registration parameters are injected to fit with the alignment of the real system. This approach is especially suited for systems that require a frequent update of the calibration with a large number of actuators. For instance, the Pseudo Synthetic Interaction Matrix (PSIM) is currently the baseline for the AOF instruments in Ground Layer Adaptive Optics (GLAO) and Laser Tomography Adaptive Optics (LTAO) modes working with a 4 SH-WFS.

1.7.1.1. On-sky calibration

With no calibration source available, an alternative method consists in measuring the interaction matrix on-sky. This strategy faces two major challenges: the impact of the turbulence on the WFS measurements and the impact of the calibration on the scientific path. In equation 1.36, the term $M_{\text{WFS}} \cdot \phi^{\text{turb}}$ becomes indeed dominant. Actuating a calibration pattern using a classical push-pull would require such a large amplitude to extract it from the turbulence noise that it may saturate the WFS. The problem becomes then pretty common: one wants to retrieve a low signal in a noisy (turbulence noise) and variable environment (seeing variation), with the constraint of not saturating neither the WFS nor the DM stroke. Taking the two extreme solutions, one could either average the turbulence using a long integration, or freeze it using a fast push-pull measurement. An alternative approach inspired from the telecommunication domain, consists in modulating signals with a low amplitude on the DM (to minimize the impact on science) but large enough to be detectable by the WFS. Using an orthogonal basis, in both temporal and spatial domain, of multiplexed signals, one can retrieve their signatures in the WFS space using a simple demodulation process (Esposito et al. 2006). This approach has been validated on several systems, at the VLT with a curvature sensor (Oberti et al. 2006), with a high order pyramid WFS at the LBT (Pinna et al. 2012), operating the demodulation in the Fourier space and with a Shack Hartmann on the CANARY Facility (Myers et al. 2008), demodulating in the direct space (Kellerer et al. 2012).

The analysis of the results has shown that an accurate knowledge of the temporal behavior of the system is required (rejection transfer function of the AO loop, effective temporal delay of the loop) and a trade-off for the modulation parameters (frequency, amplitude, sampling, multiplexing) has to be done to perform an efficient calibration taking in consideration the observing conditions, impact on the science path and accuracy required. In addition, to overcome the constraint of WFS saturation, the signals modulation has to be operated in closed-loop (at least partial) using a first interaction matrix, that could be synthetic. An analysis of the on-sky calibration developed at the LBT is given in Appendix C.

This demonstrated the feasibility of the on-sky approach as a potential alternative strategy but to our knowledge no operating system is currently using it as its baseline for its AO calibration. Such a calibration requires indeed a longer time than the usual measurement with fiber (with a lower SNR) and during this amount of time,

the system characteristics may evolve (opto-mechanical drifts due to the thermal and gravity effects) such that the interaction matrix is not representative. Moreover, in the case of a Pyramid WFS, if the on-sky calibration takes too long, the WFS response may evolve during the measurements, as it depends on the seeing conditions, and bias the interaction matrix measurement. Therefore, a full on sky calibration does not seem suited for a system with a large number of degrees of freedom, especially with Pyramid WFS. In the case of adaptive telescopes, as we saw, potential non linearities and complex internal behavior (evolution or instability of the DM/WFS registration) may appear during the operation. These techniques could then be used to retrieve only a few on-sky signals to identify key mis-registration parameters that are then injected in a synthetic model. This pseudo-synthetic approach seems indeed better suited to overcome such constraints.

1.7.1.2. Synthetic-Based calibration

The pseudo-synthetic calibration has been identified as the most promising calibration strategy for the future Extremely Large Telescopes: mis-registration parameters extracted from experimental inputs⁷ (on-sky measurements, telemetry data) are injected into a synthetic model of the AO systems. The principle is summarized in Fig. 1.26.

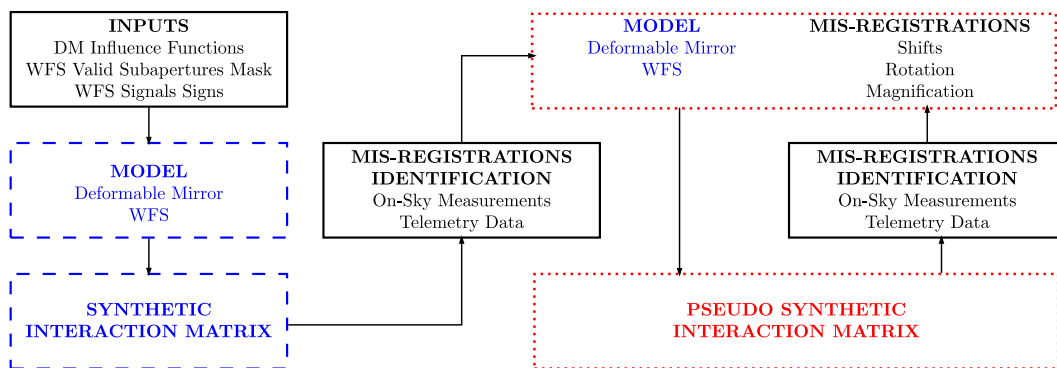


Figure 1.26. – Pseudo Synthetic Calibration: Experimental inputs (solid black lines) are injected into the synthetic model (dashed blue lines) to reproduce the registration of the real system. The pseudo-synthetic interaction matrix (dotted red lines) is then regularly updated during the operation tracking the mis-registration parameters.

The model is initially tuned using experimental inputs and a first interaction matrix is generated from the model. During the operations, the mis-registrations are regularly estimated to provide an update of the model mis-registration parameters and re-compute the interaction matrix in the simulator at each estimation cycle (see Figure 1.26). This approach provides a noise-free interaction matrix, fast to compute and thus, easy to update. The quality of the calibration relies only on two key ingredients: the ability to model accurately the WFS and the DM and the accuracy of the mis-registration parameters identification. Theoretically, if all the experimental

7. That we will call reference signals in the following

effects are perfectly reproduced, a Pseudo Synthetic interaction matrix should then provide a better calibration than a noisy experimental one.

Concerning the first ingredient, the state-of-the-art in terms of AO modeling has shown on various systems (e.g. LBT or VLT) that an accurate calibration can be generated from a synthetic model (Oberti et al. 2006, Kolb et al. 2012a, Pinna et al. 2012). The modeling of a Shack Hartmann seems to be one step ahead with respect to the Pyramid WFS case as extensive studies related to the sensitivity are available (see Kolb et al. 2012a). In the case of a Pyramid WFS, the feasibility was demonstrated in Pinna et al. 2012 but no analysis of sensitivity has been achieved so far. Further in this thesis, we will try to address this point.

The second ingredient is related to the estimation of the mis-registration parameters. The nature of the reference signals required to align the model is still open to discussion. A first attractive approach is non-invasive and consists in using telemetry data (WFS slopes and DM commands) to retrieve the corresponding mis-registration parameters. At the AOF for instance, the idea consists in using closed-loop data to estimate a noisy interaction matrix and project it on sensitivity matrices to identify these parameters (see Kolb et al. 2012a and Béchet et al. 2011). The second approach is invasive and consists in dithering signals on the DM to retrieve their signature in the WFS space (Chiuso et al. 2010). In Neichel et al. 2012, a strategy based on a Levenberg-Marquardt (Marquardt 1963) type algorithm is presented in the frame of tomographic AO systems but requires an experimental interaction matrix as a reference, that could for instance be measured on-sky. The difficulty here is to find the minimum number of signals that would be characteristic of each type of mis-registrations, independently from the others. Since the parameters are strongly correlated, the alternative solution consists in using an iterative procedure to identify each parameter.

To give more details on the characteristics of these large adaptive telescopes, the next sections will be dedicated to the presentation of three facilities that are relevant for our research. We will introduce the Large Binocular Telescope, the Adaptive Optics Facility and the future Extremely Large Telescope.

1.7.2. The Large Binocular Telescope

The LBT is located at the Mont Graham Observatory in Arizona (USA) and consists of two 8.4 m primary mirrors that can be used either in stand-alone mode or together for interferometry purposes. An illustration of the LBT optical design is given in Figure 1.27. The primary mirror of 8.4 m diameter collects the light and relays it to the Adaptive Secondary Mirror, in charge of the AO correction. The tertiary mirror is then in charge of propagating the beam either to the back bent-Gregorian focal stations for interferometry purposes or to the front-bent Gregorian Focus to the FLAO instrument. In our study, we focus on the FLAO instrument only.

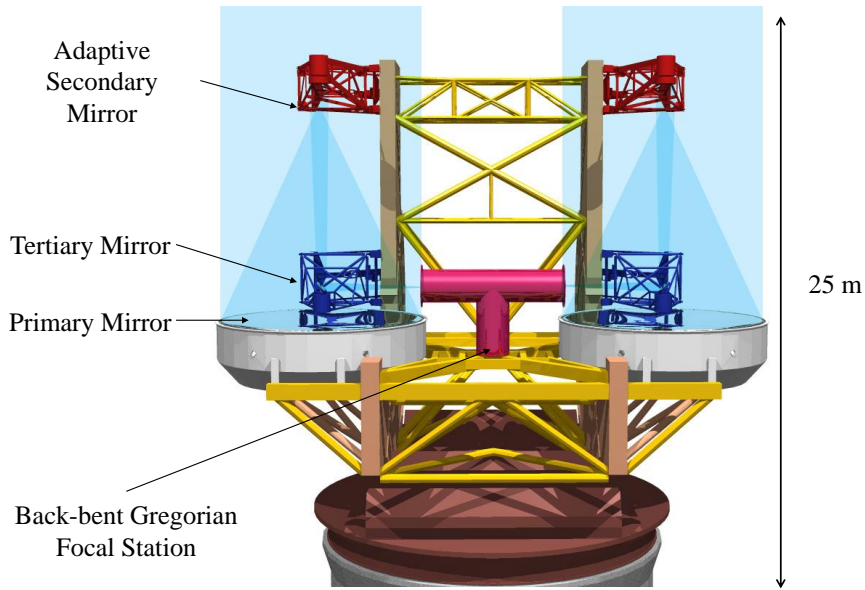


Figure 1.27. – Optical Layout of the LBT taken from <http://oldweb.lbto.org>. The Front-bent focus is not displayed in this representation.

In terms of Adaptive Optics, each telescope is equipped with its own high order AO system FLAO⁸ with an Adaptive Secondary Mirror (ASM) and a Pyramid WFS. The optical layout of the FLAO instrument is provided in Figure 1.28.

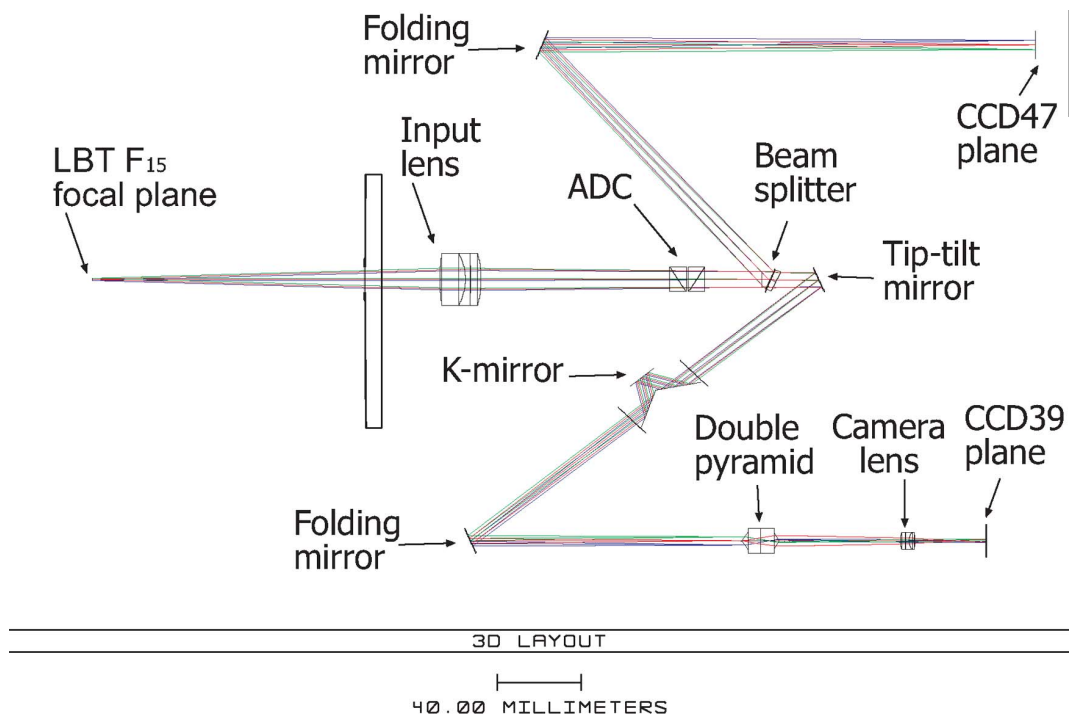


Figure 1.28. – Optical Layout of the FLAO system WFS, taken from Esposito et al. 2010b.

⁸ First Light Adaptive Optics. The system is currently being upgraded with the SOUL instrument Pinna et al. 2016

The two Adaptive Secondary Mirrors, referred to as LBT672a and LBT672b, have a diameter of 0.91 m with a radial pitch of 0.28 m projected on-sky. They consist of 672 voice-coil actuators arranged in a circular geometry and define the stop aperture of the telescope. The coordinates of the actuators with respect to the WFS subapertures have been optimized to maximize the number of "Fried-Like" actuators (Esposito et al. 2010b). The position of the actuators is controlled using an internal loop running at 72 kHz which is fast enough to support the 1 kHz AO loop.

The Pyramid WFS is a double Pyramid that allows the correction of chromatic aberrations (Tozzi et al. 2008). It is coupled with a fast Tip-Tilt mirror in charge of modulating the PSF on the top of the pyramid, adjusting the sensitivity of the sensor depending on the observing conditions (see Figure 1.28). The telescope pupils can be sampled using different numbers of subapertures by adjusting the binning of the WFS detector (up to 30 by 30 subapertures). In the case of FLAO, the detector is an E2V CCD39 that can work full frame up to 1 kHz. The main upgrade of (Pinna et al. 2016) with respect to FLAO will be to replace the WFS detector with an OCAM2K camera (Feautrier et al. 2011) to provide a shorter read-out time, a lower read-out noise and a larger number of pixels, allowing a higher spatial sampling (up to 40 by 40 subapertures). In terms of calibration, the interaction matrix is modal (400 KL Modes in high order mode) and experimentally measured using a retro-reflector. The measurement of the interaction matrix is not achieved before each observation but the system is physically re-aligned to match the ASM/WFS registration at the time of the interaction matrix measurement using specific patterns to re-align the system (see Esposito et al. 2010b). During the operations, no tracking of the mis-registrations is achieved but different gains are applied for the Tip/Tilt, Mid-Order modes and High Orders to compensate for the optical gains of the PWFS.

An example of scientific outcome of the LBT AO systems is provided in Figure 1.29. The high sensitivity of the AO system of the LBT allowed to reveal new details of the architecture of the planetary system HR8799 located 130 light-years from Earth (Esposito et al. 2013, Maire et al. 2015), in the frame of the LEECH survey (Andrew J Skemer et al. 2014). In that case the telescope is used in interferometry mode using the LMIRCam (M. Skrutskie et al. 2010, J. M. Leisenring et al. 2012) and taking benefit from the 95% Strehl Ratio in L' band and 80% in H-Band provided by FLAO.

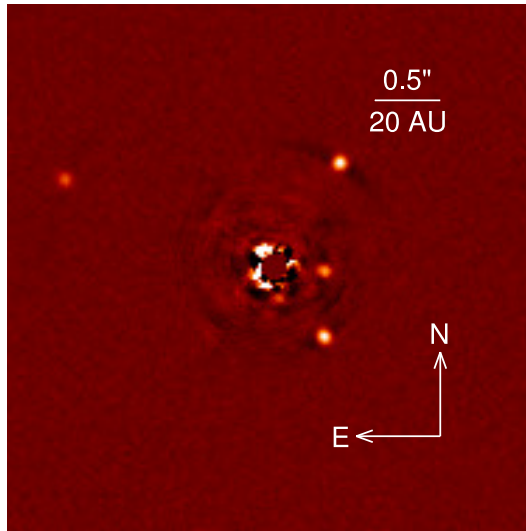


Figure 1.29. – L' Band image of the HR8799 multiple planet system using the LMIRCam. Image taken from Maire et al. 2015.

1.7.3. The Adaptive Optics Facility at the Very Large Telescope

The Unit Telescope 4 of the VLT has recently been upgraded to become the Adaptive Optics Facility (Arsenault et al. 2008, Stroebele et al. 2006) with the development of the Deformable Secondary Mirror (DSM) and the Four Laser Guide Star Facility (4LGSF). It is equipped with the two AO modules GRAAL (Paufigue et al. 2010), that provides a large field Ground Layer Adaptive Optics (GLAO) mode (7 arcmin LGS diameter) for the Hawk-I instrument (Pirard et al. 2004) diameter, and GALACSI (Ströbele et al. 2012) that provides a medium GLAO mode (2 arcmin LGS diameter) and Laser Tomography AO (LTAO) for the ultimate performance in Narrow Field Mode (7.5 arcsec square) for the MUSE instrument (Bacon et al. 2010). The layout of the AOF is provided in Figure 1.30 showing the location of the two AO modules on the two Nasmyth platforms and the location of the DSM.

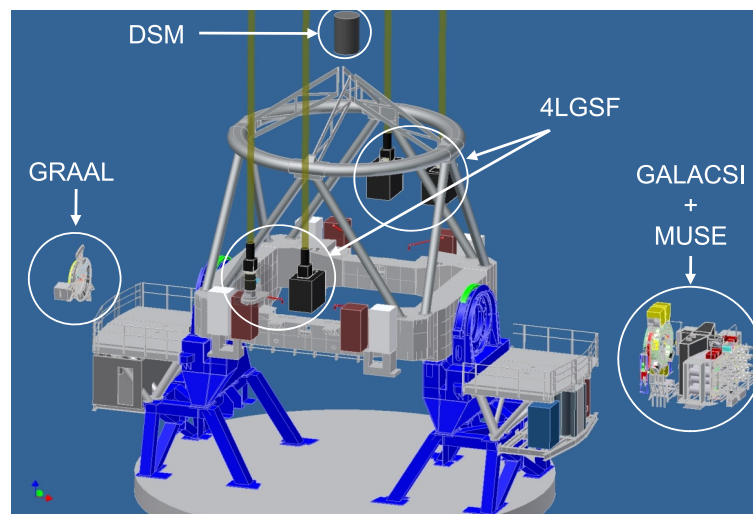


Figure 1.30. – Layout of the Adaptive Optics Facility at the UT 4 of the VLT. Image taken from <https://www.eso.org>

The Deformable Secondary Mirror (DSM) Arsenault et al. 2006 is of similar technology as the ASM's at the LBT. It is composed of 1170 voice-coil contact-less actuators⁹ arranged in a circular geometry with a diameter of 1.12 m which defines the aperture stop of the telescope. The positions of the actuators are controlled using an internal loop running at 80 kHz and the AO loop is running at 1 kHz. Each AO module is composed of 4 SH-WFS, one per laser, with a sampling of 40 by 40 subapertures using 6 by 6 pixels per subaperture which provides a pixel-scale of 0.83 arcsec. For all the instruments, the Tip/Tilt correction is controlled separately and the LGS-WFS are in charge of the High Order modes.

In terms of calibration, the particularity of the AOF is that no external calibration source is available to measure the interaction matrix. The interaction matrix of the system is thus pseudo synthetic, generated from a synthetic model of the SH-WFS and DSM (Kolb et al. 2012a, Oberti et al. 2018). During the commissioning of the instrument, the tuning and validation of the model was achieved using both in lab and on-sky measurements (Oberti et al. 2018).

The DSM model is based on a Finite Element Analysis (FEA) of the influence functions of the mirror. It was validated using experimental measurements of the influence functions. These influence functions are used to compute the KL modal basis used in the interaction matrix of the system, typically 550 in GLAO mode and 750 in LTAO mode. The WFS model is based on a geometric model of the SH-WFS since the WFS is considered linear but it requires the mask of useful subapertures defined using experimental measurements. At last, the model requires experimental inputs to identify the mis-registration parameters of the model (rotation, shift X & Y, magnifications X & Y). These experimental inputs are acquired during the operations using telemetry data (Béchet et al. 2012, Kolb et al. 2012a) to estimate a noisy interaction matrix and to project them onto sensitivity matrices. This strategy offers the capability of regularly updating numerically the interaction matrix of the system and is thoroughly investigated in the chapter 4 of this thesis. As an example of scientific outcome, we can illustrate the performance of the MUSE narrow-field mode in Figure 1.31. These images were obtained during the commissioning runs of the instrument.

9. 1156 in the pupil



Figure 1.31. – Comparison of the observation of the globular cluster NGC 6388 with the instrument MUSE in wide-field mode without Adaptive Optics (Left) and the MUSE narrow field mode (7.5" square) with Adaptive Optics (Right). Image taken from the ESO Press Release <https://www.eso.org/public/germany/news/es01824/>.

1.7.4. The Extremely Large Telescope

We propose to consider the case of the ELT (Gilmozzi et al. 2007) to illustrate the case of the future large adaptive telescopes. This project led by the European Southern Observatory (ESO) in collaboration with most of the European astronomical institutes consists in building a 39.3 m diameter telescope on the Cerro Armazones site in Chile. Its primary mirror will be composed of around 800 individual octagonal segments of 1.4 m size each, and will offer a collecting area of around 978 m^2 ! The telescope will have a Field of View of around 10 arcmin on the sky and its diffraction limit will be around 8 mas in J band ($1.2 \mu\text{m}$) and 14 mas in K band ($2.2 \mu\text{m}$). The design of the ELT is represented in Figure 1.32 and is based on a five mirrors scheme that will allow to collect the light from astronomical sources and feed the scientific instruments located on one of the Nasmyth platforms. The primary mirror (M1) of 39.3 m diameter will collect the light and relay it to the secondary (M2) and tertiary mirror (M3) and then to the adaptive mirror of the telescope (M4) and active mirror (M5). These last two mirrors will be crucial for the science as they will be in charge of respectively compensating for the atmospheric turbulence aberrations and for the telescope structure vibrations induced by the wind and the telescope movements.

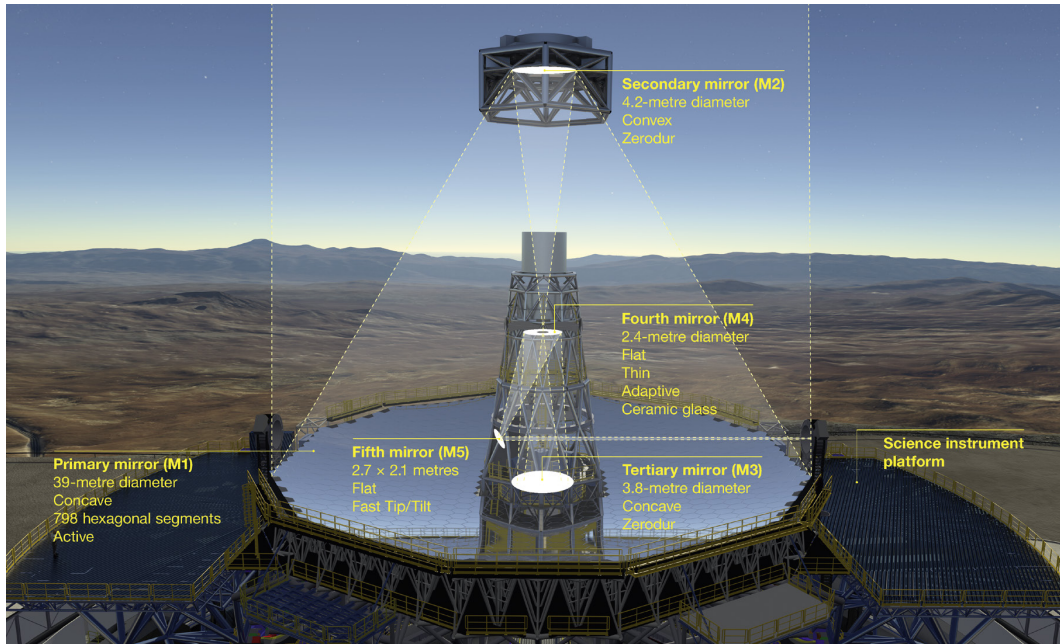


Figure 1.32. – Optical Design of the ELT (taken from Cirasuolo et al. 2018).

The adaptive Mirror M4 will have a diameter of 2.4 m, and be equipped with 4356 voice-coil actuators Vernet et al. 2012 arranged in an hexagonal symmetry. The particularity of M4 is that it will be segmented in 6 petals containing each 865 voice-coil actuators. An illustration of a petal showing the location of the actuators is provided in 1.33.

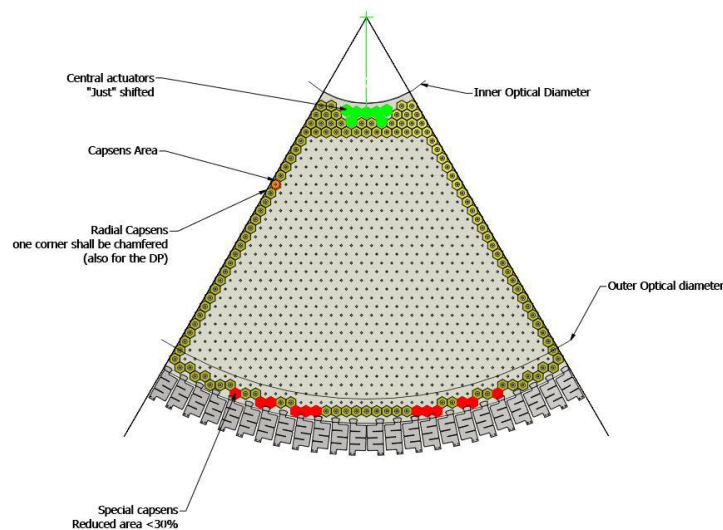


Figure 1.33. – Illustration of a petal of the M4 mirror. Taken from Elise Vernet et al. 2014

The different instruments of the ELT will be equipped with 100 by 100 Pyramid WFS operating with NGS for their SCAO modes and 80 by 80 SH-WFS operating with both NGS and LGS for the other modes considered: Multi Conjugate Adaptive Optics (MCAO), LTAO and GLAO (Neichel et al. 2016, Clénet et al. 2016, Brandl et

LBT-ASM	VLT-DSM	ELT-M4
672 Actuators	1170 Actuators	4356 Actuators
0.91 m diameter	1.12 m diameter	2.4 m diameter
0.28 m pitch projected on-sky	0.21 m pitch projected on-sky	0.5 m pitch projected on-sky

Table 1.1. – Comparison of the main differences between the ASM, DSM and M4.

al. 2016, Diolaiti et al. 2016). In terms of calibration, the baseline for all the first light instruments will be to consider a Pseudo-Synthetic approach where a synthetic model of the parameters is used to compute numerically the interaction matrix of the system. The handling of the mis-registrations will most likely be hybrid, updating numerically the interaction matrix and physically re-aligning some components of the AO systems. This will be instrument-dependent and remains to be investigated. The calibration strategy of these instruments is still a work in progress. This research aims to address some of the questions related to the AO calibration of the instruments of these future large adaptive telescopes.

In terms of scientific outcome, one of the most exciting capability of the ELT will be to benefit from its large diameter to offer a better angular separation of faint objects and allow direct imaging of Exoplanets located near the star they are orbiting, in the so called "habitable zone". These observations will provide spectroscopy capabilities that will inform on the composition of the considered objects. In addition, the ELT science objectives will include the study of the formation and evolution of planetary systems, direct measurement of the expansion of the Universe and the observation of some of the most distant objects (first stars, high red-shift galaxies, black holes) with the goal of understanding their evolution over time.

1.7.5. AO Calibration in the VLT/ELT context

In this section, we propose to summarize the information related to the AO calibration of the future Large Adaptive Telescopes. The comparison of the Deformable Mirrors is provided in Table 1.1 and the comparison in terms of Wave-front Sensing and Calibration strategy is given in Table 1.2.

From this summary, we can identify that contrary to systems equipped with SH-WFS, the feasibility of a Pseudo-Synthetic Calibration with PWFS allowing regular tracking of the parameters during the operations is yet to be investigated. This point will be the core of the research presented in this manuscript. We will first present the development of a synthetic model for the LBT AO system in chapter 2 to identify the key-elements required to efficiently model a Pyramid WFS. In a second step we will investigate different strategies to identify the model parameters during the operation (chapter 3 & 4).

	LBT-FLAO	AOF	ELT
WFS	30×30 PWFS + NGS	40×40 SH-WFS + LGS	80×80 SH-WFS + NGS/LGS & 100×100 PWFS +NGS
AO mode	SCAO	GLAO, LTAO	SCAO, MCAO, LTAO, GLAO
Interaction Matrix	Experimental	Pseudo Synthetic	Pseudo Synthetic
DM/WFS Mis-Registration Alignment	System physically re-aligned before the operations. No tracking of the parameters	Online Tracking + numerical update of the interaction matrix	Online Tracking + regular numerical update of the interaction matrix + re-alignment of some components of the system. + TBD

Table 1.2. – Comparison of the main different Wave-Front Sensing and Calibration Strategies for the LBT, AOF and ELT instruments.

This chapter introduced the context of the present and future Large Adaptive Telescopes. We highlighted the main technical challenges in terms of AO calibration that come with the developments of such giants: large number of degrees of freedom to calibrate with regular updates of the calibration required during the operations. The update of the calibration will be crucial for the scientific observation as any evolution of the mis-registrations will affect the performance of the AO systems, especially for High Orders systems.

By studying the state-of-the-art in complex AO calibration procedures, we identified that the strategy that seems to be the most suited to comply with the requirements of the future Large Adaptive Telescopes consists in working with Pseudo-Synthetic Interaction Matrices (PSIM). This strategy requires to develop complex and thorough AO models of existing systems that must provide the flexibility to integrate and reproduce accurately the features of a real system. In addition, the development of these synthetic models will also have to account for the Pyramid WFS specificities. To provide regular updates of the calibration these models require tracking capabilities for the model mis-registration parameters during the operation with the constraint of minimizing the impact on the science path. These tracking methods will also have to account for the impact of the Pyramid WFS non-linearities and optical gains variations. In this thesis, I will first address the problem of modelling an AO system with PWFS to generate synthetic-based interaction matrices. We will consider the case of the LBT AO systems. In a second step, I will present my research to optimize the identification of the mis-registration parameters using an invasive approach, where signals are dithered on the DM to provide a tracking of the parameters. Finally, I will present a thorough analysis of the non-invasive strategy developed at the AOF to understand the domain of validity of the method and consider its application with a PWFS.

2. Synthetic Based Calibration with Pyramid WFS

In Chapter 1 we have presented the current state of the art in terms of complex AO calibration strategies. We have seen that on-sky and synthetic-based calibration have been achieved for both Shack Hartman and Pyramid WFS, respectively at the VLT and LBT.

Regarding the Pyramid WFS, the feasibility of a pseudo-synthetic approach allowing fast updates of the calibration during the operation by tracking the model parameters is yet to be investigated and is the core of this research. For this purpose, it is first necessary to develop a synthetic model that is representative of a real AO system. In this chapter we present the development of such a synthetic model taking the case of the AO system of the LBT: let us recall the main properties of the LBT AO Systems. In terms of AO correction, as presented in section 1.7.2, each of the two telescopes has its own AO system, First Light Adaptive Optics (FLAO)¹ (Esposito et al. 2010b), to provide the AO correction for the instrument LUCI (Heidt et al. 2018). Each FLAO is composed of an Adaptive Secondary Mirror (ASM) (Riccardi et al. 2003) and a Pyramid WFS to operate in SCAO with NGS. A single ASM is composed of 672 voice-coil actuators organized in a circular geometry with a 30 cm radial pitch as illustrated in Figure 2.1. The PWFS of FLAO is a 30 by 30 subapertures achromatic Pyramid and operates in I Band (central wavelength 750 nm). Since the ASM is located inside the telescope, the acquisition of the interaction matrix requires a retro-reflector located at the focus point of the ASM to be able to use an external calibration source located in the WFS unit (Esposito et al. 2010b). This procedure is the baseline for the calibration of the AO system. Our work will propose an alternative strategy to generate the interaction matrix from a synthetic model of the AO system.

The purpose of this chapter is to identify the key-ingredients to compute a synthetic interaction matrix from a model that can be used at the telescope. We focus first on the modelling of the two critical components: the **DM model** and the **WFS model** introducing how to include potential mis-alignments and mis-registrations of the real system. In a second step, we present the experimental validation of the model, introducing a first strategy to identify the model parameters from an experimental interaction matrix (Heritier et al. 2018). Finally, we provide a comparison of accuracy between a model based on experimental and synthetic influence functions.

1. The system has now be decommissioned and the commissioning of the instrument upgrade (SOUL) has been completed in 2019.

2.1. Mis-registrations and mis-alignments

2.1.1. Definition

It is first important to distinguish a mis-registration from a mis-alignment. Both have to be taken into account but the means by which they are included in the model differs.

We define a **mis-alignment** as an evolution of the position of the pupil footprint on the DM and of the pyramid pupils location on the detector. The issue of pupil tracking is not considered in this thesis. For instance in the case of the LBT, the variance map of the measured influence functions clearly shows that the central ring of actuators was not perfectly centered with respect to the pupil at the time of measurement.

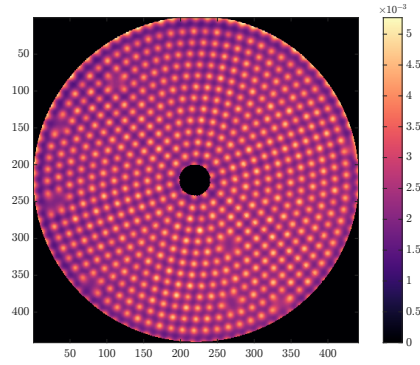


Figure 2.1. – Variance map of the influence functions of the ASM measured with an interferometer. We can notice the 9 inactive actuators.

A **mis-registration**, however, is related to an evolution of how the actuators grid is seen by the WFS subapertures. From the experience acquired at the VLT and LBT, we consider the following mis-registrations ; rotation, shifts magnification and anamorphosis. Other transformations such as the distortion could be included but were not considered in the study. We can describe them using the following mathematical operators:

The **Rotation** \mathbf{R}_θ of angle θ :

$$\begin{bmatrix} x' \\ y' \end{bmatrix} = \mathbf{R}_\theta \begin{bmatrix} x \\ y \end{bmatrix} = \begin{bmatrix} \cos(\theta) & -\sin(\theta) \\ \sin(\theta) & \cos(\theta) \end{bmatrix} \cdot \begin{bmatrix} x \\ y \end{bmatrix} \quad (2.1)$$

The **Shift** in X s_X and Y s_Y \mathbf{S}_{s_X, s_Y} :

$$\begin{bmatrix} x' \\ y' \end{bmatrix} = \mathbf{S}_{s_X, s_Y} \begin{bmatrix} x \\ y \end{bmatrix} = \begin{bmatrix} x - s_X \\ y - s_Y \end{bmatrix} \quad (2.2)$$

The **Magnification** \mathbf{M}_{m_X, m_Y} where m_X and m_Y correspond to the magnification factors in X and Y :

$$\begin{bmatrix} x' \\ y' \end{bmatrix} = \mathbf{M}_{m_X, m_Y} \begin{bmatrix} x \\ y \end{bmatrix} = \begin{bmatrix} m_X & 0 \\ 0 & m_Y \end{bmatrix} \begin{bmatrix} x \\ y \end{bmatrix} \quad (2.3)$$

The **Anamorphosis** $\mathbf{A}_{\theta, m_R, m_N}$ where m_R and m_N correspond to the radial and normal

magnification with respect to the direction θ . It can be defined as:

$$\mathbf{A}_{\theta, m_R, m_N} = \mathbf{R}_{-\theta} \cdot \mathbf{M}_{m_R, m_N} \cdot \mathbf{R}_{\theta} \quad (2.4)$$

which leads to:

$$\begin{bmatrix} x' \\ y' \end{bmatrix} = \mathbf{A}_{\theta, m_R, m_N} \begin{bmatrix} x \\ y \end{bmatrix} = \begin{bmatrix} m_R \cos^2(\theta) + m_N \sin^2(\theta) & m_N \frac{\sin(2\theta)}{2} - m_R \frac{\sin(2\theta)}{2} \\ m_N \frac{\sin(2\theta)}{2} - m_R \frac{\sin(2\theta)}{2} & m_R \cos^2(\theta) + m_N \sin^2(\theta) \end{bmatrix} \begin{bmatrix} x \\ y \end{bmatrix} \quad (2.5)$$

We can notice that \mathbf{M}_{m_X, m_Y} is a special application of $\mathbf{A}_{\theta, m_R, m_N}$ with $\theta = 0^\circ$ and that $\mathbf{A}_{\theta, m_R, m_N}$ is independent from θ if $m_R = m_N$. In the following we then include the magnification in the anamorphosis. An illustration of the different types of mis-registrations is provided in Figure 2.2.

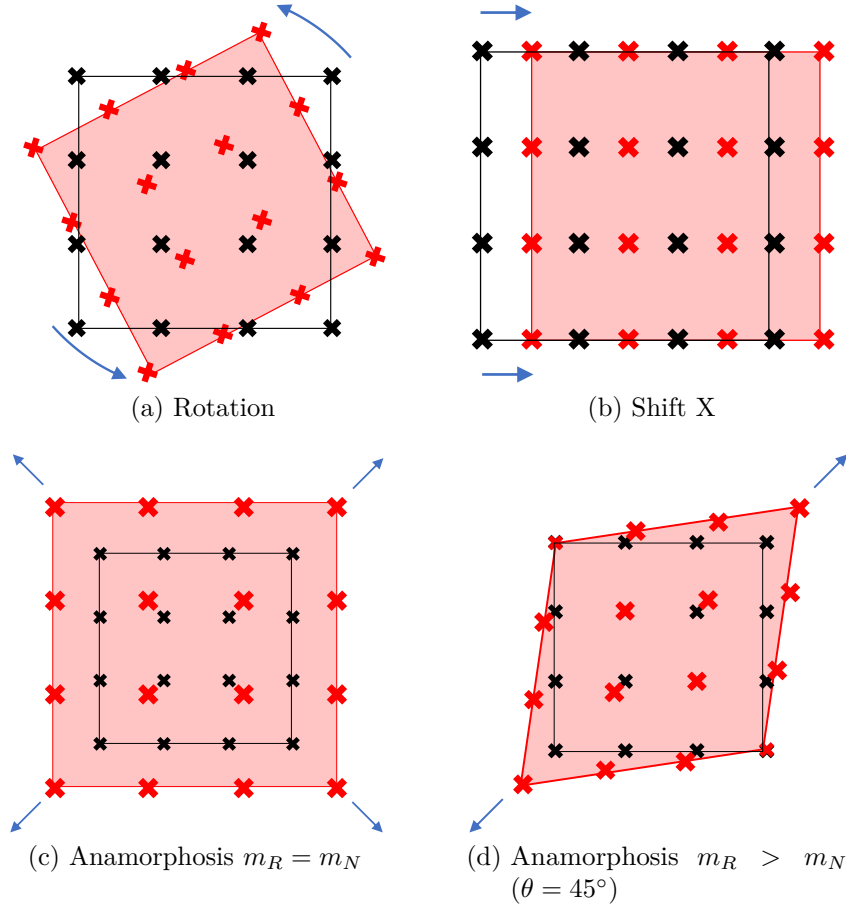


Figure 2.2. – Illustration of the different mis-registration types. The initial DM actuators position is indicated before (black crosses) and after (red crosses) application of the mis-registration.

Theoretically, the mis-registrations can then be handled either in the WFS or in the DM space.

2.1.2. Sensitivity to a mis-registration

In this section, we analyze the sensitivity of the synthetic model to the different mis-registrations considered. This analysis will help quantifying the accuracy required to identify the mis-registration parameters. We consider a model of the FLAO system with a synthetic model of the ASM and a 30 by 30 subapertures PWFS operating in I band (750 nm). As illustrated in chapter 1, the sensitivity to the mis-registrations depends on the number of modes controlled in the reconstructor \mathbf{R} . To consider a realistic case, the interaction matrix generated from the model contains 400 KL modes re-orthogonalized in the DM space (Gendron 1995) to be in line with the High Order mode of the FLAO system. The sensitivity to the different types of mis-registrations for $r_0 = 15$ cm in the visible is given in Figure 2.3.

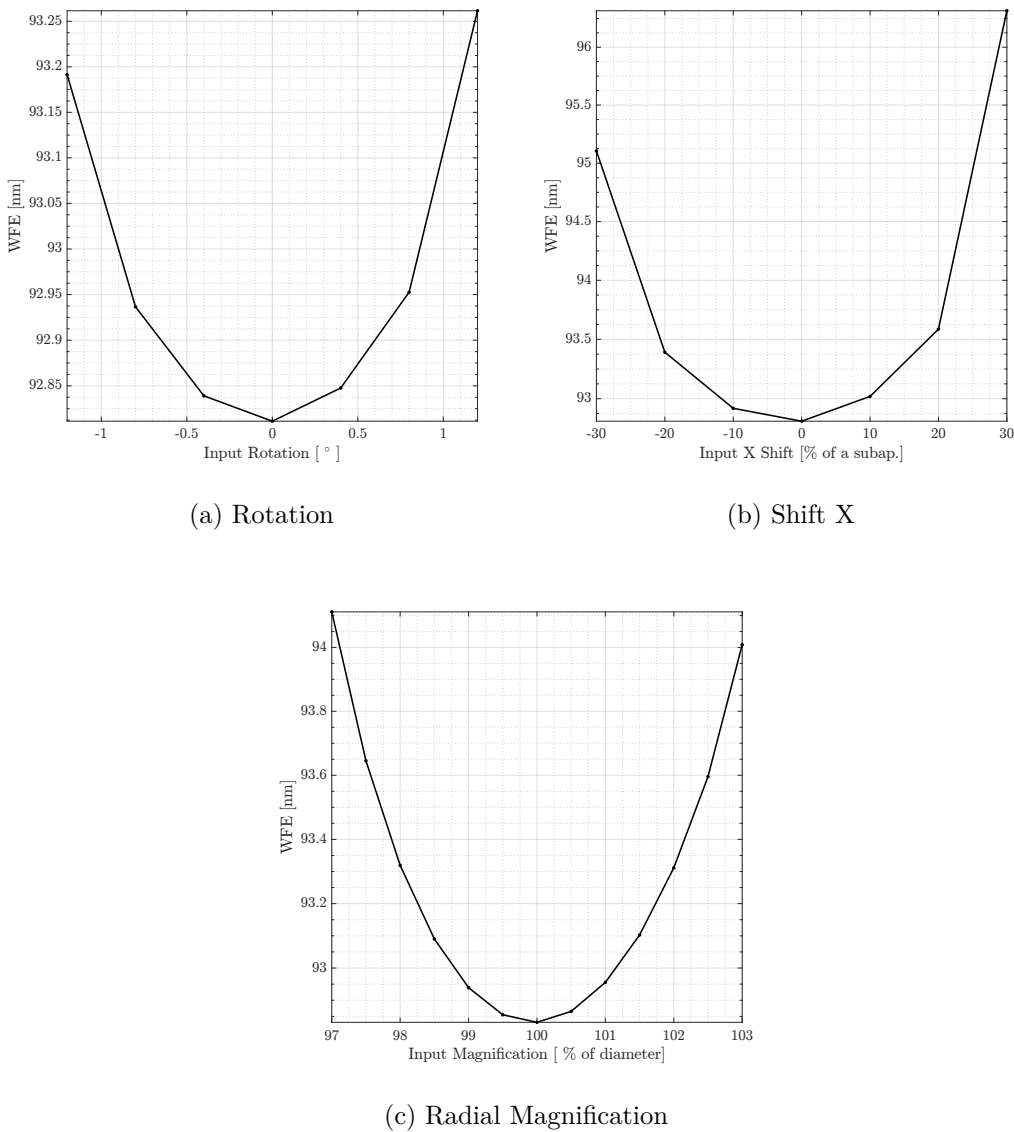


Figure 2.3. – Sensitivity in Wave Front Error to the different mis-registrations for a synthetic model of the FLAO system controlling 400 modes.

These plots indicate that to provide a high accuracy calibration, the precision on the parameters estimation should be under 10% of a subaperture for the shifts, under 0.2° for the rotation and under 0.5% of the diameter for the magnification. Such margins are necessary since the model and the real system will always exhibit small differences even after a fine tuning of the model.

2.2. Modelling of the key components of the AO System for the computation of the synthetic interaction matrix

2.2.1. Modelling of the Deformable Mirror

The overall goal of the synthetic model is to generate an interaction matrix corresponding to a given modal basis. The DM model must then be accurate enough to reproduce the corresponding modal basis projected on the mirror. As introduced in the first chapter, the most common modal basis used to control an AO system consists of KL modes re-orthogonalized in the DM space. Therefore, there is often no mathematical expression for the surface produced by the mirror (Gendron 1995) and the modes have to be computed numerically using a measurement or a model of the influence functions of the DM.

Modelling the Deformable Mirror can then be achieved by defining a set of influence functions that allows to reproduce the modal basis of the real mirror. In OOMAO, it is possible to model a deformable mirror using either a set of influence functions or directly a modal basis. Historically, the term "influence function" defines the surface deformation produced on a mirror corresponding to the poke of a single actuator, normalized by the amplitude of the poke. This optical deformation depends on the actuator position and mechanical coupling between the different actuators, that is intrinsic to the DM technology. We can notice that for a DM using voice-coil technology (which is the case for all the current large adaptive mirrors), the concept of influence function does not really make sense as the DM is controlled in position and no longer in voltages. For this specific case, we can define an influence function as setting one actuator to a delta position of one and the others to 0.

To model the set of influence functions, we can distinguish three approaches: using a fully synthetic model where the deformations are defined using theoretical mathematical functions, using experimental measurements from the real DM input to the model and an hybrid strategy with synthetic models fitted on experimental measurements. We did not have time to investigate this last option.

2.2.1.1. Experimental Influence Functions

Considering experimental measurements of the influence functions is the most instinctive approach as it includes the most important features of the real system (different response of the actuators, imperfection of the base-plate, nonlinearities, real geometry, etc). It requires a measurement of the influence functions by using an interferometer for instance. An illustration of an experimental influence function is given in Figure 2.4.

These measurements are however only valid at the time of measurement and require a good stability of the system over time. If this was not be the case, the model would require to regularly update the influence functions measurements which could become problematic in terms of telescope operations. The measurement will also include noise and bias of the measurement with areas of the DM obstructed by the telescope spiders or central obstruction. Moreover, simulating the effect of misregistrations can be complex as it requires interpolations of measured data. This has a cost in terms of computation time and can lead to numerical edge effects. Some of these edge effects are visible on Figure (2.5) where we show a quarter of an interpolated influence function after applying a rotation.

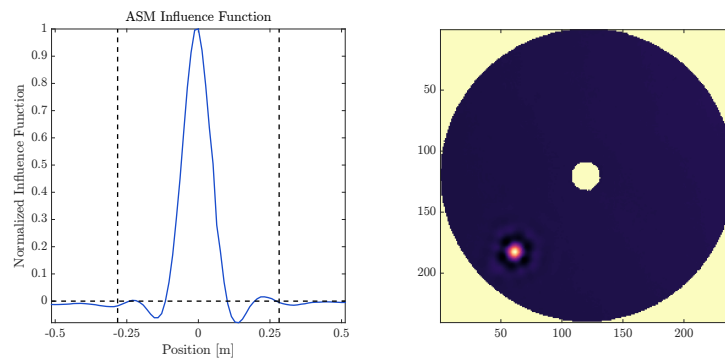


Figure 2.4. – Influence Function from the ASM measured with an interferometer showing the overshoot due to the imposed definition of the influence function.

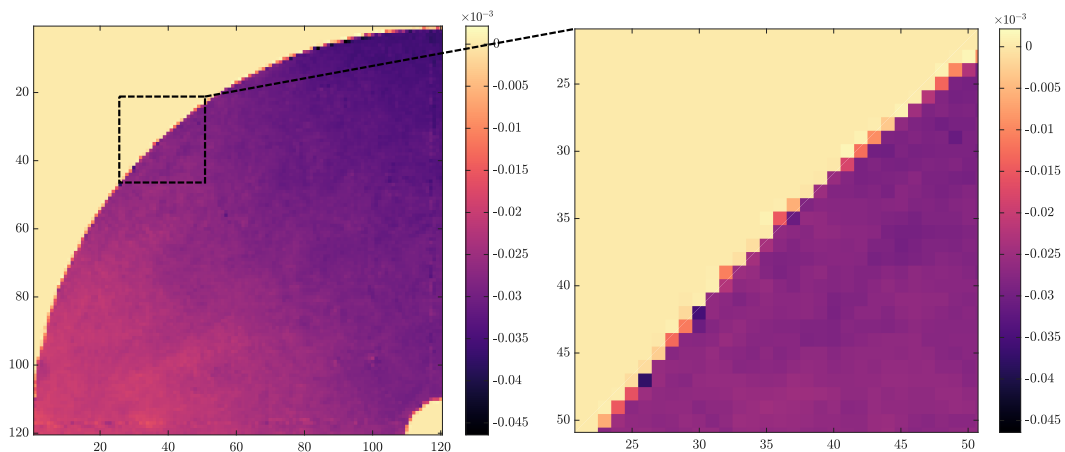


Figure 2.5. – Top-left quarter of an influence function input to the model from an experimental measurement of influence function. It exhibits numerical edge-effects due to the interpolation of the experimental data to apply a rotation to the DM model.

2.2.1.2. Synthetic Influence Functions

In this case, with only a few parameters: actuator coordinates and mechanical coupling, the DM Influence functions can be fully characterized. In addition the influence

functions are noiseless. This strategy has the advantage of being extremely flexible to update the model parameter and apply the desired mis-registrations/mis-alignments. It requires however a preliminary tuning of the influence functions parameters to reproduce accurately the modal basis of the real system.

Applying a mis-registration consists then only in setting the correct parameters to the influence functions definition. In our case, we considered 2D Gaussian influence functions as their mathematical expressions make it easy to handle. To narrow down the analysis, we focus only on this type of functions in this model but it could be easily generalized to any type of function. For example, a numeric version of the influence function shown in Figure 2.4 could be obtained via a Finite Element Analysis (FEA).

A Gaussian influence function can be written using Cartesian coordinates as:

$$f(x, y) = Ae^{-(a(x-x_0)^2+2b(x-x_0)(y-y_0)+c(y-y_0)^2)} \quad (2.6)$$

where

$$a = \frac{\cos^2(\theta)}{2m_R^2} + \frac{\sin^2(\theta)}{2m_N^2} \quad (2.7)$$

$$b = -\frac{\sin(2\theta)}{4m_R^2} + \frac{\sin(2\theta)}{4m_N^2} \quad (2.8)$$

$$c = \frac{\sin^2(\theta)}{2m_R^2} + \frac{\cos^2(\theta)}{2m_N^2} \quad (2.9)$$

We recognize the mis-registration operators introduced in section 2.1.1. It becomes obvious that the rotation, shifts and anamorphosis can be applied setting the different parameters:

- $A=1$ (normalized influence function)
- x_0 and y_0 are the coordinates of the considered actuator
- θ is the anamorphosis angle
- m_R and m_N are the spreads of the influence function in the radial and normal direction.

Rotation and shifts can be applied directly to the coordinates of the centers (x_0, y_0) while anamorphoses require to update the spread of the function to ensure that the mechanical coupling remains the same in all the directions (This is a physical constraint).

An example of Gaussian influence function is given in Figure 2.6.

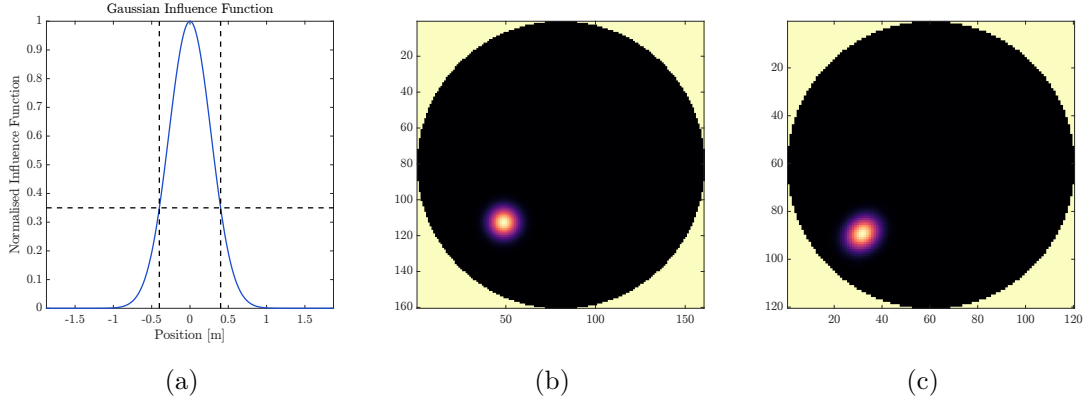


Figure 2.6. – Gaussian Influence Function with a mechanical coupling of 35%, 1D section (a) and 2D representation (b). Same influence function after applying an exaggerated anamorphosis of 120 % of the diameter for $\theta=45^\circ$ (c).

At last, we briefly mentioned that an alternative method would be to fit experimental measurements of the influence functions with theoretical functions. Since an influence function is a mechanical deformation, it can be accurately modelled when the thickness and composition of the materials is known. In that case, this will gather both advantages, to include all the features of the real system and to provide the flexibility of the synthetic model. We did not have time to investigate this last option during this study.

2.2.2. Modelling of the Pyramid WFS

In OOMAO, the Pyramid WFS is simulated using a diffractive model and in our case, we consider only monochromatic sources. To simulate the circular modulation, the light is propagated for each sampling point (one point every λ/D on the modulation circle). This section will introduce the main parameters of the model that are relevant to reproduce an existing Pyramid WFS.

2.2.2.1. Pyramid Phase Mask

As introduced in the first chapter, the Pyramid WFS is located in the focal plane of the telescope and acts as a Fourier filtering mask. A Pyramid WFS object consists then in defining a **phase mask** and a **detector object**.

The pyramid phase mask m is a function of the number of faces n and of the pyramid angle θ that will control the separation of the pupils.

$$m = m_n(\theta) \quad (2.10)$$

In our case we consider only classic pyramid WFS with $n=4$ faces.

An illustration of the mask $m_4(\frac{\pi}{2})$ and the corresponding pyramid pupils is given in Figure 2.7.

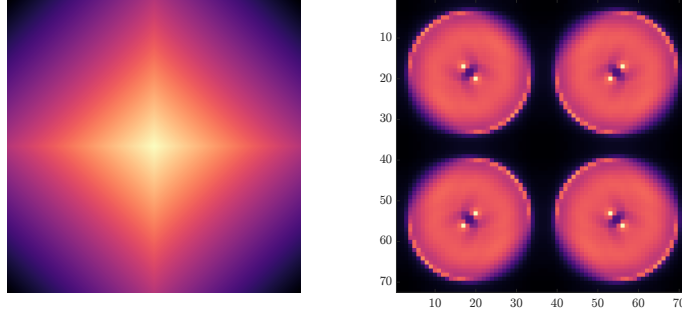


Figure 2.7. – Argument of the optical mask m_4 of the perfect Pyramid WFS. Each face has an angle of $\alpha = \frac{\pi}{2}$

In practice, each quadrant of the phase mask can be treated independently with its own angle:

$$\theta = \theta_1, \dots, \theta_n \quad (2.11)$$

This allows to include potential imperfections of the pyramid in the model and displace an individual pupil with respect to the others. An example of mask with an imperfection and its corresponding pupils is given in Figure 2.8

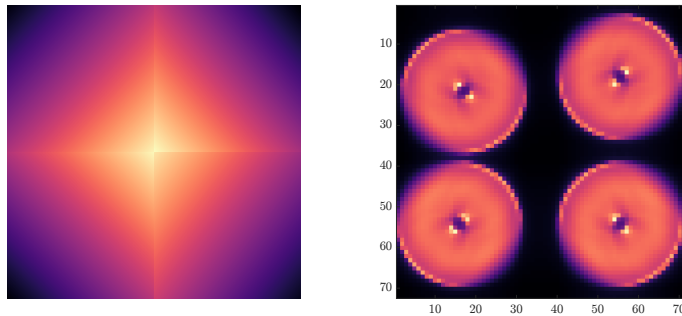


Figure 2.8. – Optical Mask and pupils of the Pyramid WFS Model in presence of an (exaggerated) imperfection.

The position of the pyramid pupils (in pixel) has to be adjusted to reproduce the ratio between the pyramid pupils separation in pixels d_{WFS} (center to center) and the diameter of a single pupil in pixel D_{WFS} (see 2.9).

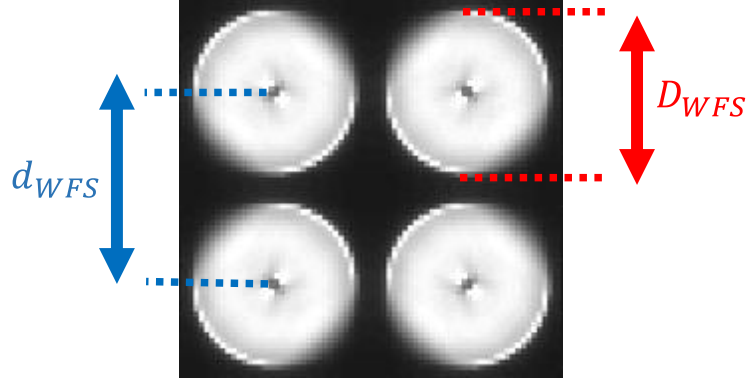


Figure 2.9. – Definition of the pyramid model parameters d_{WFS} and D_{WFS} .

2.2.2.2. Selection of the valid pixels

In the case of the LBT, we consider a quad-cell approach to compute the slopes maps:

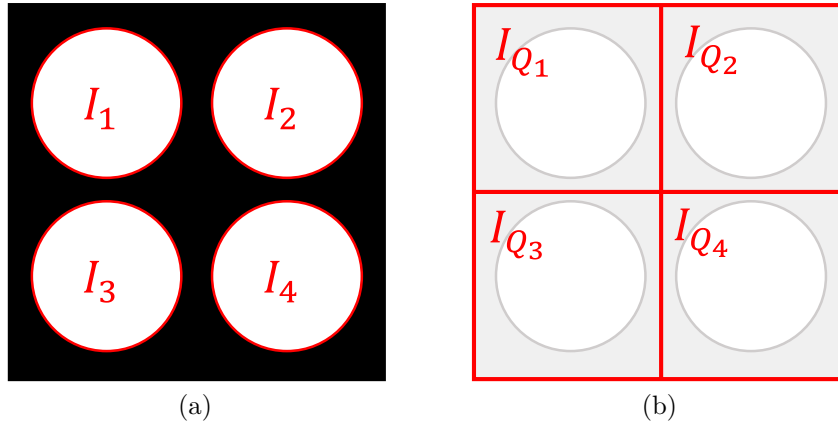


Figure 2.10. – Definition of the Pyramid Pupils I_i (a) and Pyramid Quadrants I_{Q_i} (b)

Using the definition of Figure 2.10 for the different quadrants we recall the definition of the slopes $[S_X^{glob}, S_Y^{glob}]$ introduced in section 1.3.2.2:

$$S_X(x, y)^{glob} = \frac{I_1(x, y) - I_2(x, y) + I_4(x, y) - I_3(x, y)}{I_{glob}} \quad (2.12)$$

$$S_Y(x, y)^{glob} = \frac{I_1(x, y) - I_4(x, y) + I_2(x, y) - I_3(x, y)}{I_{glob}} \quad (2.13)$$

where I_{glob} is define as

$$I_{glob} = \frac{1}{N_S} \sum_{x,y} I_1(x, y) + I_2(x, y) + I_3(x, y) + I_4(x, y) \quad (2.14)$$

where N_S is the total number of valid subapertures.

In the simulator, the mask corresponding to the valid subapertures is obtained by considering the illumination of the pixels. A large modulation is applied (typically

$50 \lambda/D$) to get a uniform illumination of the individual pupils and we consider I_{4Q} , the sum of the four quadrants of the pyramid:

$$I_{4Q} = I_{Q1} + I_{Q2} + I_{Q3} + I_{Q4} \quad (2.15)$$

The subapertures with an intensity higher than a given percentage p of the total intensity on the detector are selected:

$$m_{I_{4Q}} = I_{4Q} > p \times \sum_{i,j} I_{4Q}(i, j) \quad (2.16)$$

The detector mask $m_{detector}$ is the concatenation of the mask $m_{I_{4Q}}$ as illustrated in Figure 2.11

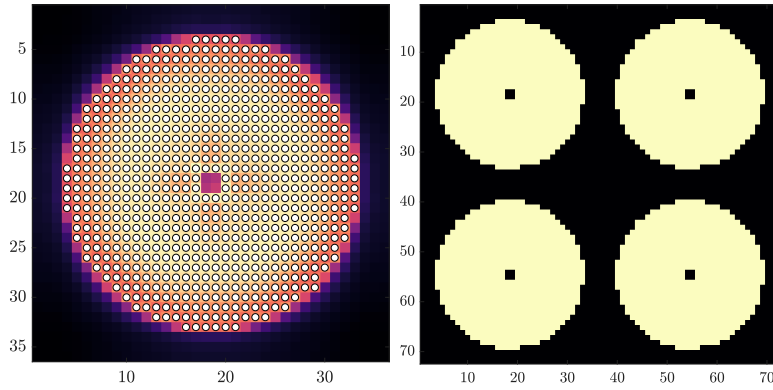


Figure 2.11. – Left: Sum of the four quadrants I_{4Q} and selection of the valid subapertures $m_{I_{4Q}}$ (white dots). Right: Detector mask $m_{detector}$ for the slopes computation

In the frame of a pseudo synthetic calibration, it is required to impose a mask $m_{I_{4Q}}^{exp}$ to the model. The annotation *exp* indicates that the mask is determined using experimental measurements. We propose to maximize the correlation between the sum of the four pupils I_{4Q} and the corresponding mask $m_{I_{4Q}}^{exp}$ to impose to the model. It is then necessary to adjust the WFS model parameters θ to maximize the amount of light that falls in the subapertures selected by $m_{I_{4Q}}^{exp}$. This is important as we want to reproduce at best the real system and thus to reproduce the proper pyramid pupils illuminations. The benefit of this procedure is well illustrated in Figure 2.12 where we see that the central obstruction is initially spread on a square of four pixels (Figure 2.12b) instead of being spread on a cross. The adjustment of the parameter θ allows the model to provide such Pyramid pupils illuminations (2.12c).

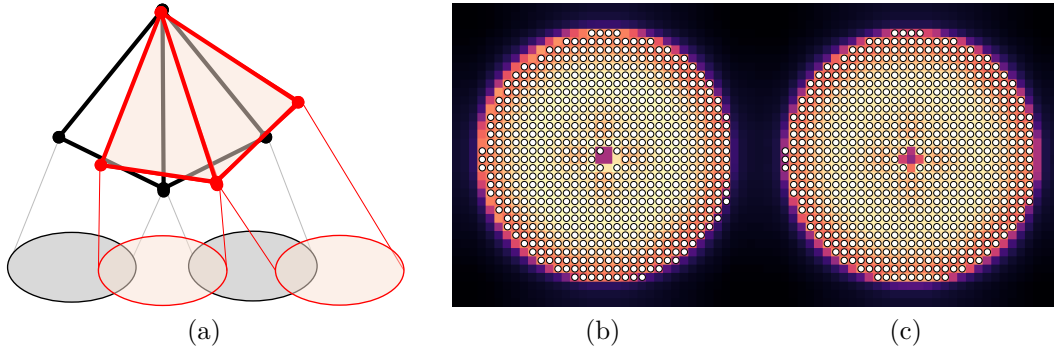


Figure 2.12. – Adjusting the parameter θ of the model to displace the pyramid pupils on the detector plane (a). Sum of the four quadrants of the pyramid model compared to the position of $m_{I_{4Q}}^{exp}$ (white dots) without adjusting θ (b) and after adjusting θ (c).

2.3. Experimental Validation: MNRAS article

This section presents the article: "A new calibration strategy for Adaptive Telescope with Pyramid WFS" that was published in the the journal *Monthly Notices of the Royal Astronomical Society*. This article presents the development of a FLAO model done in OOMAO and its experimental validation at the LBT. It describes how the experimental inputs from the telescope (DM influence functions, Modal Basis, WFS valid subapertures, Interaction Matrix) have been used to tune the model parameters and compute an interaction matrix that could be used at the telescope. This model is however not currently used at the telescope since the system is being upgraded.

Model Definition

In this model, we used experimental influence functions for the DM model as presented in Figure 2.4 and we tuned the Pyramid WFS model using the procedure introduced in section 2.2.2 to maximize the similarity of the pupils illuminations. To model the mis-registrations in the system, we handled the magnification and rotation in the DM space, interpolating the experimental measurements. The shifts were however included in the PWFS space, tilting the pyramid to displace the pyramid pupils on the detector plane, using the procedure described in section 2.2.2.2. This choice was motivated by the fact that the influence function measurements were limited to the DM illumination at the time of measurement and thus we did not have access to a full measurement of a few actuators located either on the edge of the pupils or in the center, behind the central obstruction. That is why shifting the influence functions was then problematic for these few actuators.

Model Parameter Identification

To identify the model mis-registration parameters, we had access to a full interaction matrix (400 KL modes) to tune the model parameters. We used an iterative algorithm that consisted in minimizing the RMS error between the reference signals

\mathbf{D} from the Interaction Matrix measured at the LBT and the one generated from the model $\mathbf{D}^*(\alpha_i)$, optimizing a single parameter α_i at a time. We define σ_j as the RMSE for the mode j :

$$\sigma_j(\alpha_i) = \sqrt{\frac{1}{N_S} \sum_{n=1}^{N_S} |\mathbf{D}_j - \mathbf{D}_j^*(\alpha_i)|^2} \quad (2.17)$$

where N_S is the number of WFS signals \mathbf{D}_j and $\mathbf{D}_j^*(\alpha_i)$ correspond to the signal of the mode j , respectively in the experimental interaction matrix \mathbf{D} and synthetic $\mathbf{D}^*(\alpha_i)$.

The parameter α_i selected is the one minimizing $\chi_N(\alpha_i)$ the quadratic norm of the concatenation of N different σ_j , defined as $\sigma_N(\alpha_i) = \{\sigma_j(\alpha_i)\}_{j=1:N}$:

$$\chi_N(\alpha_i) = \arg \min_{\alpha_i} \|\sigma_N(\alpha_i)\|^2 \quad (2.18)$$

In our case we considered $N = 400$ modes to tune the model parameters and minimized the criterion χ_{400} . The principle of the algorithm is summarized in figure 2.13.

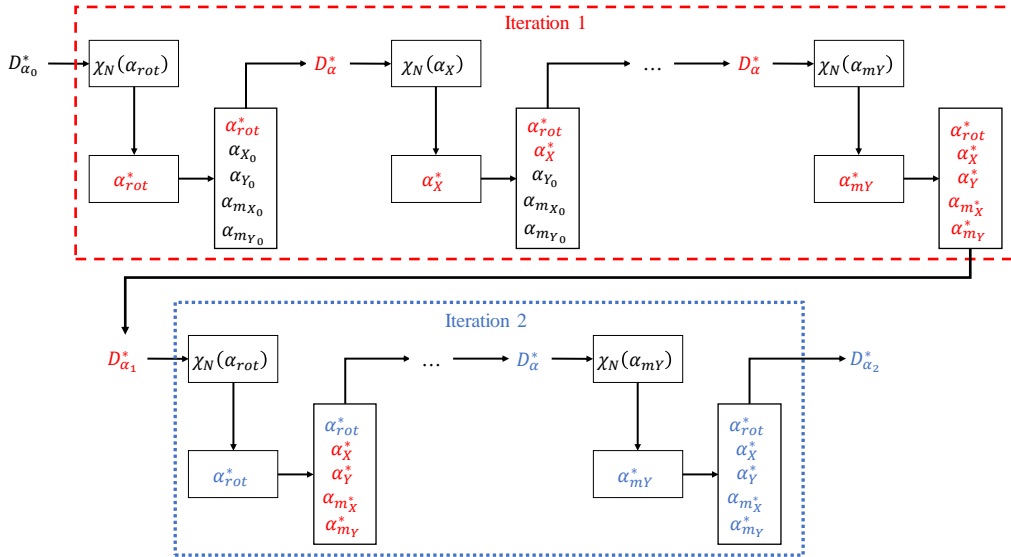


Figure 2.13. – Iterative minimization of the criteria χ_N by playing on a single parameter at a time. \mathbf{D}_{α}^* corresponds to the interaction matrix computed in the model after identifying the mis-registration parameters α .

A preliminary validation of the model was achieved by using the experimental interaction matrix to close the loop of the model in the simulator. Comparing the closed-loop performance of both synthetic and experimental reconstructors allowed to identify that only two iterations for each parameter were required to reproduce accurately the real system mis-registration alignment in the simulator. The article also includes an analysis of sensitivity of the model to the different mis-registrations using both synthetic and experimental interaction matrices in the model. This analysis shows that the best performance using the experimental interaction matrix in the simulator were achieved using the set of mis-registration parameters identified by the identification algorithm.

Summary of the experiment

A summary of the experiment is provided in Figure 2.14 where it is illustrating how the experimental inputs have been used to tune the model.

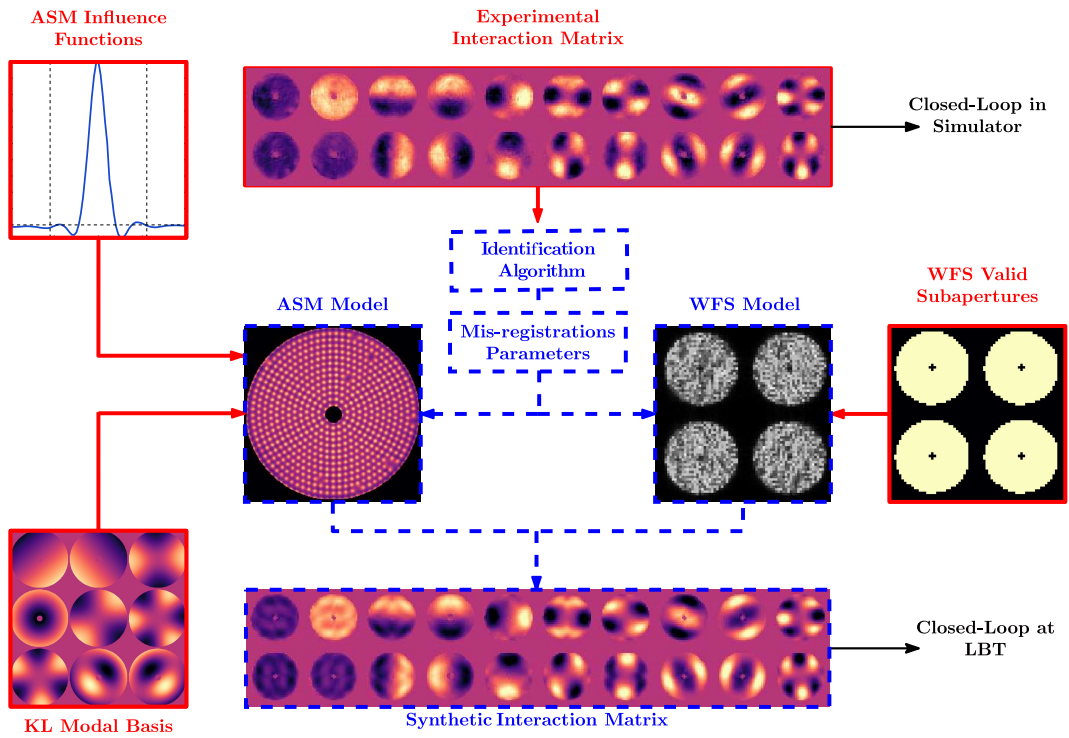


Figure 2.14. – Summary of the development of the Pseudo-Synthetic model of the LBT in the simulator. The **solid red lines** correspond to the experimental inputs and the **dashed blue lines** to the model components and outputs.

A new calibration strategy for adaptive telescopes with pyramid WFS

C. T. Heritier,^{1,2,3,4}★ S. Esposito,³ T. Fusco,^{1,2} B. Neichel,¹ S. Oberti,⁴

R. Briguglio,³ G. Agapito,³ A. Puglisi,³ E. Pinna³ and P.-Y. Madec⁴

¹ Aix Marseille Univ, CNRS, CNES, LAM, Marseille, France

² ONERA, DOTA, Unité HRA, 29 avenue de la division Leclerc, 92322 Chatillon, France

³ INAF - Osservatorio Astrofisico di Arcetri Largo E. Fermi 5, 50125 Firenze (Italy)

⁴ European Southern Observatory, Karl-Schwarzschild-str-2, 85748 Garching, Germany

Accepted 2018 September 06. Received 2018 September 06; in original form 2018 August 27

ABSTRACT

Several telescopes include large Deformable Mirrors (DM) located directly inside the telescope. These adaptive telescopes trigger new constraints for the calibration of the Adaptive Optics (AO) systems as they usually offer no access to an artificial calibration source for the interaction matrix measurement. Moreover, the optical propagation between the DM and the Wave-Front Sensor (WFS) may evolve during the operation, resulting in mis-registrations that highly affect the AO performance and thus the scientific observation. They have to be measured and compensated, for instance by updating the calibration. A new strategy consists of estimating the mis-registrations and injecting them into synthetic models to generate noise-free interaction matrices. This pseudo-synthetic approach is the baseline for the Adaptive Optics Facility working with a Shack-Hartmann WFS and seems particularly suited for the future Extremely Large Telescope as the calibration will have to be regularly updated, for a large numbers of actuators. In this paper, the feasibility of a pseudo synthetic calibration with Pyramid WFS at the Large Binocular Telescope (LBT) is investigated. A synthetic model of the LBT AO systems is developed, and the procedure to adjust the mis-registrations parameters is introduced, extracting them from an experimental interaction matrix. We successfully tested an interaction matrix generated from the model on the real system in high-order AO mode. We recorded a slightly better performance with respect to the experimental one. This work demonstrates that a high accuracy calibration can be obtained using the pseudo synthetic approach with pyramid WFS.

Key words: instrumentation: adaptive optics - telescopes

1 INTRODUCTION

Adaptive Optics (AO) is now commonly spread on large aperture optical telescope facilities to compensate in real time the variations of optical index in the atmosphere and retrieve the full angular resolution of the telescope (Babcock (1953)). The principle of a classical AO system is the following: a Wave-Front Sensor (WFS) measures a signal relative to the phase and sends it to a Real Time Computer (RTC) that computes the corresponding commands to apply on a Deformable Mirror (DM). This system is usually operated

in a feedback-loop at a higher frequency than the temporal evolution of the turbulence (typically, a few hundred Hz). However, to provide a good correction (e.g. to be able to apply the correct shape on the DM at the right time), the AO loop has to be properly calibrated before the operations. This is achieved by measuring the interaction matrix of the system which consists of recording the WFS signals corresponding to a specific command of the DM actuators.

Recent developments in telescope designs and DM technology have led to consider DM located directly into the telescope (turning them from active to adaptive telescopes) to reduce the number of optics and increase the numbers of photons available for the instruments. This concept was

★ E-mail: cedric.heritier@lam.fr

first validated on the MMT (Wildi et al. (2003)) and is now used on two of the largest ground based optical telescopes, the Large Binocular Telescope (LBT), with its two Adaptive Secondary Mirrors (ASM) (Riccardi et al. (2003), Esposito et al. (2010a)) of 672 actuators, and the Unit Telescope 4 of the Very Large Telescope, recently upgraded to become the Adaptive Optics Facility (AOF) (Arsenault et al. (2008), Stroebele et al. (2006)) with its Deformable Secondary Mirror (DSM) of 1170 actuators. The next generation telescopes, the Extremely Large Telescope (ELT) (Gilmuzzi & Spyromilio (2007)) and Giant Magellan Telescope (GMT) (Johns (2006)), will also include large adaptive mirrors in their design with respectively 4356 and 4702 actuators (Verinet et al. (2012), Hinz et al. (2010)). The Thirty Meter Telescope (TMT) is also considering this design and will thoroughly study this option in the coming months (Boyer (2018)). These numbers put light on the very first challenge for the AO calibration of this new generation of adaptive telescopes: how much of precious telescope time will be required to provide a satisfying calibration of the AO systems?

This problematic was already addressed in Oberti et al. (2006) in which a summary of the main technical challenge is provided: large number of actuators and regular update of the calibration with often no external source illuminating the DM. Indeed, such telescopes usually don't provide any access to an intermediate focal plane ahead of the DM, and thus to any artificial calibration source. This specificity requires to completely rethink the way to acquire the interaction matrix of the system. However, even in presence of such an artificial calibration source, the large distance between the DM and the WFS may frequently affect the registration between both systems (due to gravity or flexure). These so-called mis-registrations¹, affect the performance of the AO correction, especially for high order systems which are extremely sensitive to these mis-alignments and require then a high accuracy calibration. Such calibration errors impact the performance of the scientific instruments and can lead to instability of the AO loop, perturbing the telescope operation.

The ELT will take these constraints to another level. The first challenge in terms of telescope operation will be to calibrate a large number of actuators with no access to a calibration source. Moreover, the calibration will require regular updates during the operations due to the unprecedented distance between the DM and the WFS with moving optics between them.

There is then a crucial need to optimise and develop new calibration strategies to overcome these constraints and minimize the telescope time required. Some methods have already been identified to achieve the measurements. The first approach consists of measuring the interaction matrix on-sky (Wildi & Brusa (2004), Esposito et al. (2006), Pieralli et al. (2008), Pinna et al. (2012), Kellerer et al. (2012)) while the second idea is to generate it synthetically using an AO simulator, injecting experimental inputs (Oberti et al. (2006), Kolb et al. (2012b), Kolb et al. (2012a)). A summary of the classical procedure and of some of these new strategies is developed in Section 2.

¹ relative shifts, rotation, magnification or higher order pupil distortion between the DM actuators and WFS subapertures

The community seems to be converging towards the second approach, working on synthetic models of the AO systems in which are injected some mis-registrations parameters to fit with the alignment of the real system. This approach is especially suited for systems that require a frequent update of the calibration with a large number of actuators. The Pseudo Synthetic Interaction Matrix (PSIM) is currently the baseline for the AOF instruments in Ground Layer Adaptive Optics (GLAO) and Laser Tomography Adaptive Optics (LTAO) modes working with a Shack-Hartmann WFS (Hartmann (1900), Shack (1971)).

It is however still to be investigated in the case of the LBT that operates in Single Conjugate Adaptive Optics (SCAO) mode, working with a pyramid WFS (Ragazzoni (1996)) and Natural Guide Stars (NGS). The pyramid WFS specificities could add constraints for the calibration. This WFS provides a gain in sensitivity with respect to the Shack Hartmann (Ragazzoni & Farinato (1999)) but can be complex to model with a modal linearity and sensitivity (Esposito & Riccardi (2001), Vérinaud (2004), Fauvarque et al. (2017)). The response of the sensor is also seeing dependent (Ragazzoni & Farinato (1999)) as the PSF shape on the top of the pyramid will depend on the seeing conditions. Some work has also shown that tracking the modal gains during the operations will improve the closed loop performance (Korkiakoski et al. (2008), Esposito et al. (2012), Esposito et al. (2015), Bond et al. (2018), Deo et al. (2018)). Considering that all of the first light instruments of the ELT will include a pyramid WFS in their design (Neichel et al. (2016), Clénet et al. (2016), Brandl et al. (2016)) it is necessary to identify the key-elements and the accuracy requirements to reproduce the behaviour of an AO system with pyramid WFS with the overall goal to generate calibration data that can be used on a real system.

After a short introduction of the classical and new calibration methods in the context of the adaptive telescopes (section 2), this paper will introduce the development of a synthetic model, reproducing the FLAO-LBT systems (Esposito et al. (2010b)), focusing on the model definition and sensitivity (section 3). Section 4 details the adjustment procedure for the mis-registrations parameters that have been thoroughly verified in simulation. Section 5 presents the results of day-time validation at the LBT.

2 AO CALIBRATION OF AN ADAPTIVE TELESCOPE

This section aims to present the calibration procedure for a classical AO system and provides a short summary of the different calibration strategies in the frame of the future Extremely Large Telescopes.

2.1 General case

Mathematically, the interaction matrix of an AO system is the transfer matrix between the DM and the WFS space. Following the notations introduced in Meimon et al. (2015), the interaction matrix D of an AO system is:

$$D = M_{WFS}.M_{DM} \quad (1)$$

where M_{DM} is the conversion matrix between the DM commands and the optical phase deformations and M_{WFS} the corresponding WFS measurement matrix. This matrix is then inverted to provide the reconstructor R that is used in closed loop.

$$R = D^\dagger \quad (2)$$

The most common inversion method consists of using a Truncated Singular Values Decomposition (SVD), filtering the modes badly seen by the WFS for stability (Boyer et al. (1990) but using a Generalised SVD adding priors on the noise and turbulence statistics provides a gain in the reconstruction (Wallner (1983), Fusco et al. (2001), Gilles (2005)).

The measurement of the interaction matrix is achieved by recording the WFS signals Y corresponding to a given set of actuation pattern U . These measurements are impacted by two sources of noise, the WFS detector noise W and the local turbulence Φ during the measurements.

$$Y = DU + W + M_{WFS} \cdot \Phi \quad (3)$$

Multiplying (3) by the pseudo inverse of the calibration pattern U^\dagger provides the estimation of the interaction matrix \hat{D} .

$$\hat{D} = Y \cdot U^\dagger \quad (4)$$

The calibration pattern is usually chosen to be full rank (for instance a zonal actuation or a modal basis such as DM stiffness modes or Kharunen-Loève modes) to calibrate all the degrees of freedom of the DM, providing $U \cdot U^\dagger = Id$. That way, we can define the calibration error ΔD :

$$\Delta D = D - \hat{D} = -(W + M_{WFS} \Phi) \cdot U^\dagger \quad (5)$$

This equation consists of two independent terms, W the noise related to the WFS detector and $M_{WFS} \cdot \Phi$ the noise related to the turbulence, both multiplied by the pseudo inverse of the calibration pattern U .

In the optimal case, both noise contribution can be minimized using a bright artificial calibration source and reducing Φ to the local turbulence of the optical bench. In that case, the choice of calibration patterns becomes arbitrary as a good SNR is easily achievable. However, if these contributions become non negligible, and if the number of actuators becomes important, it is necessary to optimise the choice of calibration pattern to maximize the SNR and speed up the measurement. Such optimisation have already been investigated by Oberti et al. (2004), Kasper et al. (2004) and Meimon et al. (2015) showing that using system modes or Hadamard patterns to maximize the signal provides a consistent gain in calibration time.

In any case, quantifying the quality of an interaction matrix is still an open question. Some metrics have been investigated in Meimon et al. (2015) and Oberti et al. (2004) but no clear criteria have been identified yet. The only solution to validate the accuracy of an interaction matrix is then to try using it to close the loop of the AO system.

2.2 On-sky calibration

With no calibration source available, an alternative method consists of measuring the interaction matrix on-sky. This strategy faces one major challenge: the impact of the turbulence on the WFS measurements. In equation 3, the term

$M_{WFS} \cdot \Phi$ becomes indeed dominant. Actuating a calibration pattern using a classical push-pull would require such a large amplitude to extract it from the turbulence noise that it will completely saturate the WFS.

The problem becomes then pretty classical: one wants to retrieve a low signal in a noisy (turbulence noise) and variable environment (seeing variation), with a constraint of not saturating the WFS nor the DM stroke.

Taking the two extreme solutions, one could either average the turbulence using a long integration, or freeze it using a fast push-pull measurement. An alternative approach inspired from the telecommunication domain, consists of modulating signals with a low amplitude on the DM (to minimize the impact on science) but large enough to be detectable by the WFS. Using an orthogonal basis, in both temporal and spatial domain, of multiplexed signals, one can retrieve their signatures in the WFS space using a simple demodulation process (Esposito et al. (2006)). This approach has been validated on several systems, at the VLT with a curvature sensor by Oberti et al. (2006), with a high order pyramid WFS at the LBT by Pinna et al. (2012) (operating the demodulation in the Fourier space) and with a Shack Hartmann on the CANARY Facility (Myers et al. (2008)) by Kellerer et al. (2012) (demodulating in the direct space).

The analysis of the results has shown that an accurate knowledge of the temporal behaviour of the system is required (rejection transfer function of the AO loop, temporal delay of the loop) and a trade-off for the modulation parameters (frequency, amplitude, sampling, multiplexing) has to be done to perform an efficient calibration. If these methods are applied during the observation, the impact on science is still to be investigated. In addition, to overcome the constraint of WFS saturation, the signals modulation has to be operated in closed-loop (at least partial) using a first interaction matrix, that could be synthetic.

This demonstrated the feasibility of the on-sky approach as a potential alternative strategy but to our knowledge no operating system is currently using it as its baseline for its AO calibration. Such a calibration requires indeed a longer time than a classical measurement with fibre (with a lower SNR). Moreover, in the case of a Pyramid WFS, if the on-sky calibration takes too long, the WFS response may evolve during the measurements, as it depends on the seeing conditions, and bias the interaction matrix measurement. Therefore, a full on sky calibration does not seem suited for a system with a large number of degrees freedom, especially with pyramid WFS. In the case of adaptive telescopes, potential non linearities and complex internal behaviour (evolution or instability of the DM/WFS registration) may also appear during the operation. These techniques could however be used to retrieve only a few signals on-sky to identify key mis-registrations parameters that are then injected in a synthetic model. This pseudo-synthetic approach seems then to be a better strategy to overcome such constraints.

2.3 New pseudo-synthetic calibration

The pseudo-synthetic calibration has been identified as the most promising calibration strategy for the future Extremely Large Telescopes: mis-registrations parameters extracted

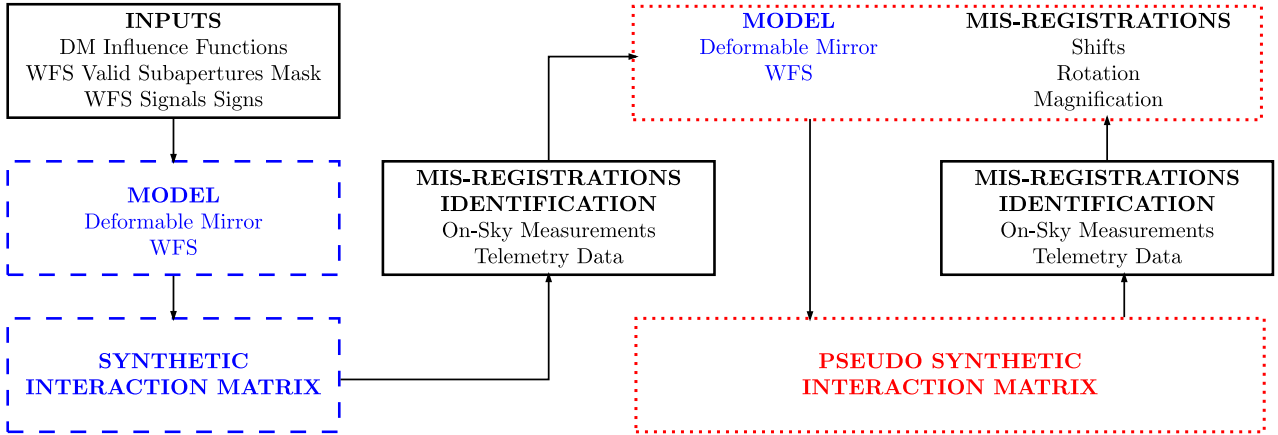


Figure 1. Pseudo Synthetic Calibration: Experimental inputs (solid black lines) are injected into the synthetic model (dashed blue lines) to reproduce the registration of the real system. The pseudo-synthetic interaction matrix (dotted red lines) is then regularly updated during the operation tracking the mis-registrations parameters.

from experimental inputs² are injected into a synthetic model of the AO systems. The principle is summarised in Fig. 1.

This approach provides a noise free interaction matrix, fast to compute and thus, easy to update. The good quality of the calibration relies only on two key ingredients: the ability to model accurately the WFS and the DM and the accuracy of the mis-registrations parameters. Theoretically, if all the experimental effects are perfectly reproduced, a Pseudo Synthetic interaction matrix should then provide a better calibration than a noisy experimental one.

Concerning the first ingredient, the state of the art in terms of AO modeling has shown on various systems (e.g. LBT or VLT) that an accurate calibration can be generated from a synthetic model (Oberti et al. (2006), Kolb et al. (2012a), Pinna et al. (2012)). The modeling of a Shack Hartmann seems to be one step ahead with respect to the Pyramid WFS case as extensive studies related to the sensitivity are available (see Kolb et al. (2012a)). In the case of a Pyramid WFS, the feasibility was demonstrated in Pinna et al. (2012) but no analysis of sensitivity was achieved so far. In the following of this paper, we will try to address this point.

The second ingredient is related to the estimation of the mis-registrations parameters. The nature of the reference signals required to align the model is still open to discussion. The first approach is non-invasive and consists of using telemetry data (WFS slopes and DM commands) to retrieve the corresponding mis-registrations parameters. At the AOF for instance, the idea consists of using closed-loop data to estimate a noisy interaction matrix and project it on sensitivity matrices to identify these parameters (see Kolb et al. (2012a) and Béchet et al. (2011)).

The second approach is invasive and consists of dithering signals on the DM to retrieve their signature in the WFS space (Chiuso et al. (2010)). In Neichel et al. (2012), a strategy based on a Levenberg-Marquardt (Marquardt (1963)) type algorithm is presented in the frame of tomographic AO systems but requires an experimental interaction matrix as

a reference, that could for instance be measured on-sky. The difficulty here is to find the minimum number of signals that would be characteristic of each type of mis-registrations, independently from the others. Since the parameters are strongly correlated, the solution consists here in using an iterative procedure to identify each parameter.

Optimising the accuracy of a pseudo-synthetic interaction matrix is another question. The matrix generated is indeed noise-free and equation 5 takes another form as the only source of error comes from the model: both M_{DM} and M_{WFS} become \widehat{M}_{DM} and \widehat{M}_{WFS} . So far, the only way consists of validating the model against experimental inputs.

3 MODELLING OF THE LBT AO SYSTEMS FOR A PSEUDO SYNTHETIC INTERACTION MATRIX CALIBRATION

3.1 Model definition

We reproduce the FLAO systems (Esposito et al. (2010b)) at the LBT in the end to end simulator OOMAO (Conan et al. (2014)) with the overall goal to generate an interaction matrix that can be used on the real system. It required a fine tuning of the two key elements of the model, ASM and Pyramid WFS, using experimental inputs from the telescope to take in consideration all the features of the existing systems. A summary of the model definition is given in Fig. 2.

The **Adaptive Secondary Mirror** model is composed of 663 valid actuators arranged in circular concentric rings with a 30 cm radial pitch projected on-sky. The ASM Influence Functions measured with interferometer are input to the model. The modal commands matrix from the telescope to produce the 594 modes on the ASM is used in the simulator. The modal basis consists of Kharunen-Loève modes, computed by diagonalising the covariance matrix of the turbulence and re-orthogonalised in the DM space (Esposito et al. (2010a)). The amplitude of the modes used for the interaction matrix computation is low enough to prevent non-linearity effects. As in the real system, the ASM is the stop aperture of the optical system. The arm of the telescope is not taken into consideration as it is done on site for the

² That we will call reference signals in the following of the paper.

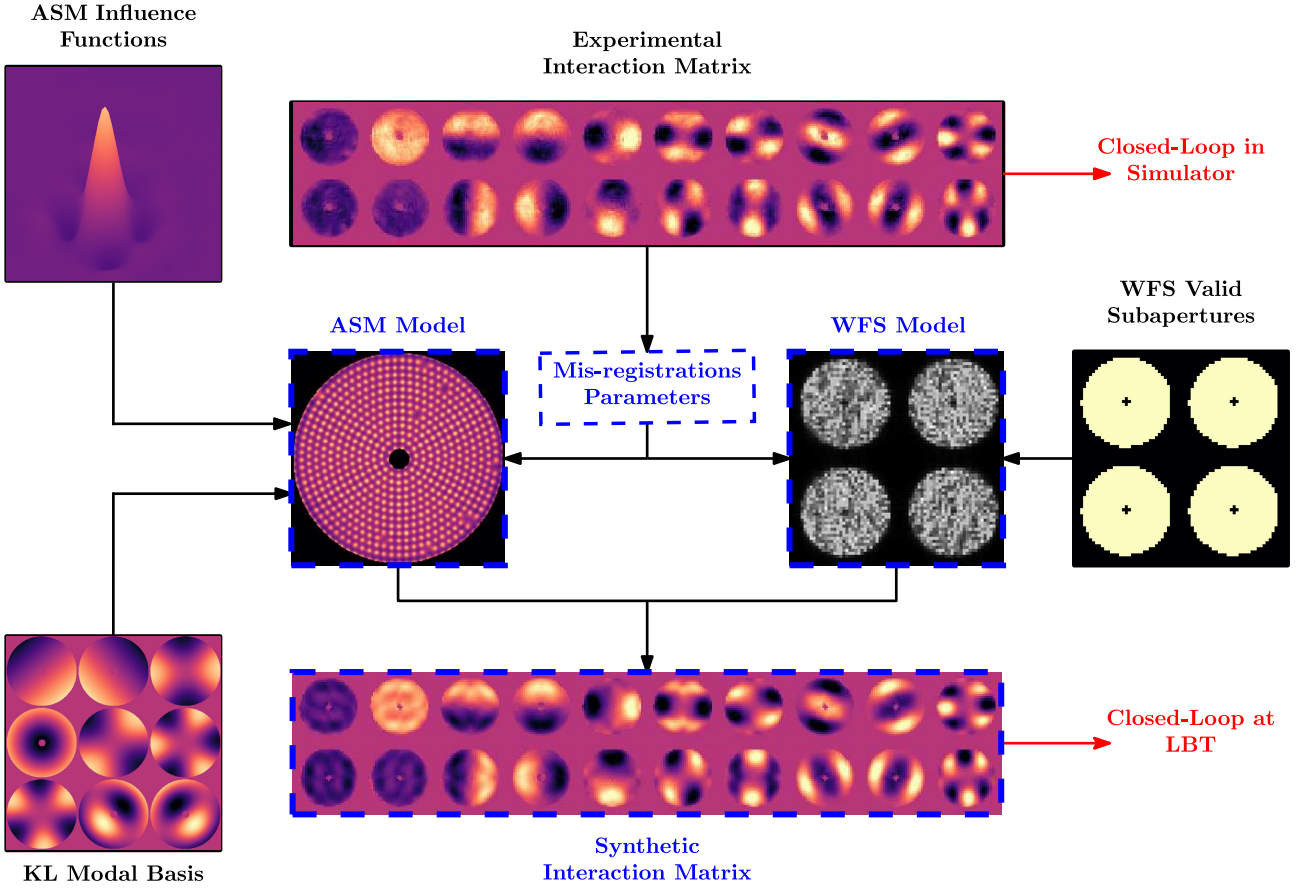


Figure 2. Summary of the model definition. Experimental inputs (solid black lines) are injected into the synthetic model of the AO systems (dashed blue lines). The model mis-registrations parameters are first calibrated so that the experimental interaction matrix can be used to closed the loop in the simulator. The synthetic interaction matrix can then be tested on the real system.

interaction matrix measurement procedure, achieved using a retro-reflector during day-time (Esposito et al. (2010a)). The four spiders of the retro-reflector are not considered either.

The **Pyramid WFS** diffractive model is based on the FLAO pyramid WFS with 30 by 30 subapertures (1 pixel per subaperture) and 36 pixels separating each pupil image centres. The WFS model is a perfect single pyramid³ with no scratches or faces mis-alignment and operates at 750 nm, the central wavelength of the FLAO WFS. The FLAO valid subapertures mask is input to the model, selecting its position to maximize the amount of light in the WFS model pupils. The WFS model is using the optimal Tip/Tilt modulation⁴ of $3 \lambda/D$ considered at the telescope during the observations in high order mode. To reproduce the exact LBT configuration for the interaction matrix measurement, the WFS signals are normalised with a factor 2 to be in line with the double pass procedure using a retro-reflector (Esposito et al. (2010a)).

The computation of the synthetic interaction matrix is

³ The FLAO pyramid WFS is a double pyramid to avoid chromatic dispersion (Esposito et al. (2010a)) but the WFS model is achromatic as it operates at a single wavelength.

⁴ No tuning of the Tip/Tilt modulation was achieved so far.

achieved in a noise-free environment. This feature is well illustrated on the interaction matrix eigen values spectra (Fig. 3). In the synthetic case, the distribution of eigen values is flatter and the knee of the curve occurs for a larger eigen mode number. Here, note that the eigen modes will be slightly different as we still have residual differences between the two interaction matrices. However, the synthetic interaction matrix is better conditioned suggesting that it would be easier to control more modes using a synthetic interaction matrix than an experimental one, taking profit from the infinite SNR of the synthetic WFS signals. These considerations are however only valid if the registration of the real system is well reproduced in the simulator.

The Pyramid sensitivity to the modal basis depends on the Tip/Tilt modulation used for the WFS. A rough estimation of the WFS sensitivity is obtained by considering the WFS slopes Root Mean Square (RMS). The comparison between the model and the experimental WFS is provided in Fig. 4. Both sensitivity plots follow the same tendency which show that the model reproduces well the real system with the same parameter values.

3.2 Sensitivity to a mis-registration

The accuracy of the model mis-registrations parameters is a key ingredient for high order AO systems. In practice, with

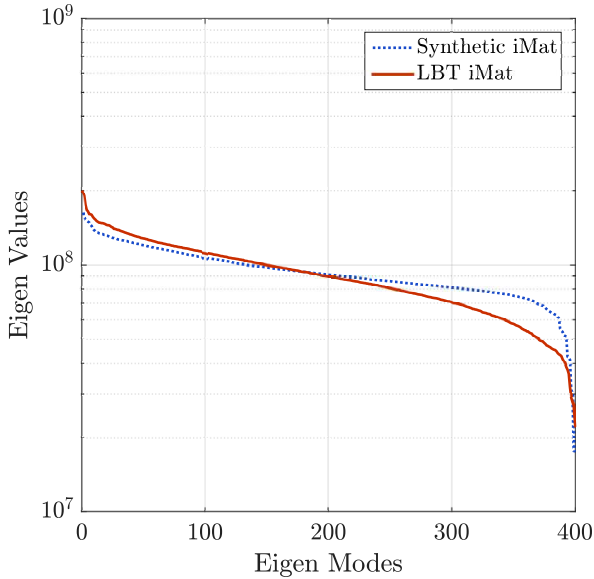


Figure 3. Comparison of the interaction matrices eigen Values distributions between the experimental and synthetic cases. The synthetic interaction matrix has a lower conditioning number (8.1 vs 8.85).

a Shack Hartmann WFS, the common rule is not to exceed an error of 10 % of a subaperture (Béchet et al. (2011)). This result has to be taken carefully as the sensitivity to a mis-registration will depend on the DM geometry and on the number and type of modes controlled in the reconstructor.

Using our model of Pyramid WFS and ASM with circular geometry, we could simulate the impact of each type of mis-registrations on the performance for a seeing of 1" in the visible. The corresponding Wave-Front Error (WFE) as a function of each type of mis-registrations, controlling 400 and 594 modes in the reconstructors is given Fig. 5. In the case of the LBT, a rotation of 1° corresponds to a shift of around 25 % of a subaperture on the border of the pupil.

More details are provided Fig. 6 displaying the modal PSD corresponding to the first mis-registration value after the drop of performance when controlling 594 modes (0.8° for the rotation and 40 % for the shift). It is clearly visible that the high order modes are the most impacted by the mis-registrations and get amplified even to higher values than the incoming turbulence, confirming that high order AO systems are more sensitive to mis-registrations.

These results show that the most critical mis-registrations parameters, the shifts and the rotation should be accurately identified (with less than 10 % of a subaperture for the shifts and less than 0.1° for the rotation which corresponds to a shift of 2.5 % on the border of the pupil) while the impact of a magnification becomes significant when controlling a high number of modes only.

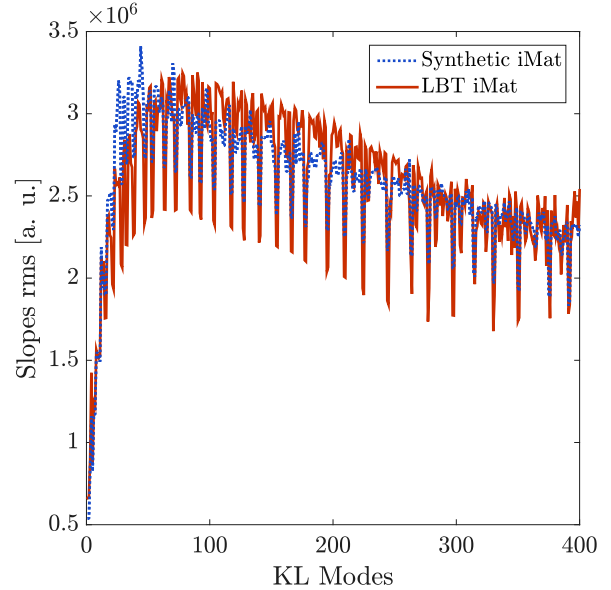


Figure 4. Comparison of slopes RMS plots. Both WFS have the same sensitivity to the KL modes.

4 ASM/WFS MIS-REGISTRATIONS ADJUSTMENT PROCEDURE

This section describes the procedures to finely tune the model mis-registrations parameters and provide a functional interaction matrix for the telescope. We consider here only the fine tuning and rely on a first rough estimation of the parameters (+/- 1 subaperture shift and +/- 2° of rotation) that could be done using flux considerations for instance (Kolb et al. (2012b)).

The tuning of the model requires to define a metric to quantify the error between the model and the real system (4.2). In our case, we use reference WFS signals that correspond to the measurement of 400 KL modes (the current interaction matrix used at the telescope). We then play on the model mis-registrations parameters to generate the corresponding synthetic WFS measurements and use an iterative procedure to minimize the error with the reference.

4.1 Mis-registrations Parameters

The model has 4 **mis-registrations parameters**, the shifts α_x and α_y , the rotation α_{rot} and the radial magnification α_{magn} as it appears to be symmetric. We define α as the corresponding model mis-registrations parameter vector:

$$\alpha \triangleq \{\alpha_x, \alpha_y, \alpha_{rot}, \alpha_{magn}\} \quad (6)$$

In practice, the relative shift between WFS and ASM is applied by shifting the WFS pupils on the WFS detector pixel grid by tilting the pyramid model (providing a sub pixel sensitivity). Both rotation and magnification are applied on the ASM model, interpolating the influence functions.

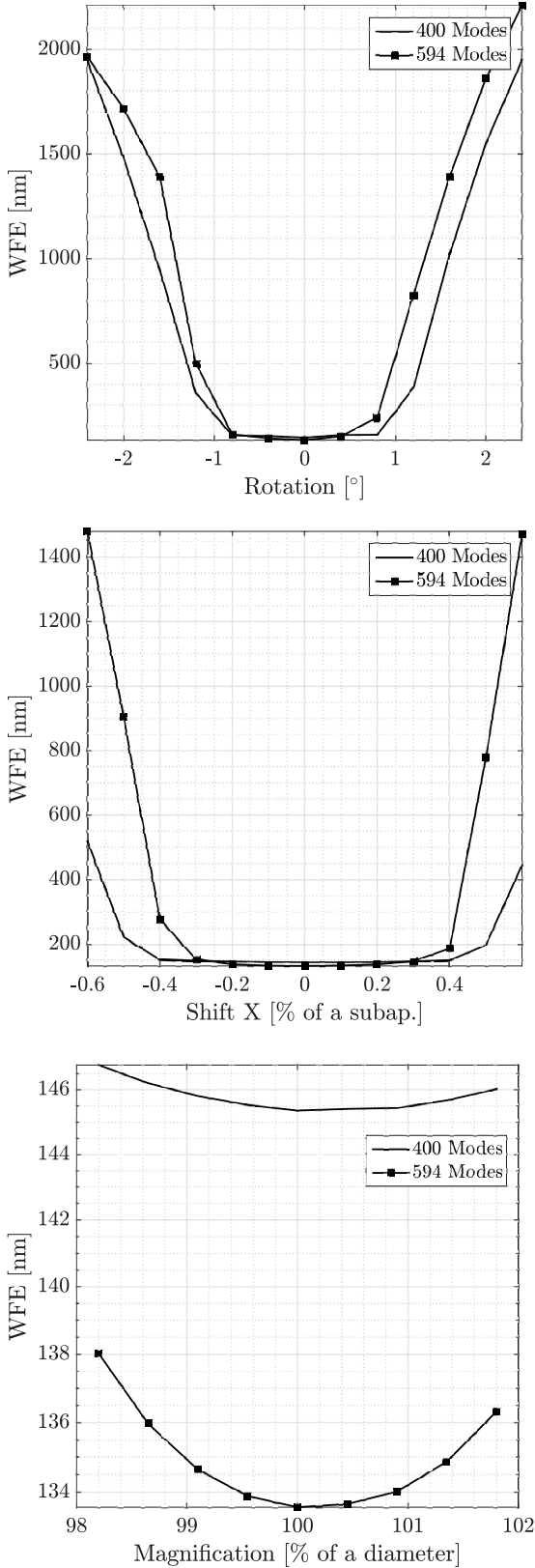


Figure 5. Impact of a mis-registration on the performance (Wave-Front RMS) for a rotation (Top), a shift in X (Middle) and a magnification (Bottom). Results are given for two configurations, controlling 400 and 594 modes.

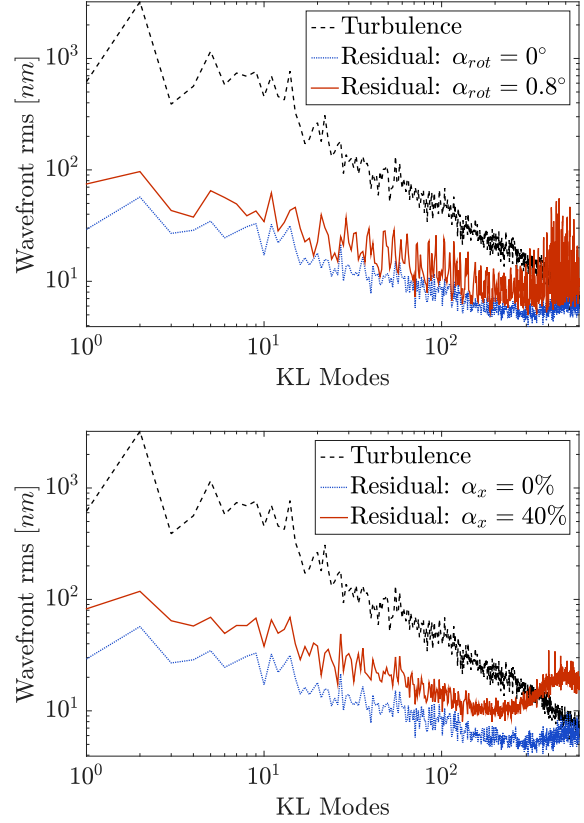


Figure 6. Modal PSD for the nominal and a mis-registered case in the case of a rotation (Top) and a shift in X (Bottom)

4.2 Minimization Criteria

We define σ_j as the Root Mean Square Error (RMSE) between the synthetic WFS measurement $Y^*(\alpha)$ in the configuration α and the reference WFS measurement Y from a real interaction matrix of the mode j :

$$\sigma_j = RMSE(Y_j, Y_j^*(\alpha)) = \sqrt{\frac{1}{N_S} \sum_{n=1}^{N_S} |Y_j - Y_j^*(\alpha)|^2} \quad (7)$$

where N_S is the number of WFS slopes. The criteria χ_N to minimize is the quadratic norm of $\sigma_N = \{\sigma_i\}_{i=1,2,\dots,N}$ adjusting α and eventually considering different numbers of reference signals N :

$$\chi_N(\alpha) = \arg_{\min} \|\sigma_N\|^2 \quad (8)$$

The optimal value chosen for α is the convergence value of the iterative minimization of χ_{400} using all the reference signals available.

4.3 Model Adjustment Procedure

The mis-registrations parameters of the model, especially the shifts and rotation, are strongly correlated in the WFS space. It is therefore necessary to achieve an iterative procedure to adjust correctly the mis-registrations parameters.

Table 1. Model alignment iterative procedure. The values are in fraction of a subaperture (shift), in fraction of pupil diameter (magnification) and in degrees (rotation).

Step	α_i	$\delta\alpha_i$	Value
1	α_{rot}	0.125°	65.33°
2	α_x	25 %	-100 %
3	α_y	25 %	25 %
4	α_{rot}	0.1°	65.08°
5	α_x	2 %	-92 %
6	α_y	2 %	35 %
7	α_{rot}	0.025°	65.08°
8	α_x	2 %	-92 %
9	α_y	2 %	35 %
10	α_{magn}	0.45 %	98 %

The parameters are estimated one by one and the procedure is summarised in Table 1. A first estimation of each shift and rotation is achieved using a large step and then a second estimation using a smaller step. Applying a third estimation does not change the value of the estimated parameters therefore two steps for the iterative procedure are sufficient. The magnification is identified as a last step as its effect is less crucial (see Fig. 5).

The starting point α_0 is defined using the Tip and Tilt WFS signals to roughly estimate the starting rotation value as these modes do not have a circular symmetry.

$$\alpha_0 = \{\alpha_{rot} = 64.5^\circ, \alpha_x = 0\%, \alpha_y = 0\%, \alpha_{magn} = 100\%\} \quad (9)$$

Fig. 7 gives the second step of the parameters estimation, showing a quadratic behaviour around each optimal value. The final value taken for the mis-registrations parameter α_f is obtained from a second order polynomial fit of $\chi_{400}(\alpha)$ and is illustrated in Fig. 8.

$$\alpha_f = \{\alpha_{rot} = 65.08^\circ, \alpha_x = -92\%, \alpha_y = 35\%, \alpha_{magn} = 98\%\} \quad (10)$$

As a last step, we also tuned the modal gains of the pyramid model by playing on the amplitude of the KL modes during the interaction matrix computation and minimize the residual slopes RMS with the reference. The corresponding plots are given in Fig. 4.

4.4 Validation of the mis-registrations parameters adjustments in simulation

The adjustment of the model was intensively validated in simulation. A comparison of a few slopes maps from both interaction matrices is given in Fig. 9 and shows only negligible differences. It also shows that some features of the real measurements are missing from the model especially close to the central obscuration. These features seem to be purely experimental as evolving between different experimental interaction matrices (see Fig. 10). We did not consider these features in the model and their impact is still to be investigated.

To provide a meaningful comparison, the first milestone

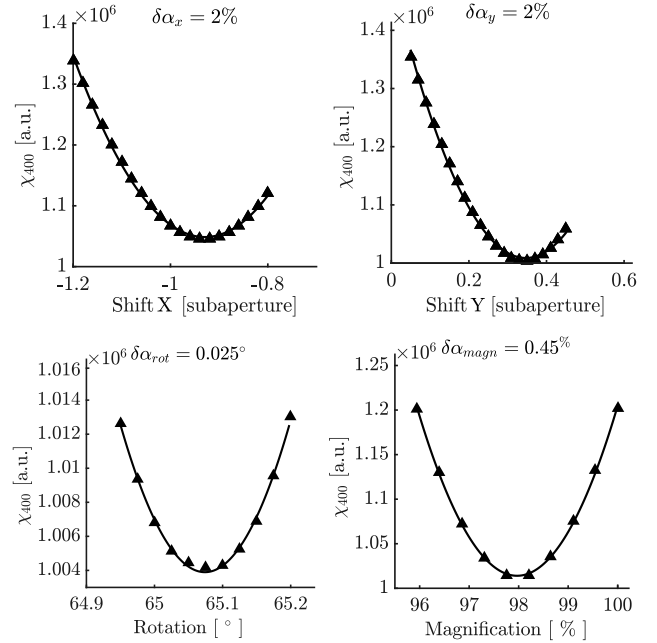


Figure 7. Last step of the minimization criteria χ_{400} for the shifts, rotation and magnification parameters using all the reference signals available. The solid line is a second order polynomial fit.

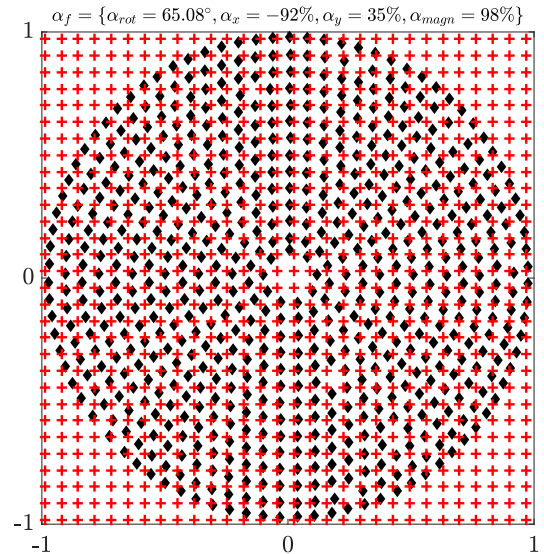


Figure 8. Final configuration for the registration between the ASM actuators (diamonds) and the WFS subapertures (crosses) in normalised units.

was to use the interaction matrix measured at the telescope to close the loop of the simulated AO system. The comparison of simulated closed loop performance of both synthetic and measured interaction matrices provides an indication of the model accuracy. This is given in Fig. 11 and as expected, the synthetic calibration provides a better correction (the corresponding calibration is the optimal calibration for the

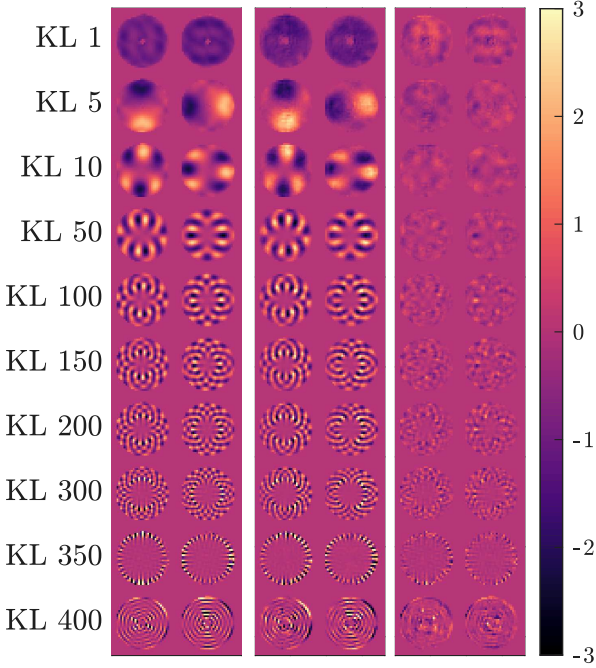


Figure 9. Comparison of pseudo synthetic (Left), LBT (Center) and residual (Right) normalised slopes maps after adjustment of the model. These slopes maps correspond to KL modes 1, 5, 10, 50, 100, 200, 300, 350 and 400.

model) but overall, both reconstructors provide an equivalent correction with a residual variance of 128 nm in the synthetic case and 147 nm using the experimental reconstructor. The differences in residual variance come from the remaining model errors and/or calibration errors from the experimental data. To get rid of these residual differences in performance, some eventual upgrade of the model could be to take in consideration the imperfect illumination identified on the experimental interaction matrix to improve the accuracy of the model.

Moreover, Fig. 12 gives the simulated closed loop performance using the experimental reconstructor and around the optimal mis-registration parameters value identified in section 4. For each parameter, the optimal value provides the best AO performance, confirming the high accuracy of the mis-registrations parameters identification. We also retrieve the same sensitivity to the mis-registrations as in the synthetic case (see Fig. 5).

5 EXPERIMENTAL VALIDATION

The model was validated using day-time remote tests at the LBT. In that configuration, a star of magnitude 7 is simulated using an external fibre and a retro-reflector. A disturbance signal is then applied on the ASM to simulate a turbulence with a seeing of 1" in the visible. A summary of the calibration procedure of the LBT is developed in [Esposito et al. \(2010a\)](#).

Before closing the loop, a tuning of the integrator gain is applied for the Tip/Tilt, the following modes up to 100 and

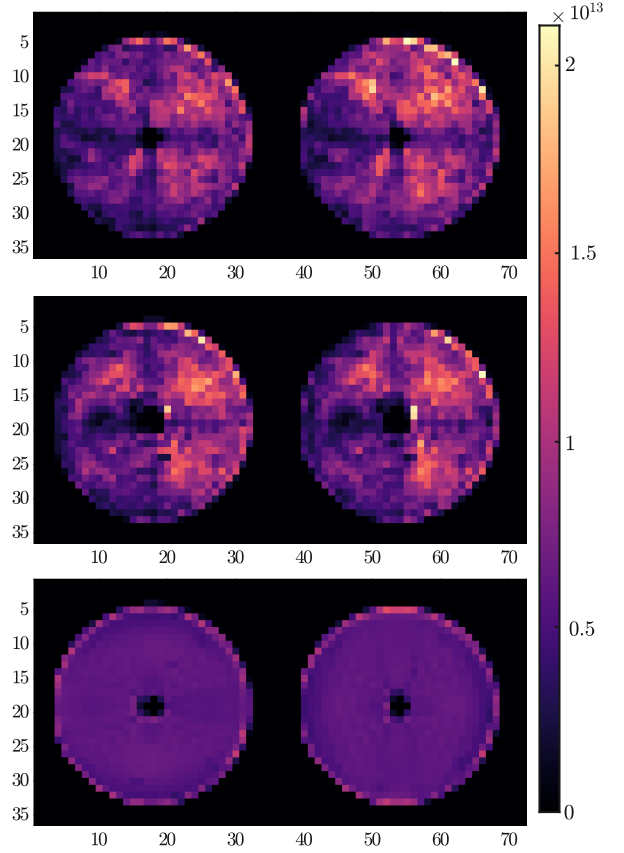


Figure 10. Slopes variance map $[S_x S_y]$ corresponding to the 400 KL modes contained in the Interaction matrices of the LBT from 2016 (Top), 2017 (Middle) and from the simulator (Bottom). It is visible that some parts of the pupils gathered less signals than others, the bottom left part, the central obscuration and behind the spiders of the retro-reflector. These features were not considered in the model.

for the remaining modes up to 400. The tuning of the gains consists of applying a ramp of gain values and select the one minimizing the RMSE of the residual slopes. That way, a different gain value will be used for each group of modes during the closed-loop operation. For our experimental tests, we applied this procedure to the experimental interaction matrix and used the corresponding values for our synthetic interaction matrix with no further tuning.

Fig. 13 provides the comparison of performance between the pseudo-synthetic and experimental interaction matrix using the mis-registrations values identified from the iterative procedure defined in 4. Both reconstructors provide an equivalent correction and the details of the corresponding residuals are summarised in Table 2, showing that the pseudo-synthetic interaction matrix provided a slightly better correction than the experimental one. We can notice on the modal PSD that some low order modes (mostly Tip/Tilt and Focus) have a significantly higher variance compared to what we could expect with a simulated turbulence and a bright star. This effect takes origin from the estimation of the residuals. These are computed from the DM positions which include the correction for the vibrations of the tele-

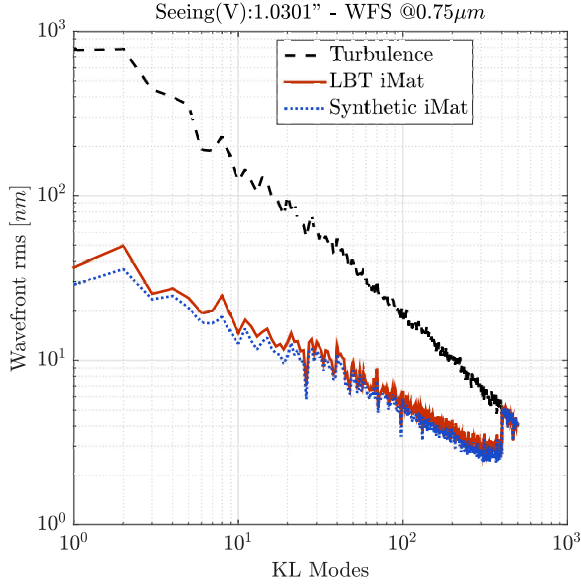


Figure 11. Comparison of simulated closed loop Modal Power Spectral Density (PSD) using both reconstructors, synthetic and measured at the telescope.

Table 2. Summary of the experimental closed loop performance for both pseudo synthetic and experimental interaction matrices.

Int. Mat.	WFE	TT rem.	50 KL rem.
PSIM 400 Modes	195 nm	41.7 nm	30.1 nm
LBT 400 Modes	216 nm	42.1 nm	30.8 nm
PSIM 500 Modes	228.3 nm	42.5 nm	27.39 nm

scope. These modes should then not be considered for the performance comparison.

In addition, we managed to push the synthetic interaction matrix to correct up to 500 modes and get stable closed-loop with high order correction visible in Fig. 14. This validates the high accuracy of the mis-registrations parameters estimation while having WFS reference measurements for only 400 KL modes. The corresponding PSF from the instrument LUCI (Heidt et al. (2018)) for 400 and 500 modes using the synthetic interaction matrix are also given in Fig. 14.

6 CONCLUSIONS

We developed a synthetic model of the FLAO Pyramid WFS and Adaptive Secondary Mirror using experimental inputs from the telescope. We considered a perfect pyramid WFS and used measured influence functions for the ASM model. To identify the mis-registrations parameters, we defined an iterative procedure using an experimental interaction matrix as a reference to adjust the model mis-registrations parameters. The accuracy of these parameters has been thoroughly verified in simulation.

The interaction matrix generated from the model has

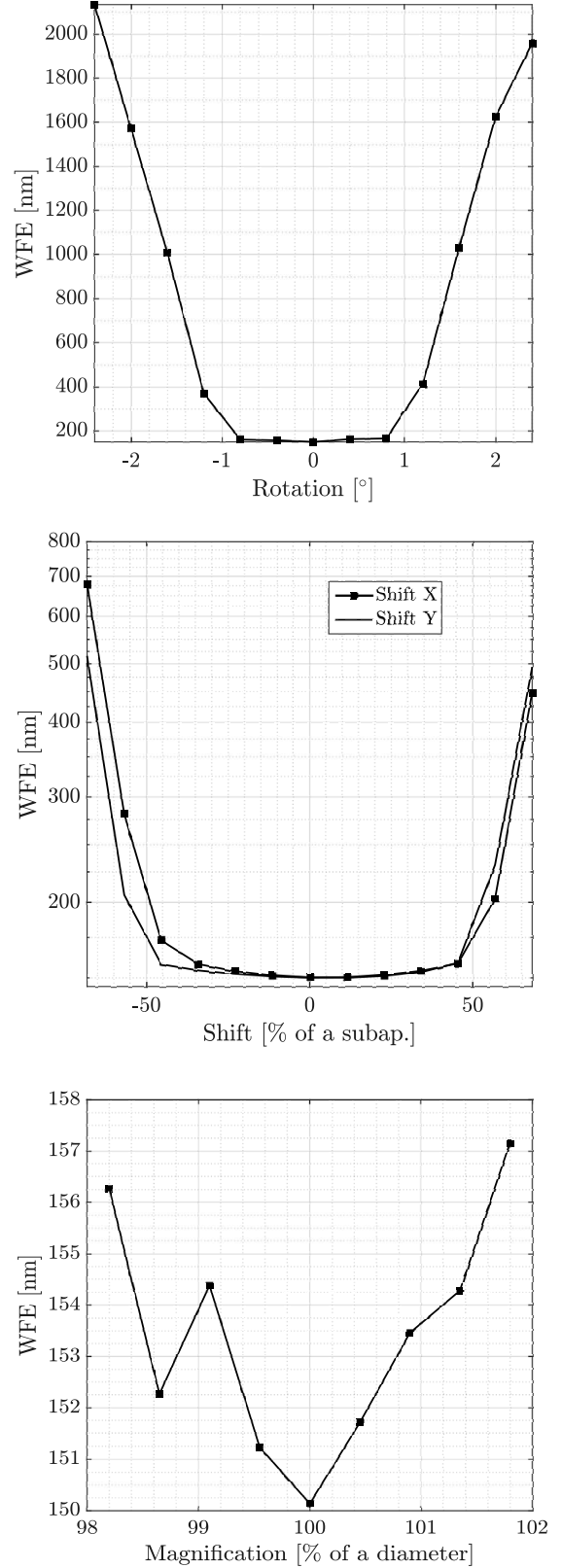


Figure 12. Simulated closed loop performance using the experimental reconstructor in the same conditions as Fig. 5, playing around the optimal value of rotation (Top), both shifts (Middle) and magnification (Bottom) identified during the model adjustment procedure.

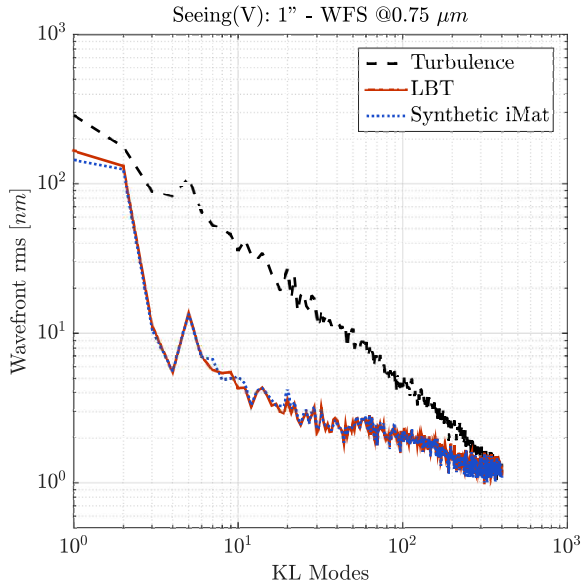


Figure 13. Comparison of modal PSD using both interaction matrices, Synthetic and Reference for a same disturbance applied on the ASM.

been validated experimentally using day-time at the LBT. This demonstrates the feasibility of the pseudo synthetic calibration for high-order AO systems with pyramid WFS. Using the mis-registrations parameters identified from the experimental reference, no further tuning on-site was required to efficiently close the loop of the real system. It provided slightly better performance than the experimental one and we could control up to 500 modes with the synthetic reconstructor.

Through this experimental validation, we have now a tool to achieve meaningful analysis by simulations. As a first result, we could study the sensitivity of the AO system to the different mis-registrations, showing that the most critical parameters are the shifts and rotation.

This work will be very relevant for the future ELT as all the SCAO modules of the first light instruments will most likely include a pyramid WFS in their design. The next step will be to consider the constraints of this telescope for the AO calibration. For instance, with no calibration source, a whole reference interaction matrix may not be available as it would most probably have to be acquired on-sky. In that case, acquiring only a few WFS signals (selected to maximize the sensitivity to each type of mis-registrations) might be sufficient to provide an accurate estimation of the mis-registrations parameters. There is a need to study the number and type of signals required to adjust the model mis-registrations parameters. If these signals are acquired on-sky, the impact of the noise on the parameters estimation will also have to be investigated.

In this paper, we highlighted that the key ingredients to generate an accurate pseudo synthetic interaction matrix is the estimation of the mis-registrations parameters. There is a need to optimise the identification and especially the

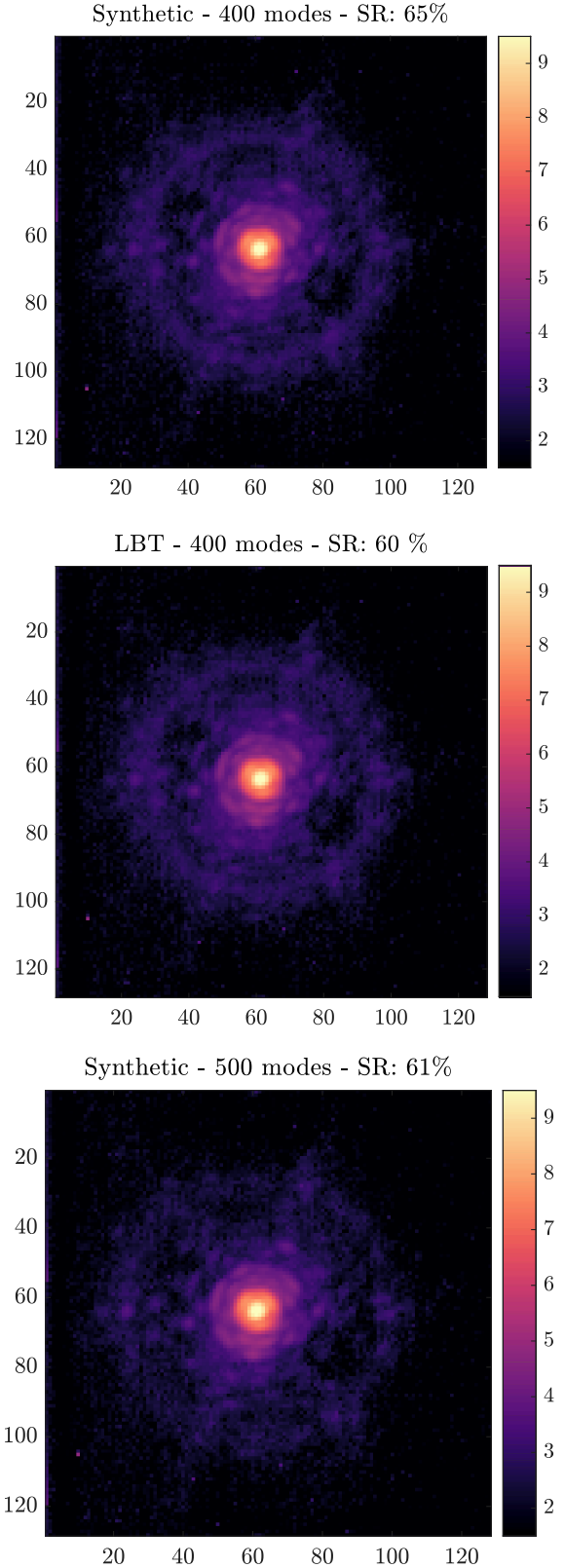


Figure 14. PSF in H band (log scale) controlling 400 and 500 modes with the synthetic and experimental interaction matrix. The Field of View of the instrument is $30''$.

tracking of these parameters during the operation, if possible without injecting any perturbation. This had to be done taking into account the complexity of the Pyramid WFS (modal sensitivity and linearity dependent on the seeing conditions and on the WFS modulation). Many concepts have already been proposed to this purpose. They still have to be carefully evaluated.

ACKNOWLEDGEMENTS

This project has received funding from the European Union’s Horizon 2020 research and innovation programme under grant agreement No 730890. This material reflects only the authors views and the Commission is not liable for any use that may be made of the information contained therein.

REFERENCES

- Arsenault R., et al., 2008, pp 7015 – 7015 – 12
- Babcock H. W., 1953, Publications of the Astronomical Society of the Pacific, 65, 229
- Béchet C., Kolb J., Madec P.-Y., Tallon M., Thiébaud E., 2011, AO4ELT II Conference
- Bond C., Correia C., Sauvage J., Hadi K., Abautret Y., Neichel B., Fusco T., 2018, Adaptive Optics for Extremely Large Telescopes
- Boyer C., 2018, in Adaptive Optics Systems VI. p. 107030Y
- Boyer C., Michau V., Rousset G., 1990, in Adaptive Optics and Optical Structures. pp 63–82
- Brandl B. R., et al., 2016, in Ground-based and Airborne Instrumentation for Astronomy VI. p. 990820
- Chiuso A., Muradore R., Marchetti E., 2010, IEEE Transactions on Control Systems Technology, 18, 705
- Clénet Y., et al., 2016, in Adaptive Optics Systems V. p. 99090A
- Conan R., Correia C., et al., 2014.
- Deo V., Gendron É., Rousset G., Vidal F., Buey T., 2018, in Adaptive Optics Systems VI. p. 1070320
- Esposito S., Riccardi A., 2001, Astronomy & Astrophysics, 369, L9
- Esposito S., Tubbs R., Puglisi A., Oberti S., Tozzi A., Xompero M., Zanotti D., 2006, *Proc.SPIE*, 6272, 6272
- Esposito S., et al., 2010a, Applied Optics, 49, G174
- Esposito S., et al., 2010b, in Adaptive Optics Systems II. p. 773609
- Esposito S., et al., 2012, in Adaptive Optics Systems III. p. 84470U
- Esposito S., Pinna E., Puglisi A., Agapito G., Veran J. P., Herriot G., 2015, in Adaptive Optics for Extremely Large Telescopes 4–Conference Proceedings.
- Fauvarque O., Neichel B., Fusco T., Sauvage J.-F., Girault O., 2017, Journal of Astronomical Telescopes, Instruments, and Systems, 3, 019001
- Fusco T., Conan J.-M., Rousset G., Mugnier L. M., Michau V., 2001, JOSA A, 18, 2527
- Gilles L., 2005, Applied Optics, 44, 993
- Gilmozzi R., Spyromilio J., 2007, The Messenger
- Hartmann J., 1900, Zeitschrift für Instrumentenkunde, 20, 47
- Heidt J., et al., 2018. pp 10702 – 10702 – 15
- Hinz P. M., Bouchez A., Johns M., Shectman S., Hart M., McLeod B., McGregor P., 2010, in Adaptive Optics Systems II. p. 77360C
- Johns M., 2006, in Ground-based and Airborne Telescopes. p. 626729
- Kasper M., Fedrigo E., Looze D. P., Bonnet H., Ivanescu L., Oberti S., 2004, JOSA A, 21, 1004
- Kellerer A., Vidal F., Gendron E., Hubert Z., Perret D., Rousset G., 2012, in Adaptive Optics Systems III. p. 844765
- Kolb J., Madec P.-Y., Louarn M. L., Muller N., Béchet C., 2012a, in Proc. of SPIE Vol. pp 84472D–1
- Kolb J., Muller N., Aller-Carpentier E., Andrade P., Girard J., 2012b, in Proc. of SPIE Vol. pp 84475U–1
- Korkiakoski V., Vérinaud C., Le Louarn M., 2008, Applied optics, 47, 79
- Marquardt D. W., 1963, Journal of the society for Industrial and Applied Mathematics, 11, 431
- Meimon S., Petit C., Fusco T., 2015, *Opt. Express*, 23, 27134
- Myers R. M., et al., 2008, in Adaptive Optics Systems. p. 70150E
- Neichel B., Parisot A., Petit C., Fusco T., Rigaut F., 2012, in Proc. SPIE. p. 84475N
- Neichel B., et al., 2016, in Adaptive Optics Systems V. p. 990909
- Oberti S., Bonnet H., Fedrigo E., Ivanescu L., Kasper M. E., Paufique J., 2004, in Advancements in Adaptive Optics. pp 139–151
- Oberti S., et al., 2006, in Proc. SPIE. p. 627220
- Pieralli F., Puglisi A., Quirós-Pacheco F., Esposito S., 2008, Adaptive Optics Systems N. Norbert Hubin and EM Claire and and PL Wizinowich and eds, 7015, 70153A
- Pinna E., et al., 2012, in Proc. SPIE. p. 84472B
- Ragazzoni R., 1996, Journal of modern optics, 43, 289
- Ragazzoni R., Farinato J., 1999, Astronomy and Astrophysics, 350, L23
- Riccardi A., Brusa G., Salinari P., Gallieni D., Biasi R., Andrighettoni M., Martin H. M., 2003, in Adaptive Optical System Technologies II. pp 721–733
- Shack R. V., 1971, J. Opt. Soc. Am., 61, 656
- Stroebele S., et al., 2006, in Advances in Adaptive Optics II. p. 62720B
- Vérinaud C., 2004, Optics Communications, 233, 27
- Vernet E., Cayrel M., Hubin N., Mueller M., Biasi R., Gallieni D., Tintori M., 2012, in Adaptive Optics Systems III.
- Wallner E. P., 1983, JOSA, 73, 1771
- Wildi F. P., Brusa G., 2004, in Advancements in Adaptive Optics. pp 164–174
- Wildi F. P., Brusa G., Lloyd-Hart M., Close L. M., Riccardi A., 2003. pp 5169 – 5169 – 9

This paper has been typeset from a $\text{\TeX}/\text{\LaTeX}$ file prepared by the author.

2.4.2. Influence Functions

The set of influence functions is defined using normalized Gaussian Influence Functions with the coordinates of the ASM. We adjusted the parameters of coupling of the influence function to minimize the residual variance between the experimental basis and the one produced by the synthetic model (see Figure 2.16a). According to these results, the value of 45 % of mechanical coupling was selected as its maximum residual is the smallest of all the other cases. We can see that a specific mode (KL 373) is particularly badly reconstructed by the synthetic model. An illustration of this mode is provided in Figure 2.17. Another model of influence function could improve the accuracy of the model but the impact seems negligible. In addition, Figure 2.16b shows that the matrix $\mathbf{B}_{\text{synth}}^T \cdot \mathbf{B}_{\text{exp}}$ is well diagonal, where \mathbf{B}_{exp} corresponds to the experimental basis and $\mathbf{B}_{\text{synth}}$ to the modal basis produced by the model for different values of mechanical coupling.

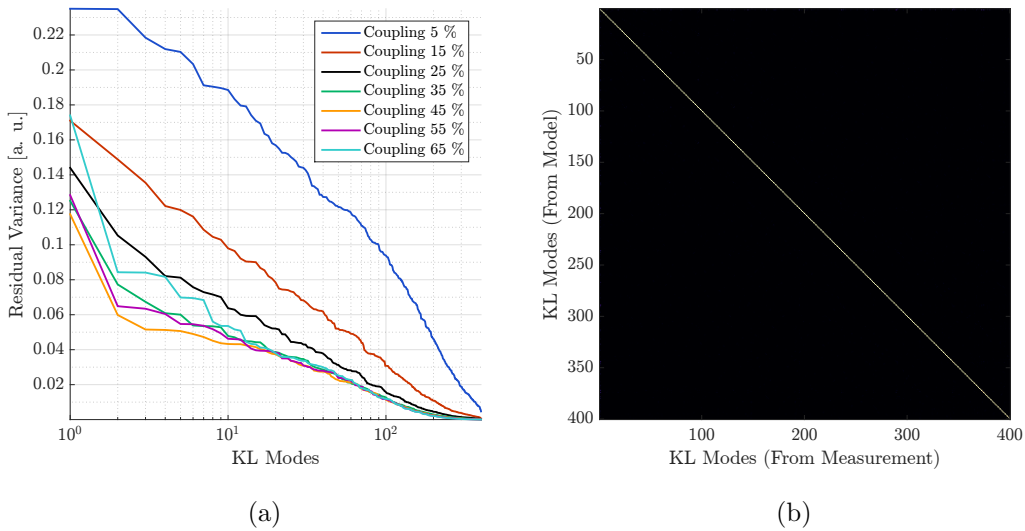


Figure 2.16. – (a) Residual variance between the experimental and synthetic modal basis for the different mechanical coupling of the influence functions. The values are ordered in decreasing order. (b) Illustration of the cross-matrix $\mathbf{B}_{\text{synth}}^T \cdot \mathbf{B}_{\text{exp}}$ in the case of 45% mechanical coupling showing that the matrix is well diagonal.

	α_{rot}	α_X	α_Y	α_{m_X}	α_{m_Y}
Iteration 0	0 °	0%	0%	100 %	100%
Iteration 1	-0.03 °	32.48 %	0.56 %	98.9 %	98.1%
Iteration 2	0.02°	38.77%	0.45%	98.5%	98.35%

Table 2.1. – Mis-registration parameters estimation from the new identification algorithm. The values for the shifts are in fraction of a subaperture and the values for the magnifications in percentage of diameter.

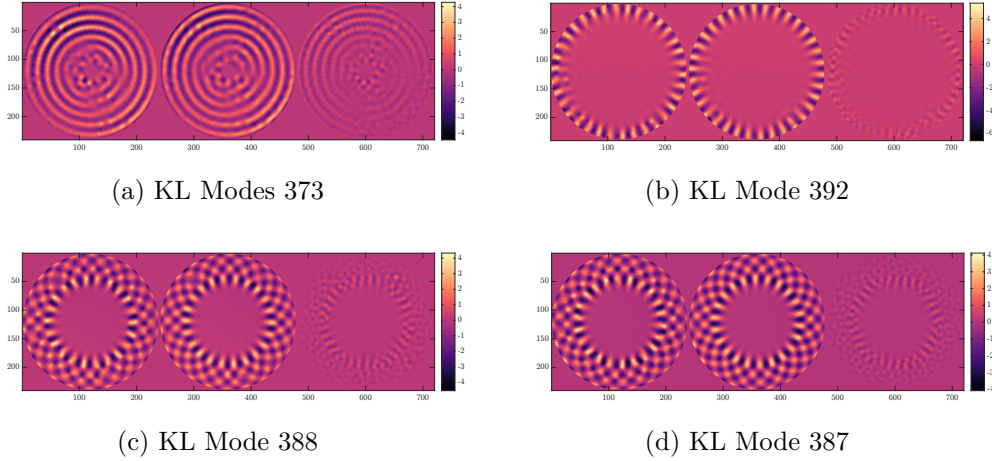


Figure 2.17. – Illustration of the 4 worst modes reproduced by the model. Each sub-figure provides the experimental mode (left), synthetic (center) and residual (right).

2.4.3. Model mis-registration parameters identification

For the mis-registration identification, we used a different approach than the method presented for the LBT experiment. The purpose of this section is to compare the accuracy of the two models, we prefer then to introduce the new identification algorithm separately. Its principle is presented in section 2.5. Using this new algorithm and the experimental interaction matrix available, we identified the mis-registrations listed in 2.1. The starting point for α is different from the experiment at the LBT which explains the different values identified for both models.

As presented in the experimental validation (section 2.3), Figure 2.18 displays the comparison of simulated closed loop performance. The modal PSD shows that both interaction matrices provide the same correction and that the remaining differences are extremely small.

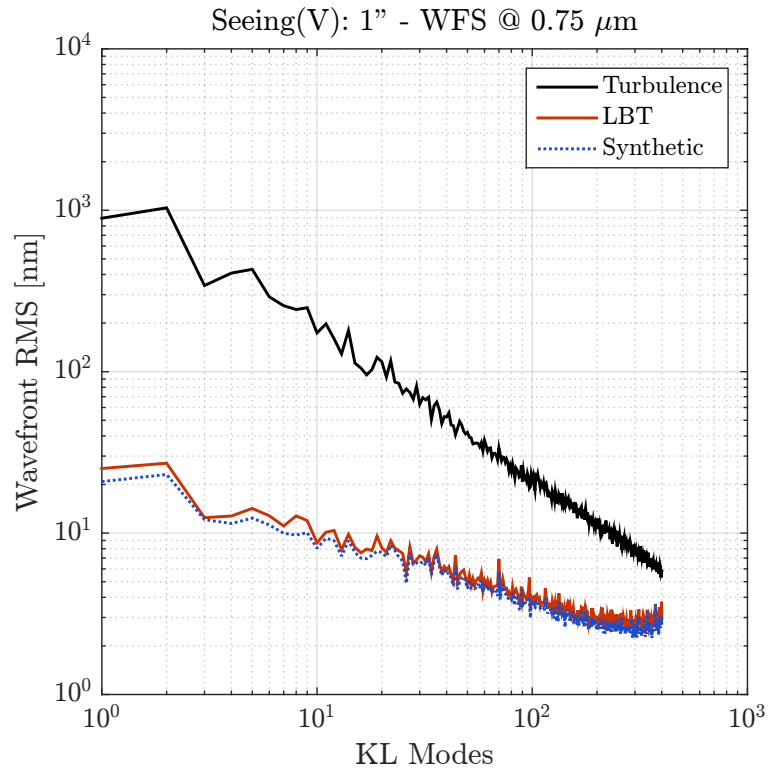


Figure 2.18. – Comparison of simulated closed loop modal PSD using both interaction matrices, synthetic and experimental. The model was developed using fully synthetic influence functions.

In addition, Figure 2.19 provides a comparison of the interaction matrix slopes maps, showing the high accuracy achieved using both models.

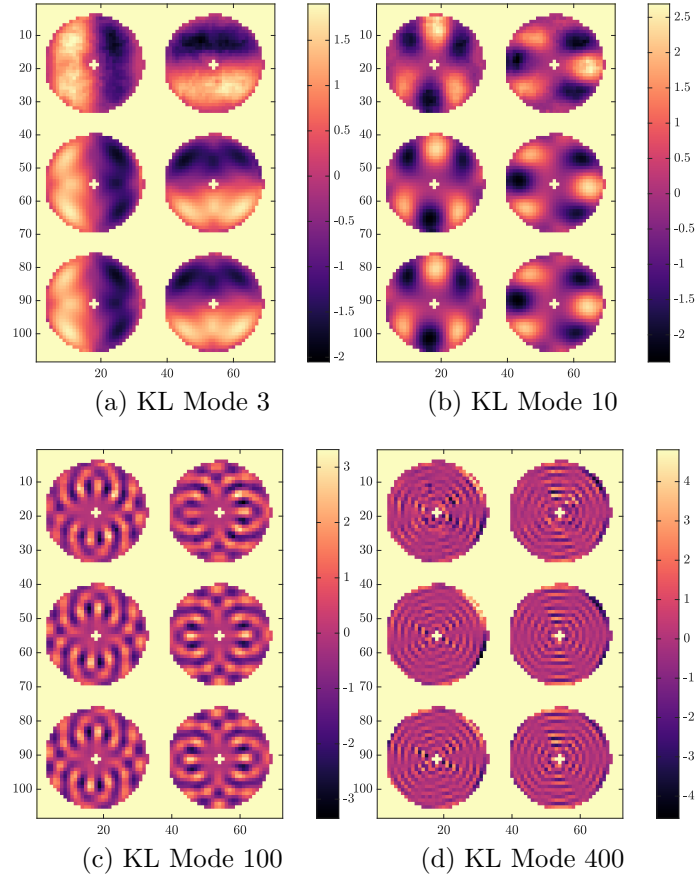
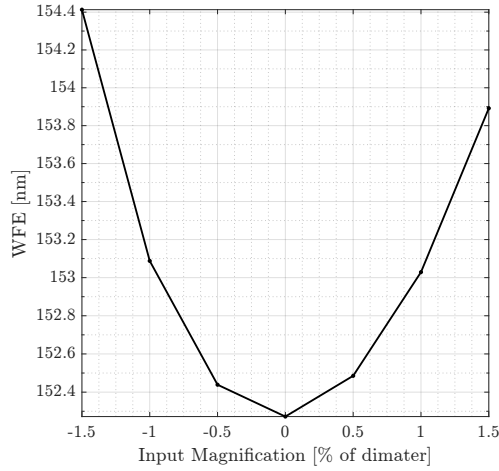
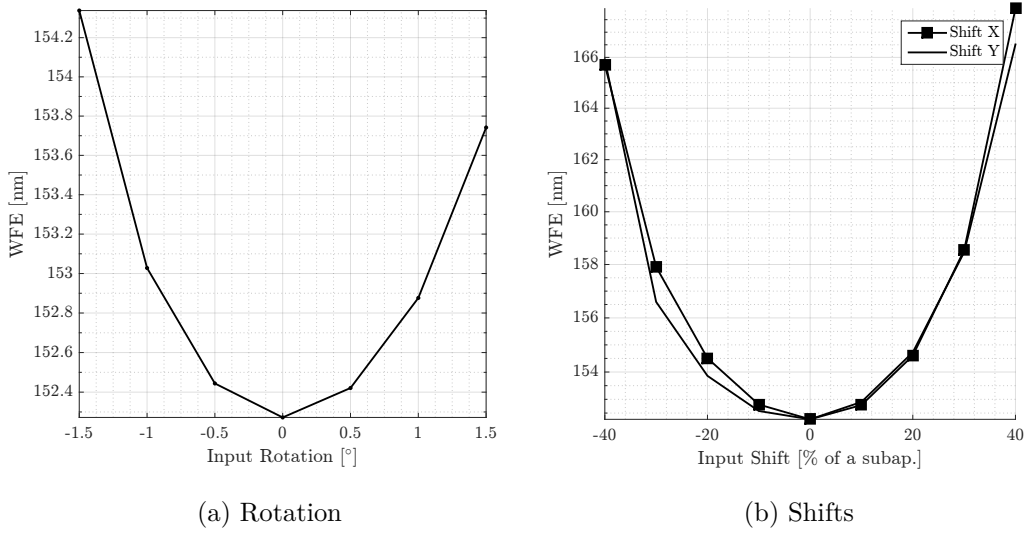


Figure 2.19. – Comparison of 2D slopes maps $[S_x S_y]$ for the KL modes 3,10,100 and 400. From Top to bottom: Experimental, Fully Synthetic Model, Synthetic Model with Experimental Influence Functions.

We can present the same analysis as presented in the MNRAS paper, investigating mis-registration values around the optimal set of mis-registration parameters identified by the identification algorithm. The idea is to consider the experimental interaction matrix to compute the reconstructor used to close the loop in the simulator and study the corresponding AO performance (see 2.15). That way, if the model mis-registration parameters are indeed optimal, the best closed loop performance should be obtained using them in the model. This is what we can witness on the closed loop performance presented in Figure 2.20.



(c) Radial Magnification

Figure 2.20. – Closed loop performance using the experimental reconstructor in the simulator and playing around the convergence value of the mis-registration parameters.

These numerical results show that the accuracy of the model remains extremely good while using purely synthetic influence functions. Since we could not access the telescope to validate the model experimentally, we decided not to investigate it further. We are confident however that the real AO system would perform as well when using this new synthetic interaction matrix as when using the experimental one since we applied the same validation procedure as the first model presented in the MNRAS article (section 2.3) and that provided excellent results at the telescope.

In addition to this analysis of pseudo-synthetic models with PWFS, we developed another model for the AO systems of the ESO High Order Test-bench (HOT) (Aller-Carpentier et al. 2008), also equipped with a PWFS and a high order correction DM. In that case, by contrast with the two models previously introduced, the DM

influence functions and modal basis were fully synthetic. We could adapt the LBT model to reproduce this new system in the simulator and close the loop of the test-bench controlling 100 KL modes. Further tuning of the model would be required to control more modes. The presentation of this work is given in Appendix A.

2.5. Optimizing the Mis-Registration Identification Algorithm

2.5.1. Principle

In this section we present an alternative algorithm to extract the mis-registration parameters from a given interaction matrix. This algorithm is drawing on the work presented in Kolb et al. 2012a. The general idea is to project an estimation of the interaction matrix on a set of sensitivity matrices that describe the sensitivity of the system to a given type of mis-registration around a given working point (in a small perturbation regime). This is based on the hypothesis that a given interaction matrix \mathbf{D}_α can be decomposed as a linear combination of sensitivity matrices around the working point α_0 :

$$\mathbf{D}_\alpha = \gamma \left(\mathbf{D}_{\alpha_0} + \sum_i \alpha_i \cdot \delta \mathbf{D}_{\alpha_0}(\varepsilon_i) \right) \quad (2.19)$$

where γ is the scaling factor accounting for any global optical gain between real and theoretical WFS measurements and DM final shapes, and the sensitivity matrices $\delta \mathbf{D}_{\alpha_0}(\varepsilon_i)$ are defined as the gradient of the interaction matrix corresponding to a mis-registration of type i and amplitude ε_i :

$$\delta \mathbf{D}_{\alpha_0}(\varepsilon_i) = \left(\frac{\mathbf{D}_{\alpha_0 + \varepsilon_i} - \mathbf{D}_{\alpha_0 - \varepsilon_i}}{2\varepsilon_i} \right)_{i=rot,X,Y,mX,mY} \quad (2.20)$$

with ε_i , the amplitude of a mis-registration of type i , chosen to be small enough to remain in the domain of validity of the hypothesis of linearity (some typical values are given in equation 2.31). The notation ε_i corresponds to the small mis-registration applied to compute the interaction matrix and is different from the parameter α_i that corresponds to the mis-registration to identify.

For each type of mis-registration, the corresponding sensitivity matrices are concatenated in a meta sensitivity matrix $\mathbf{\Lambda}_{\alpha_0}$ ²:

$$\mathbf{\Lambda}_{\alpha_0} = \left[\delta \mathbf{D}_{\alpha_0}(\varepsilon_{rot}) \quad \delta \mathbf{D}_{\alpha_0}(\varepsilon_X) \quad \dots \quad \delta \mathbf{D}_{\alpha_0}(\varepsilon_{mY}) \right] \quad (2.21)$$

Such that equation 2.19 can be written:

$$\mathbf{D}_\alpha = \gamma (\mathbf{D}_{\alpha_0} + \boldsymbol{\alpha} \cdot \mathbf{\Lambda}_{\alpha_0}) \quad (2.22)$$

2. In practice the matrices $\delta \mathbf{D}_{\alpha_0}(\varepsilon_i)$ are reshaped as vectors $\delta \mathbf{d}_{\alpha_0}(\varepsilon_i)$, of length $N_S = N_{WFS}$ WFS signals $\times N_{DM}$ sets of DM commands but for the sake of clarity, we prefer the matrices notation.

where α is the vector of mis-registration parameters defined as

$$\alpha = \begin{Bmatrix} \alpha_{rot} \\ \alpha_X \\ \alpha_Y \\ \alpha_{mX} \\ \alpha_{mY} \end{Bmatrix} \quad (2.23)$$

We now want to identify α^* that minimize the criterion

$$\alpha^* = \arg \min_{\gamma, \alpha} \|\mathbf{D}_\alpha - \gamma(\mathbf{D}_{\alpha_0} + \alpha \cdot \Lambda_{\alpha_0})\|^2 \quad (2.24)$$

The solution of the Least Square criterion is given by:

$$\gamma^* = (\mathbf{D}_{\alpha_0} + \alpha^* \Lambda_{\alpha_0})^\dagger \cdot \mathbf{D}_\alpha \quad (2.25)$$

and

$$\alpha^* = (\Lambda_{\alpha_0})^\dagger \cdot \left(\frac{\mathbf{D}_\alpha}{\gamma^*} - \mathbf{D}_{\alpha_0} \right) \quad (2.26)$$

Since we want to identify both γ^* and α^* , the algorithm has to be iterative. The first step consists in estimating the scaling factor taking $\alpha^* = \mathbf{0}$ as starting point. By replacing in equation 2.25:

$$\gamma_1^* = (\mathbf{D}_{\alpha_0})^\dagger \cdot \mathbf{D}_\alpha \quad (2.27)$$

We can now inject the value of γ_1^* in equation 2.26 to get the first estimation of α^* :

$$\alpha_1^* = (\Lambda_{\alpha_0})^\dagger \cdot \left(\frac{\mathbf{D}_\alpha}{\gamma_1^*} - \mathbf{D}_{\alpha_0} \right) \quad (2.28)$$

From the estimation α_1^* , we can now update \mathbf{D}_{α_0} by computing the new interaction matrix $\mathbf{D}_{\alpha_1^*}$ corresponding to the mis-registration α_1^* and get the next estimation of γ^* :

$$\gamma_2^* = (\mathbf{D}_{\alpha_1^*})^\dagger \cdot \mathbf{D}_\alpha \quad (2.29)$$

The summary of the iterative procedure is given in Figure 2.21

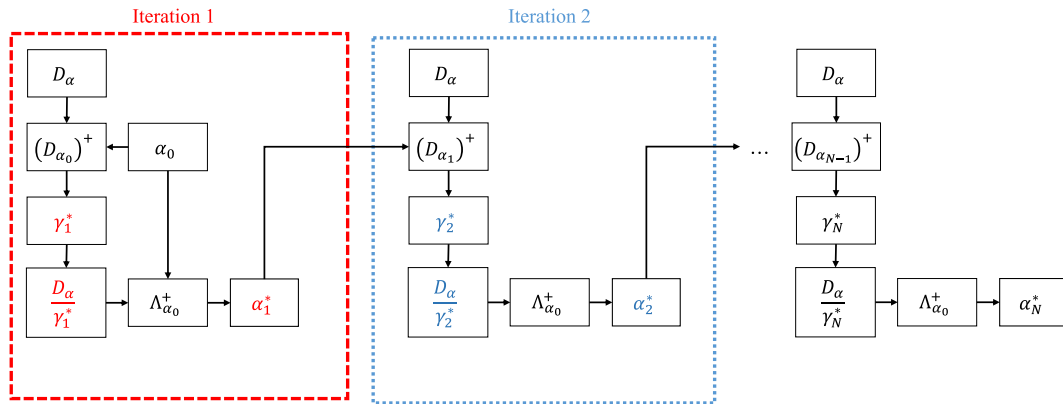


Figure 2.21. – Iterative estimation of the scaling parameter γ^* and mis-registration parameters α^* from the interaction matrix \mathbf{D}_α .

	DM	WFS	Pitch On Sky
LBT	ASM Circular Geometry	30x30 Subapertures	30 cm
Cartesian 20 × 20	Fried Geometry	20x20 Subapertures	40 cm
Cartesian 30 × 30	Fried Geometry	30x30 Subapertures	30 cm

Table 2.2. – Definition of the three AO Systems considered to characterized the linearity of the identification algorithm

The advantage of this algorithm is that it provides an estimation of all the parameters at each iteration which offers a significant gain in speed with respect to the algorithm considered for the LBT experiment (see section 2.3). In practice, we identified that using 3 iterations to estimate both scaling factor γ^* and mis-registration parameters α^* were sufficient to provide a relative error of 1% between two successive estimations. In the whole manuscript it is checked that the successive estimations of the parameters have a relative error of 1%.

It is important to notice that the validity of the meta sensitivity matrix Λ_{α_0} will be extremely dependent on the working point α_0 around which it was computed and to the value of mis-registrations to identify. The characterization of the algorithm is presented in section 2.5.2.

2.5.2. Linearity of the mis-registration parameters estimation

Since the identification algorithm is based on an hypothesis of linearity around a working point α_0 , it is important to first analyze the linearity of the mis-registrations estimation α^* and scaling factor γ^* as a function of the input mis-registration. We consider three different geometries for the AO systems, an ASM-like deformable mirror and a Cartesian DM with 20 by 20 and 30 by 30 subapertures as defined in Table 2.2.

For each system, we compute its corresponding meta sensitivity matrices around α_0 :

$$\Lambda_{\alpha_0}^{LBT}, \Lambda_{\alpha_0}^{20 \times 20}, \Lambda_{\alpha_0}^{30 \times 30} \quad (2.30)$$

using

$$\alpha_0 = \left\{ \begin{array}{l} \alpha_{0,rot} = 0^\circ \\ \alpha_{0,X} = 0 \% \text{ of a subap.} \\ \alpha_{0,Y} = 0 \% \text{ of a subap.} \\ \alpha_{0,mX} = 0 \% \text{ of diameter} \\ \alpha_{0,mY} = 0 \% \text{ of diameter} \end{array} \right\} \text{ and } \varepsilon = \left\{ \begin{array}{l} \varepsilon_{rot} = 0.1^\circ \\ \varepsilon_X = 1 \% \text{ of a subap.} \\ \varepsilon_Y = 1 \% \text{ of a subap.} \\ \varepsilon_{mX} = 0.25 \% \text{ of diameter} \\ \varepsilon_{mY} = 0.25 \% \text{ of diameter.} \end{array} \right\} \quad (2.31)$$

The computation of the mis-registered interaction matrices D_α to be input in the model is achieved by playing on a single type of mis-registration at any one time, so that we focus on a single parameter only. If not explicitly stated, we consider noise-free interaction matrices that are computed in the linear range of the WFS operating at the limit of diffraction of the telescope (no modal gains variations). In such conditions, the scaling factor γ estimation always converges to 1. For the characterization of the algorithm we consider full zonal interaction matrices but the same results were obtained considering the full KL modal basis of the system.

To study the linearity of the parameters estimation and the eventual coupling effects, we compute a set of \mathbf{D}_α , applying a ramp of amplitudes for α . We consider the following mis-registrations : rotation ($\alpha = \alpha_{rot}$), shift X ($\alpha = \alpha_X$), radial magnification ($\alpha = \alpha_{mX} = \alpha_{mY}$) and X magnification ($\alpha = \alpha_{mX}$). Figure 2.22 provides the mis-registration estimation errors as a function of the different types of mis-registrations. The presented results show that in this ideal case, the accuracy is satisfying on a large range of value around α_0 and starts to be degraded for large mis-registrations (half of a subaperture shift, 1.5° of rotation). In the frame of this study, we are interested in a fine tuning of these parameters during online operations. This means that the mis-registration parameters to identify are not too far from the working point α_0 and thus that the linearity of the algorithm is satisfying for this purpose.

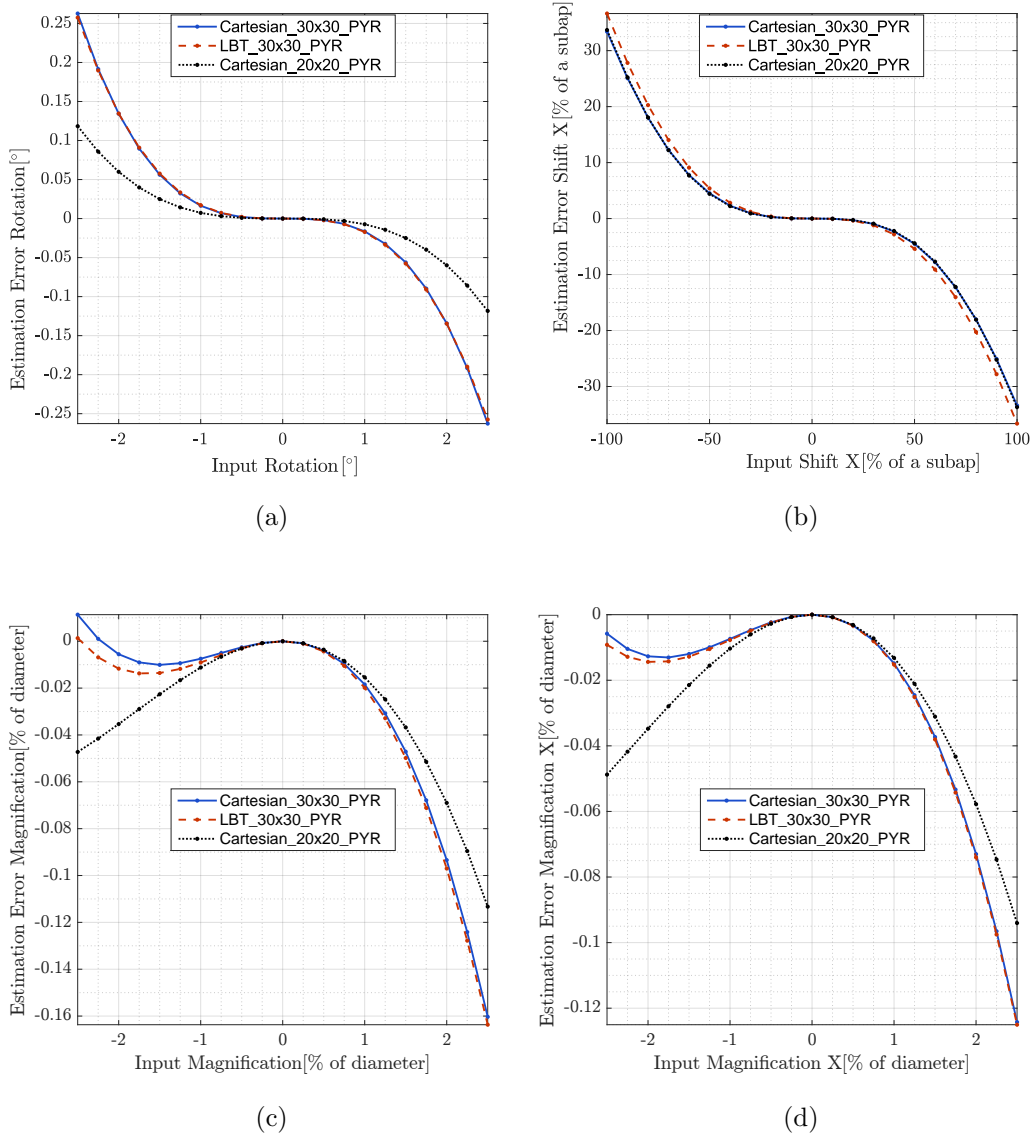


Figure 2.22. – Linearity Curves of the identification algorithm for $\alpha = \alpha_{rot}$ (a), $\alpha = \alpha_X$ (b), $\alpha = \alpha_{mX}$ (c) and $\alpha = \alpha_{mX} = \alpha_{mY}$ (d) in a 30x30 Cartesian Geometry (solid blue), ASM Geometry (dashed red) and 20x20 Cartesian Geometry (dotted black).

Concerning the different geometry considered, it appears that the linearity of the algorithm depends little on the geometry of the system if we compare the accuracy reached using the 30 by 30 Cartesian model and using the LBT model. We note however the number of subapertures changes the linearity curve for the parameters: the system with a smaller subaperture size (LBT and 30 by 30 Cartesian) appear to be less linear than the 20 by 20 Cartesian model³.

3. This is also true for the shift parameter since we quantify the shift in fraction of subaperture.

2.5.3. Coupling between the parameters

The previous section showed that the linearity of the algorithm is satisfying for all the parameters. In this section, we want to quantify the effects of cross-coupling between the parameters. The estimation of the other parameters as a function of the given mis-registration is given in Figures 2.23, 2.24 and 2.25.

These plots exhibit the high coupling between the shift and the magnification (Figure 2.24). This is not a surprising result as the transformation applied to the actuators on the edge of the pupil in the case of a magnification or a shift is almost the same. However, this time we notice that the geometry of the system does impact the estimation of the parameters: the coupling between the shift and the magnification is different for all the systems, especially for the 20 by 20 Cartesian system that shows a high coupling between the shift in X and the Y magnification. The only other coupling identified is the impact of the rotation on the magnification (Figure 2.23) but this remains negligible (under 0.05 % of the diameter in the worst case).

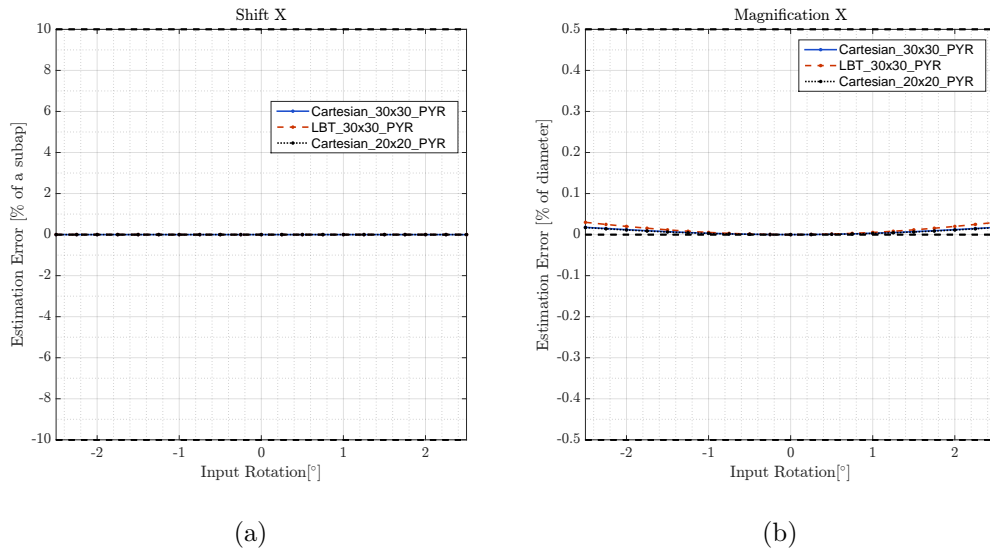


Figure 2.23. – Coupling of the parameters with the rotation. The results are the same for both shifts and for both magnifications. The horizontal black dashed lines give the maximum error that can be accepted (see Figure 2.3).

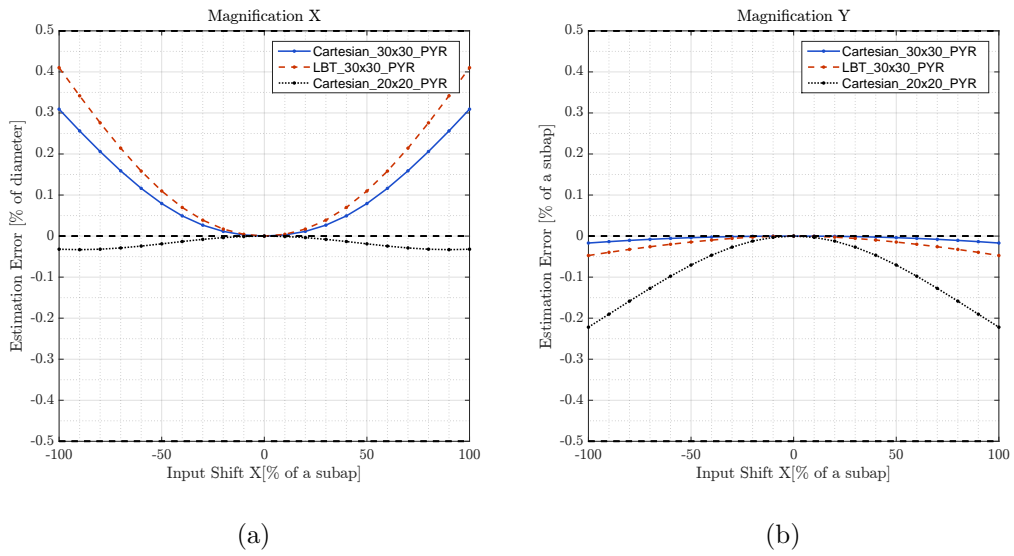
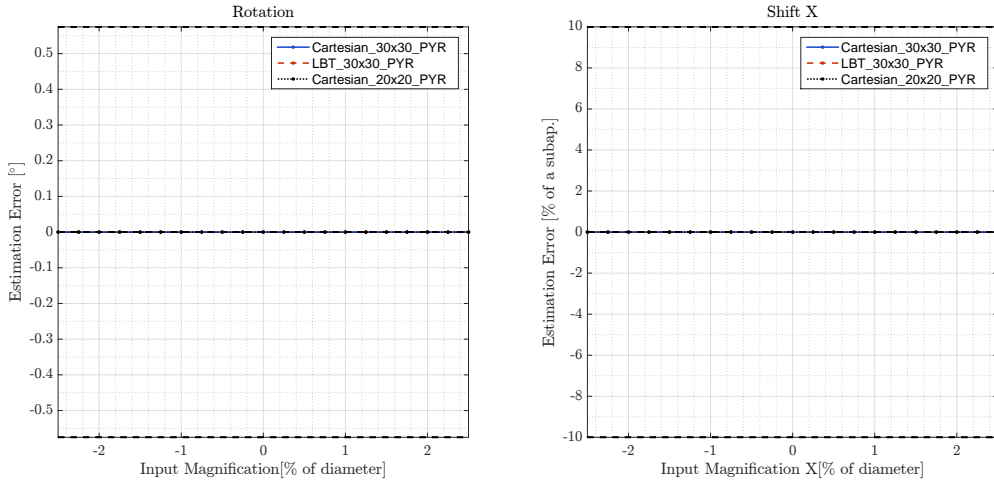
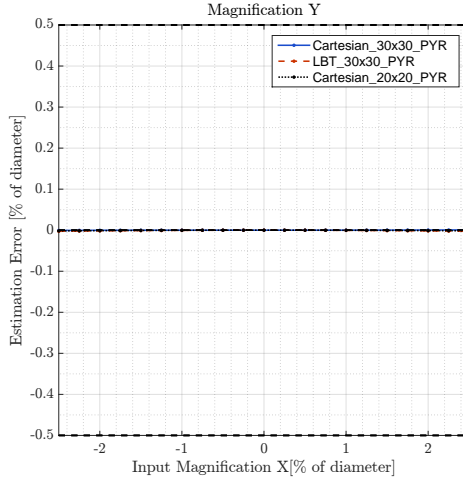


Figure 2.24. – Coupling of the parameters with the shift X. The algorithm does not exhibit any coupling with the rotation and shift Y parameters. The horizontal black dashed lines give the maximum error that can be accepted (see Figure 2.3).



(a) Coupling Shift X

(b) Coupling Shift Y



(c) Coupling Magnification X

Figure 2.25. – Coupling of the parameters with the magnification. The results are the same for both shifts. The horizontal black dashed lines give the maximum error that can be accepted (see Figure 2.3).

2.5.4. Identification of large amplitude mis-registrations

If the mis-registrations to identify are too far from the initial working point α_0 and out of the linear range, the accuracy of the algorithm can be improved by using an iterative approach, updating the working point of the model by computing Λ_{α^*} after each estimation⁴ or by physically re-aligning the system after each estimation. This will allow the algorithm to converge to the right parameters. We consider an exaggerated mis-registered case α that includes at the same time large shifts and

4. the estimation of α^* is the convergence value of the iterative procedure to identify both scaling factors γ and mis-registration parameters α^* .

rotation:

$$\alpha = \left\{ \begin{array}{l} \alpha_{rot} = 2^\circ \\ \alpha_X = 70 \% \text{ of a subap.} \\ \alpha_Y = -50 \% \text{ of a subap.} \\ \alpha_{mX} = 0 \% \text{ of diameter} \\ \alpha_{mY} = 0 \% \text{ of diameter} \end{array} \right\} \quad (2.32)$$

After each estimation of α^* , we compute the new meta-sensitivity matrix around the new working point Λ_{α^*} to proceed to the next iteration of the algorithm. Figure 2.26 shows the estimation of α^* as a function of the number of iterations of the algorithm.

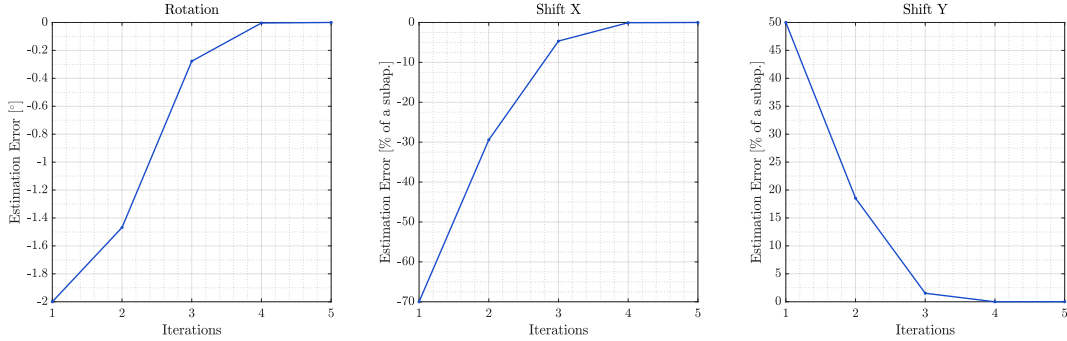


Figure 2.26. – Iterative estimation of large values of mis-registrations updating the meta-sensitivity matrix Λ_{α^*} after each estimation of the parameter α^*

In this exaggerated case, we show that when using only 4 iterations the algorithm is able to converge to the true value of the mis-registration parameters with only negligible errors. Updating the working point and thus the meta sensitivity matrices Λ_{α^*} at each iteration provides a significant optimization of the algorithm by extending its domain of validity. This strategy has however a cost in computation time as for each iteration, the computation of $1 + 2 \times N_\alpha$ interaction matrices is required, with N_α the number of mis-registration parameters considered. In the example of Figure 2.26 $N_\alpha=3$. To address this technical issue, the algorithm could be used on reduced interaction matrices corresponding to a few modes only. This point is investigated in detail in chapter 3. We could comment that in the frame of this thesis, we are interested in the fine tuning of the parameters and such mis-registrations should not occur if a regular tracking of the parameters is achieved. In the following part of the thesis the algorithm will not use updates of the meta-sensitivity matrices.

However, such updates might be justified in the first phases of the model validation, in bootstrap or commissioning phase of the instruments for instance, when the knowledge of the registration of the system is approximate. We could comment that if the method chosen to compensate the mis-registrations consists in re-aligning physically the system, such update of the meta-sensitivity matrix Λ_{α_0} will not be necessary since the system will be back to its initial operating point.

2.5.5. Sensitivity to a modal scaling

We propose to investigate the impact of a modal scaling on the parameter estimation to simulate the impact of the optical gains of the Pyramid WFS (Esposito et al. 2015, Vérinaud 2004, Korkiakoski et al. 2008, Deo et al. 2018a, Chambouleyron et al.

in prep). To do so, we multiply the noise-free mis-registered interaction matrices \mathbf{D}_α with a diagonal matrix \mathbf{G}_{r_0} which coefficients contain the modal gains corresponding to an on-sky measurement obtained for an atmosphere characterized with the Fried Parameter r_0 :

$$\mathbf{D}_{\alpha r_0} = \mathbf{D}_\alpha \cdot \mathbf{G}_{r_0} \quad (2.33)$$

The diagonal of \mathbf{G}_{r_0} is given in Figure 2.27 and has been estimated using the method introduced in Deo et al. 2018a, averaging a few measurements on-sky.

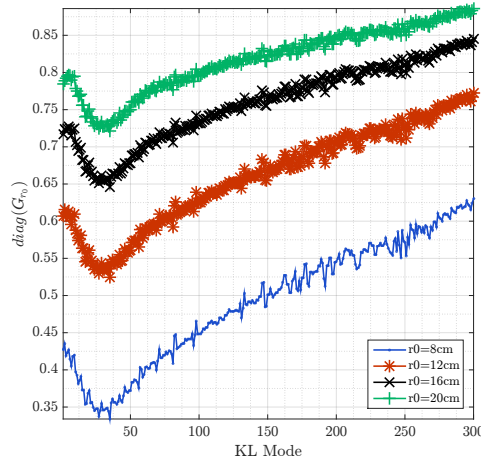


Figure 2.27. – Diagonal coefficients of the matrix \mathbf{G}_{r_0} for different value of r_0 in the visible.

The estimation of the parameters for different r_0 is given in figure 2.28.

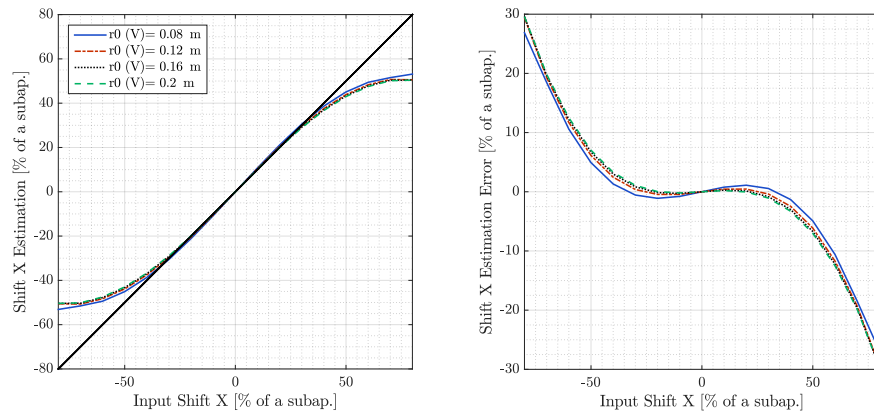


Figure 2.28. – Comparison of the estimation of the shift X for interaction matrices impacted by optical gains variations.

The global scaling correction allows us to take into consideration the optical gains and provides a satisfying accuracy for the parameters estimation. We witness how-

ever that for a strong attenuation of the signals, the algorithm tends to slightly overestimate the parameters but this remains negligible.

This chapter has introduced the concept of synthetic based calibration, putting light on the key ingredients required to efficiently model an AO system with a Pyramid WFS and make it adaptable to experimental features.

We developed a first model of the LBT AO system, using experimental influence functions to produce the ASM model and introduced a first procedure to identify the model parameters. The validity of these parameters has been thoroughly challenged numerically, injecting the experimental interaction matrix in simulated closed loop and studying the corresponding simulated AO performance.

In a second step, we could validate the model experimentally at the LBT and demonstrate the high accuracy achieved with our model as we could get the same level of AO correction using both synthetic and experimental reconstructors, simulating a turbulence on the ASM. The high precision of the tuning of the model even allowed us to control up to 500 modes, demonstrating that a high order AO correction can be achieved with our model.

We then developed a second model of the same AO system using synthetic influence functions to model the DM and projecting the experimental modal basis of the ASM on the synthetic influence functions. According to our metric, we could reach an equivalent accuracy of the model with respect to the model developed with experimental influence functions. As this strategy provides a much more flexible model to tune the mis-registration parameters, it seems to be the best alternative to model the DM. The model parameters estimation was achieved using an optimized algorithm that is shown to be much faster and more efficient than for the first model.

3. Online Identification of Mis-Registration Parameters: The Invasive Approach

The previous chapter was focused on the development of a synthetic model of the LBT AO system to generate a pseudo-synthetic reconstructor. We could demonstrate the feasibility of the pseudo-synthetic approach using a Pyramid WFS. In our model, we had access to a full interaction matrix measured on site with an external fiber that was used to tune the mis-registrations parameters of the model. For the experimental validation, the identification algorithm used was iterative, playing on a single parameter at a time. This strategy can become time consuming, especially if it requires to explore 5 degrees of freedom or more so we introduced a second algorithm that consists in projecting the target interaction matrix (here the full experimental matrix) onto sensitivity matrices to estimate the mis-registration parameters.

However, if such a high SNR measurement is not available, it is necessary to investigate different strategies to estimate the mis-registration parameters required by the model to compute the interaction matrix of the system, and, if possible to allow a tracking and upstate of the parameters during the operations. The scope of this chapter is to address this particular point. We limit the study to a fine tuning of the model online. We assume that the system will not drift too far from its initial working point so that the initial interaction matrix can still be used to close the loop of the system, at least partially. This approach is then complementary with the work developed for the LBT experiment as the initial interaction matrix required to close the loop could be obtained using the method introduced in chapter 2.

The global structure of the identification strategy is summarized in figure 3.1.

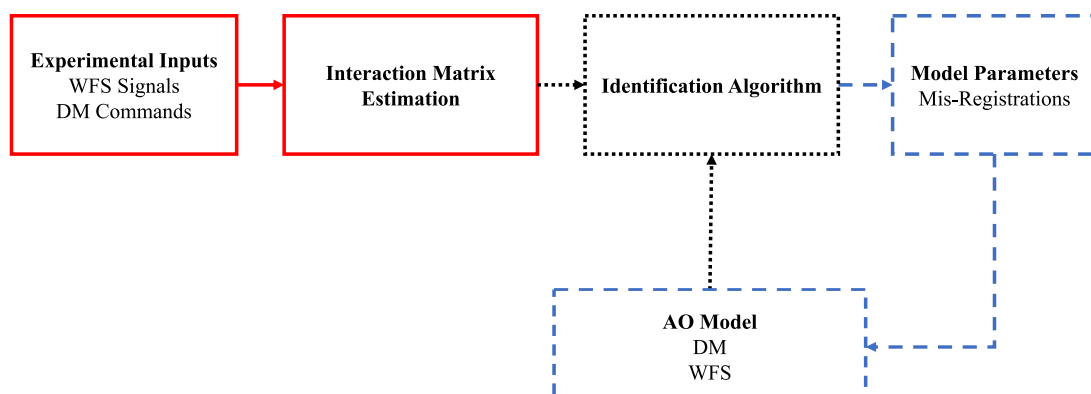


Figure 3.1. – Identification of the model mis-registration parameters from reference signals. The estimated interaction matrix can be reduced to only given number of modes N .

The path corresponding to the AO modelling (dashed blue) and the identification algorithm (dotted black) have been presented in the previous chapter. This chapter is thus organized to analyze the type of experimental inputs (solid red) required by the algorithm.

We identified two different strategies to get the reference signals required by the algorithm, the first one is presented in this chapter and the second one is presented in chapter 4. The first approach is **invasive** and consists in dithering signals on the DM (during the operation or bootstrapping phase) to retrieve their signature in the WFS measurements. In particular, we investigate if a full interaction matrix is required to identify the model parameters or if we can reduce the interaction matrix to only a few well selected modes that provide a good estimation of the mis-registration parameters. In this section, we investigate the on-sky acquisition of signals that will be injected in the identification algorithm to identify the mis-registration parameters. The particularity of this approach is that it can be applied either offline or during the operation with the constraint of minimizing the impact on the science path as the signals act as a noise on the scientific measurements. In chapter 1, we introduced the state of the art in terms of on-sky calibration. The strategy to acquire the reference signals required by the algorithm will use the same methods: dithering specific signals over the closed-loop DM commands using either fast push-pull measurements or continuous periodic modulation. More details about on-sky calibration can be found in Oberti et al. 2004, Oberti et al. 2006, Pieralli et al. 2008 or Pinna et al. 2012.

If the acquisition has to be achieved during the operation, a scheme based on a temporal modulation of the signals and a demodulation seems better suited since it allows to reduce the amplitude of the dithering signals to reach the same SNR obtained using a push pull approach, hence reducing the impact on the science. For both methods, the SNR of the on-sky acquisition depends on the observing conditions (turbulence, level of noise) and on the AO system properties (dimension, bandwidth). The parameters for the acquisition of the signals such as duration of an acquisition, amplitude of the signals have then to be tailored accordingly. Since both methods allow to retrieve signals with equivalent SNR, we propose to consider only the push-pull measurements to narrow down the analysis and reduce the computation time. An analysis on the impact of dithering signals on the science is available in Deo et al. 2019.

In a first step, we investigate the accuracy of the mis-registration parameters estimation exploring different levels of SNR, considering full interaction matrices (see 3.4.1). These results will be used as a baseline to estimate the accuracy achieved with respect to a given SNR. In a second step we will investigate the core of this research: minimizing the number of signals required while efficiently estimate the mis-registration parameters. To do so, we propose to study the sensitivity to a mis-registration to identify the most sensitive modes to the mis-registrations (see 3.3.2). We will investigate the accuracy of the mis-registration estimation reducing the number of signals to these most sensitive modes, exploring various levels of SNR (see 3.4.1). We will also investigate the case of dynamical mis-registrations that evolve simultaneously in time (see 3.4.4).

3.1. Definition of the model

The simulations presented in this chapter have been obtained for an AO system which properties are listed in Table 3.1.

Turbulence	$r_0(V)$	15 cm	PWFS	Subapertures	20×20
	L_0	30 cm		Modulation	3 λ/D
Control	Cn^2 profile	1-2 layers	RON	none	
	Windspeed	5-30 m/s	Photon Noise	On	
	Frequency	1 kHz	Photons/subap.	10-1000	
	Delay	2 Frames	Signal Processing	Global ¹	
	Integrator	$g=0.5$	DM	Actuator	357
Bandwidth	75 Hz	Inf. Functions		Gaussian	
NGS	Int. Matrix	300 KL	Coupling	35%	
	OG control	Yes ²	Diameter	8 m	
	Wavelength	850 nm	Obstruction	None	
	Magnitude	7.5-13.5	Resolution	160 px	

Table 3.1. – Numerical Simulations parameters for the chapter 3

Regarding the compensation of the optical gains, the method implemented in the simulations consists in using a convolutionnal model of the PWFS developed in Fauvarque et al. 2019 to analytically estimate the optical gains as a function of a given residual phase seen by the PWFS (see Chambouleyron et al. in prep). This method assumes that we have access to the residual phase and the measurements of the optical gains are in agreement with other methods based on on-sky measurements such as the one introduced in Deo et al. 2018a. In terms of specifications related to the accuracy of the mis-registration parameters estimation, we consider as a baseline that we can accept an error of 10% of a subaperture for the shifts and the equivalent shift on the border of the pupil for the rotation (0.56° in our case).

3.2. On-sky acquisition of reference signals

As explained in the introduction of this section, we will consider only push-pull measurements of a single mode at a time. The measurement y_k of the WFS at the loop sample k is given by:

$$y_k = M_{\text{WFS}} \cdot \phi_k^{\text{res}} + \eta_k \quad (3.1)$$

Where M_{WFS} defines the WFS measurement model (see equation 1.24). The push-pull measurement of a mode, represented by a phase vector \mathbf{b} requires:

$$y_k^{+\mathbf{b}} = M_{\text{WFS}} \cdot \phi_k^{\text{res}} + \eta_k + a \cdot M_{\text{WFS}} \cdot \mathbf{b} \quad (3.2)$$

and

$$y_k^{-\mathbf{b}} = M_{\text{WFS}} \cdot \phi_{k+1}^{\text{res}} + \eta_{k+1} - a M_{\text{WFS}} \cdot \mathbf{b} \quad (3.3)$$

1. see section 1.3.2

2. Chambouleyron et al. in prep

where a is the amplitude of the mode considered. The push-pull measurement y_k^b of the mode b is then given by computing:

$$y_k^b = \frac{y_k^{+b} - y_k^{-b}}{2a} = M_{WFS} \cdot b + \frac{M_{WFS} \cdot (\phi_k^{res} - \phi_{k+1}^{res}) + \eta_k - \eta_{k+1}}{2a} \quad (3.4)$$

We can define the noise on the measurement as :

$$z_k = \frac{-M_{WFS} \cdot \delta\phi_k^{res} + \eta_k - \eta_{k+1}}{2a} \quad (3.5)$$

where we define the incremental residual turbulence $\delta\phi_k^{res}$ as:

$$\delta\phi_k^{res} = \phi_{k+1}^{res} - \phi_k^{res} \quad (3.6)$$

The push-pull measurement y_k^b is then given by:

$$y_k^b = M_{WFS} \cdot b + z_k \quad (3.7)$$

In practice, to improve the SNR of the measurement we average N push-pull measurements to estimate \bar{y}^b :

$$\bar{y}^b = \frac{1}{N} \sum_k y_k^b = M_{WFS} \cdot b + \frac{1}{N} \sum_k z_k \quad (3.8)$$

From the composition of z_k , we understand that the SNR of \bar{y}^b will depend on the **level of noise** η_k , the **amplitude** of the signal a , the difference between two successive **residual phases** $\delta\phi_k^{res}$ and the **number of measurement** N averaged. Through our analysis, it will be relevant to investigate the measurement and thus the estimation of the mis-registrations playing on each of these parameters: different levels of noise η , different amplitudes a and different incremental turbulence $\delta\phi^{res}$.

3.3. Maximizing the sensitivity to a mis-registration

3.3.1. Defining the sensitivity to a mis-registration

Identifying the most sensitive modes to a given mis-registration requires to have a metric that quantify this modal sensitivity. A natural criteria is to consider the RMSE between a mis-registered WFS signal y_α and a centered WFS signal y_{α_0} . The signals are normalized by the amplitude of the mode in nm RMS. We then define ξ_{RMS} as:

$$\xi_{RMS} = \sqrt{\frac{\sum_{i=1}^{N_{WFS}} (y_\alpha(i) - y_{\alpha_0}(i))^2}{N_{WFS}}} \quad (3.9)$$

This criteria will then inform on the modes that produce the highest signal between a mis-registered and centered case.

3.3.2. An Optimal Modal Basis for the Mis-Registration Identification?

To identify the most sensitive modes to a given mis-registration, we propose to apply a Principal Component Analysis (PCA) (Pearson 1901) on a sensitivity matrix. We recall the definition of the sensitivity matrix $\delta\mathbf{D}_{\alpha_0}(\varepsilon_i)$:

$$\delta\mathbf{D}_{\alpha_0}(\varepsilon_i) = \left(\frac{\mathbf{D}_{\alpha_0+\varepsilon_i} - \mathbf{D}_{\alpha_0-\varepsilon_i}}{2\varepsilon_i} \right)_{i=rot,X,Y,mX,mY} \quad (3.10)$$

where α_0 is the working point of the system, or in other words the vector of mis-registration amplitudes corresponding to the alignment of the system at this operating point and ε_i a vector of mis-registration amplitudes to compute the sensitivity matrices. We first proceed to the Singular Value Decomposition (SVD) of $\delta\mathbf{D}_{\alpha_0}(\varepsilon_i)$ ³ that contains the measurement for the N_{DM} degrees of freedom of the DM (a zonal interaction matrix for instance):

$$\delta\mathbf{D}_{\alpha_0}(\varepsilon_i) = \mathbf{U} \cdot \mathbf{S} \cdot \mathbf{V}^T = \begin{bmatrix} \mathbf{u}_1 & \mathbf{u}_2 & \dots & \mathbf{u}_{N_{WFS}} \end{bmatrix} \begin{bmatrix} s_1 & & & \\ & s_2 & & \\ & & \ddots & \\ & & & s_{N_{DM}} \end{bmatrix} \begin{bmatrix} \mathbf{v}_1^T \\ \mathbf{v}_2^T \\ \vdots \\ \mathbf{v}_{N_{DM}}^T \end{bmatrix} \quad (3.11)$$

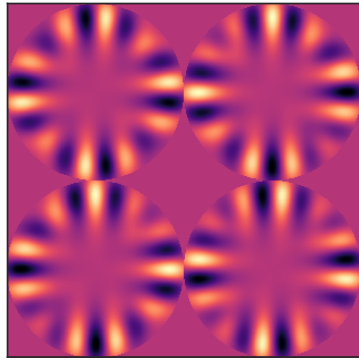
By definition, the variance contained in the signals of $\delta\mathbf{D}_{\alpha_0}(\varepsilon_i)$ and due to the input mis-registration α_i is given by

$$\lambda_i = \frac{1}{N_{DM}} s_i^2 \quad (3.12)$$

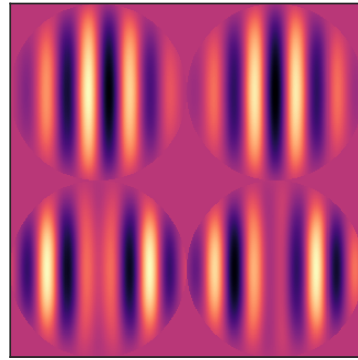
By construction, the first eigen-modes \mathbf{v} contain the most variance due to the perturbation injected (the mis-registration ε_i). They contain the N_{DM} actuators commands to produce the desired modes on the DM. The advantage of this procedure is that it allows to determine the most sensitive modes to a mis-registration, including the whole AO system properties (DM geometry, mechanical coupling, maximum stroke, WFS sampling and sensitivity). Moreover the procedure is really general so it could also be used for other types of transformations that were not considered in this study (the distortion for instance).

An illustration of these PCA Modes is given in the Figure 3.2, displaying the most sensitive modes to different mis-registrations. These modes were obtained using small values for ε_i : 0.1 ° of rotation, 1% of a subaperture shift and 100.25% of magnification. The corresponding WFS signal measurements are given in 3.3. The modes of Figure 3.2 are consistent with what we would expect: a radial non-symmetry with the signal localized on the edge of the pupil for the rotation, some Fourier-like Modes for the shifts and some modes with localized signal on the edges for the magnification. We notice that the spatial frequency of the modes is actually quite low, we could have expected higher spatial frequencies but the procedure includes all the features of the AO system that have to be taken into account. For different AO systems, we would retrieve different modes (see Appendix B).

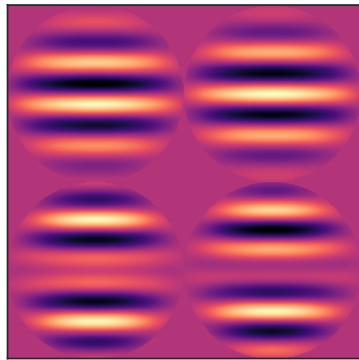
3. To apply the PCA, the mean value of each mode measurement (*ie* a row of the sensitivity matrix) has to be subtracted to provide mean centered sensitivity matrices.



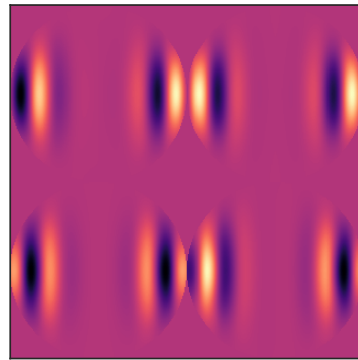
(a) Rotation



(b) Shift X

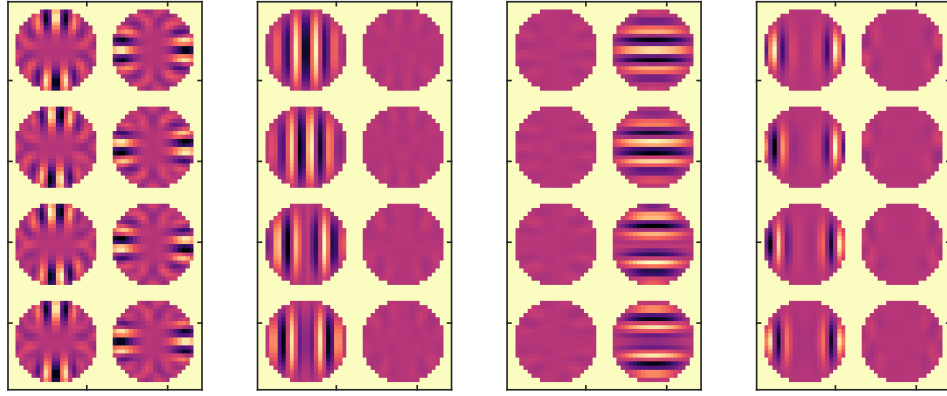


(c) Shift Y



(d) Magnification X

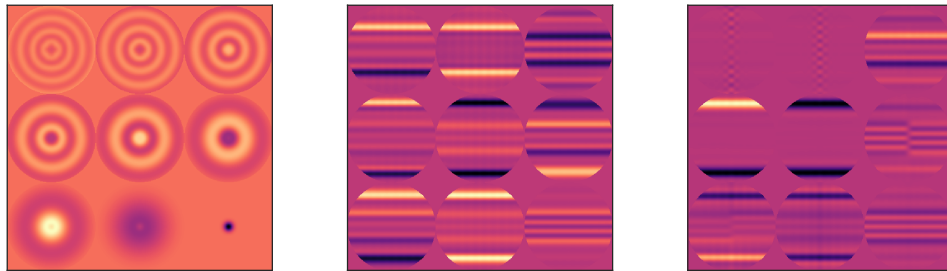
Figure 3.2. – 4 most sensitive modes to a given mis-registration derived from the PCA of $\delta\mathbf{D}_{\alpha_0}(\varepsilon_i)$.



(a) Rotation (b) Shift X (c) Shift Y (d) Magnification X

Figure 3.3. – WFS measurement $[S_x S_y]$ corresponding to the 4 most sensitive modes to a given mis-registration derived from the PCA of $\delta\mathbf{D}_{\alpha_0}(\varepsilon_i)$.

In addition, the least sensitive modes are given in Figure 3.4. Once again, the shapes displayed correspond to a result that is quite intuitive: the modes with a circular symmetry will be nonsensitive to a rotation, the ones for the shifts are orthogonal to the X direction and similarly with the X magnification, including modes where the signal is localized in the center of the pupil. This information is important as the most sensitive modes for the shift X will be poorly sensitive to the shift Y. If we want to minimize the number of modes using PCA modes, it will then be necessary to consider at least the most sensitive PCA mode per type of mis-registration.



(a) Rotation (b) Shift X (c) Magnification X

Figure 3.4. – 9 Less sensitive modes to a given mis-registration derived from the PCA of $\delta\mathbf{D}_{\alpha_0}(\varepsilon_i)$.

In addition, we provide the eigen values distribution of the sensitivity matrices in Figures 3.6 and corresponding cumulative variance in and 3.5. Figure 3.5 indicates an important information: to explain 90% of the variance due to the mis-registration, the PCA requires around 100 modes for each case. Considering that the system has 357 degrees of freedom, this means that the reduction of dimensionality is not so efficient. An explanation could be due to the locality of the signals: the signals of

the actuators are extremely localized which is not optimal for a PCA. In other words, this means that the sensitivity to the considered mis-registrations will not change too much from one mode to another.

To clarify this point, this result does not indicate that 100 modes will be required to accurately estimate the mis-registrations but it indicates that the difference of sensitivity between the first mode PCA and the second one will be small. This is well illustrated in Figure 3.7 that displays the estimation of a ramp of shift X when the interaction matrix is reduced to 3 modes, taking the i^{th} most sensitive modes for the rotation and both shifts. Using the first PCA modes provides a better estimation than using the 100th and 200th PCA modes while the 1st or 10th give almost the same results.

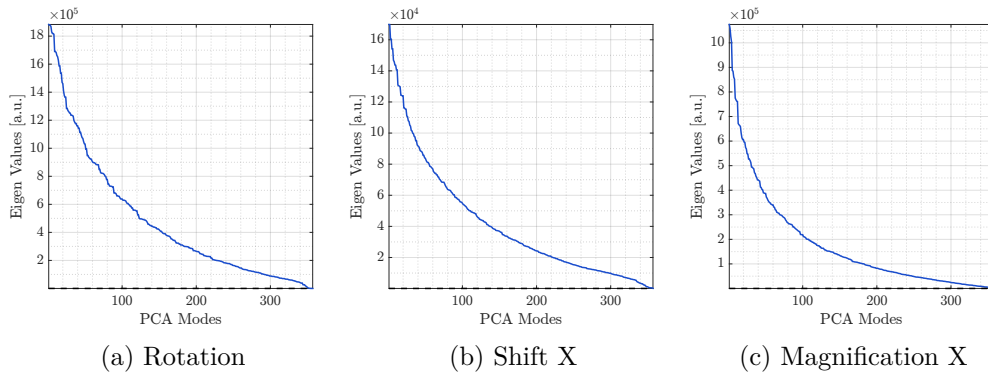


Figure 3.5. – Eigen Values distribution of the sensitivity matrices $\delta\mathbf{D}_{\alpha_0}(\varepsilon_i)$.

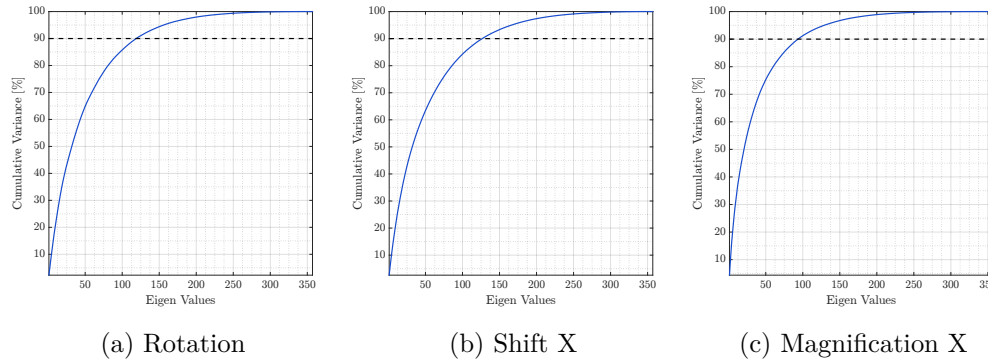


Figure 3.6. – Cumulative variance corresponding to the different mis-registrations. Around 100 modes are required to explain 90% of the variance in all cases.

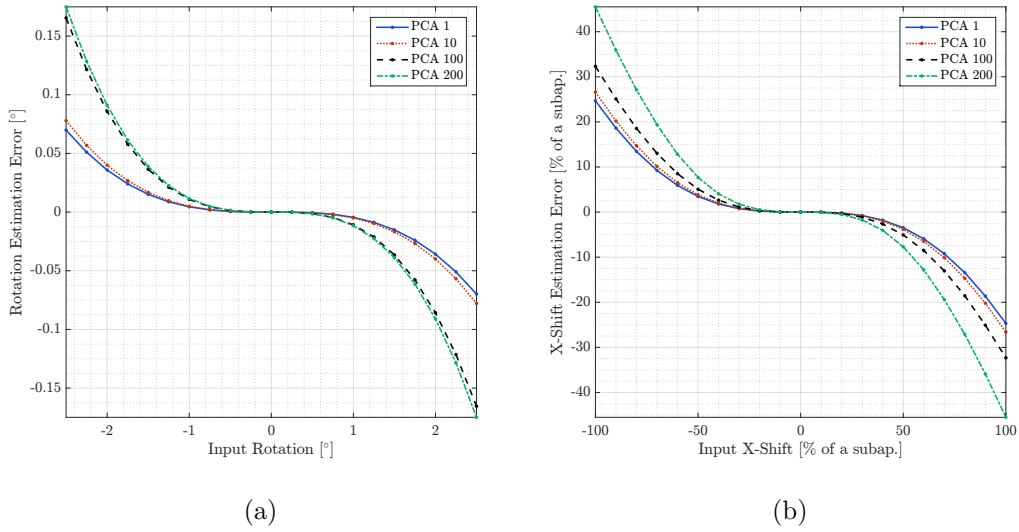
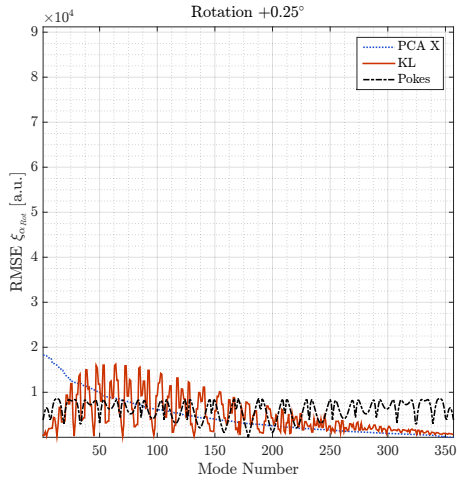


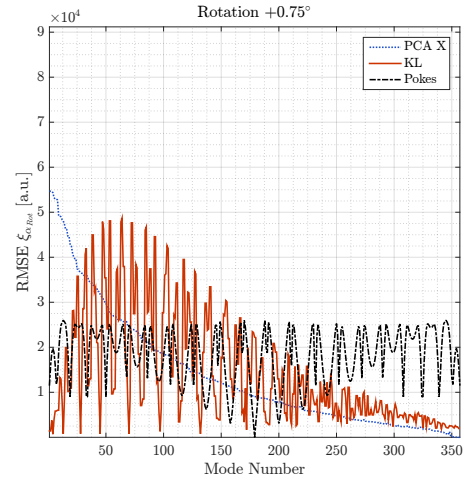
Figure 3.7. – Estimation error for a ramp of mis-registration. The results are given for interaction matrices reduced to the 1st, 10th, 100th and 200th most sensitive modes for each type of mis-registration.

If we now consider the sensitivity criteria ξ_{RMS} defined in equation 3.9 we can provide a sensitivity comparison between different modal basis: PCA modes, KL modes and DM pokes. We get the results presented in Figures 3.8, 3.9 and 3.10.

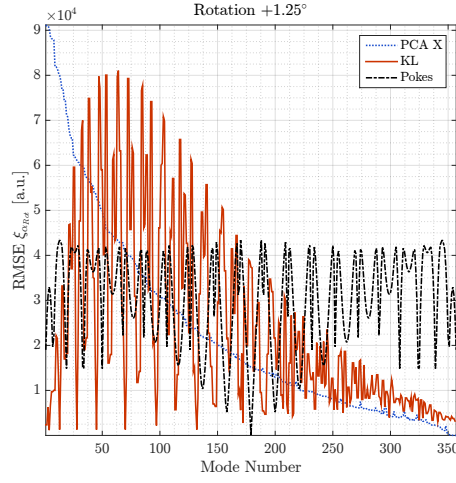
These results show that according to the criteria ξ_{RMS} , the PCA modes are indeed the most sensitive modes to the considered mis-registration. Indeed the sensitivity of the most sensitive PCA mode is always higher than the other modal basis considered. What is interesting to notice is that when the mis-registration reach values out of the linear range of the algorithm, the ordering of the modes in terms of sensitivity evolves, especially in the case of the KL modal basis but significantly less in the case of the PCA modes.



(a) Rotation 0.25°

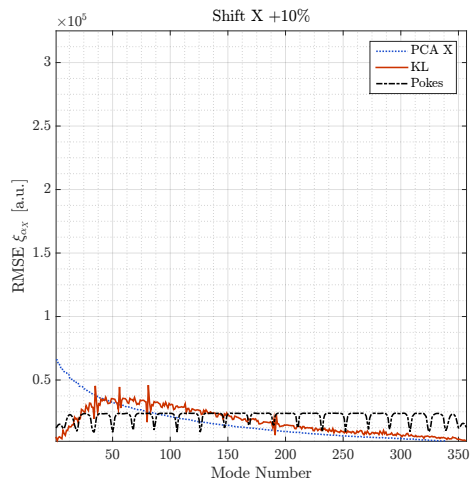


(b) Rotation 0.75°

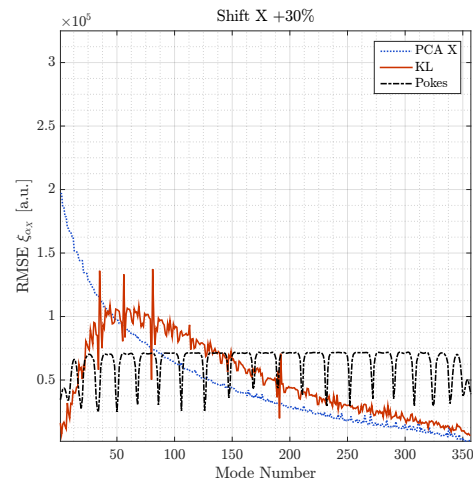


(c) Rotation 1.25°

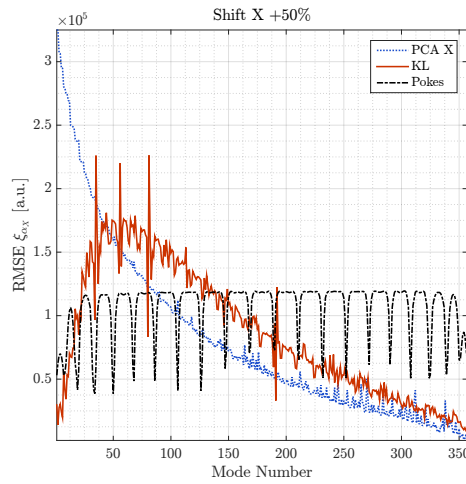
Figure 3.8. – Sensitivity criteria ξ_{RMS} corresponding to various modal basis. The results are given for a rotation of 0.25 , 0.75 and 1.25°



(a) Shift X 10 % of a subap.

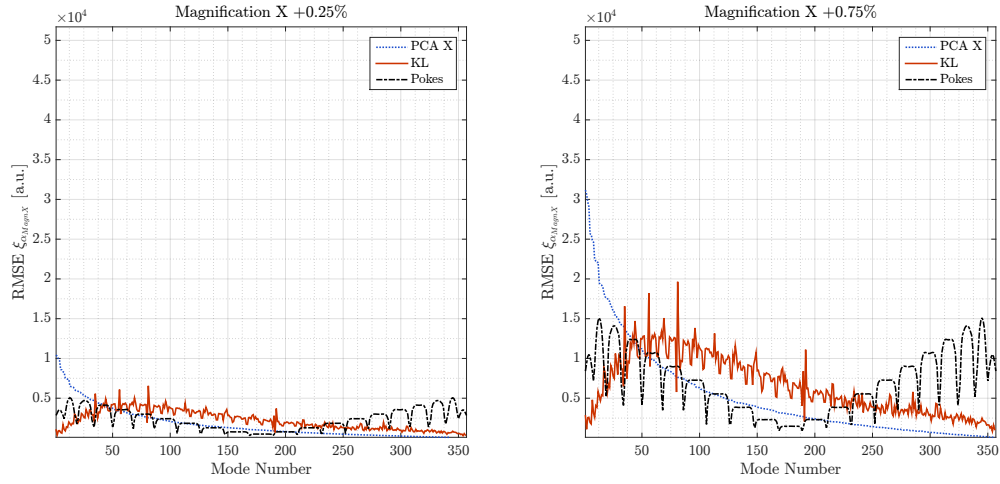


(b) Shift X 30 % of a subap.



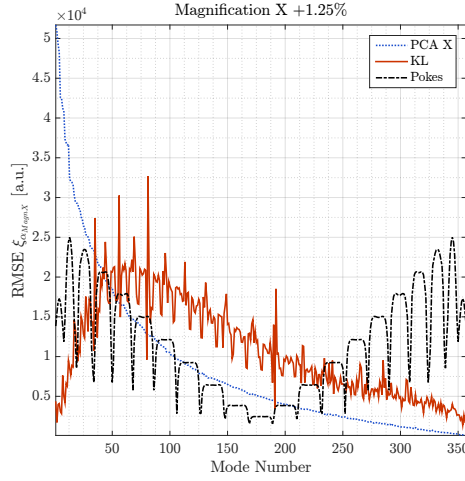
(c) Shift X 50 % of a subap.

Figure 3.9. – Sensitivity criteria ξ_{RMS} corresponding to various modal basis. The results are given for a shift X of 10, 30 and 50 % of a subaperture.



(a) Magnification X 100.25%

(b) Magnification X 100.25%



(c) Magnification X 100.75%

Figure 3.10. – Sensitivity criteria ξ_{RMS} corresponding to various modal basis. The results are given for a magnification X of 100.25, 100.75 and 101.25% of the diameter.

Although it seems quite natural that the modes that will create the more signal with respect to a given mis-registration will be the most accurate to estimate the corresponding mis-registration parameter, we propose to verify this point by considering the estimation of the parameters.

Similarly to what was presented in section 2.5.2, we apply a ramp of mis-registration and we estimate the corresponding mis-registration parameters. This time, the interaction matrices contain only a few modes to estimate the parameters: the most sensitive modes identified by the PCA. In figure 3.11, we compare the estimation of the parameters using the most sensitive PCA modes (2 and 10) and using the full interaction matrix. The estimation using only a few modes PCA provides the same accuracy than a full interaction matrix (negligible differences) but they provide

a slightly better linearity. This seems consistent with the fact that some of the signals included in the full interaction matrix are poorly sensitive to the mis-registrations. **In this noise-free configuration, reducing the modal basis to only a few modes provides a better estimation of the parameters.**

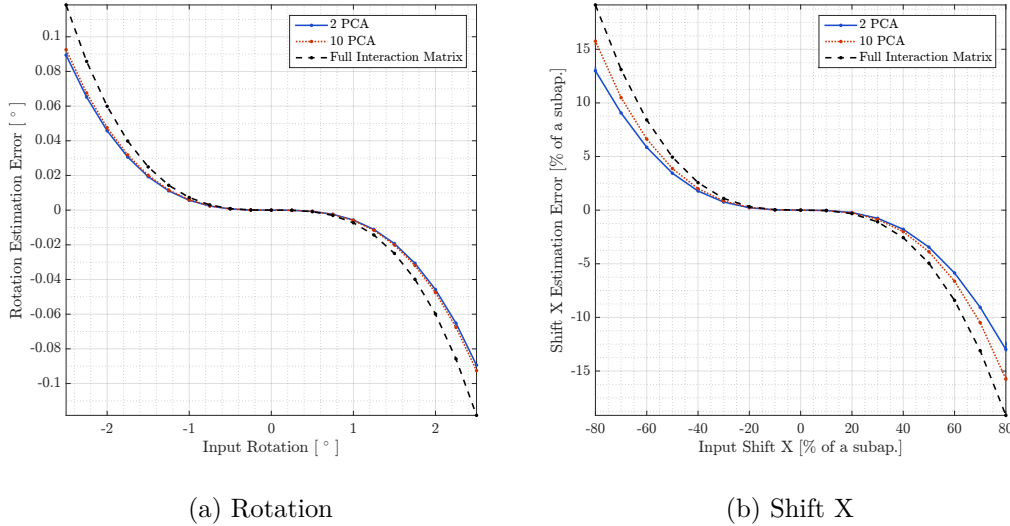


Figure 3.11. – Estimation Error for the Rotation (a) and the Shift X (b). The estimation using 2 (solid blue) and 10 modes PCA (dotted red) is given and can be compared to the estimation using the full interaction matrix (black dashed)

These results suggest that the identification of the mis-registration parameters **can be optimized by reducing the modal basis to only a few well selected modes**. To select the optimal modes in terms of sensitivity to a mis-registration, we propose a procedure based on a PCA of a sensitivity matrix. The mis-registration parameters estimation using noise free mis-registered interaction matrices has shown to be slightly better using a few PCA modes instead of a full interaction matrix. This demonstrates that the modes derived from the PCA provide an excellent accuracy for the identification of the parameters. This procedure offers a strategy to identify easily an optimal set of modes for each type of mis-registration, taking into account the specificity of the DM and WFS.

3.3.3. Impact on the scientific observations

As mentioned in the introduction of this chapter, the dithering of the modes will act as a noise on the science and it is important to quantify the impact on the science path. For instance, we can illustrate the impact in the focal plane of the most sensitive PCA modes on diffraction limited PSF, using an amplitude $a=10 \text{ nm}$ RMS. The comparison of the H-Band PSF is given in 3.12. The comparison of the PSF (a & b) exhibits negligible differences that are not visible in the Figure. The difference between the two PSF displays however how the perturbation impacts the structure of

the PSF. These figures indicate that the perturbation is negligible with a really small impact on the PSF if we consider the maximum values of the residual PSF.

Here, we consider an **optimal** case operating at the limit of diffraction. In real conditions, the PSF will be impacted by a residual phase that will already modify its shape. For a classical imaging mode, the perturbation will then have no impact on the scientific observations. This might be different for a high-contrast mode but this requires further investigations. In addition, in this case we consider the impact of a single mode at a time. A scheme with a multiplexing of the signals would have a bigger impact and remains to be investigated.

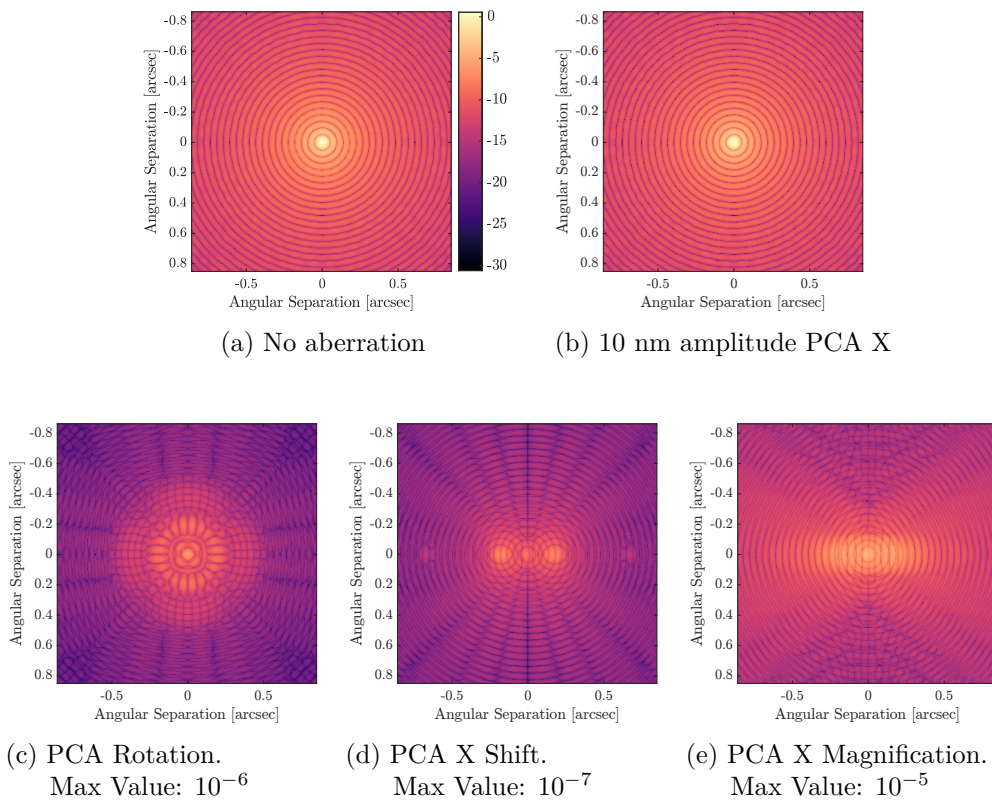


Figure 3.12. – **Top:** H Band PSF (log scale) when no mode is applied (a) and applying a 10 nm RMS mode corresponding to most sensitive PCA mode to the shift X. **Bottom:** Residual H-Band PSF (log scale) for the most sensitive PCA modes of the different types of mis-registrations.

The impact of a dithering with an amplitude of 10 nm appears then to be negligible with no effect visible on the display of the PSF. Focusing on the PCA mode corresponding to the rotation, Figure 3.13 provides the impact for larger amplitudes.

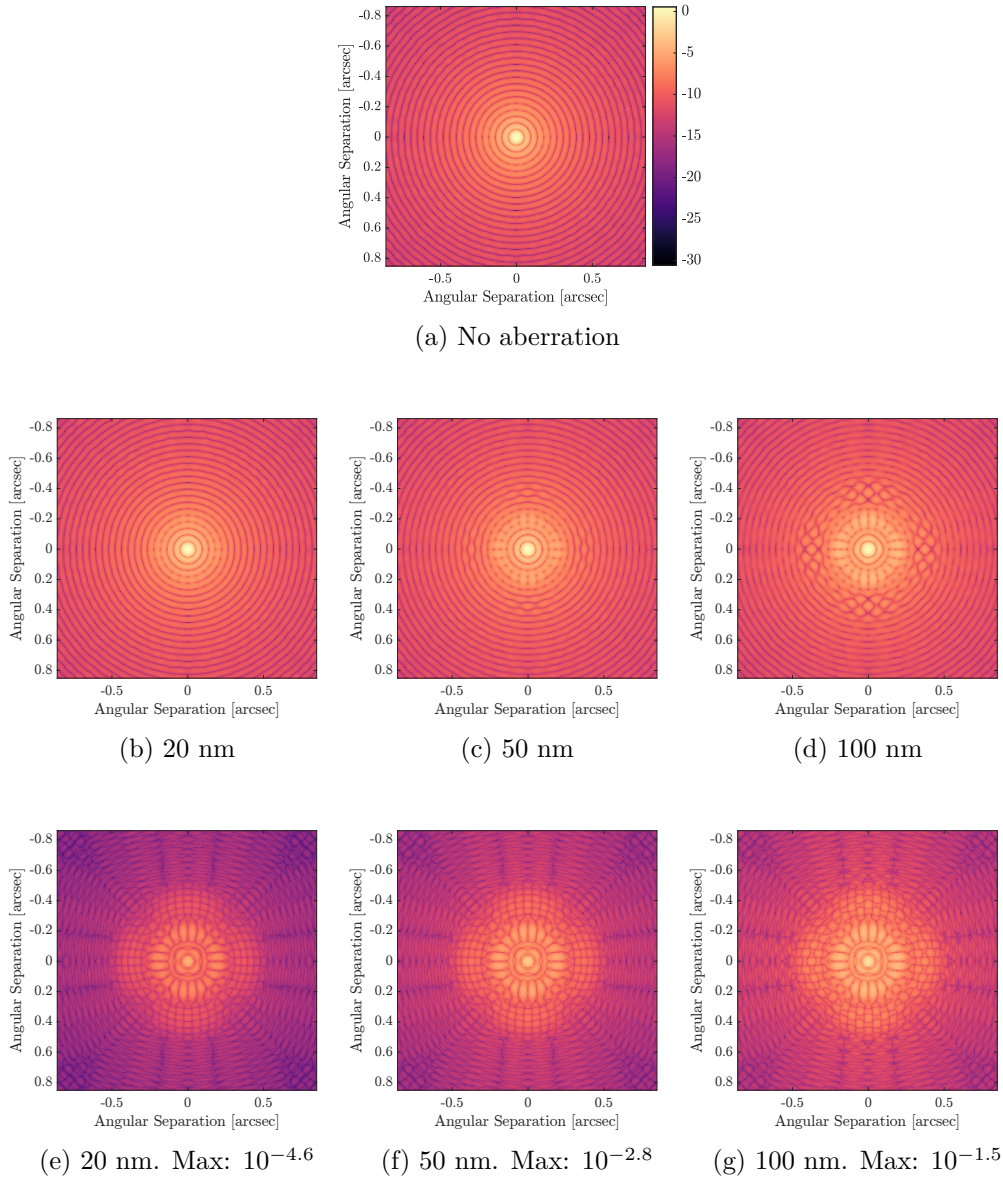


Figure 3.13. – **Top:** H Band PSF (log scale) and applying different amplitudes for the most sensitive PCA mode to the rotation. **Bottom:** Corresponding residual H-Band PSF (log scale).

This time, for larger amplitudes, the impact is more visible on the PSF. It is still acceptable for an amplitude of 20 nm RMS with a maximum value of $10^{-4.6}$ for the residual PSF. Using amplitudes of 50 and 100 nm RMS, the effects become more problematic as the structures of the mode are directly visible on the PSF itself.

As expected, the impact depends on the amplitude and spatial properties of the signals. In terms of operation, the choice of the signals properties has to be tailored to the observing conditions (level of noise?, turbulence?, level of AO correction?), on the accuracy requirements and on the type of scientific observation (impact in the focal plane? on the performance?). The measurement strategy results then of a trade-off between all these different considerations and will be system dependant.

In this section we propose to define a methodology to identify the modes that are

the most relevant to estimate the mis-registrations. We recall the expression of the measurement noise z_k :

$$z_k = \frac{-M_{\text{WFS}} \cdot \delta\phi_k^{res} + \eta_k - \eta_{k+1}}{2a} \quad (3.13)$$

The procedure should include:

- Definition of the requirements in terms of **accuracy** ω for the -mis-registration parameters with a sensitivity analysis of the system (see section 3.9).
- Identification of the **observing conditions**: level of noise η , level of turbulence ($\delta\phi^{res}$) and level of AO correction.
- Investigate the **impact on the science path** (impact of the modes on the PSF? AO performance? Acquisition time T allocated to identify the parameters?) to identify the constraints for the amplitude a and the spatial properties of the modes considered.
- Determine the **trade-off** between number of modes N_{modes} , the acquisition time allocated T , amplitude a required to reach the accuracy ω .

If the amplitudes of the modes are small (typically 20 nm RMS), and the measurement time required as well (hundreds of frames for a few PCA modes), the impact will be negligible on long-exposures PSF. By contrast if higher amplitudes are required, the dithering could be applied during the read-out time of the detectors, when the scientific shutter is closed. This would provide a way to regularly acquire high SNR signals during the operations without impacting the scientific path.

3.4. Application: Mis-Registration Identification using on-sky signals

In the previous section, we did not investigate the considerations of SNR. We propose to analyze this point using the most sensitive PCA modes. We present the estimation of the mis-registrations exploring different conditions of noise η , playing on the amplitude of the modes a . We consider a simple system with an 8-m telescope equipped with a 20 by 20 subapertures PWFS modulated at $3\lambda/D$ and operating in I Band at 850 nm. The DM is composed of 21 by 21 actuators arranged in a Fried Geometry. We consider a Frozen Flow atmosphere with a constant wind speed of 10 m/s in the X direction and a Fried parameter r_0 of 15 cm in the visible. In a first step, we propose to study the noise contribution $\eta_k - \eta_{k+1}$ in the measurement noise z_k (equation 3.5) and analyze how it impacts the SNR of the on-sky measurements and corresponding parameters estimation. To do so, we consider a static mis-registration (shift X of 20% of a subaperture) and explore different levels of noise and amplitudes to retrieve the signals on-sky.

Similarly, in a second step, (see 3.4.2) we propose to study the contribution of the incremental residual turbulence $\delta\phi_k^{res}$ in the measurement noise z_k (equation 3.5)

and analyze the impact the SNR of the on-sky measurements and corresponding accuracy on the parameters estimation. To do so, we consider a ramp of mis-registration (shift X from -30% to 30% of a subaperture) and explore different wind speed to retrieve the signals on-sky.

At last (see 3.4.4), we will consider the estimation of the parameters considering ramps of mis-registrations for the rotation, the shift X and the shift Y and investigate the accuracy of the parameters for different level of noise η and amplitude a .

For each situation, we propose to analyze the estimation of the mis-registration parameters considering different numbers of PCA modes. We narrow down the analysis to the rotations and shifts. We will then consider either 10 or 1 PCA modes per mis-registration which corresponds to a total of 30 and 3 modes to measure on-sky (see Figure 3.16). To give an idea of the SNR of the signals retrieved in the different configurations of noise and for various amplitudes, let us display the slopes maps retrieved on-sky for the first PCA mode corresponding to the shift X in Figure 3.14. In addition, we display the corresponding slopes RMS in Figure 3.15 that shows the convergence of the slopes estimation as a function of the number of push-pull measurements averaged.

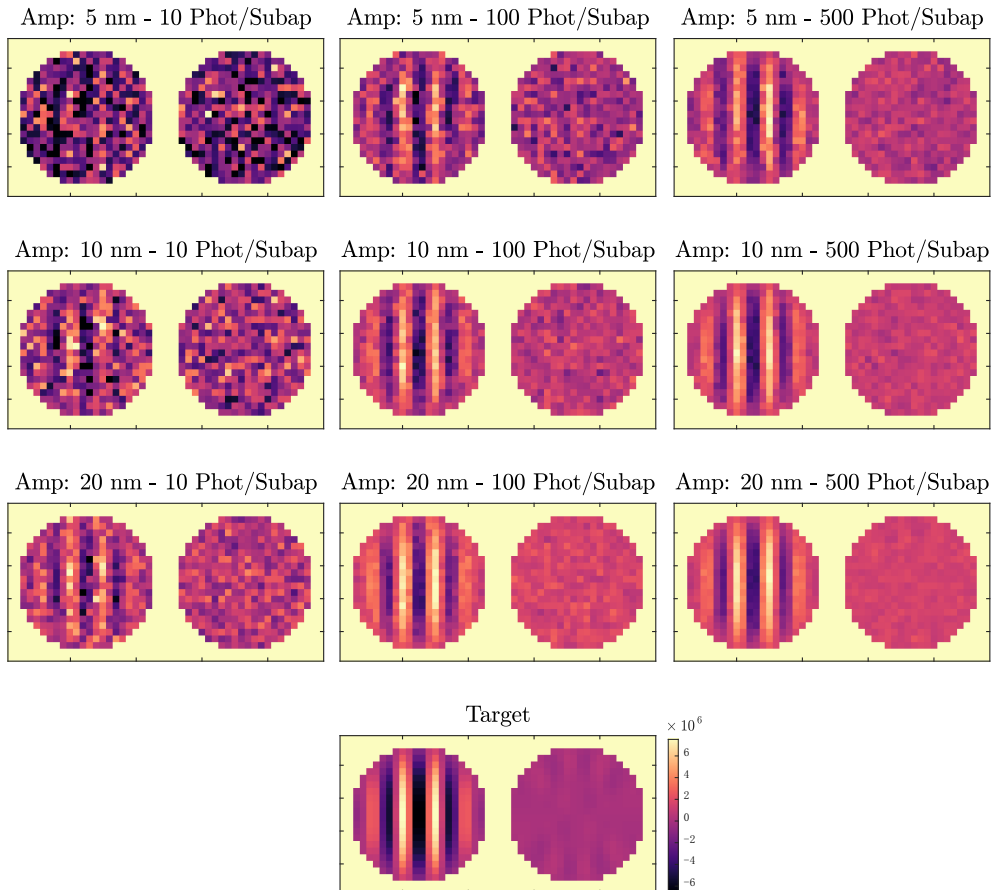


Figure 3.14. – WFS signals $[S_X S_Y]$ retrieved averaging 20 push/pull measurements for different levels of noise η and different amplitudes a . The signal corresponds to the PCA mode most sensitive to the shift X.

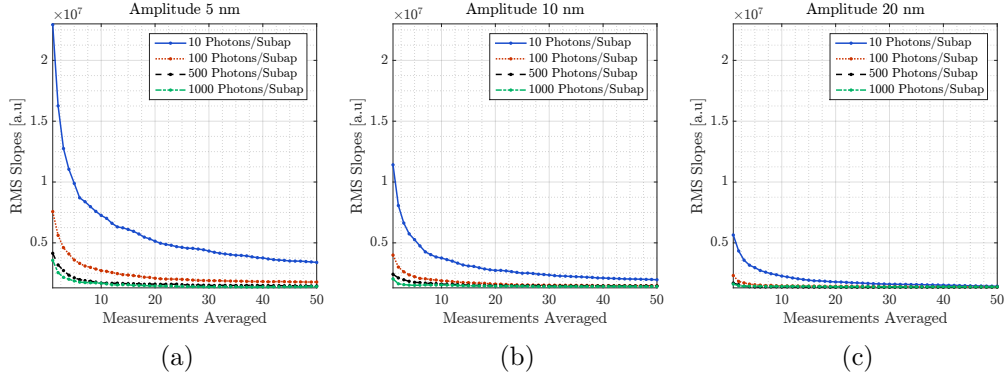


Figure 3.15. – Slopes RMS corresponding to the most sensitive PCA mode to the shift X as a function of the number of measurements averaged.

Considering these results, in the following, we will only consider measurements using an amplitude of 10 or 20 *nm* RMS to narrow down the analysis.

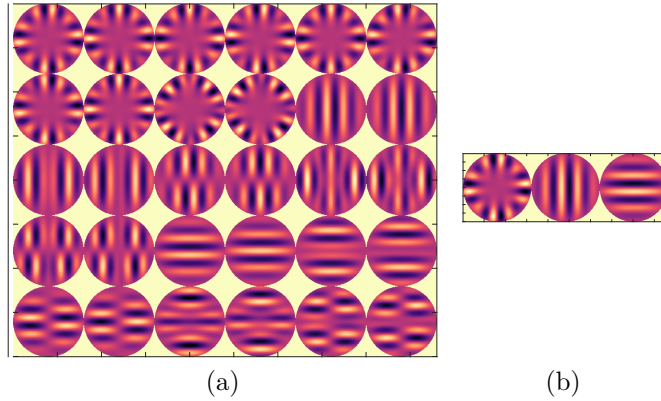


Figure 3.16. – Illustration of the different modal basis, 30 PCA Modes (a) and 3 PCA Modes (b), used to retrieve the mis-registration parameters

3.4.1. Impact of the SNR on the parameters identification

In this section we consider different number N of push-pull measurements averaged per mode and we investigate the impact on the estimation of the mis-registration parameters for different noise conditions and amplitude of the signals. We consider a static mis-registration (a shift X of 20% of a subaperture) and we analyze the convergence of the estimation as a function of the number of push-pull averaged.

We first consider a full interaction matrix (300 KL modes) where each mode is measured on-sky individually. The total number of push pull measurements required in this case is then $300 \times N$. The results are presented in Figure 3.17. Focusing on the case with 20 *nm* amplitude, it appears that averaging $N = 5$ measurements of the full interaction matrix offers an excellent estimation of the mis-registration parameters with an error of less than 1% of a subaperture in almost all the conditions. The drawback is that it is required to dither **all the modes**.

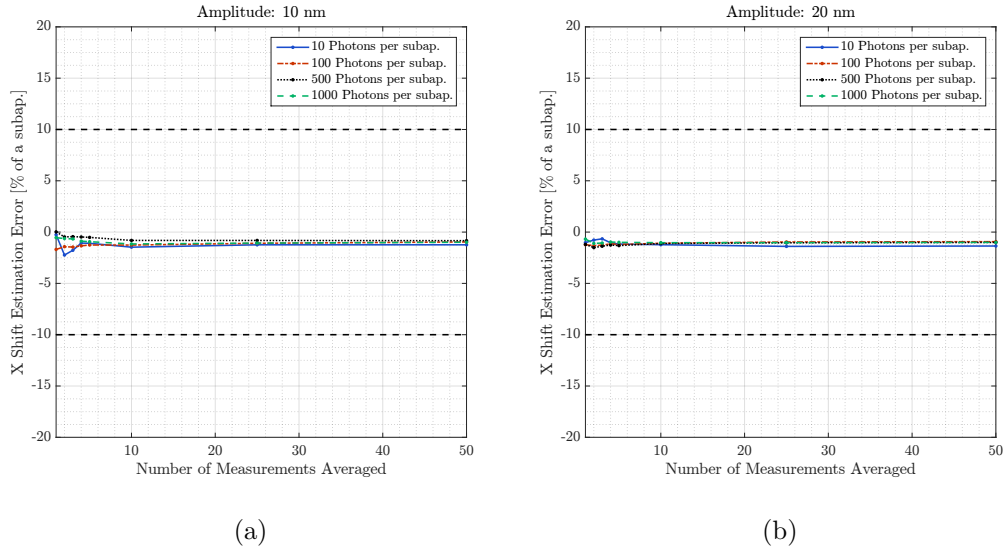


Figure 3.17. – Estimation Error corresponding to a shift X of 20% of a subaperture as a function of the number of measurement averaged. This case corresponds to a full interaction interaction matrix (300 KL Modes). The dashed black lines correspond to our specification in terms of accuracy.

If we now consider 30 PCA modes, the total number of measurements required is $30 \times N$. The estimation of the shift X is presented in Figure 3.18. This time, we notice that the estimation is more sensitive to the noise. Once again, considering the case with an amplitude of 20 nm , the convergence is reached with $N = 25$ measurements.

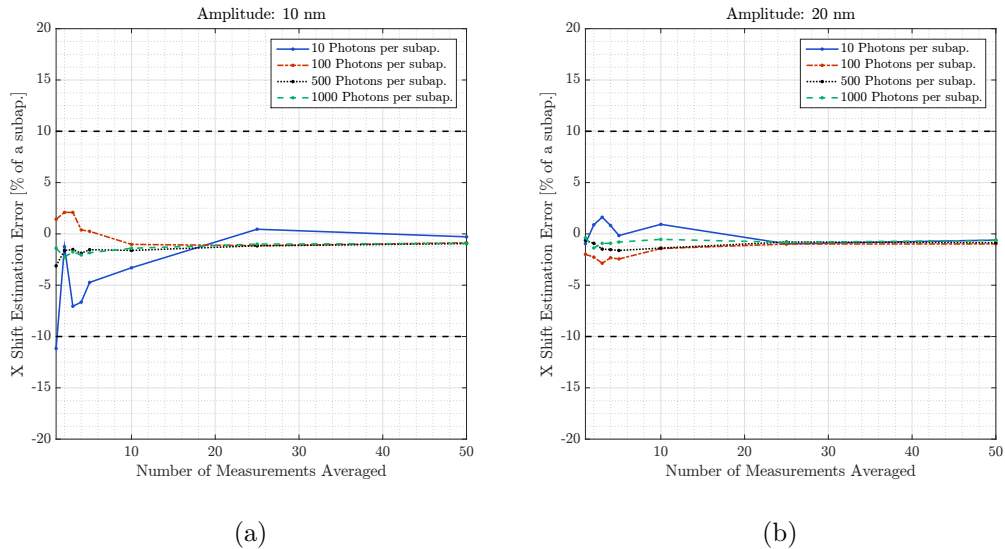


Figure 3.18. – Estimation Error corresponding to a shift X of 20% of a subaperture retrieving 30 PCA Modes on-sky. The dashed black lines correspond to our specification in terms of accuracy.

At last, if we now consider the 3 most sensitive PCA modes, which corresponds to

a total of $3 \times N$ push pull measurements, we obtain the results presented in Figure 3.19. This time, to reach convergence on the estimation of the parameter using an amplitude of 20 nm in all the cases considered, the number of measurements N required must be superior to 50.

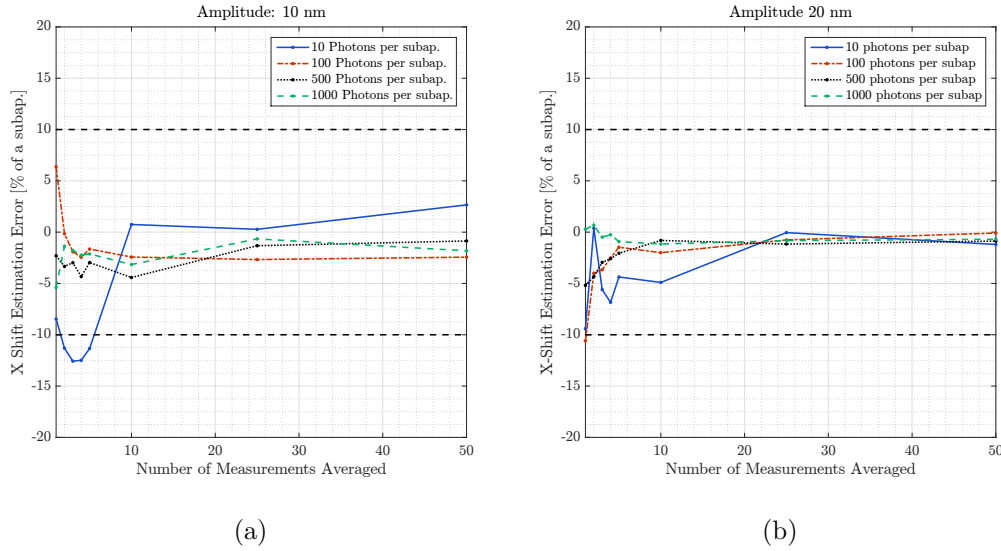


Figure 3.19. – Estimation Error corresponding to a shift X of 20% of a subaperture retrieving 3 PCA Modes on-sky. The dashed black lines correspond to our specification in terms of accuracy

As a sanity check, Figure 3.20 provides a comparison of the convergence achieved using the 1st or the 100th most sensitive PCA modes for each type of mis-registration. It appears that in high SNR regime the convergence is almost equivalent, which is consistent with the result presented in Figure 3.7 but the estimation requires a higher number of measurements to converge than using the first PCA modes, which confirm the advantage of the first PCA modes to identify the mis-registrations.

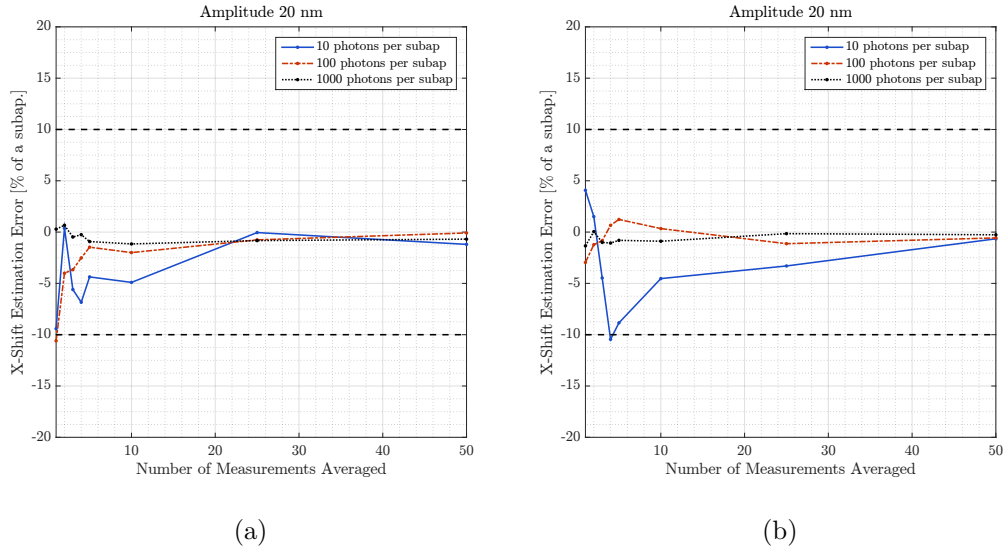


Figure 3.20. – Estimation Error corresponding to a shift X of 20% of a subaperture retrieving 3 PCA modes on sky. In the first case (a) we consider the most sensitive modes for each type of mis-registration and in the second case (b), we consider the 100th PCA modes for each mis-registration. The dashed black lines correspond to our specification in terms of accuracy

The results presented in the previous figures are summarized in Table 3.2 that gives the total number of push pull measurements required to reach convergence for the estimation of a shift X of 20% of a subaperture. To optimize the identification of the mis-registration identification, a trade-off is required, using either many modes with a small number of measurements or using few modes with a larger number of measurements. Overall, the PCA modes allows to reduce significantly the acquisition time to measure the experimental signals required by the identification algorithm and estimate accurately the mis-registration parameters.

Amplitude a	300 KL Modes	30 PCA Modes	3 PCA Modes
20 nm RMS	1500	750	150
10 nm RMS	3000	>1500	>150

Table 3.2. – Total number of averaged push pull Measurements required to reach convergence ($< 1\%$ of a subaperture) for the mis-registration estimation of a shift X in all the conditions of noise investigated (10,100,500 and 1000 photons per subaperture per frame).

3.4.2. Impact of the wind on the parameters identification

In this section we investigate if the wind speed and direction can have an effect on the estimation of the parameters. We apply a ramp of shift in X and we consider different wind speed in a Frozen Flow configuration. The results are presented in Figure 3.21 and show that there is no effect on the parameters estimation. The only

impact lies in the fact that in presence of a strong wind, the temporal error is higher, hence a higher residual phase $\delta\phi_k^{res}$ which acts as a noise on the measurement: a higher number of measurement is required to reach a given SNR.

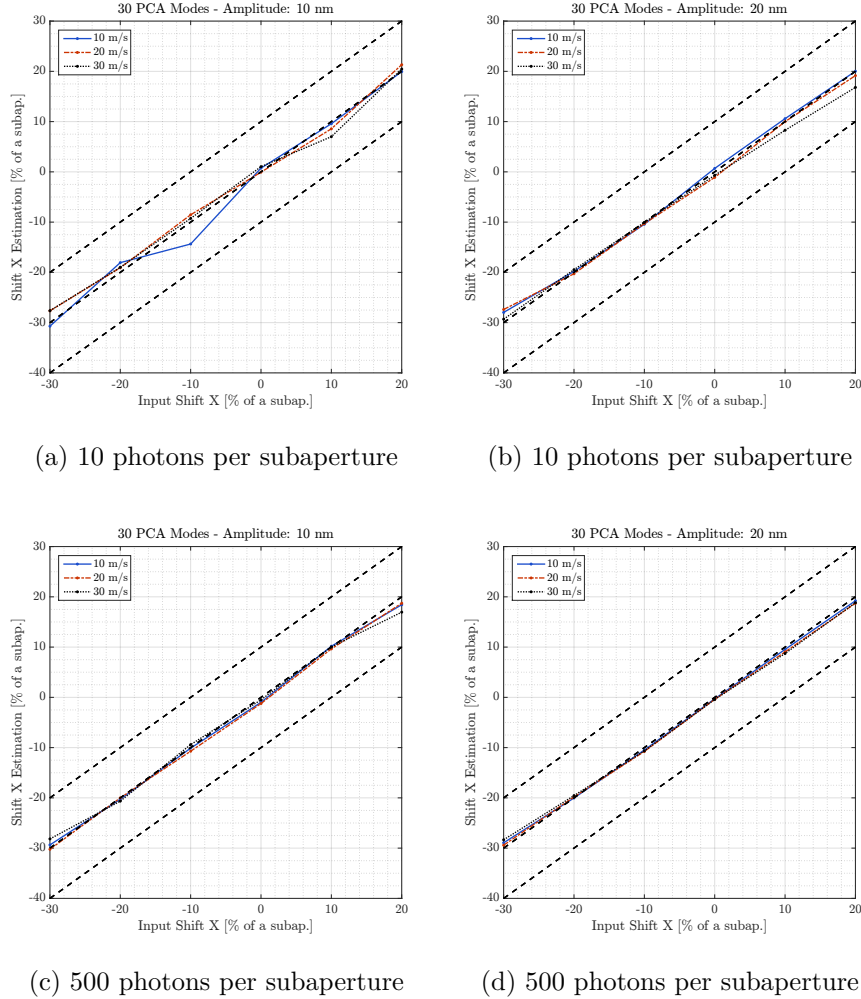


Figure 3.21. – Estimation corresponding to a shift X using 30 PCA modes. The results are given for different wind speed considering an amplitude a of 10 nm (left) and 20 nm RMS (right) and for different levels of noise (from the top to the bottom). We consider $N = 20$ measurements are averaged per mode. The dashed black lines correspond to our specification in terms of accuracy

From these results, we can conclude that the method is robust to the different wind conditions.

3.4.3. Ramps of mis-registrations

In this section we display the mis-registration parameters estimation applying ramps of mis-registrations in different observing conditions, playing on the level of noise η . For each case, we display the results for 30 and 3 PCA modes for an amplitude a of 10 and 20 nm RMS, averaging $N=20$ measurements per mode.

3.4.3.1. Ramp of rotation

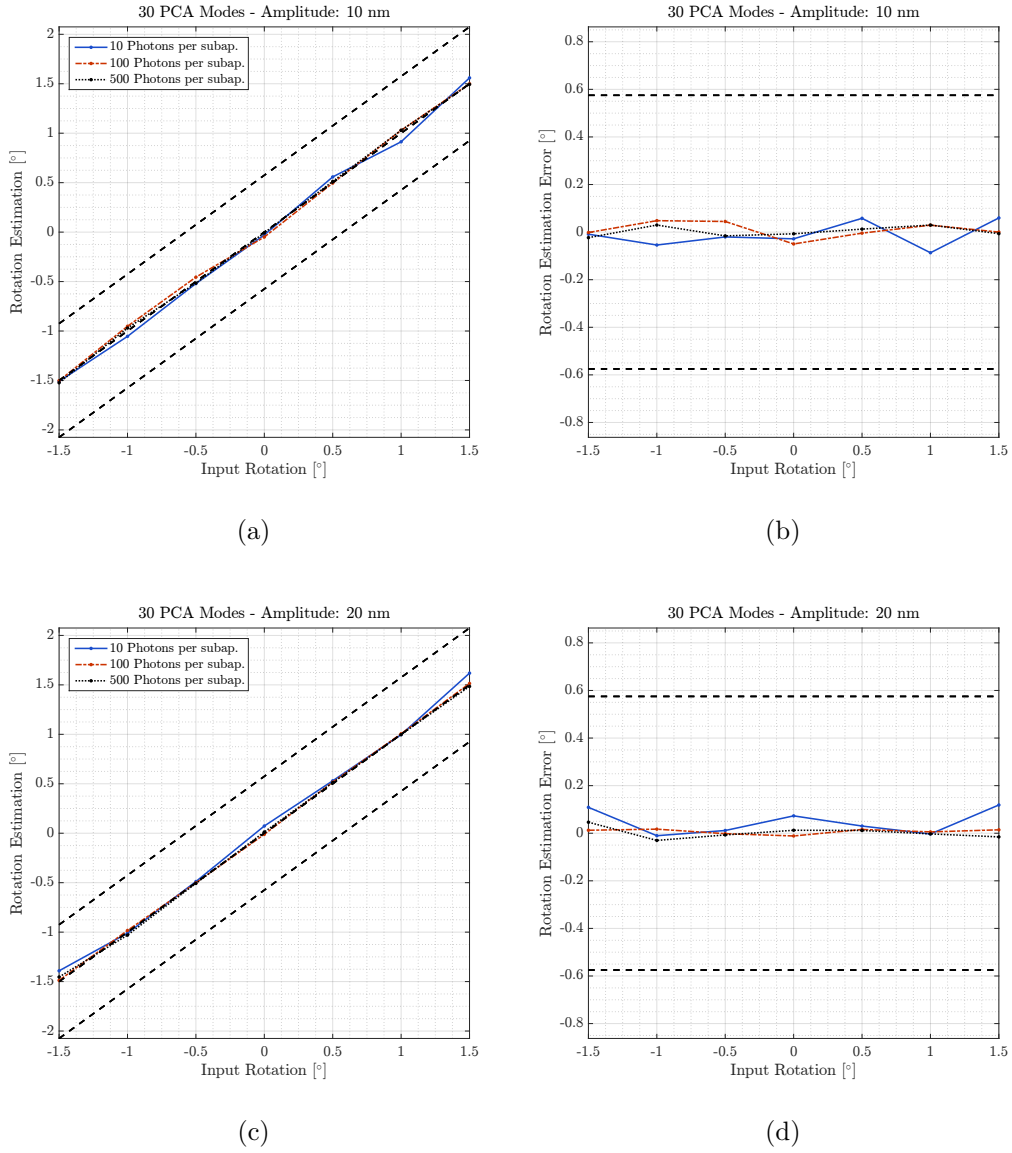
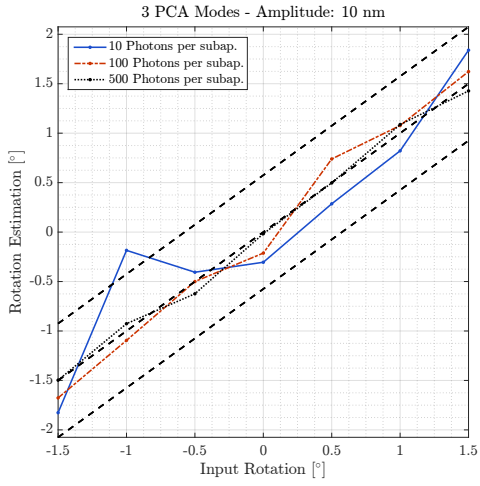
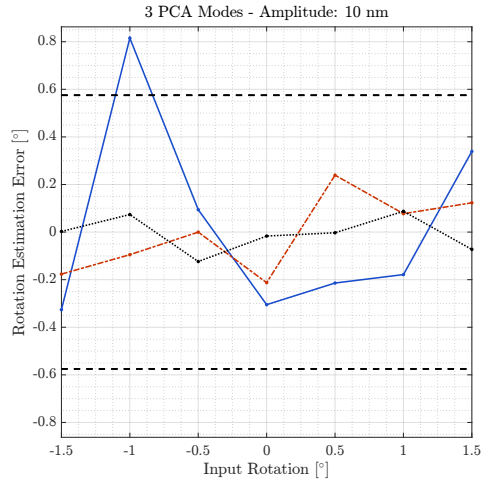


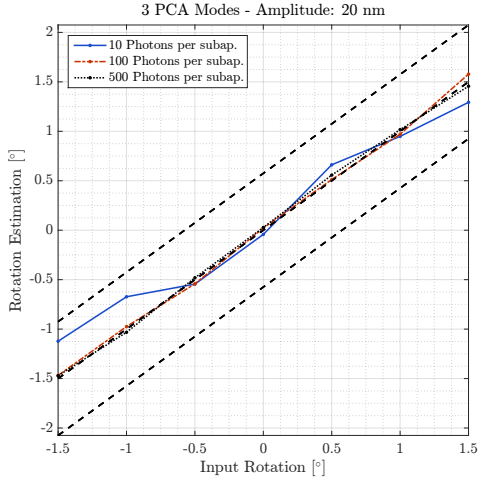
Figure 3.22. – Estimation (left) and corresponding Error (right) of a ramp of rotation using 30 PCA modes. The results are given for different level of noise η and amplitude of push-pull a . In this case, we consider $N=20$ measurements for each mode. The dashed black lines correspond to our specification in terms of accuracy



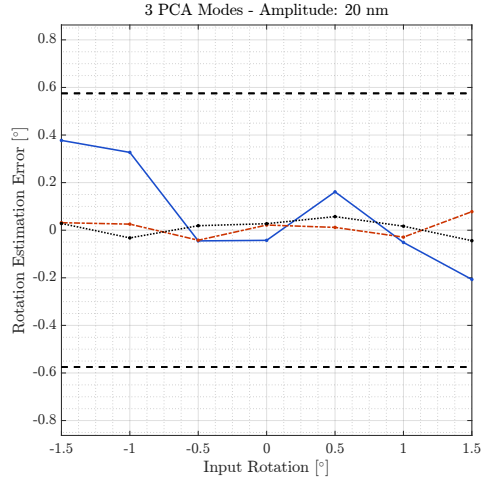
(a)



(b)



(c)



(d)

Figure 3.23. – Estimation (left) and corresponding Error (right) of a ramp of rotation using 3 PCA modes. The results are given for different level of noise η and amplitude of push-pull a . In this case, we consider $N=20$ measurements for each mode. The dashed black lines correspond to our specification in terms of accuracy

3.4.3.2. Ramp of shift X

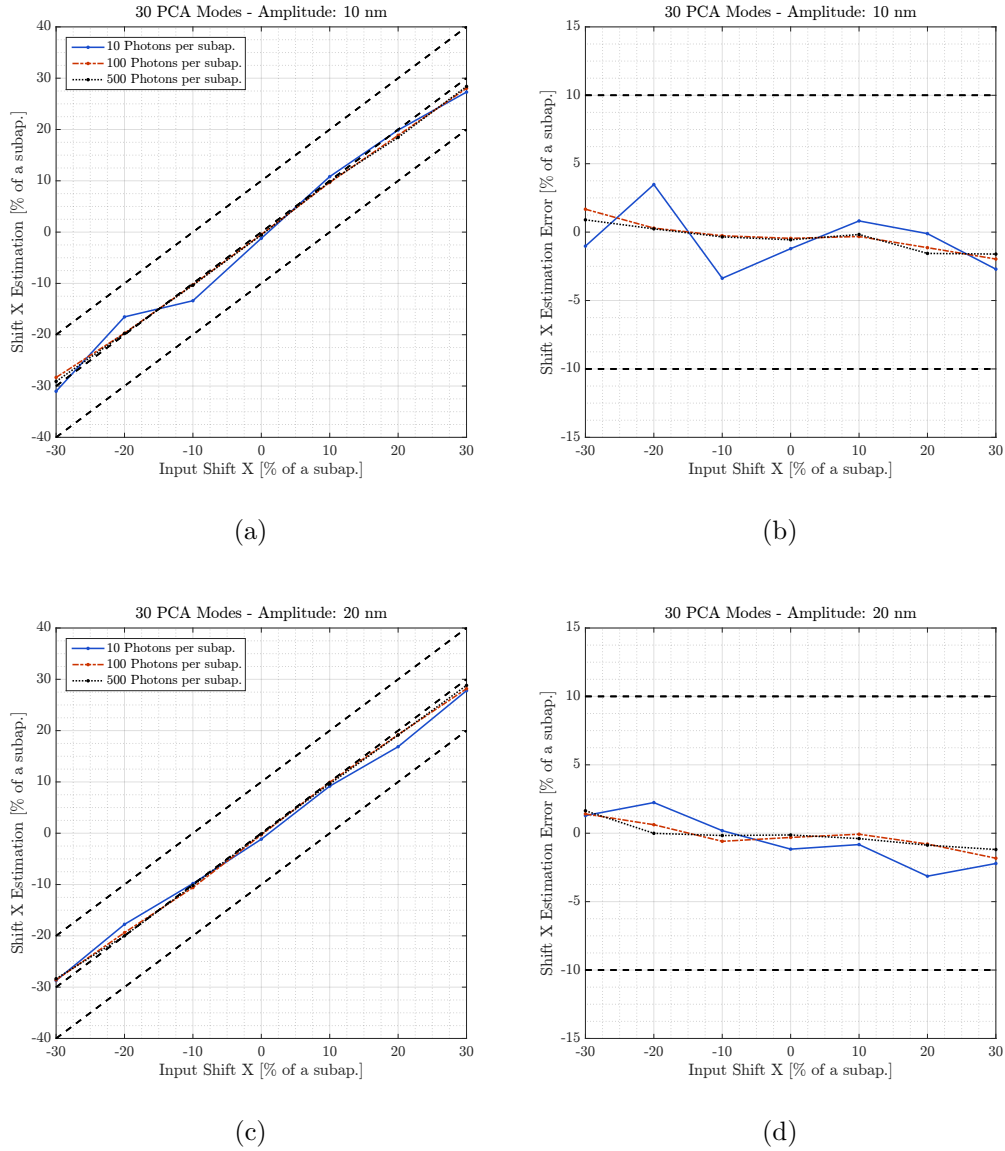
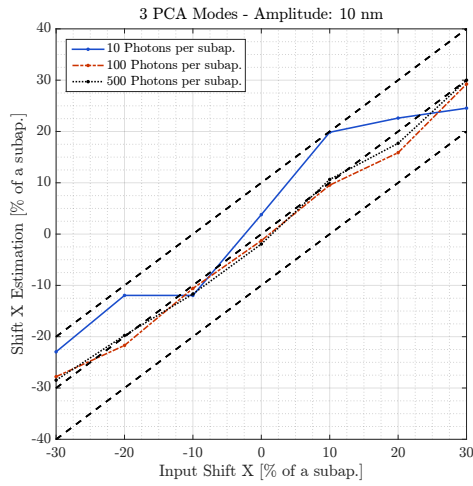
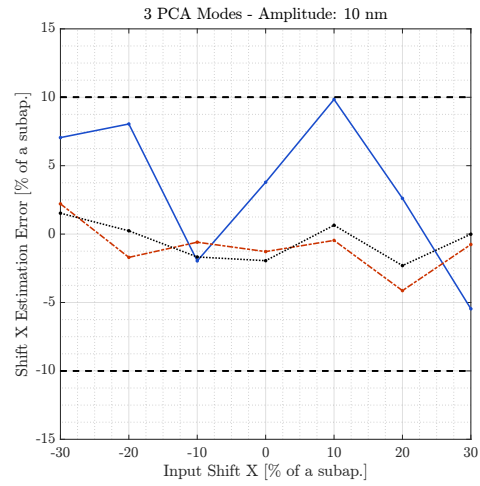


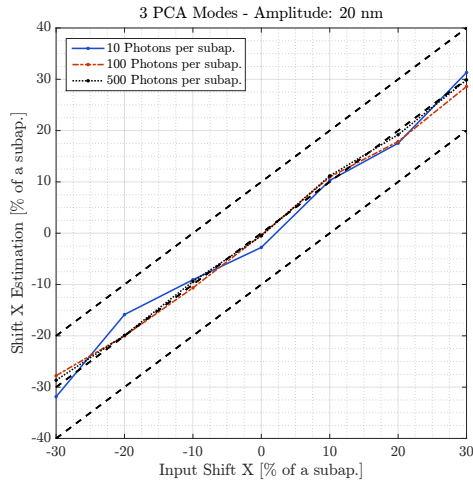
Figure 3.24. – Estimation (left) and corresponding Error (right) of a ramp of shift Y using 30 PCA modes. The results are given for different level of noise η and amplitude of push-pull a . In this case, we consider $N=20$ measurements for each mode. The dashed black lines correspond to our specification in terms of accuracy



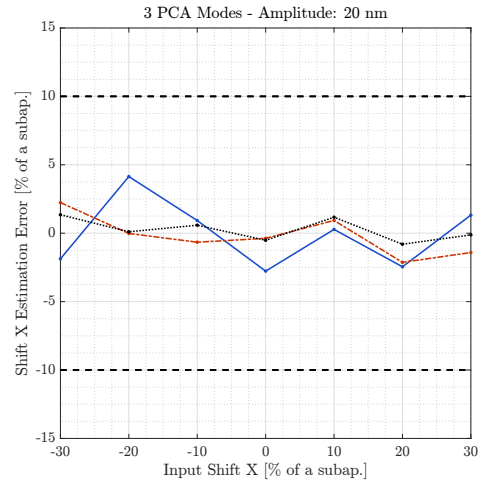
(a)



(b)



(c)



(d)

Figure 3.25. – Estimation (left) and corresponding Error (right) of a ramp of shift Y using 3 PCA modes. The results are given for different level of noise η and amplitude of push-pull a . In this case, we consider $N=20$ measurements for each mode. The dashed black lines correspond to our specification in terms of accuracy

3.4.3.3. Ramp of shift Y

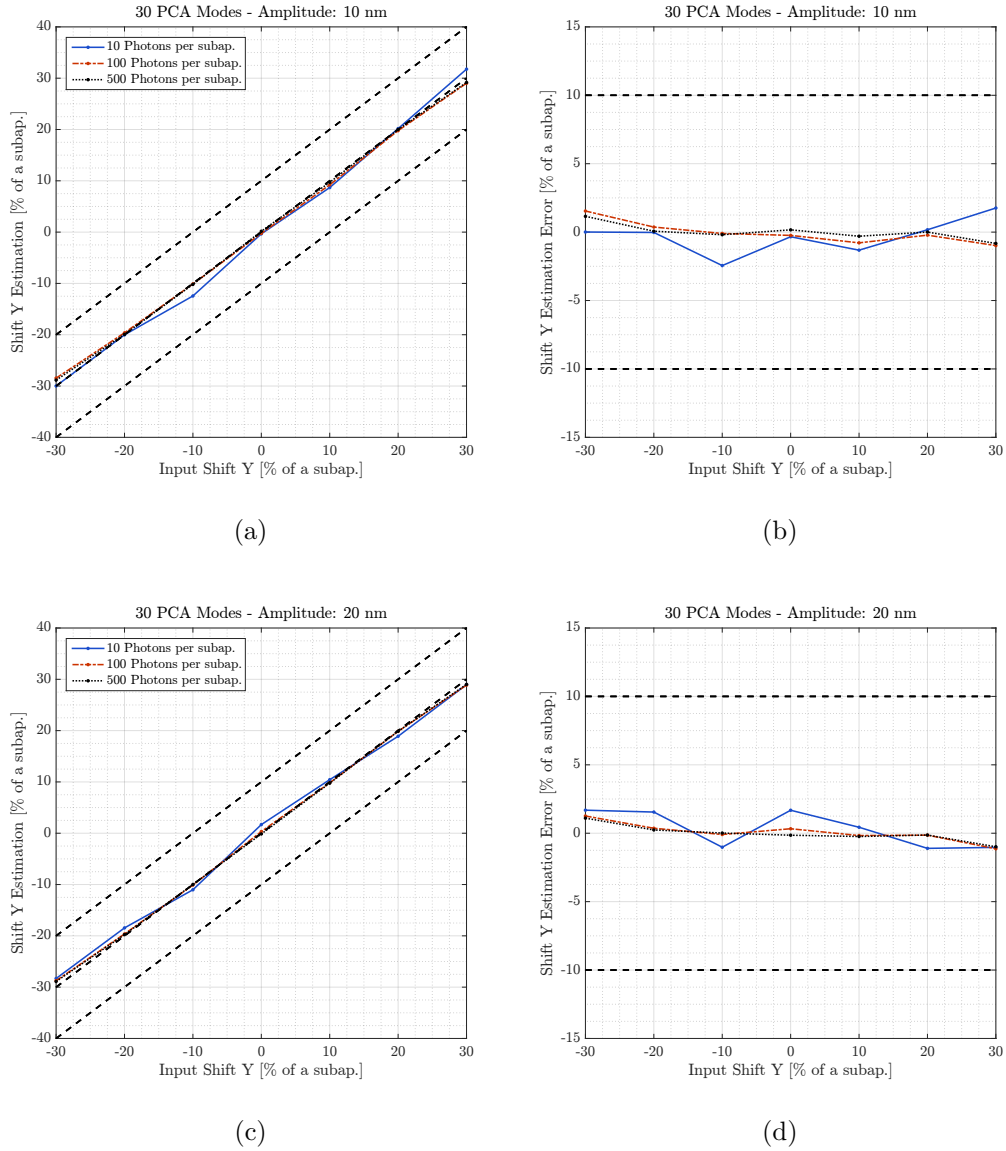


Figure 3.26. – Estimation (left) and corresponding Error (right) of a ramp of shift Y using 30 PCA modes. The results are given for different level of noise η and amplitude of push-pull a . In this case, we consider $N=20$ measurements for each mode. The dashed black lines correspond to our specification in terms of accuracy

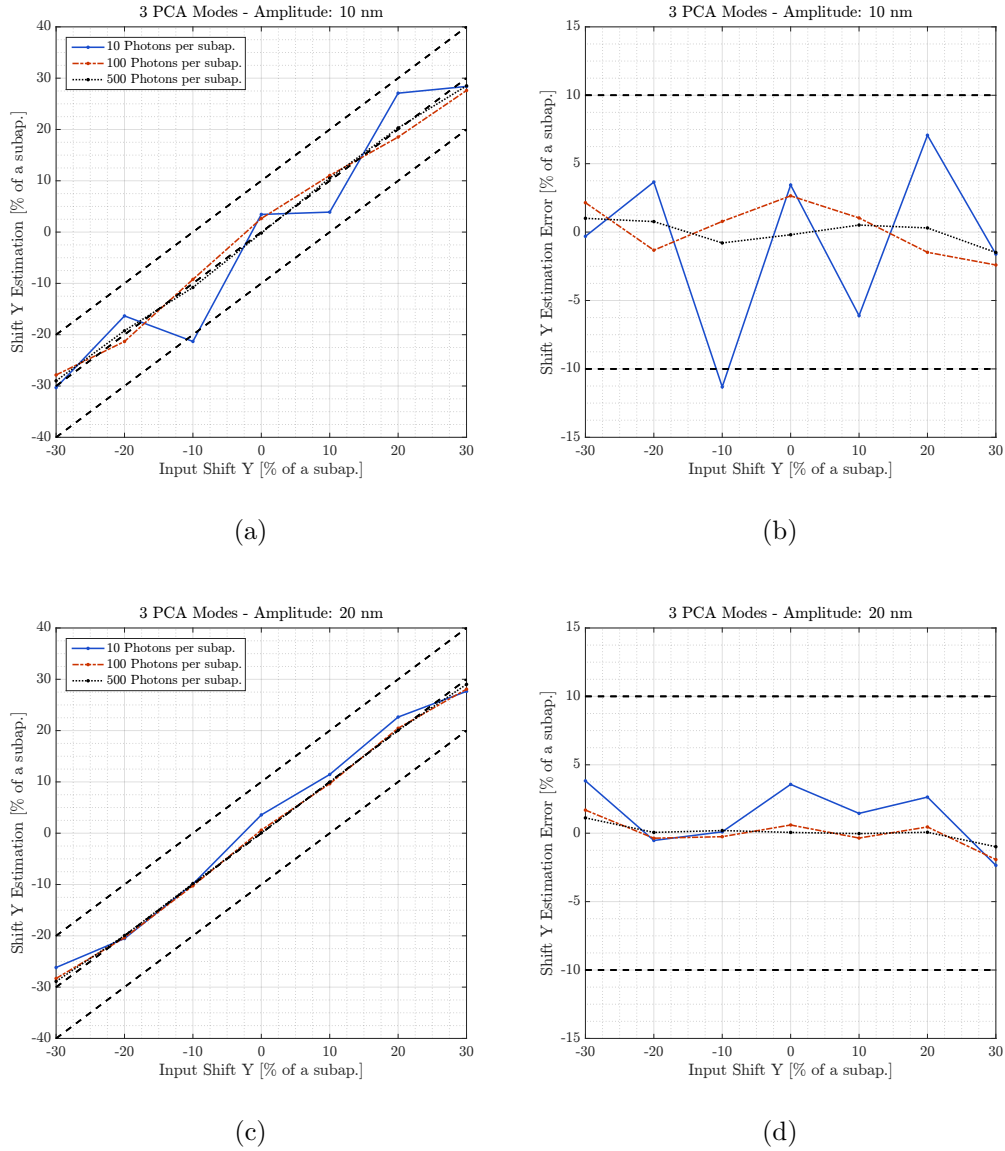


Figure 3.27. – Estimation (left) and corresponding Error (right) of a ramp of shift Y using 3 PCA modes. The results are given for different level of noise η and amplitude of push-pull a . In this case, we consider $N=20$ measurements for each mode. The dashed black lines correspond to our specification in terms of accuracy

These results exhibit the high accuracy achieved using only a few PCA modes and inform on the amplitude of mis-registrations that can be retrieved using the invasive approach. Considering the minimum number of modes, the accuracy achieved using good SNR measurements (amplitudes of 10 and 20 nm RMS) is under a few percents of a subaperture for the shifts and under 0.25° for the rotation in all the cases considered. These results are then under the values specified in the introduction of this chapter (10% of a subaperture for the shifts and 0.56° for the rotation).

3.4.4. Dynamic case with various mis-registrations

In this last case, we consider a case that includes several mis-registrations simultaneously, evolving in time. We consider good SNR on-sky measurements (amplitude 20 nm RMS) and good flux conditions (100 and 500 photons per subapertures) and we average 20 measurements for each estimation. The corresponding mis-registrations estimation for each parameter as a function of the time is given in Figure 3.28. The time units are arbitrary here as we assume that the mis-registrations remain the same during the acquisition of the signals. In that case we consider only the tracking of the parameter and we do not update the interaction matrix between two successive iterations.

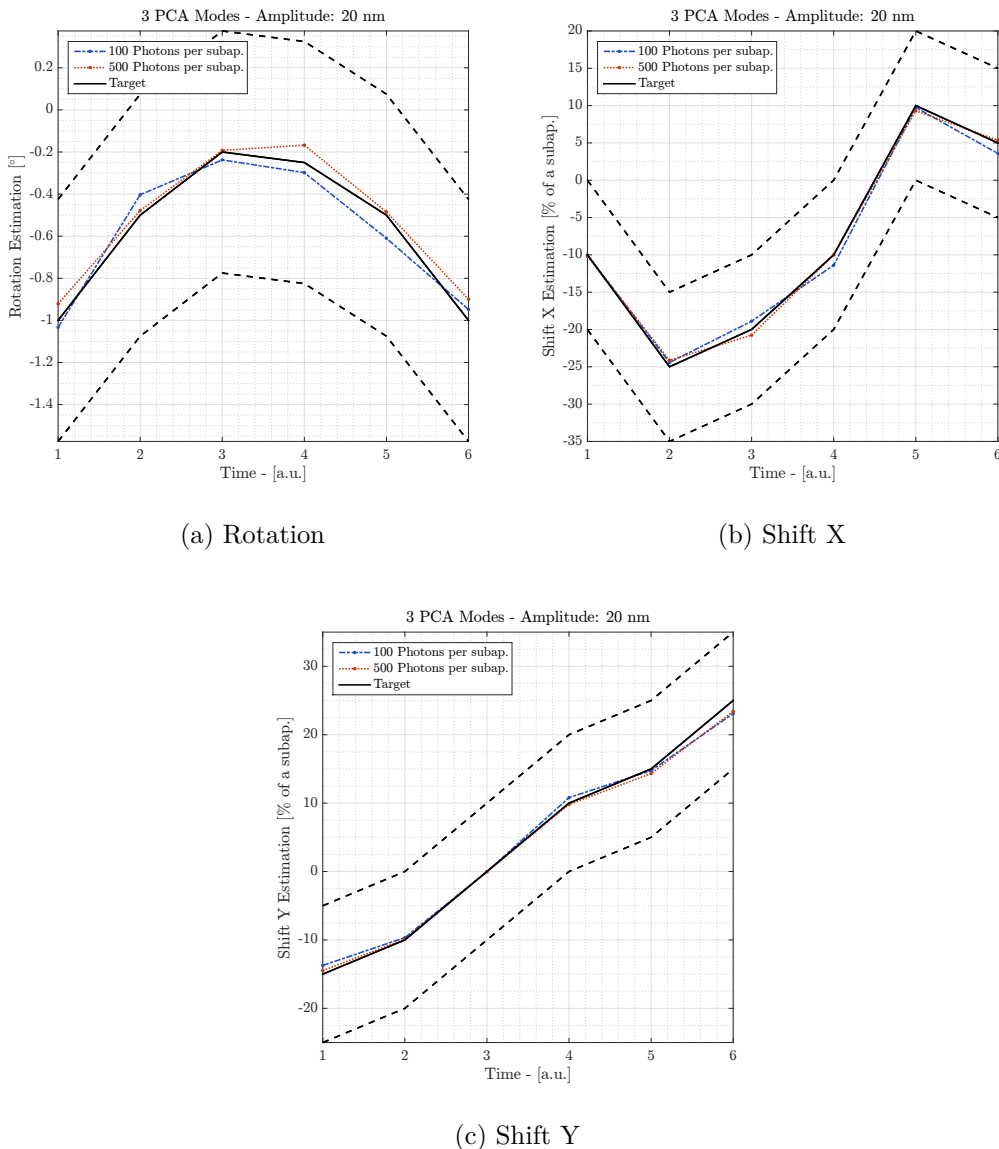


Figure 3.28. – Dynamic estimation of the mis-registration parameters as a function of the time using an amplitude a 20 nm RMS. In this case, we consider $N=20$ measurements for each mode. The dashed black lines correspond to our specification in terms of accuracy

These results show that using only the 3 PCA modes, we manage to reach an good accuracy for each type of mis-registration and we do not witness any coupling effects in the estimation. This demonstrates that a tracking of the parameters retrieving only a few PCA modes on-sky provides an excellent strategy for a system requiring regular updates of its interaction matrix.

To address the question of a regular tracking of the mis-registrations during the operation, we introduce a first strategy based on an invasive approach. This strategy is inspired from the state of the art in terms of on-sky calibration and consists in applying these calibration techniques (modulation/demodulation, push-pull) to retrieve the reference signals required by an identification algorithm and estimate the mis-registration parameters.

Our research is oriented to minimize the number of signals required by the algorithm to estimate accurately the mis-registration parameters by identifying the most sensitive modes to the mis-registrations using a Principal Component Analysis of a sensitivity matrix. The analysis of the eigen values of these sensitivity matrices showed that the reduction of dimensionality is not so optimal (hundreds of modes required to explain 90% of the variance) which suggest that the sensitivity of the first PCA modes will be really similar, for a given mis-registration. However, using only the first PCA will always be better than using a single more classical modes such as a KL mode or a DM poke.

Using on-sky push-pull measurements we investigated the accuracy achieved using different numbers of PCA modes exploring different observing conditions. We established that considering a large numbers reference signals allows to reduce the amplitude required with the cost of increasing the measurement time.

On the opposite, minimizing the numbers of signals requires high SNR measurements to provide the same level of accuracy but the time required remains really inferior with respect to the measurement of a full interaction matrix. The amplitude required remains quite small (excellent accuracy in all cases using an amplitude of 20 nm RMS) and has to be tailored according to the observing conditions and accuracy requirements. Moreover, assuming a sufficient SNR for the reference signals, we demonstrated that this procedure is suited for various mis-registrations evolving dynamically. By using only 3 PCA modes with an amplitude of 20 nm RMS, we could provide a tracking of the mis-registration parameters with an accuracy better than 1% of a subaperture.

4. Online Identification of Mis-Registration Parameters: The Non-Invasive Approach

Let's introduce another strategy that is different from the method introduced in chapter 3. This second approach is **non invasive** and consists in accumulating enough telemetry data to reconstruct a noisy interaction matrix and extract the mis-registration parameters using the algorithm introduced in section 2.5. About this second strategy, we could comment that estimating the full interaction matrix may not be optimal and a more efficient algorithm could estimate the mis-registration parameters directly from the experimental inputs. Indeed, the step of estimating the interaction matrix will propagate noise on signals that are eventually not necessary for the estimation of the parameters (the signals of the actuators are extremely localized in the interaction matrix). However, in our case, this step was necessary to well understand the physics behind the estimation of the parameters. Going directly from the signals to the mis-registration parameters would be the next step to study, based on the results presented in this chapter.

This attractive approach has been introduced in (Béchet et al. 2012 and Kolb et al. 2012a). In this approach, by contrast with the previous chapter, no external disturbance is applied on the DM and only the closed loop telemetry data are required. Although the SNR of the interaction matrix is not high enough to be directly used to close the loop of the system, it allows to retrieve a few mis-registration parameters. This method is currently the baseline for the tracking of mis-registrations at the AOF, working with SH-WFS. The purpose of this study is to understand the underlying physics, limitations and accuracy of this calibration strategy. In a second step we propose to generalize it to the case of the Pyramid WFS to include the sensor specificity.

4.1. Estimation of the interaction matrix from closed loop data

In this section we introduce the formalism to derive the AO closed loop equation and apply the reconstruction strategy presented in Béchet et al. 2012.

4.1.1. AO equations

At the loop sample k , the WFS measurement y_k corresponding to the residual phase ϕ_k^{res} is :

$$y_k = M_{WFS} \cdot \phi_k^{res} + \eta_k \quad (4.1)$$

where M_{WFS} represents the WFS measurement model (light propagation to the detector and slopes computation) and η_k the WFS noise (Photon and Read-out Noise) at the loop sample k .

ϕ_k^{res} can be written as the difference between the turbulent phase ϕ_k^{turb} and the correction phase ϕ_k^{corr} :

$$\phi_k^{res} = \phi_k^{turb} - \phi_k^{corr} \quad (4.2)$$

where ϕ_k^{corr} can be expressed as the application of a set of commands c_k on the DM :

$$\phi_k^{corr} = M_{\text{DM}\alpha} \cdot c_k \quad (4.3)$$

where the notation α indicates that a mis-registration α is applied within the operator M_{DM} . Equation 4.1 can then be written as:

$$y_k = M_{\text{WFS}} \cdot (\phi_k^{turb} - M_{\text{DM}\alpha} \cdot c_k) + \eta_k \quad (4.4)$$

Small signals amplitudes ensure to operate in the linear range of the WFS to allow equation 4.4 to be distributive. From equation 4.1, we define the incremental signals:

$$\delta y_k = y_k - y_{k-1} = M_{\text{WFS}} \cdot \delta \phi_k^{res} + \delta \eta_k \quad (4.5)$$

Such that equation 4.4 can be developed as follows:

$$\delta y_k = M_{\text{WFS}} \cdot (\delta \phi_k^{turb} - M_{\text{DM}\alpha} \cdot \delta c_k) + \delta \eta_k \quad (4.6)$$

Since everything is now linear, we can develop equation 4.6 :

$$\delta y_k = M_{\text{WFS}} \cdot \delta \phi_k^{turb} - M_{\text{WFS}} \cdot M_{\text{DM}\alpha} \cdot \delta c_k + \delta \eta_k \quad (4.7)$$

where we recognize the interaction matrix $D_\alpha = M_{\text{WFS}} \cdot M_{\text{DM}\alpha}$ of the system in the mis-registration state α (See chapter 1):

$$\delta y_k = M_{\text{WFS}} \cdot \delta \phi_k^{turb} - D_\alpha \cdot \delta c_k + \delta \eta_k \quad (4.8)$$

we then end up on the same equation as presented in Béchet et al. 2012 but our justification to consider incremental signals is related to an hypothesis of linearity.¹ From here, we want to estimate the interaction matrix D_α of the system based on equation 4.8.

4.1.2. Estimation of the interaction matrix from incremental closed loop data

This section recalls the strategy introduced in Béchet et al. 2012 to estimate the interaction matrix from the closed loop data. The idea consists in considering the propagation of $\delta \phi_k^{turb}$ in the WFS space and the noise $\delta \eta_k$ as a disturbance δz_k over

1. Their justification is related to the diagonality of the covariance matrix of the disturbance with respect to the signals of interest (see equation 4.1.2)

the WFS measurement corresponding to the actuation $\delta \mathbf{c}_k$:

$$\delta \mathbf{z}_k = \mathbf{M}_{\text{WFS}} \cdot \delta \phi_k^{\text{turb}} + \delta \boldsymbol{\eta}_k \quad (4.9)$$

so that

$$\delta \mathbf{y}_k = -\mathbf{D}_\alpha \cdot \delta \mathbf{c}_k + \delta \mathbf{z}_k \quad (4.10)$$

This situation is then quite different from the invasive case where we can control the type of signal of interest applied on the DM while here the commands are determined by the AO loop, depending on the residual phase ϕ^{res} . The composition of the disturbance on the measurement is therefore different for the two methods. An analysis of the composition of the disturbance term is presented in 4.1.3. The noise and the turbulence follow zero-mean Gaussian statistics and are independent. We can then write the covariance matrix of the disturbance $\delta \mathbf{z}_k$ as:

$$\begin{aligned} \mathbf{C}_{\delta \mathbf{z}_k} &= \langle \delta \mathbf{z}_k^T \cdot \delta \mathbf{z}_k \rangle = \langle (\mathbf{M}_{\text{WFS}} \cdot \delta \phi_k^{\text{turb}})^T \cdot (\mathbf{M}_{\text{WFS}} \cdot \delta \phi_k^{\text{turb}}) \rangle + \langle \delta \boldsymbol{\eta}_k^T \cdot \delta \boldsymbol{\eta}_k \rangle \\ \mathbf{C}_{\delta \mathbf{z}_k} &= \mathbf{C}_{\delta \boldsymbol{\eta}_k} + \mathbf{C}_{\delta \phi_k^{\text{turb}}}^{\text{WFS}} \end{aligned} \quad (4.11)$$

where $\mathbf{C}_{\delta \phi_k^{\text{turb}}}^{\text{WFS}}$ is the covariance matrix of the incremental turbulence in the WFS space. We consider both noise and turbulence to be stationary so that $\mathbf{C}_{\delta \mathbf{z}}$ becomes independent of k and we can define the covariance matrix² of the disturbance $\mathbf{C}_{\delta \mathbf{z}}$ as:

$$\mathbf{C}_{\delta \mathbf{z}} = \mathbf{C}_{\delta \boldsymbol{\eta}} + \mathbf{C}_{\delta \phi^{\text{turb}}}^{\text{WFS}} \quad (4.12)$$

The criterion $\chi(\mathbf{D}_\alpha)$ that we aim to minimize is the distance between the WFS incremental signals and the projection of the incremental commands in the WFS space:

$$\chi^2(\mathbf{D}_\alpha) = \arg \min_{\mathbf{D}_\alpha} \|\mathbf{y}_k + \mathbf{D}_\alpha \mathbf{c}_k\|^2 \quad (4.13)$$

Using a maximum likelihood approach, assuming the independence of $\delta \mathbf{c}_k$ and $\delta \mathbf{z}_k$, the criterion becomes

$$\chi^2(\mathbf{D}_\alpha) = (\delta \mathbf{y}_k + \mathbf{D}_\alpha \cdot \delta \mathbf{c}_k)^T \mathbf{C}_{\delta \mathbf{z}}^{-1} (\delta \mathbf{y}_k + \mathbf{D}_\alpha \cdot \delta \mathbf{c}_k) \quad (4.14)$$

In practice, to reach a sufficient SNR, we should select a large number N sets of increments to average out the contribution of $\delta \mathbf{z}_k$. The criterion to minimize becomes:

$$\chi_N^2(\mathbf{D}_\alpha) = \sum_{k=1}^{k=N} (\delta \mathbf{y}_k + \mathbf{D}_\alpha \cdot \delta \mathbf{c}_k)^T \mathbf{C}_{\delta \mathbf{z}}^{-1} (\delta \mathbf{y}_k + \mathbf{D}_\alpha \cdot \delta \mathbf{c}_k) \quad (4.15)$$

Here, we could comment that including some priors on the disturbance $\delta \mathbf{z}_k$ with a Minimum Mean Square Estimator (MMSE) could improve the handling of the noise and reduce the time required to average it. We did not have time to investigate this strategy but this may be done in a further step. To minimize the $\chi_N^2(\mathbf{D}_\alpha)$, we want to solve

$$\frac{\partial \chi_N^2(\mathbf{D}_\alpha)}{\partial \mathbf{D}_\alpha} = 0 \quad (4.16)$$

2. The justification to consider incremental signals in B chet et al. 2012 is related to the diagonality of $\mathbf{C}_{\delta \mathbf{z}}$ with respect to \mathbf{C}_z .

where

$$\frac{\partial \chi_N^2(\mathbf{D}_\alpha)}{\partial \mathbf{D}_\alpha} = \mathbf{C}_{\delta \mathbf{z}}^{-1} \sum_{k=1}^{k=N} (\delta \mathbf{y}_k + \mathbf{D}_\alpha \cdot \delta \mathbf{c}_k)^T \cdot \delta \mathbf{c}_k^T \quad (4.17)$$

Since $\mathbf{C}_{\delta \mathbf{z}}^{-1}$ is a covariance matrix, it is symmetric definite positive so its inverse is symmetric definite positive as well. To solve equation 4.16, the right term must then be equal to zero:

$$\sum_{k=1}^{k=N} (\delta \mathbf{y}_k + \mathbf{D}_\alpha \cdot \delta \mathbf{c}_k) \cdot \delta \mathbf{c}_k^T = 0 \quad (4.18)$$

which leads to

$$\mathbf{D}_\alpha \sum_{k=1}^{k=N} (\delta \mathbf{c}_k \cdot \delta \mathbf{c}_k^T) = - \sum_{k=1}^{k=N} (\delta \mathbf{y}_k \cdot \delta \mathbf{c}_k^T). \quad (4.19)$$

Diving both sides with the number of increments N , we identify the two covariance matrices:

$$\mathbf{C}_{\delta \mathbf{y}, \delta \mathbf{c}} = \frac{\sum_{k=1}^{k=N} (\delta \mathbf{y}_k \cdot \delta \mathbf{c}_k^T)}{N} \quad \mathbf{C}_{\delta \mathbf{c}, \delta \mathbf{c}} = \frac{\sum_{k=1}^{k=N} (\delta \mathbf{c}_k \cdot \delta \mathbf{c}_k^T)}{N} \quad (4.20)$$

An estimation of the interaction matrix \mathbf{D}_α^* is then given by

$$\mathbf{D}_\alpha^* = -(\mathbf{C}_{\delta \mathbf{y}, \delta \mathbf{c}}) \cdot (\mathbf{C}_{\delta \mathbf{c}, \delta \mathbf{c}})^\dagger \quad (4.21)$$

This is the basic equation that we will study now.

4.1.3. Analysis of the composition of the signals of interest

To evaluate the quality of the interaction matrix reconstructed from the closed loop data and to investigate the corresponding accuracy of estimation of the mis-registration parameters, it is relevant to analyze the composition of the signals $\delta \mathbf{c}_k$ that will be used to estimate the interaction matrix.

From a simple integrator command law with two frames delays, we can write:

$$\mathbf{c}_k = \mathbf{c}_{k-1} - g \cdot \mathbf{R} \cdot \mathbf{y}_{k-2} \quad (4.22)$$

We can replace \mathbf{y}_{k-2} using equation 4.1:

$$\mathbf{c}_k = \mathbf{c}_{k-1} - g \cdot \mathbf{R} \cdot [\mathbf{M}_{\text{WFS}} \cdot \phi_{k-2}^{\text{res}} + \boldsymbol{\eta}_{k-2}] \quad (4.23)$$

so that $\delta \mathbf{c}_k = \mathbf{c}_k - \mathbf{c}_{k-1}$ can be written

$$\delta \mathbf{c}_k = -g \cdot \mathbf{R} \cdot [\mathbf{M}_{\text{WFS}} \cdot \phi_{k-2}^{\text{res}} + \boldsymbol{\eta}_{k-2}] \quad (4.24)$$

For most of the AO systems, the reconstructor \mathbf{R} is obtained computing the pseudo-inverse of the interaction matrix:

$$\mathbf{R} = \mathbf{D}_\alpha^\dagger \quad (4.25)$$

We recall the expression of the pseudo-inverse of the product of two matrices \mathbf{A} and \mathbf{B} :

$$(\mathbf{AB})^\dagger = (\mathbf{A}^\dagger \mathbf{AB})^\dagger (\mathbf{ABB}^\dagger)^\dagger \quad (4.26)$$

Using the definition of D_α , we then get the following expression for R :

$$R = \left((M_{WFS})^\dagger \cdot M_{WFS} \cdot M_{DM_\alpha} \right)^\dagger \cdot \left(M_{WFS} \cdot M_{DM_\alpha} \cdot (M_{DM_\alpha})^\dagger \right)^\dagger \quad (4.27)$$

Assuming a perfect WFS (linear and no gain variations), we can consider that

$$(M_{WFS})^\dagger \cdot M_{WFS} = \text{Id} \quad (4.28)$$

Moreover, M_{DM_α} is full rank, providing:

$$M_{DM_\alpha} \cdot (M_{DM_\alpha})^\dagger = \text{Id} \quad (4.29)$$

Under these hypothesis we can simplify equation 4.27:

$$R \approx (M_{DM_\alpha})^\dagger \cdot (M_{WFS})^\dagger \quad (4.30)$$

Replacing R in equation 4.24 yields to:

$$\delta c_k = -g \cdot (M_{DM_\alpha})^\dagger \cdot (M_{WFS})^\dagger \cdot \left[M_{WFS} \cdot \phi_{k-2}^{res} + \eta_{k-2} \right] \quad (4.31)$$

that can be simplified under the hypothesis 4.28:

$$\delta c_k = -g \cdot (M_{DM_\alpha})^\dagger \cdot \phi_{k-2}^{res} - g \cdot R \cdot \eta_{k-2} \quad (4.32)$$

Under a few hypothesis, these developments gives the structure of the δc_k with two independent components: $g \cdot R \cdot \eta_{k-2}$ corresponds to the noise propagation from the previous frame and $g \cdot (M_{DM_\alpha})^\dagger \cdot \phi_{k-2}^{res}$ corresponds to the projection of the residual phase on the deformable mirror from two frames before.

If the nature of the term related to the noise propagation can be easily understood, the second term requires a bit more development. We can indeed write ϕ_{k-2}^{res} using a similar approach as an error budget:

$$\phi_{k-2}^{res} = \phi_{k-2}^{res,temporal} + \phi_{k-2}^{res,aliasing} + \phi_{k-2}^{res,noise} + \phi_{k-2}^{res,fitting} + \phi_{k-2}^{res,calib} \quad (4.33)$$

Where :

- $\phi_{k-2}^{res,temporal}$ is the temporal error due to the finite bandwidth of the loop. This term will depend on the wind speed and direction.
- $\phi_{k-2}^{res,aliasing}$ is the propagation of the aliasing error of the WFS.
- $\phi_{k-2}^{res,fitting}$ is the fitting error at the loop sample $k - 2$.
- $\phi_{k-2}^{res,noise}$ is the noise propagation at the loop sample $k - 2$.
- $\phi_{k-2}^{res,calib}$ is the calibration error such as mis-registrations.

To summarize, we can recall the expression of δy_k :

$$\delta y_k = M_{WFS} \cdot \delta \phi_k^{turb} - D_\alpha \cdot \delta c_k + \delta \eta_k \quad (4.34)$$

where $\delta \mathbf{c}_k$ can be written under a few hypothesis:

$$\begin{aligned} \delta \mathbf{c}_k = & \\ -g \cdot (\mathbf{M}_{\text{DM}\alpha})^\dagger \cdot & \left(\phi_{k-2}^{\text{res,temporal}} + \phi_{k-2}^{\text{res,aliasing}} + \phi_{k-2}^{\text{res,fitting}} + \phi_{k-2}^{\text{res,noise}} + \phi_{k-2}^{\text{res,calib}} \right) \\ & - g \cdot \mathbf{R} \cdot \boldsymbol{\eta}_{k-2} \end{aligned} \quad (4.35)$$

We can comment that the term related to the fitting error $\phi_{k-2}^{\text{res,fitting}}$ can be removed as we consider the projection on the DM of the residual phase ϕ_{k-2}^{res} .

$$\begin{aligned} \delta \mathbf{c}_k = & \\ -g \cdot (\mathbf{M}_{\text{DM}\alpha})^\dagger \cdot & \left(\phi_{k-2}^{\text{res,temporal}} + \phi_{k-2}^{\text{res,aliasing}} + \phi_{k-2}^{\text{res,noise}} + \phi_{k-2}^{\text{res,calib}} \right) \\ & - g \cdot \mathbf{R} \cdot \boldsymbol{\eta}_{k-2} \end{aligned} \quad (4.36)$$

These developments give the structure of the signals that will be used to estimate the interaction matrix of the system and shed light on the three components that will be of interest: the noise, the calibration errors and the temporal error. Although this is not intuitive at first, we understand that the presence of noise acts both as a noise on the measurement (through the term $\delta \boldsymbol{\eta}_k$ in equation 4.34) and as a signal of interest through the terms $-g \cdot \mathbf{R} \cdot \boldsymbol{\eta}_{k-2}$ and $\phi_{k-2}^{\text{res,noise}}$ in equation 4.36. All of these terms being uncorrelated, we expect the noise on the measurement to average out for a large number of measurements and the matrix estimation to converge to the true interaction matrix.

The term $\phi_{k-2}^{\text{res,calib}}$ includes the errors due to the mis-registrations and acts as a signal of interest. Intuitively, this suggests that a system with mis-registrations will propagate signals that will help estimate the interaction matrix of the system and the more the system will be mis-registered the higher the corresponding signals. In other words, a shorter time should be required to reach the same SNR for the interaction matrix estimation for a mis-registered system than with small or no mis-registrations. This point remains however to be investigated more thoroughly.

At last, we understand that the temporal error of the system will also create signals that will be used to reconstruct the interaction matrix through the term $\phi_{k-2}^{\text{res,temporal}}$. The difference with the other components of $\delta \mathbf{c}_k$ is that this term will be correlated to the $\delta \phi_k^{\text{turb}}$ of equation 4.34 which might impact the estimation of the interaction matrix since the hypothesis of independence between the signals is no longer verified.

Before presenting the results of numerical simulations, we can already predict that the method will provide good results when the composition of the disturbance $\delta \mathbf{z}_k$ is dominated by the noise and when the contribution of the temporal term is low. This will ensure to respect the hypothesis that the signals of interest $\delta \mathbf{c}_k$ are uncorrelated with the disturbance $\delta \mathbf{z}_k$. By contrast, we can predict that the application of the method will be more problematic when the $\delta \mathbf{c}_k$ will be correlated with the disturbance $\delta \mathbf{z}_k$ which corresponds to a configuration with no noise and a high temporal error, typically for a Frozen Flow atmosphere.

To characterize our approach, we propose to first investigate cases that get as close as possible to the hypothesis of the method to validate the method and quantify its accuracy in the nominal case (see 4.2). In a second step, we propose to focus on the limitations of the method by exploring different closed loop conditions (noise

level and atmosphere properties). This will allow us to evaluate the impact of the spatio-temporal correlation between the signals and the disturbance on the parameter estimations (see 4.3). At last, we propose to consider the method using a Pyramid WFS to include its operational complexity that will challenge the hypothesis of a perfect WFS (see 4.4).

4.2. Validation of the method

In this section we propose to consider a nominal case to validate the method introduced previously. Although this manuscript is focused on the Pyramid WFS, we start by considering a case with SH-WFS. This choice is motivated by the fact that the sensor is linear and is not impacted by gains variations. As an example, we can plot the modal gains estimation when properly dimensioned (sampling, Field of View) obtained with an on-sky calibration for a SH-WFS (see Figure 4.1). With such a system we get quite close to the hypothesis of perfect WFS presented in the previous section.

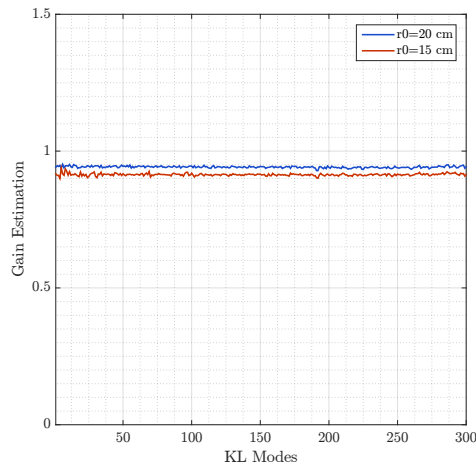


Figure 4.1. – Modal gains of a SH-WFS for an r_0 of 15 and 20 cm in the visible. The curves are flat and close to 1 in both cases. The difference between the two curves is due to the different level of residual during the on-sky calibration.

We then consider a system corresponding to an 8-m diameter telescope with a 20 by 20 subapertures Shack Hartmann WFS, operating in I band at $850 \mu m$, and a Cartesian DM with 357 controlled actuators, arranged in the Fried Geometry. The WFS is sampled with 8 by 8 pixels per subaperture which provides a pixel scale of 0.22" per pixel. We recall that for all the results presented in this thesis, the atmosphere is simulated using the method introduced by Assémat et al. 2006 to generate long sequences of phase screens. If not specified, we consider a Fried Parameter r_0 of 15 cm in the visible. In terms of control, the loop is simulated using two frames delays and we consider a simple integrator with a gain of 0.5. The interaction matrix is modal and corresponds to 300 KL modal basis, re-orthogonalized in the DM space (Gendron 1995). The properties of the system considered are summarized in

Table 4.1 and the initial working point of the algorithm is the centered position (no mis-registration) defined in equation 2.31.

Turbulence	$r_0(V)$	15 cm	SH-WFS	Subapertures	20×20
	L_0	30 cm		Pixel Scale	0.22"
	Cn^2 profile	1-2 layers		RON	none
	Windspeed	5-30 m/s		Photon Noise	On
Control	Frequency	1 kHz	DM	Photons/subap.	5-500
	Delay	2 Frames		Signal Processing	CoG
	Integrator	$g=0.5$		Actuator	357
	Bandwidth	75 Hz	Inf. Functions	Gaussian	
	Int. Matrix	300 KL	Coupling	35%	
NGS	Modal control	No	Telescope	Diameter	8 m
	Wavelength	850 nm		Obstruction	None
	Magnitude	7.5-13.5		Resolution	160 px

Table 4.1. – Numerical Simulations parameters for the sections 4.2 and 4.3

The first questions that come to mind when implementing this method is: what SNR is required to estimate the mis-registration parameters? and how long should we average to get a good SNR for the estimated interaction matrix? This will of course depend on the conditions of observation but from the experience acquired at the AOF, a rough estimation of the time required is around 30 to 40 seconds running at 1 kHz. This corresponds to 30 000 to 40 000 frames. For instance in a nominal case, Figure 4.2 gives the relative error to the convergence value as a function of the number of frames used to estimate the interaction matrix. We see that after 40 000 frames, the relative error between the estimated parameter and the convergence value obtained using 100 000 frames is less than 2.5 %. In other words, assuming that the convergence value would be a shift of 10% of a subaperture, the absolute difference between the estimation using 40 000 frames and 100 000 frames would be of 0.25 % of a subaperture which is negligible.

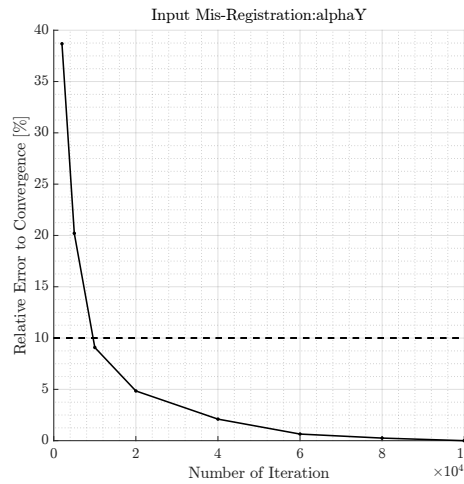


Figure 4.2. – Relative error with respect to the convergence value for the estimation of a shift Y in a nominal case (slow boiling with low flux).

The question is now to investigate the estimation of the parameters. For that, we define a Frozen Flow Atmosphere with a wind speed of 10 m/s in the X direction and we consider different levels of flux. For each type of mis-registration, we apply a ramp of amplitude and we reconstruct the interaction matrix using 20 000 frames to reduce the computation time. The results are presented in Figures 4.3, 4.4 and 4.5.

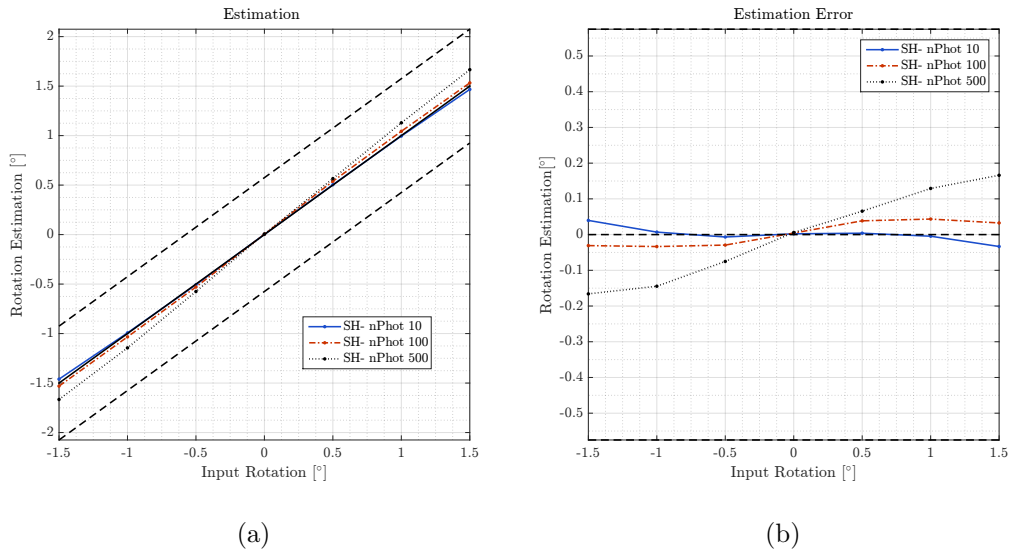


Figure 4.3. – Rotation Estimation (a) and Estimation Error (b) as a function of the input rotation for a Frozen Flow of 10 m/s for different levels of noise.

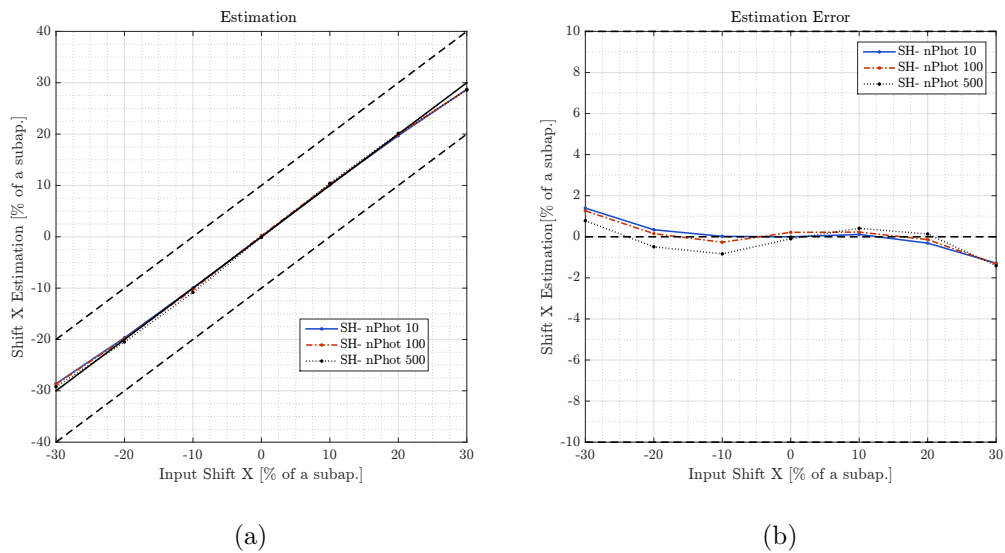


Figure 4.4. – Shift X Estimation (a) and Estimation Error (b) as a function of the input shift X for a Frozen Flow of 10 m/s for different levels of noise.

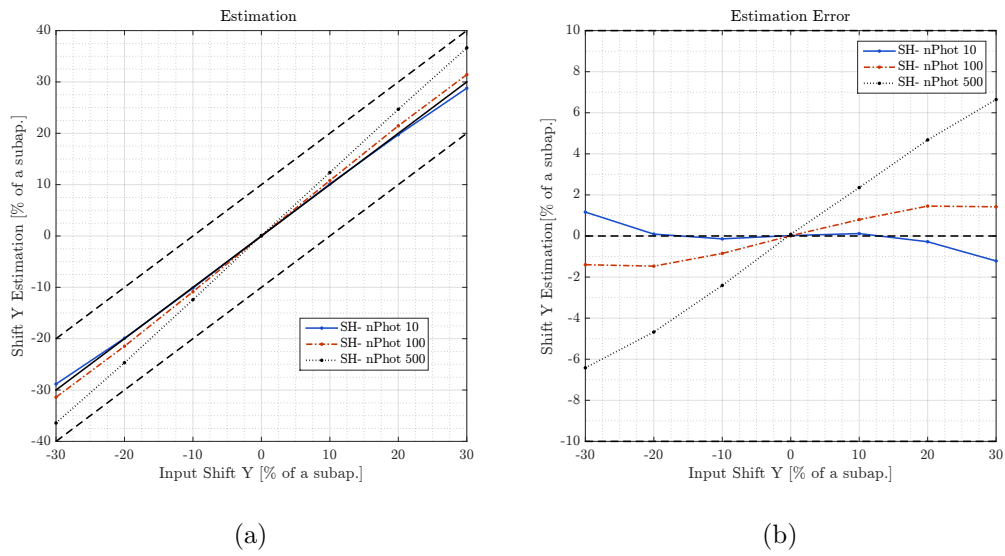


Figure 4.5. – Shift Y Estimation (a) and Estimation Error (b) as a function of the input shift Y for a Frozen Flow of 10 m/s for different levels of noise.

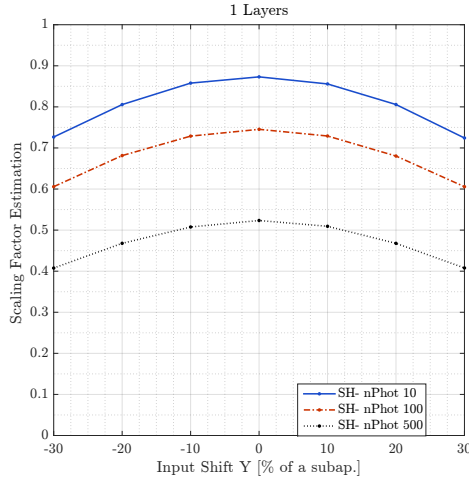
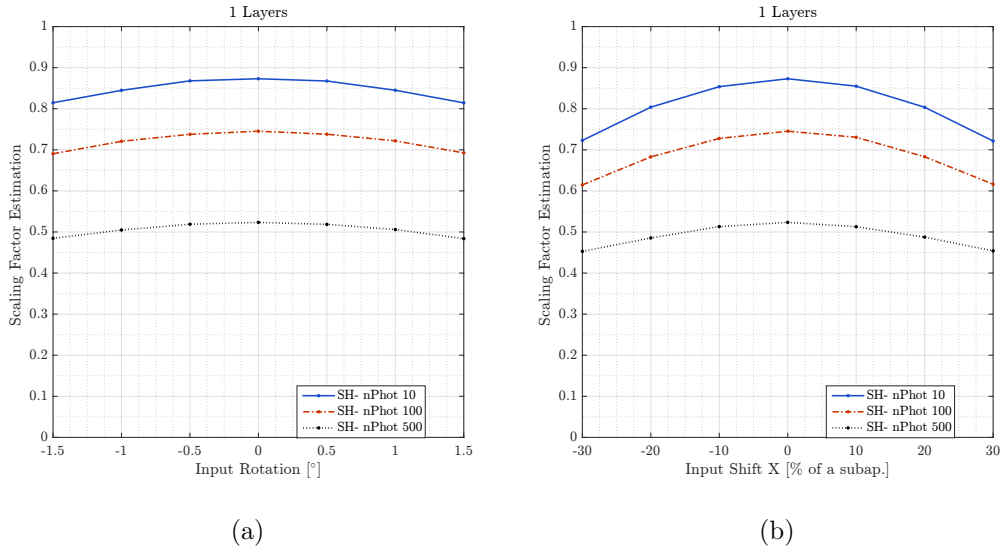


Figure 4.6. – First Estimation of the scaling factor γ as a function of the input mis-registration in a Frozen Flow configuration with a wind of 10 m/s for different levels of noise.

The figures presented show different results. The first one is that the level of flux highly impacts the estimation of the parameters. A high flux seems to lead to an over-estimation of the parameters that can go up to 6 % of a subaperture in the case of the shift Y. If we look at the corresponding values of scaling factor (Figure 4.6), we see that the scaling variations depend on the level of noise and on the value of mis-registration. In the worst case (high flux and shift Y), the scaling factor goes down to 0.4 instead of 1.

If we now analyze the shift X estimation (Figure 4.4), it appears to be slightly biased (estimation non symmetric with respect to the origin) in the configuration with high flux. Since the AO system is symmetric, there should not be any difference between the estimation of the shift X and Y. The direction of the wind seems then

to have an impact on the estimation of the parameters. If we proceed to the same test taking an opposite wind direction, we retrieve the same estimation for the shift Y and the rotation but the bias of the shift X has an opposite sign (see Figure 4.7).

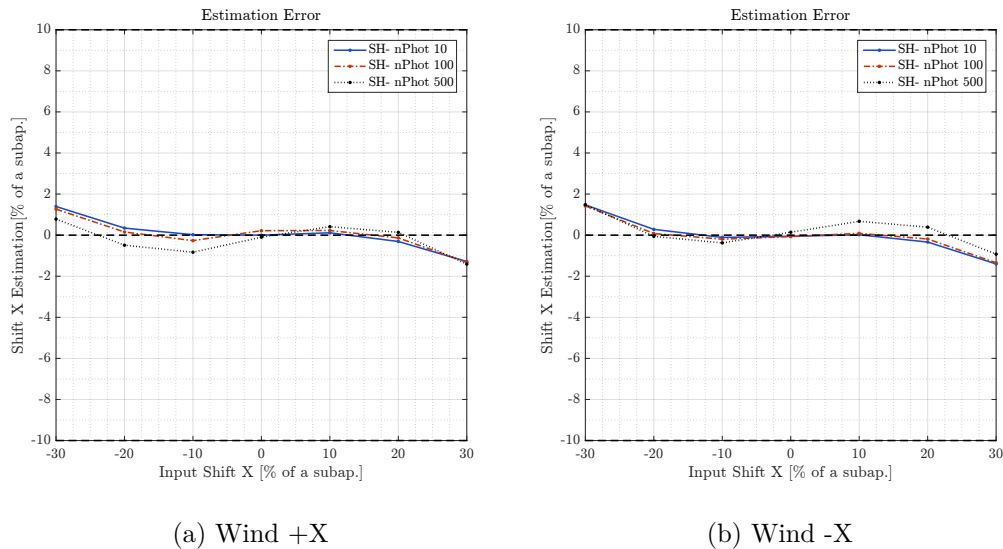


Figure 4.7. – Estimation Error of the shift X parameter for a Frozen Flow configuration with a wind of 10 m/s in the X (a) and -X direction (b)

These preliminary results give already an idea of the accuracy that can be reached with the algorithm for different levels of noise. We put in evidence that :

- the wind direction has an effect on the parameters estimation.
- the impact becomes higher in low noise regime.

Let us consider the composition of the signals used to estimate the interaction matrix. The Frozen Flow configuration in low noise regime corresponds to a case where the signals due to the noise propagation become smaller with respect to the ones due to the temporal error, when the disturbance is dominated by a colored noise. In this situation, it appears to include a bias in the parameter estimation. We propose to investigate this point more thoroughly in the next section.

4.3. Challenging the validity of the hypothesis: limitations of the method

From the considerations of section 4.1.3 , it is relevant to investigate the estimation of the interaction matrix when the composition of the δc_k is dominated by a component or another. For this purpose, we propose to consider two structures for the atmosphere:

A **Frozen Flow** atmosphere modeled using a single layer and a constant wind speed. This profile will create strong spatial and temporal correlations between the δc_k and the $\delta \phi_k^{turb}$ through the term $\phi_{k-2}^{res,temporal}$.

A **Boiling** atmosphere modeled using two layers with opposite wind direction and constant wind speed. This profile will provide smaller correlations between the δc_k

and the $\delta\phi_k^{turb}$ through the term $\phi_{k-2}^{res,temporal}$.

For both profiles, we explore **different levels of noise** that will act both as a noise on the measurement (through the term $\delta\eta_k$ in equation 4.34) and as a signal of interest through the terms $-g.R.\eta_{k-2}$ and $\phi_{k-2}^{res,noise}$ in equation 4.36.

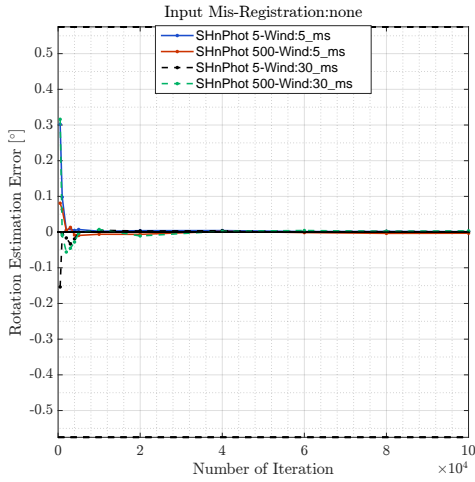
The profiles considered for the atmosphere are given in table 4.8

Profile	Direction	Speed [$m.s^{-1}$]	Photons/subap.
Slow FF - Low Flux	X	5	5
Slow FF - High Flux	X	5	500
Fast FF - Low Flux	X	30	5
Fast FF - High Flux	X	30	500
Slow Boiling - Low Flux	[X, -X]	[5,5]	5
Slow Boiling - High Flux	[X, -X]	[5,5]	500
Fast Boiling - Low Flux	[X, -X]	[30,30]	5
Fast Boiling - High Flux	[X, -X]	[30,30]	500

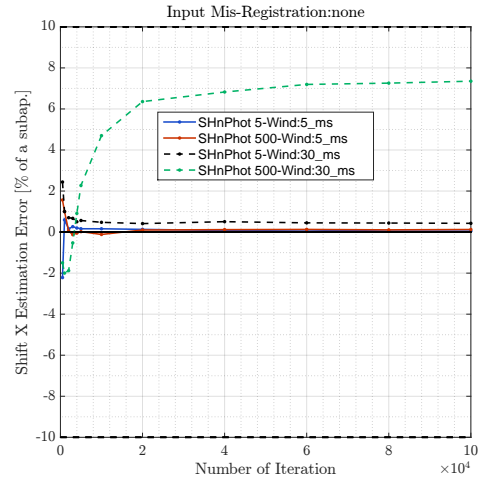
Figure 4.8. – Definition of the different configurations identified to characterize the estimation of the interaction matrix using telemetry data. FF stands for Frozen Flow.

4.3.1. Centered System

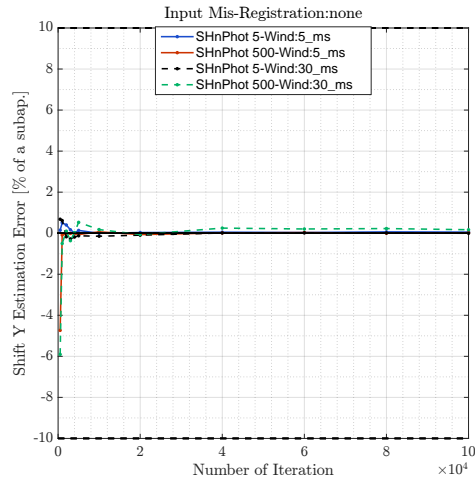
We first consider a system with no mis-registrations. The estimation of the mis-registration parameters is then expected to give 0. To ensure that convergence is reached, the results presented in this section have been obtained using 100 000 frames. The estimation of the rotation and both shift parameters in the case of a Frozen Flow are given in Figure 4.9. These plots show an interesting result: the estimation of the shift X does not converge to a null value when the wind is strong. If this remains negligible when the flux is low, (0.5% of a subaperture), the high flux configuration displays a drift of 7% of a subaperture. This situation corresponds to a case where the incremental commands and $\delta\Phi_k^{turb}$ are strongly correlated through $\delta\phi_{k-2}^{res}$ and the signal due to the noise propagated in the AO loop is negligible. The other parameters (shift Y and rotation) are however not impacted and well estimated in any situation. If we consider the estimation of the scaling factor, we retrieve the trend identified in Figure 4.6 with a scaling factor lower when the flux gets higher. We notice however that the scaling factor is highly dependant on the wind speed as well.



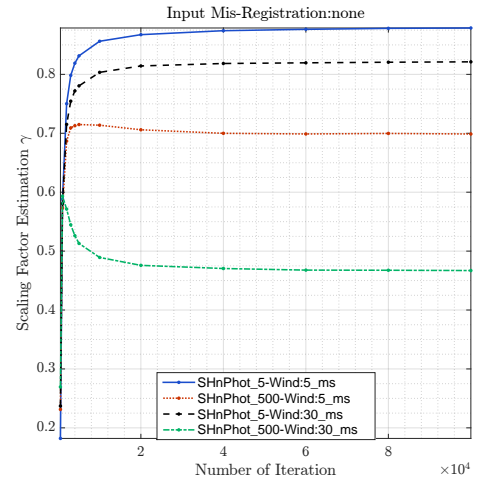
(a) Rotation



(b) Shift X



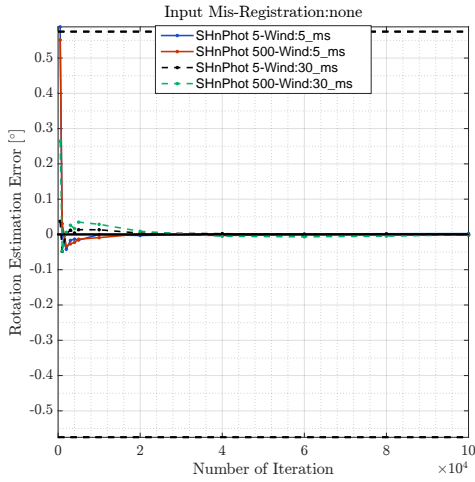
(c) Shift Y



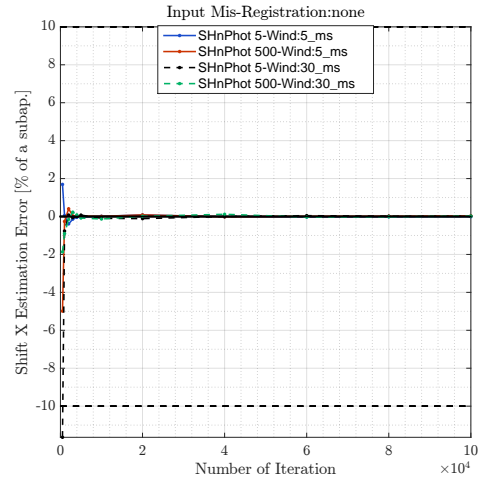
(d) Scaling Factor

Figure 4.9. – Estimation of the mis-registration parameters as a function of the number of signals used to estimate the interaction matrix from closed loop data in the case of a Frozen Flow turbulence with slow and strong wind for a low and high flux.

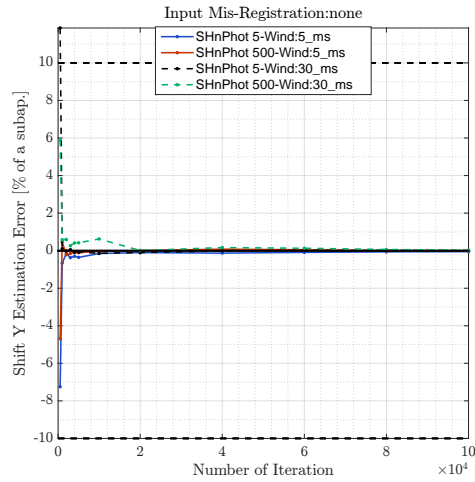
If we proceed to the same analysis with a Boiling turbulence (see Figure 4.10), we notice that the bias of the shift X disappears. The estimation of all the other parameters remains unchanged, including the scaling factor.



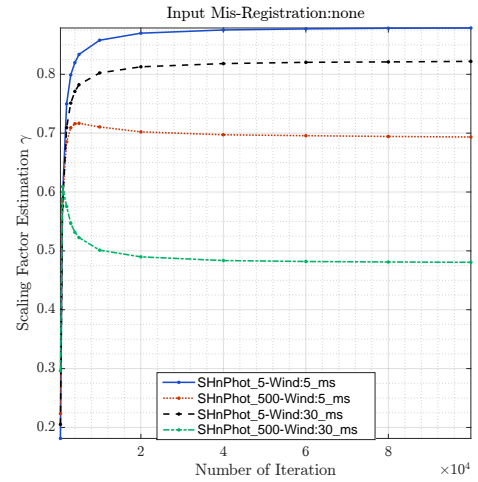
(a) Rotation



(b) Shift X



(c) Shift Y



(d) Scaling Factor

Figure 4.10. – Estimation of the mis-registration parameters as a function of the number of signals used to estimate the interaction matrix from closed loop data in the case of a Boiling turbulence with slow and strong wind for a low and high flux.

To explain the different results obtained with the Boiling and Frozen Flow configurations, we propose to analyze more in depth the signals of the estimated interaction matrices. Let us focus on the signal from a single actuator (here the actuator 100, located well in the center of the pupil). This corresponds to plotting one column of the interaction matrix. For each configuration of wind speed and flux, we compare the target signal (corresponding to a non mis-registered noise-free interaction matrix) with the signal retrieved using 100 000 frames. The results are presented in the Figures 4.11, 4.12, 4.13 and 4.14 where each plot represents the signal retrieved in a Frozen Flow and Boiling configurations. The analysis of these signals reveals that the cases with low flux (Figures 4.11 and 4.12) give the best estimation of the inter-

action matrix with residuals slightly above the noise level. In both cases however, we witness that the estimated signals are slightly attenuated, and that this attenuation gets higher with a strong wind. The cases with high flux and slow wind exhibit an even higher attenuation. However, the most interesting case is the configuration with high flux and strong wind (Figure 4.14) because untrue structures can be noticed in the interaction matrix signals. Since the mis-registration estimation is based on the interaction matrix morphology identification, these structures will consequently bias the results of the estimation.

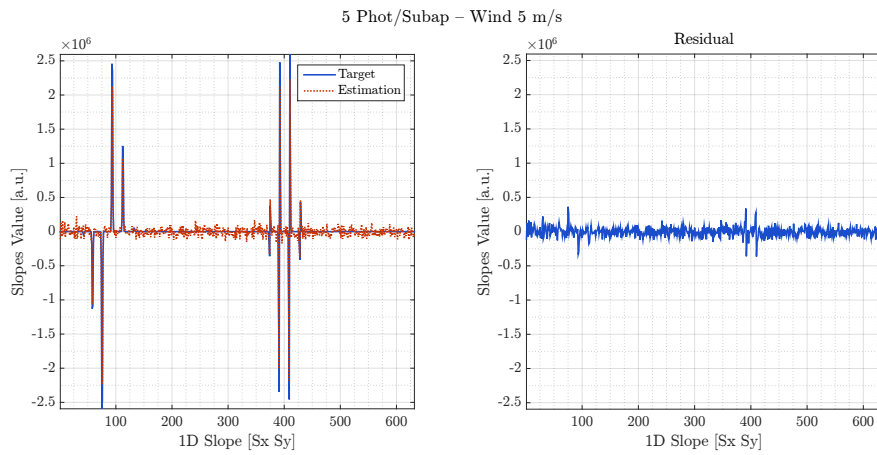
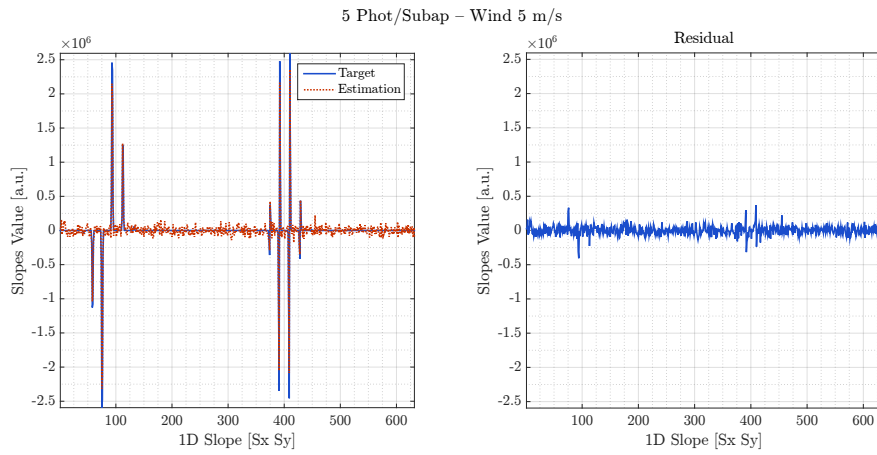
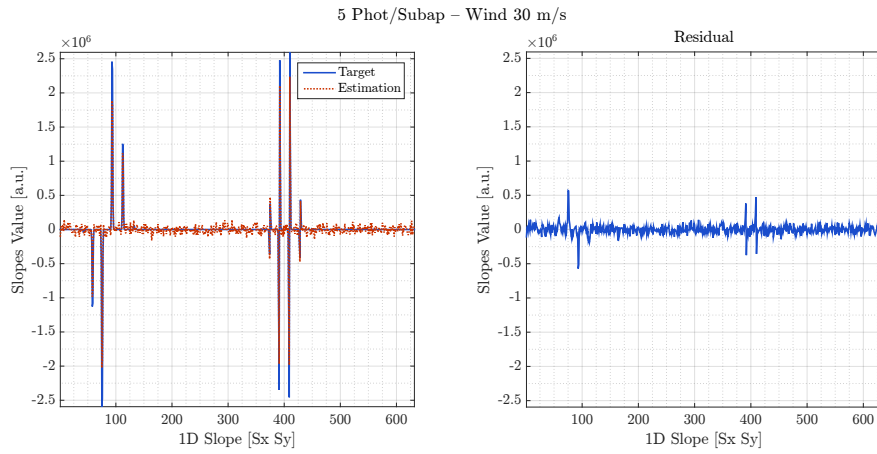
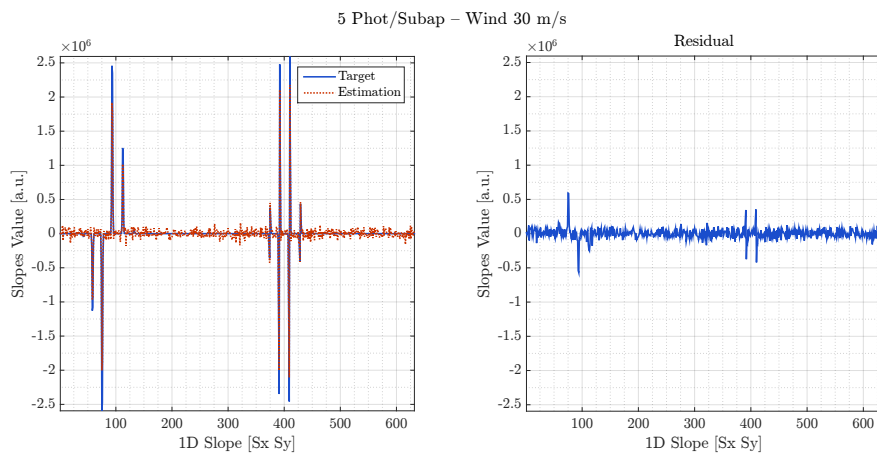


Figure 4.11. – Interaction matrix signal corresponding to the actuator 100 for a Frozen Flow (a) and a Boiling (b) atmosphere in the case of a slow wind and a low flux.

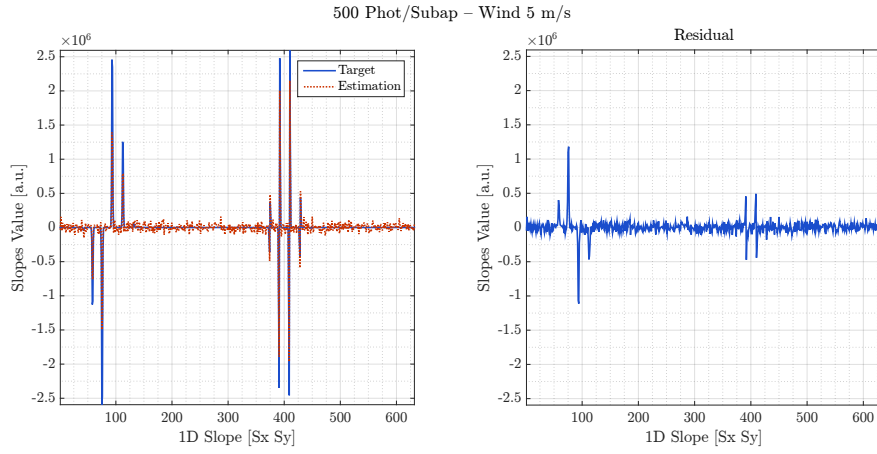


(a) Frozen Flow

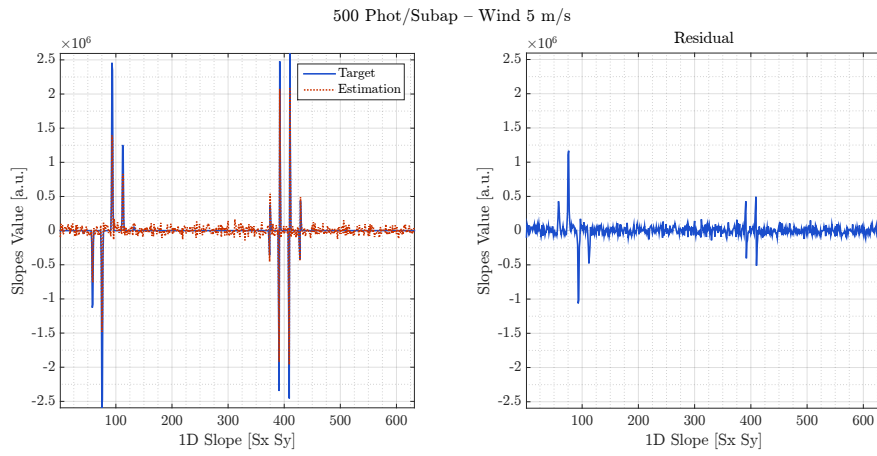


(b) Boiling

Figure 4.12. – Interaction matrix signal corresponding to the actuator 100 for a Frozen Flow (a) and a Boiling (b) atmosphere in the case of a fast wind and a low flux.

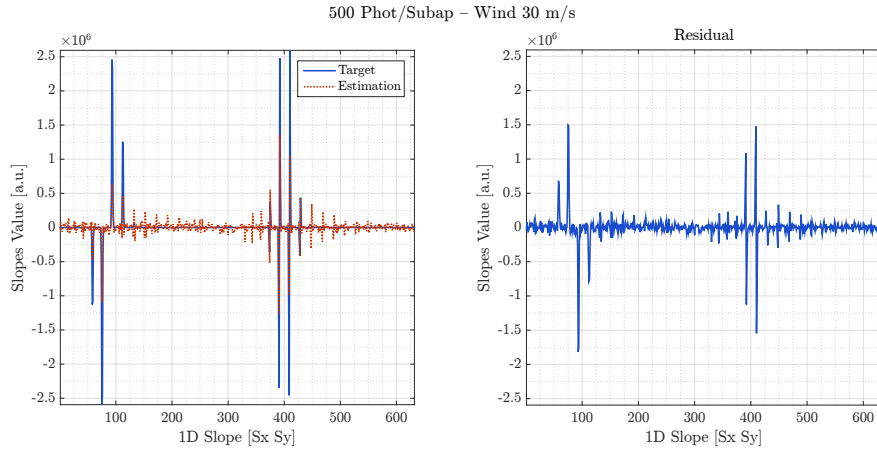


(a) Frozen Flow

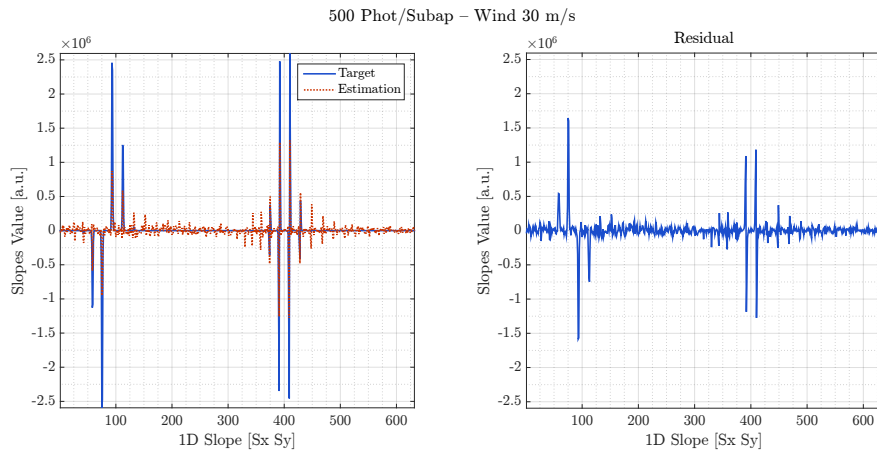


(b) Boiling

Figure 4.13. – Interaction matrix signal corresponding to the actuator 100 for a Frozen Flow (a) and a Boiling (b) atmosphere in the case of a slow wind and a high flux.



(a) Frozen Flow



(b) Boiling

Figure 4.14. – Interaction matrix signal corresponding to the actuator 100 for a Frozen Flow (a) and a Boiling (b) atmosphere in the case of a fast wind and a high flux.

If we now compare the Frozen Flow and Boiling cases in high flux regime, we notice that the signals obtained in Frozen Flow exhibit a non symmetry that is similar to the impact of a mis-registration. This non-symmetry is not visible in the case of a Boiling configuration. This is well illustrated in Figure 4.15. The presence of such structures in the interaction matrix retrieved in a Frozen Flow configuration explains the bias identified in the estimation of the parameters (Figure 4.9) and although the structures are still present in a Boiling configuration, they appear to compensate each other cancelling the effects of bias on the shift X estimation.

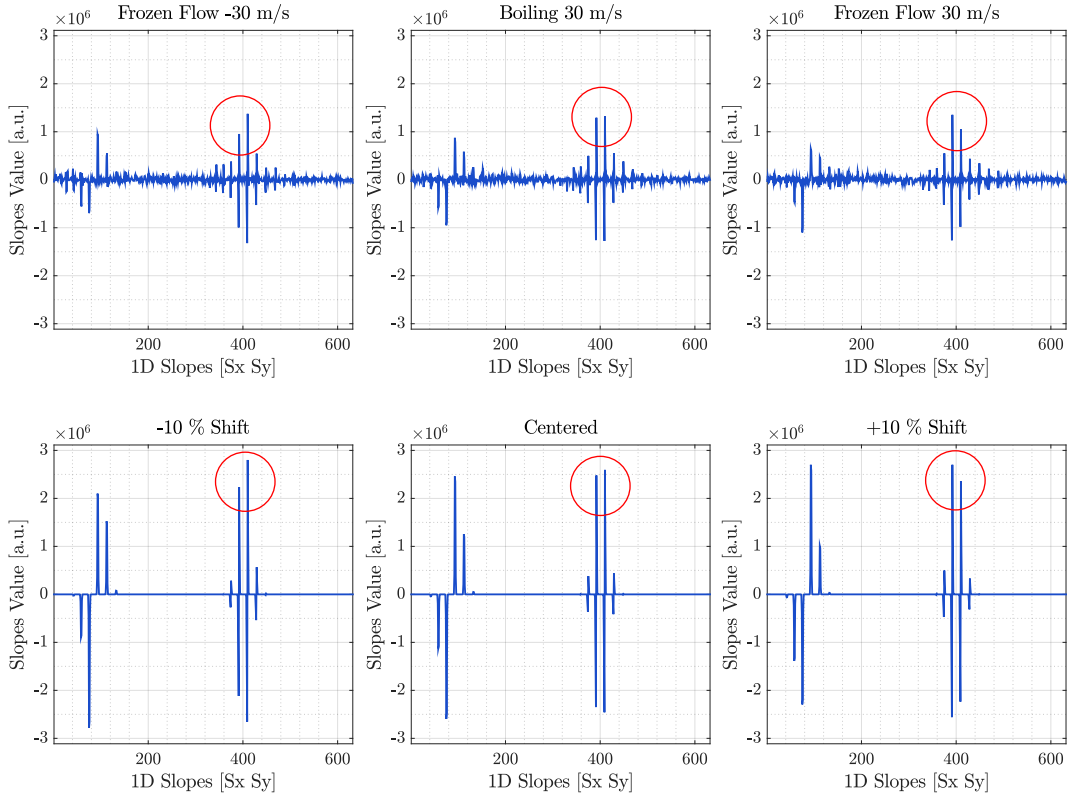


Figure 4.15. – 1D signal of the estimated interaction matrices signals with no mis-registration, corresponding to the actuator 100 for a high flux regime and different configurations of atmosphere (top). 1D signals of noise-free interaction matrices for different shift X (bottom). We retrieve the same symmetry in the estimated signals with a Frozen Flow as in the mis-registered matrices.

In the results presented in the Figure 4.11, 4.12, 4.13 and 4.14, it appears that the attenuation of the signal is sometimes different for the slopes in X and Y. It is thus relevant to consider a different scaling factor γ_X and γ_Y for the slopes X and Y. The estimation of the different scaling factors for different configurations of atmosphere (Frozen Flow in X, Boiling in X and Boiling in X & Y) is summarized in Table 4.2 and Table 4.3. These results show that depending on the conditions, the signals display a **high attenuation**, an **intermediate attenuation** or a **low attenuation**. In addition, in the situation where the wind has a unique direction (same results for Frozen Flow and Boiling in X) the attenuation is higher for the slopes in X than in Y. To witness the same level of attenuation in X and Y, we need to consider the configuration with a wind direction in X and Y. Moreover, the level of attenuation is dependent on the wind speed: the attenuation gets higher with a strong wind.

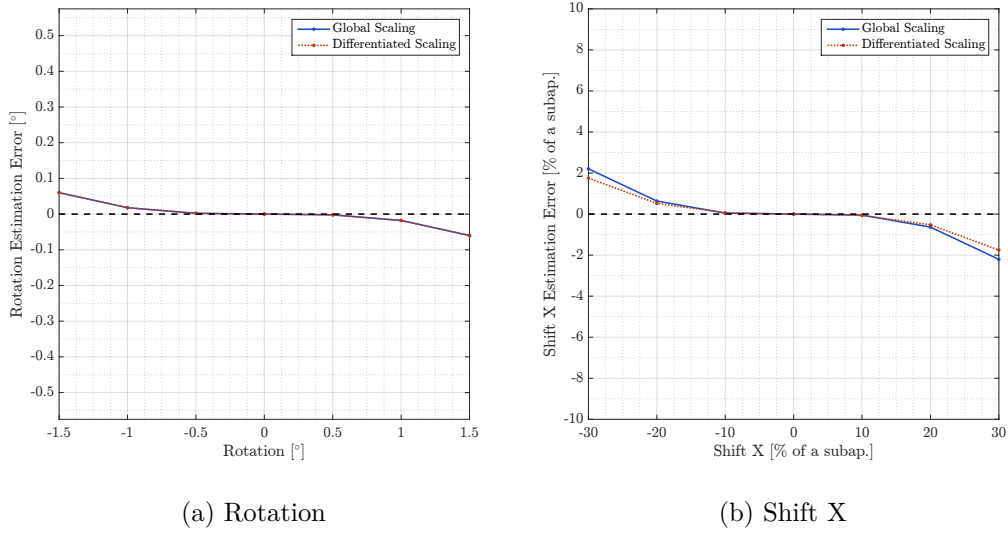
	Low Flux	High Flux
Frozen Flow - X Direction	[0.86, 0.84]	[0.6, 0.8]
Boiling - X Direction	[0.86, 0.85]	[0.59, 0.8]
Boiling X and Y Direction	[0.89, 0.88]	[0.59, 0.58]

Table 4.2. – Scaling factors $[\gamma_X, \gamma_Y]$ for a wind speed of 5 m/s.

	Low Flux	High Flux
Frozen Flow - X Direction	[0.77, 0.82]	[0.43, 0.53]
Boiling - X Direction	[0.77, 0.82]	[0.43, 0.56]
Boiling X and Y Direction	[0.74, 0.74]	[0.43, 0.43]

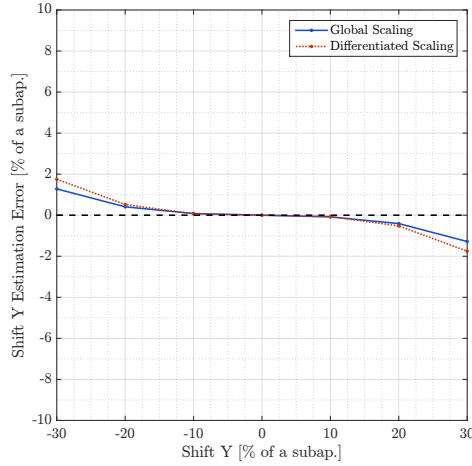
Table 4.3. – Scaling factors $[\gamma_X, \gamma_Y]$ for a wind speed of 30 m/s.

To investigate the impact of a different scaling γ_X in X and γ_Y in Y, we compute noise-free interaction matrices that contain such variations of scaling for the slopes X and Y, taking the values corresponding to a fast Frozen Flow and high flux from Table 4.3: $[\gamma_X=0.43, \gamma_Y=0.53]$. In addition, the algorithm is modified to provide a separated estimation of the scaling for the slopes in X and Y. The comparison of estimation is provided in 4.16. It appears that, similarly to the modal scaling (see Figure 2.28), using a global scaling allows to compensate for a differentiated scaling in the interaction matrix. The difference of estimation between an algorithm with differentiated scaling and a global scaling is negligible (0.5% of a subaperture for the shifts in the worst case, no difference for the rotation). In the following of the thesis, the results are presented using the algorithm with global scaling for the interaction matrices since it appears to have a negligible impact on the parameters estimation.



(a) Rotation

(b) Shift X



(c) Shift Y

Figure 4.16. – Difference of estimation between an algorithm using a global scaling γ or a different scaling γ_X in X and γ_Y in Y.

With this analysis of the interaction matrices signals, we established that the direction and speed of the wind will **affect the scaling of the slopes in the corresponding direction**. However, this different scaling does not seem to affect the estimation of the parameters using the identification algorithm.

Nevertheless, we identified that the term due to the temporal error in the composition of δc_k will impact the reconstruction of the interaction matrix by adding **complex structures** that do not correspond to a simple shift of the system. These structures originate from the spatio-temporal correlation between the signal and the disturbance and in the case of a Frozen Flow, they are interpreted as a shift in the corresponding wind direction by the identification algorithm. We propose an explanation for the origin of these structures in 4.3.3.1.

4.3.2. Mis-registered System

After analyzing a non mis-registered case, let us now proceed with the analysis of a mis-registered system. Since we identified that the direction of the wind can bias the estimation of the shift parameter in the same direction, we consider a system shifted in Y to be orthogonal to the wind direction. To remain in the linear regime of the algorithm, we consider a shift of only 10% of a subaperture. The results of the estimation of the shift Y are given in Figure 4.17 that provides the estimation error as a function of the number of frames used to estimate the interaction matrix. We do not show the curves corresponding to the rotation and the shift X since they are identical to the ones presented in Figure 4.9.

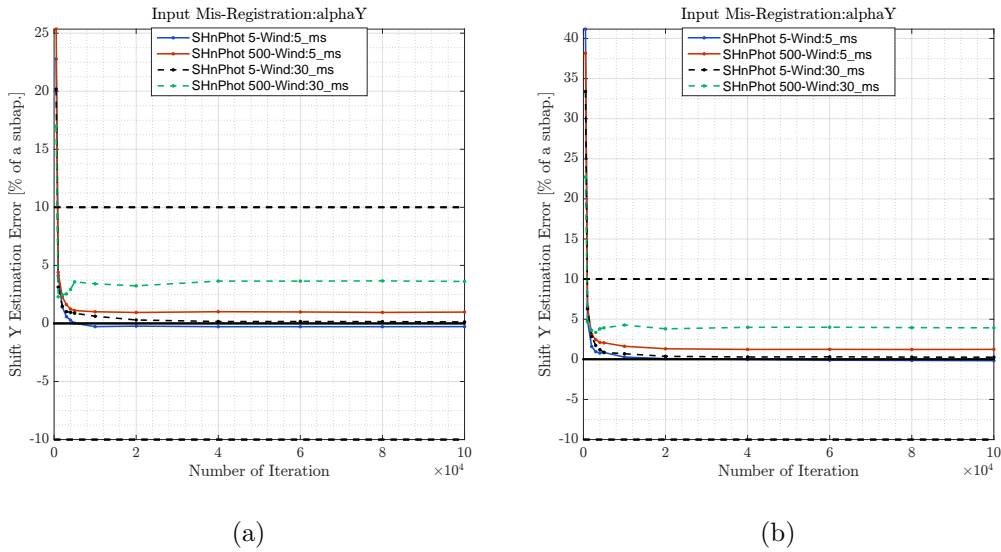


Figure 4.17. – Estimation Error of the Shift Y as a function of the number of frames considered. The results are given for a Frozen Flow (a) and a Boiling configuration (b) with different wind speeds and levels of noise.

We see here is that the results are identical for a Frozen Flow and Boiling configuration for the Y shift estimation. As expected, we witness that depending on the regime of noise, the parameter is more or less over-estimated. The cases with high noise regimes give the best estimation of the interaction matrix and thus of the parameters to identify. By contrast, the cases with low noise regimes are more impacted by the attenuation and the presence of the complex structures identified in Figure 4.15 which tends to over-estimate the parameters. This effect is higher for a strong wind.

4.3.3. Analysis of the spatio-temporal correlations

4.3.3.1. Impact of the loop gain

In the previous section, we identified that the spatio-temporal correlations between the component $\phi_{k-2}^{res,temporal}$ and the $\delta\phi_k^{turb}$ lead to undesired structures in the estimation of the interaction matrix and bias the algorithm. Since these effects are related to the temporal error, we propose to study the estimation of the interaction matrix

as a function of the loop gain. In terms of control, the loop can be optimized with respect to the temporal error (and thus with respect to the wind speed). Figure 4.18 gives the WFE as a function of the loop gain for a 30 m/s wind and shows that the optimal gain in a case of high flux is around 0.6 and gets smaller for a lower flux which is an expected behavior since more noise is propagated in the loop.

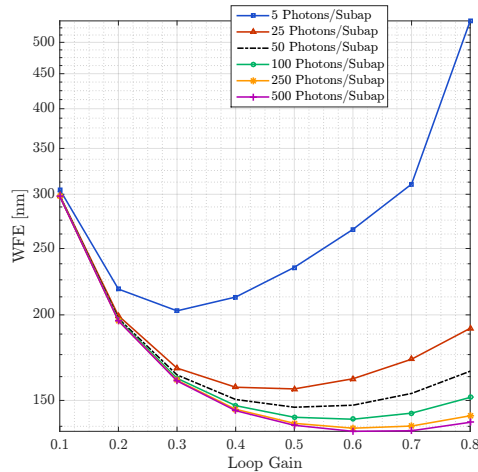


Figure 4.18. – Wave Front Error (WFE) as a function of the loop gain for a Frozen Flow configuration and a wind of 30 m/s.

We consider a centered system (no mis-registrations) in a Frozen Flow configuration with a wind of 30 m/s in the X direction and we reconstruct the interaction matrices averaging 20 000 signals. An illustration of the estimated matrices for a high flux (500 Photons per subaperture) is given in Figure 4.19 and shows that the gain applied in closed loop has a big impact on the quality of estimation of the Interaction Matrix. The matrices retrieved using a small gain (high temporal error) display similar structures as identified in Figure 4.14. On the contrary, the matrices retrieved using a gain allowing a better correction of the temporal error (gain superior to 0.5) provide a better estimation of the interaction matrix. The origin of the structures identified in Figure 4.15 is then related to the level of correction of the temporal error. In the context of estimating the interaction matrix with closed loop data, this term should be as small as possible to minimize the impact on the matrix estimation. Of course, in a more general context, the choice of the gain will depend on other terms of the error budgets and has to be chosen to provide the best AO performance.

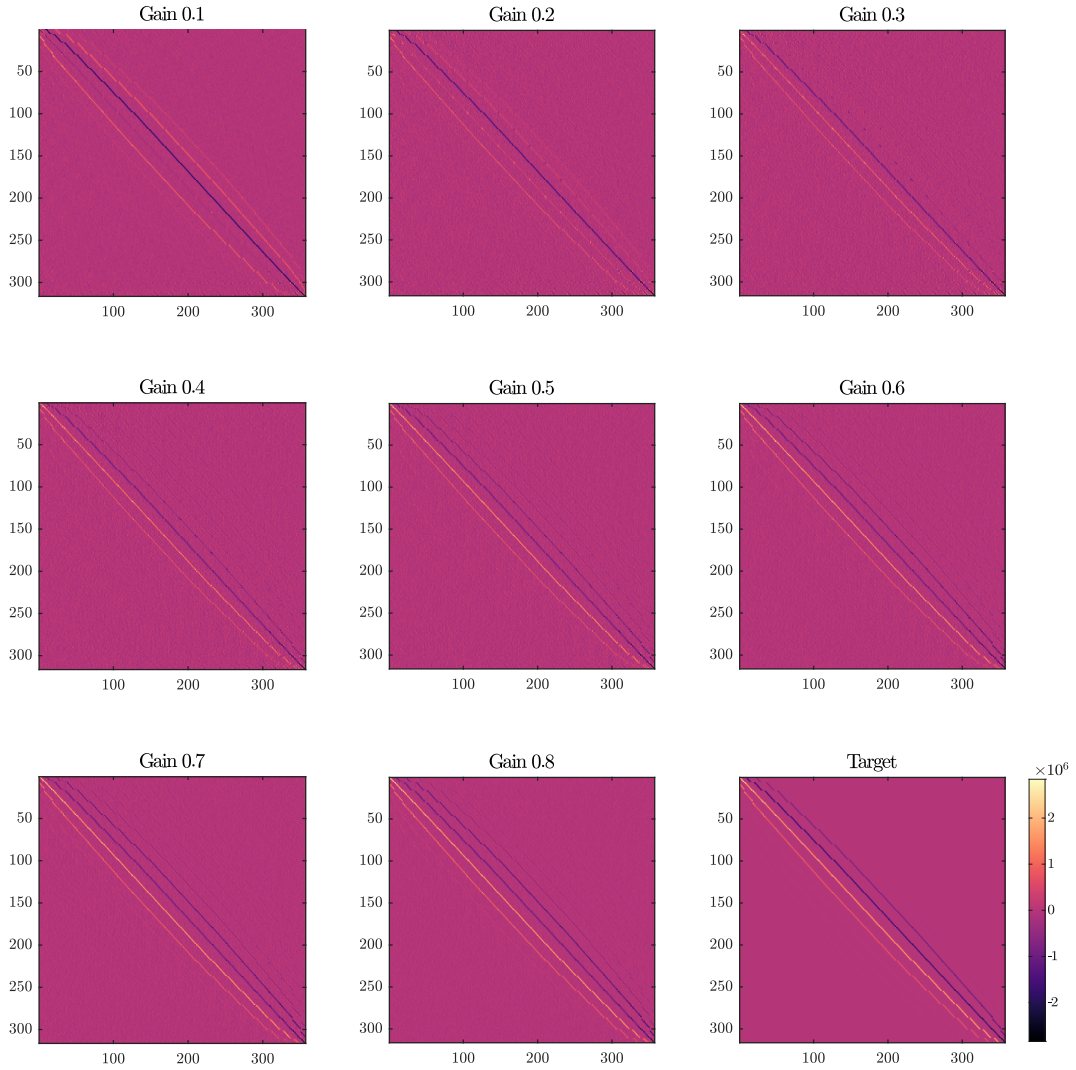


Figure 4.19. – Estimated interaction matrices (slopes X only) in the case of a Frozen Flow of 30 m/s using different loop gains for a high flux (500 Photons per subapertures).

If we now look at the estimation of the parameters, focusing on the estimation of the shift X with a wind of 30 m/s (Figure 4.20), we retrieve a consistent estimation: the cases with the structures identified in Figure 4.19 are interpreted as a shift, sometimes even of more than 100% of a subaperture in the worst case for the matrix estimation ($g=0.1$)! The cases with a gain superior to 0.5 provide however a better estimation with an error inferior to 5% of a subaperture. These effects are symmetric if we consider a wind in the opposite direction.

The cases for intermediate wind speeds are given in Figure 4.21. The effect becomes smaller when the wind speed decreases but it follows the same logic: the bias due to the spatio-temporal correlations becomes negligible for gains higher than 0.5.

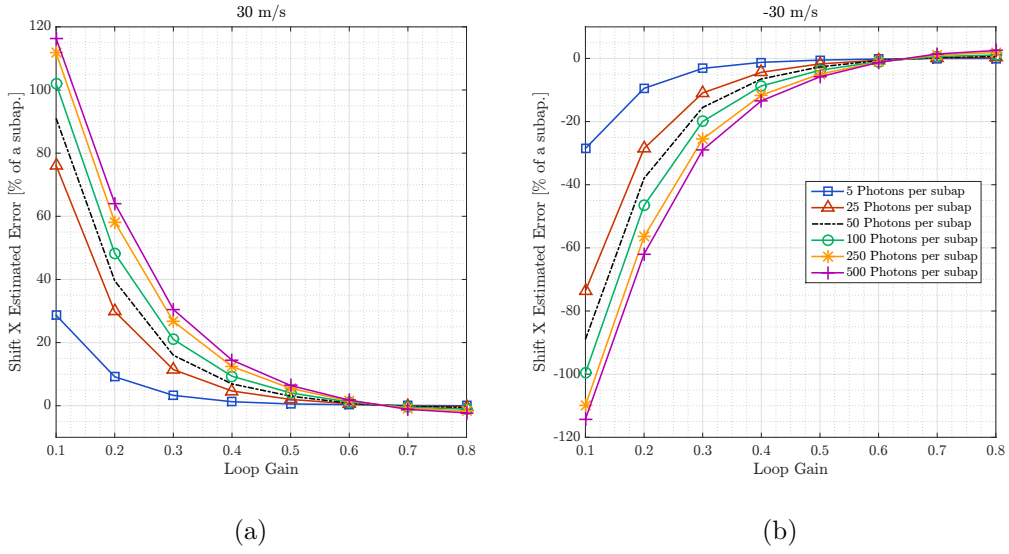


Figure 4.20. – Shift X estimation in a Frozen Flow configuration with a wind speed of 30 m/s and -30 m/s. We show the estimation for different fluxes (in number of photons per subaperture) as a function of the loop gain.

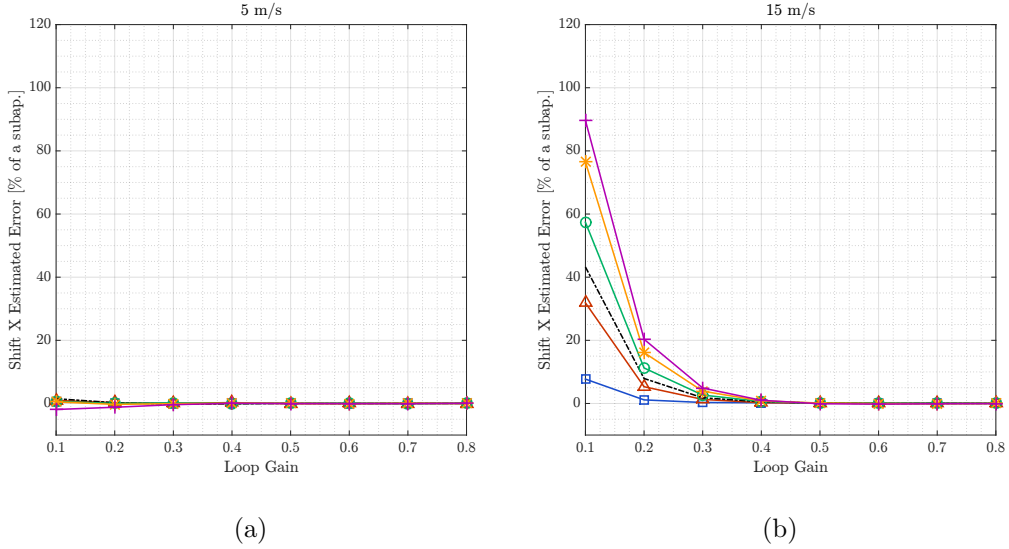


Figure 4.21. – Shift X estimation in a Frozen Flow configuration with a wind speed of 5 m/s and 15 m/s. We show the estimation for different fluxes (in number of photons per subaperture) as a function of the loop gain.

As a preliminary conclusion, these latest results show that the effects of the spatio-temporal correlations are intrinsically related to the bandwidth of the loop. Minimizing the temporal error allows to reduce the apparition of structures in the estimated interaction matrix that can jeopardize the estimation of the mis-registration parameters. The origin of these structures has not been clarified yet. We propose to focus on this point in the next section.

4.3.3.2. Focusing on the structures due to the spatio-temporal correlations

We propose an experiment to better understand the nature of the structures identified in the previous sections. We established that these structures were due to the level of correction of the temporal error that create spatio-temporal correlations between the signal of interest and the disturbance.

To analyze these structures, we apply a ramp of wind in such a way that the point where 2 successive frames are uncorrelated is reached. Once this point is reached, the structures in the interaction matrices should then disappear. This test implies to explore large values of wind speed (up to 8000 m/s for an 8-m telescope and a loop running at 1 kHz!) and the loop will naturally diverge due to the limited bandwidth. For the experiment, we then consider a Fried parameter r_0 of 10 m in the visible to operate in a low aberrations regime so that the sensor remains linear. In terms of control, we consider a simple integrator with a gain of 0.5 and we remove all the sources of noise (both photon noise and read-out noise).

We first provide the WFE as a function of the wind speed in Figure 4.22. This figure shows the different regimes as a function of the wind speed. For the "slow" wind speed, the loop is able to correct most of the turbulence since the temporal error remains small. Then, the temporal error increases such that the loop becomes unstable and we witness the knee of the curve after 0.125 subapertures per frame (50 m/s). After reaching more than 10 subapertures per frame³, we witness a small improvement of the performance that will converge to the value obtained for the point corresponding to 20 subapertures per frame.⁴

The 2D representation of the estimated interaction matrices for each configuration is given in 4.23. These images illustrate the effect of the spatio-temporal correlations in the reconstruction of the interaction matrix. It appears that the structures identified in the matrices correspond to replicas of the signal of a single actuator in the WFS space. Once the phase screens become uncorrelated (speed superior to 20 subapertures per frame, which corresponds to the diameter of the pupil per frame), these effects disappear, as predicted, and we retrieve the correct interaction matrix (bottom right corner). However, for intermediate speeds, the structures are quite complex (especially the case with a wind speed of 5 subapertures per frame). An interesting point is that the location of these structures corresponds to the fraction of the pupil where the signals are still correlated. For instance, the case with 10 subapertures per frames, that corresponds to half of the diameter of the pupil per frame, shows that half of the interaction matrix is well reconstructed while half of it contains structures that should not be there. From these considerations, we understand that if these structures overlap with the signals of interest, they will alter the morphology of the interaction matrix. This will become problematic for the parameters estimation and explain the strong attenuation witnessed in the configurations with high flux and strong wind.

The estimation of the shift X for each situation is given in Figure 4.22. This figure shows that for the "slow" wind, for which the AO loop can still efficiently apply a correction, the estimation follows the tendency identified so far. It exhibits a small

3. which correspond to half of the diameter of the pupil: half of the phase screen is still correlated.

4. which corresponds to a full diameter of the pupil: the phase screens are uncorrelated from one frame to another.

bias in the parameter estimation due to the fact that the temporal error is either under-corrected (negative bias) or over-corrected (positive bias) since the gain is fixed at 0.5 (see Figure 4.20). The estimation of the parameters keeps drifting with the wind speed until it reaches the wind speed of 1 subaperture per frame. After this value, the estimated error starts decreasing until it converges back to 0 for the case where two successive frames are uncorrelated.

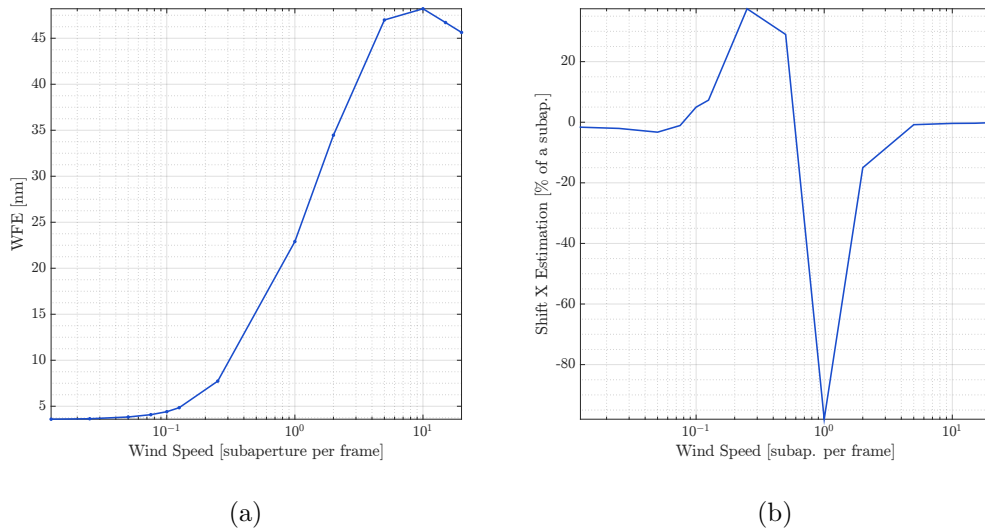


Figure 4.22. – (a) Wave Front Error (WFE) as a function of the wind speed (in subapertures per frames). (b) Shift X Estimation as a function of the wind speed (in subapertures per frames). For this specific case, we do not normalize the parameters estimation with the scaling parameter identified by the algorithm.

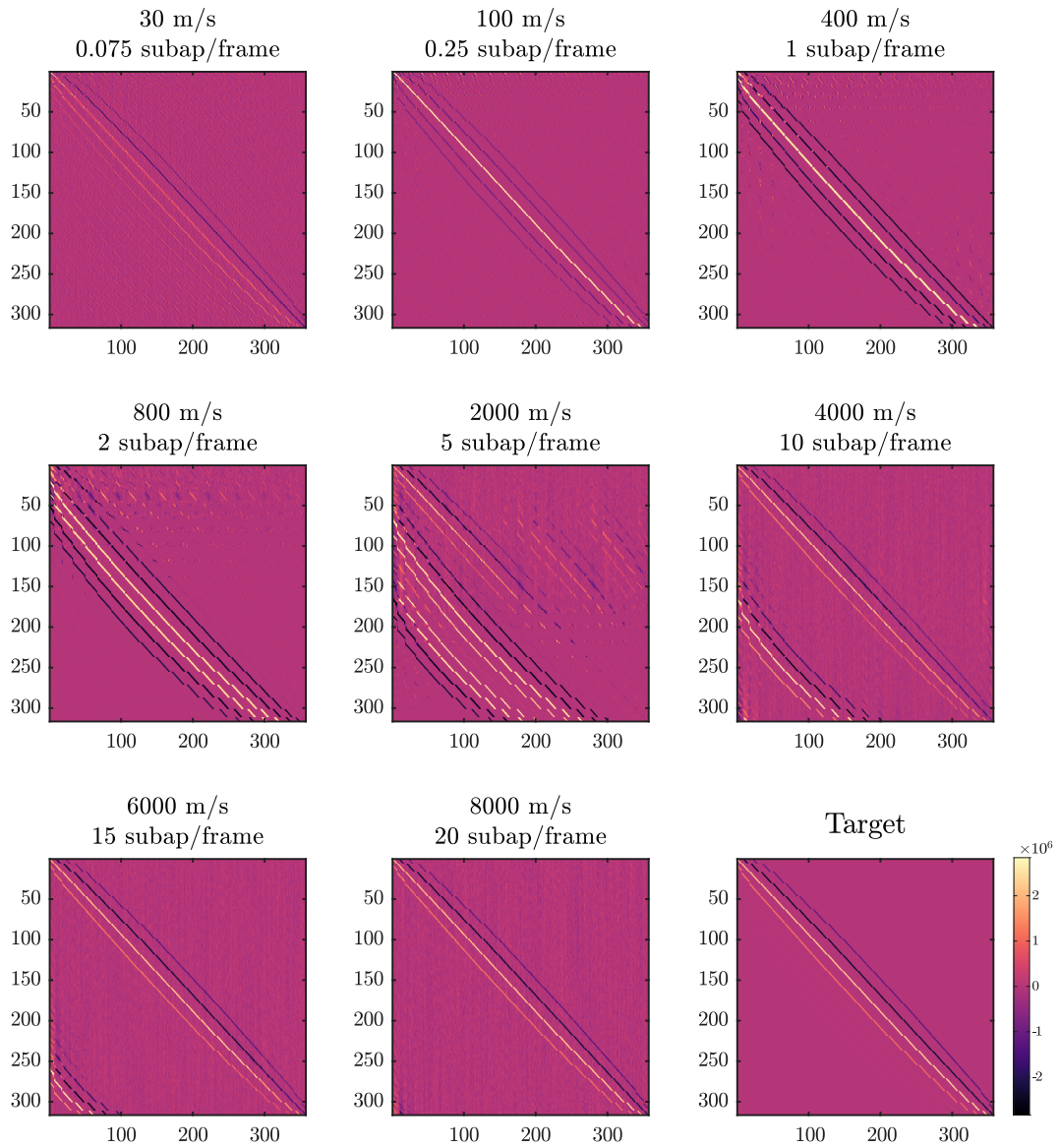


Figure 4.23. – Estimated interaction matrices (slopes X only) for different wind speeds using 20 000 frames.

These last results illustrate the effects of the spatio-temporal correlations in the estimation of the interaction matrix by creating replicas of the actuator signals that will overlap with the signal of interest. As expected when the phase screens become uncorrelated from one frame to another, these perturbing signals disappear and we retrieve the correct interaction matrix.

4.3.4. Ramp of mis-registrations

The previous sections were focused on understanding the underlying physics behind the estimation of the reference signals injected in the identification algorithm. In this section, we present the application of the method by studying the estimation of the mis-registration parameters corresponding to a ramp of mis-registration amplitudes, playing on a single parameter at a time. We consider the limit cases: slow and fast Frozen Flow in the X direction with 3 different levels of noise: low, intermediate

Profile	Direction	Speed	Phot/subap.	Loop Gain
Slow FF - Low Flux	X	5 m.s^{-1}	5	0.1
Slow FF - Intermediate Flux	X	5 m.s^{-1}	100	0.3
Slow FF - High Flux	X	5 m.s^{-1}	500	0.3
Fast FF - Low Flux	X	30 m.s^{-1}	5	0.3
Fast FF - Intermediate Flux	X	30 m.s^{-1}	100	0.6
Fast FF - High Flux	X	30 m.s^{-1}	500	0.6

Table 4.4. – Definition of the different configurations identified to characterize the estimation of the interaction matrix using telemetry data. FF stands for Frozen Flow.

and high flux. For each configuration, we apply the loop gain that minimizes the WFE of the non mis-registered system (see Figure 4.24). We consider 20 000 frames to estimate the interaction matrix to speed up the simulations. A summary of the configuration tested is provided in Table 4.4.

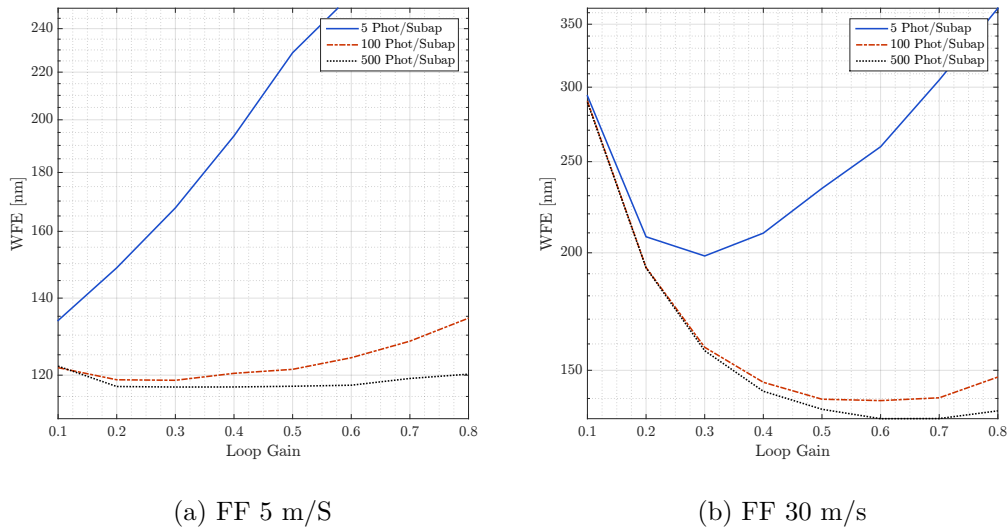
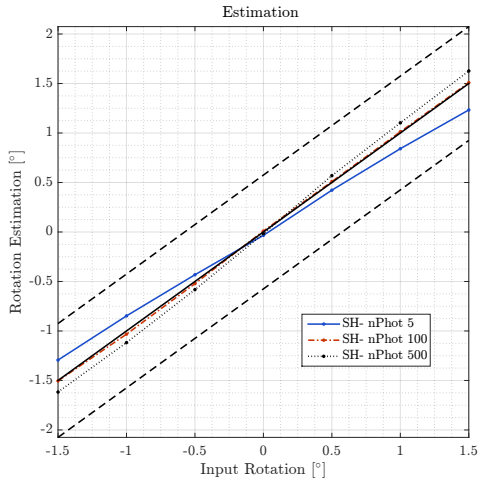


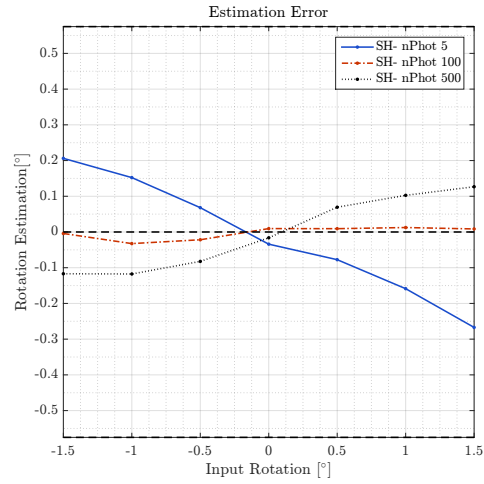
Figure 4.24. – WFE as a function of the loop gain for a slow (a) and fast Frozen Flow (b). We present the results for different levels of flux.

4.3.4.1. Ramp of Rotation

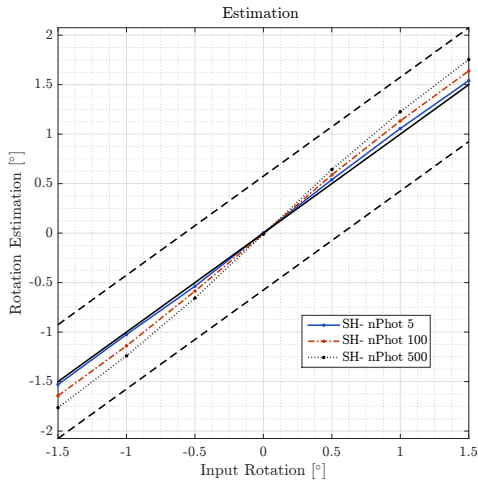
The results corresponding to the rotation are given in Figure 4.25.



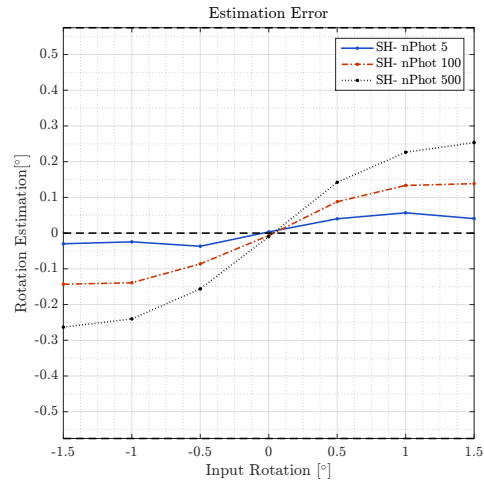
(a) Estimation - FF 5 m/s



(b) Estimation Error - FF 5 m/s



(c) Estimation - FF 30 m/s



(d) Estimation Error - FF 30 m/s

Figure 4.25. – Rotation estimation (left) and corresponding estimation error (right) as a function of the input rotation in $^{\circ}$. The results are given for a wind of 5 m/s (top) and 30 m/s (bottom). The dashed lines are the rotation value that corresponds to a shift of 10% of a subaperture for an actuator located on the border of the pupil.

In these limit cases, the estimation of the rotation is quite accurate with a maximum error of 0.3° for all the situations considered. The best estimation is obtained for the case with high noise regime and strong wind. The estimation tends then to be over-estimated when either the flux gets high (low noise propagation) or when the wind becomes strong (high temporal error) but this remains acceptable. The estimation of the rotation appears not to be biased by the spatio/temporal correlations due to the Frozen Flow as the plots are symmetric with respect to the origin.

4.3.4.2. Ramp of Shift Y

The results corresponding to the shift Y are given in Figure 4.26.

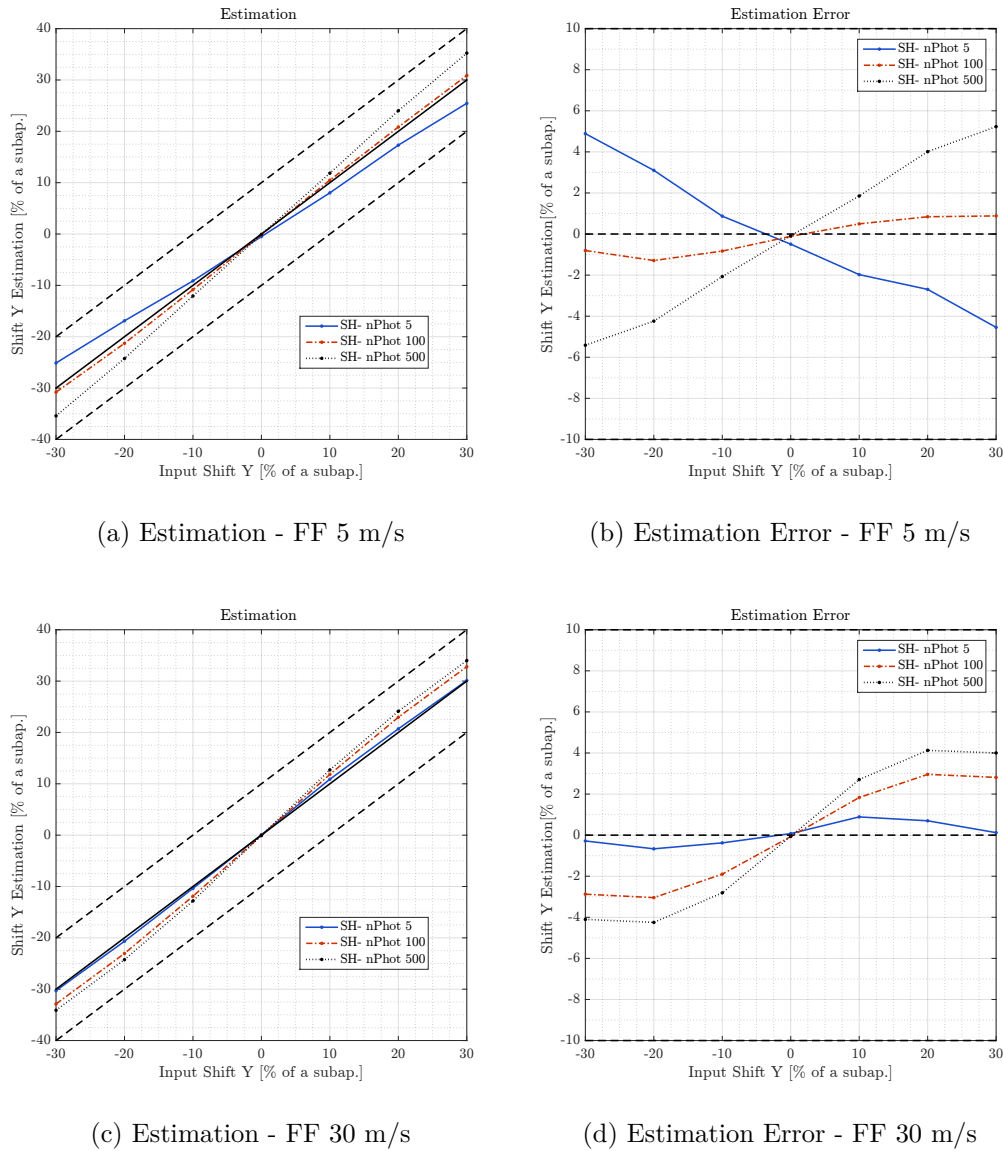


Figure 4.26. – Shift Y estimation (left) and corresponding estimation error (right) as a function of the input shift Y % of a subaperture. The results are given for a slow (top) and fast (bottom) Frozen Flow, corresponding to a wind speed of respectively 5 m/s and 30 m/s.

Similarly to the rotation, the estimation of the shift Y is quite accurate in high noise regime and strong wind. The estimation tends to be over-estimated when either the flux gets high (low noise propagation) or the wind becomes strong (high temporal error). Once again, the estimation of the shift Y is not biased by the spatio/temporal correlations due to the Frozen Flow.

4.3.4.3. Ramp of Shift X

Since the wind is in the X direction, we consider both Frozen Flow and Boiling configurations. The results corresponding to the shift X for the Frozen Flow are given in Figure 4.27 and for the boiling in Figure 4.28

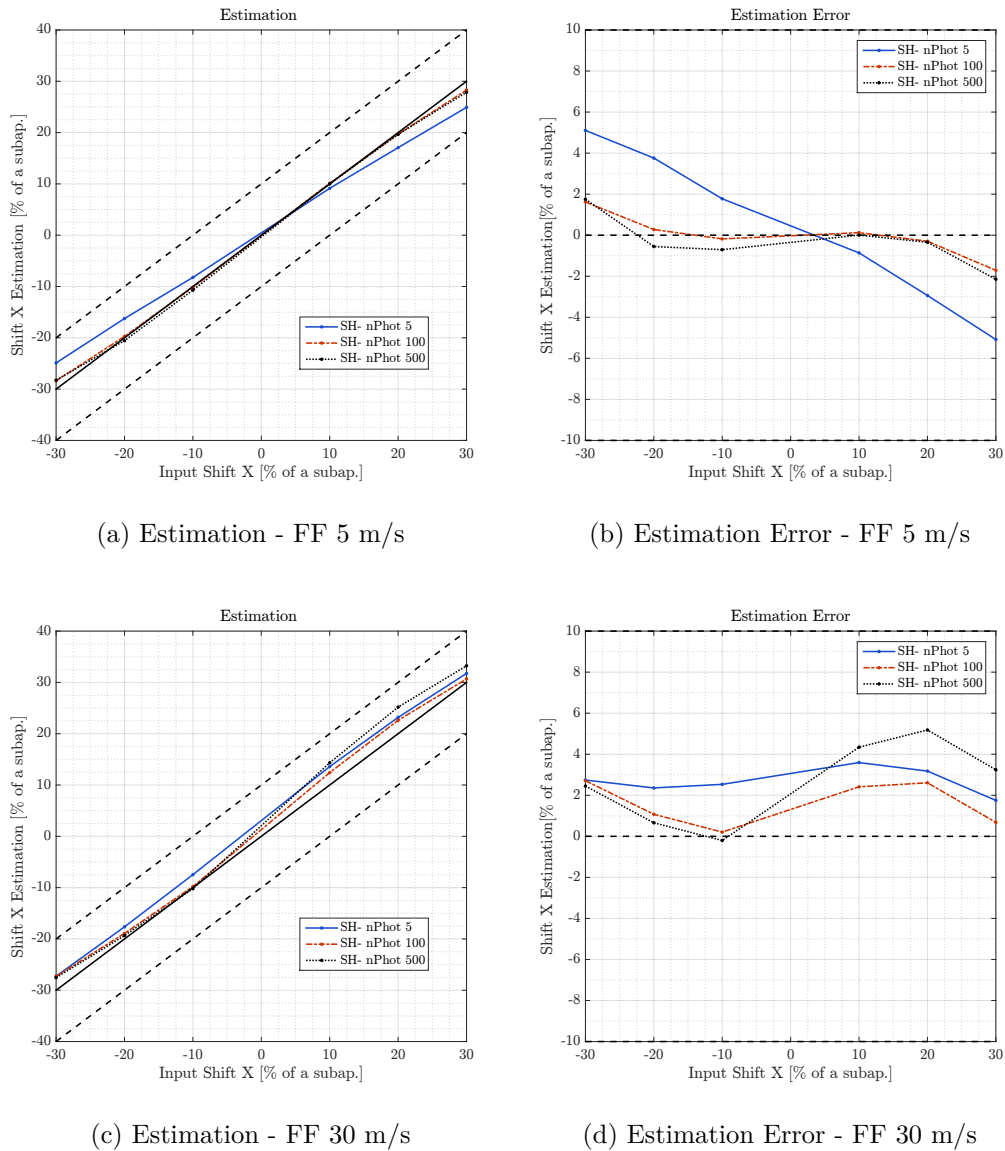
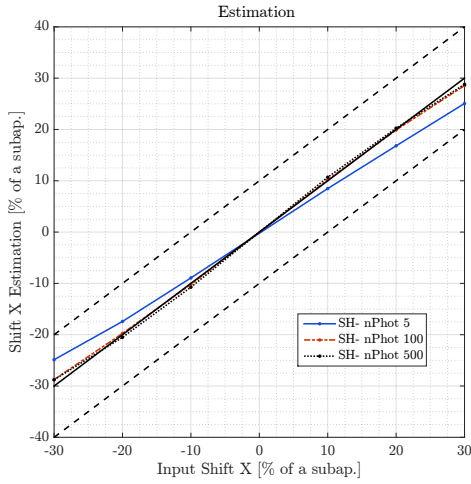
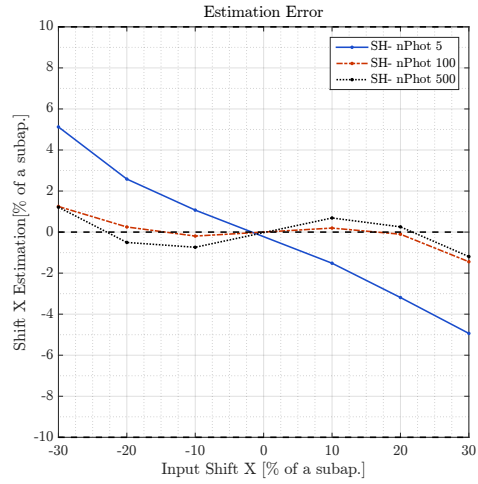


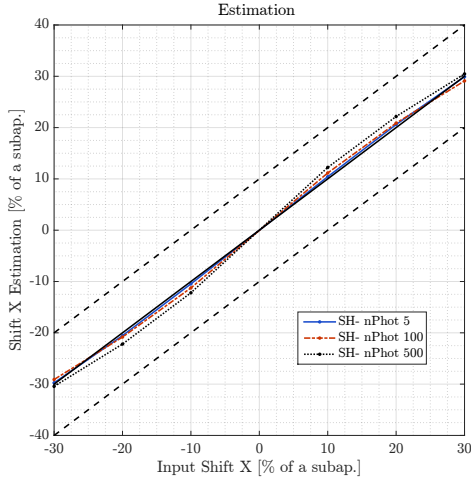
Figure 4.27. – Shift X estimation (left) and corresponding estimation error (right) as a function of the input shift X % of a subaperture. The results are given for a slow (top) and fast (bottom) Frozen Flow, corresponding to a wind speed of respectively 5 m/s and 30 m/s.



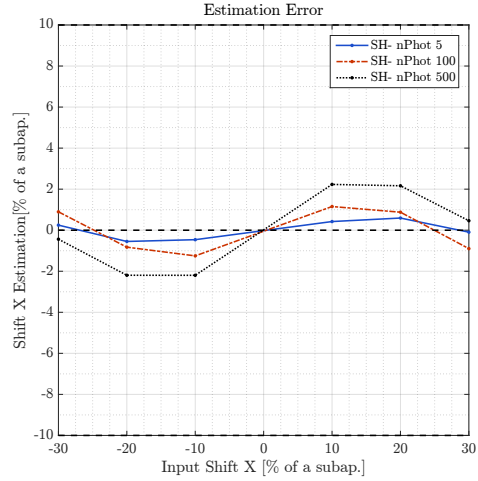
(a) Estimation - Boiling 5 m/s



(b) Estimation Error - Boiling 5 m/s



(c) Estimation - Boiling 30 m/s



(d) Estimation Error - Boiling 30 m/s

Figure 4.28. – Shift X estimation (left) and corresponding estimation error (right) as a function of the input shift X % of a subaperture. The results are given for a slow (top) and fast (bottom) Boiling, corresponding to a wind speed of respectively 5 m/s and 30 m/s.

Concerning the shift X, we really witness the bias on the estimation due to the spatio/temporal correlations, especially in the case of the strong wind in a Frozen Flow configuration (Figure 4.27). As expected, this effect disappears for a boiling configuration (Figure 4.28) and the accuracy of the estimation is improved. Overall, even when considering these extreme cases, the estimation of the parameters remains satisfying with a maximum error of 6% of a subaperture for the shifts and 0.3° for the rotation. The case with low flux and slow wind is the only one that tends to under-estimate the parameters. This situation corresponds to a case where the loop gain was equal to 0.1. For this specific case, it might be required to average longer than 20 000 frames to converge to a better estimation of the interaction matrix.

As a partial conclusion, we have shown that the results provided with the numerical simulations are in agreement with what we expected from the analysis of the composition of the signals. The method will provide a good estimation of the mis-registration parameters when the noise is dominating in the disturbance δz_k and will be impacted by the spatio-temporal correlations when it is dominated by the temporal error, in a Frozen Flow configuration with high flux for instance. We will now study the other hypothesis related to the WFE being perfect and consider the application with a PWFS.

4.4. Application with the Pyramid WFS

The equations presented in section 4 are independent from the type of WFS but rely on the hypothesis of a perfect WFS and on the independence between the interesting commands δc_k and disturbance δz_k . In the previous section, we demonstrated that the non validity of this last point could lead to the apparition of structures in the interaction matrix reconstruction that can bias the estimation of the parameters. In this section we propose to consider the case of the PWFS to challenge the hypothesis of perfect WFS with the specificities of the sensor (non linearities and optical gains).

We consider a system with the same dimensions as in section 3.1: a 20 by 20 subaperture Pyramid WFS modulated at $3 \lambda/D$ and operating in I band at 850 nm. The properties of the system considered are summarized in Table 4.5.

Turbulence	$r_0(V)$	15 cm	PWFS	Subapertures	20×20
	L_0	30 cm		Modulation	3 λ/D
Control	Cn^2 profile	1-2 layers	RON	none	
	Windspeed	5-30 m/s	Photon Noise	On	
	Frequency	1 kHz	Photons/subap.	5-500	
	Delay	2 Frames	Signal Processing	Global ⁵	
	Integrator	$g=0.5$	DM	Actuator	357
	Bandwidth	75 Hz		Inf. Functions	Gaussian
NGS	Int. Matrix	300 KL	Coupling	35%	
	OG control	Yes ⁶	Telescope	Diameter	8 m
	Wavelength	850 nm		Obstruction	None
Magnitude	7.5-13.5	Resolution		160 px	

Table 4.5. – Numerical Simulations parameters for the section 4.4

Similarly to the analysis presented for the SH-WFS we propose to consider first a nominal case of application (see 4.4.1), with normal conditions of wind. In a second step we will present the impact of strong spatio-temporal correlations considering the more extreme conditions of wind and noise levels investigated in the previous section (see 4.4.3). The simulations presented are achieved by applying a compensation of the optical gains of the PWFS. The method applied to compensate the PWFS gains is based on a convolutionnal model of the PWFS (Fauvarque et al. 2019) to estimate the modal gains from the residual phase (Chambouleyron et al. [in prep](#)) as introduced in chapter 3.

5. see section 1.3.2

6. Chambouleyron et al. [in prep](#)

4.4.1. Nominal Case

In this nominal case, we consider an integrator with a loop gain of 0.5 and we apply a compensation of the optical gains. The atmosphere is simulated using a Frozen Flow with a wind of 10 m/s and we average 20 000 frames to reconstruct the interaction matrix. The results are presented in the Figures 4.29, 4.30 and 4.31.

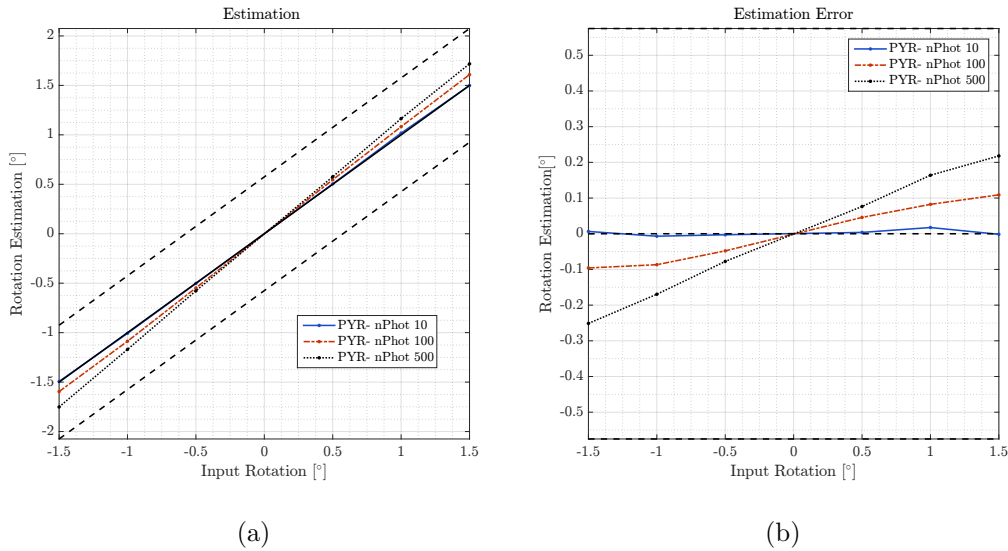


Figure 4.29. – Estimation (a) and corresponding error (b) corresponding to a ramp of rotation using a PWFS in a Frozen Flow configuration with a wind speed of 10 m/s in the X direction.

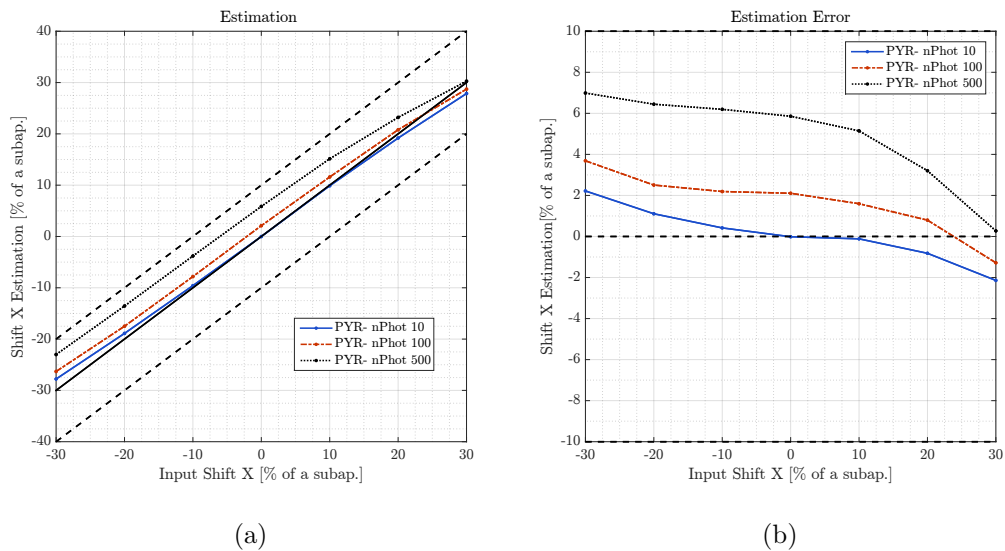


Figure 4.30. – Estimation (a) and corresponding error (b) corresponding to a ramp of shift X using a PWFS in a Frozen Flow configuration with a wind speed of 10 m/s in the X direction.

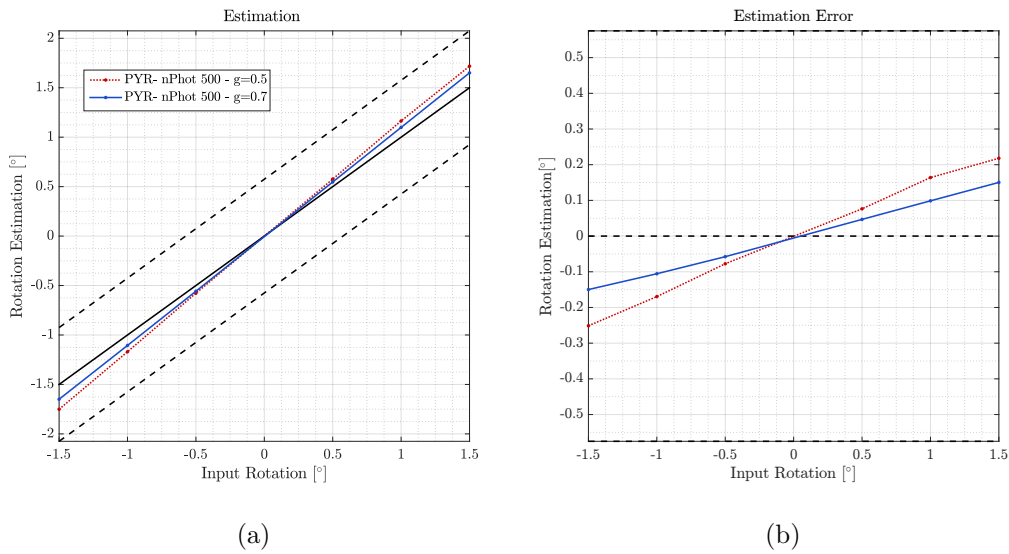


Figure 4.32. – Estimation (a) and corresponding error (b) corresponding to a ramp of rotation using a PWFS in a Frozen Flow configuration with a wind speed of 10 m/s in the X direction. The results are given for a high flux (500 photons per subaperture) and a loop gain of 0.5 and 0.7.

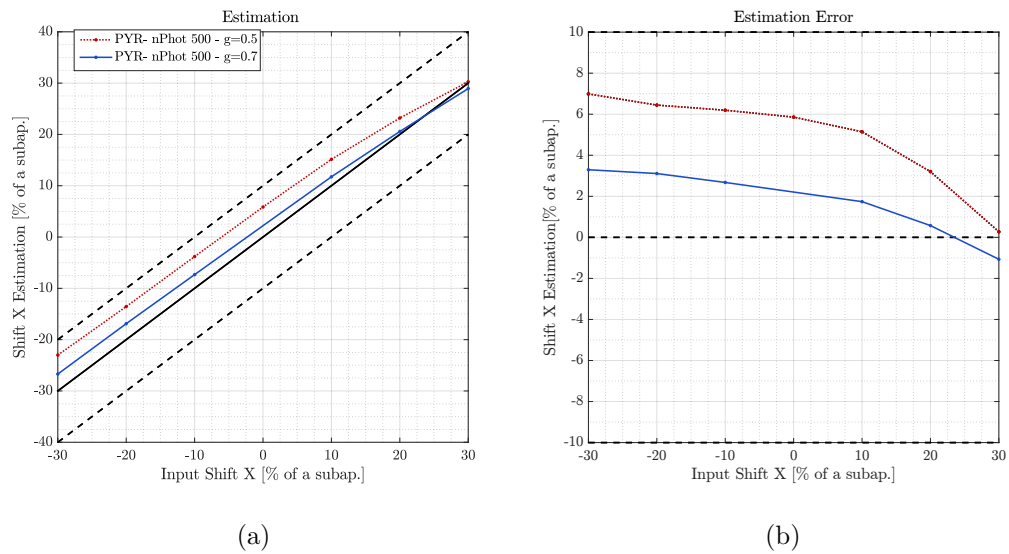


Figure 4.33. – Estimation (a) and corresponding error (b) corresponding to a ramp of shift X using a PWFS in a Frozen Flow configuration with a wind speed of 10 m/s in the X direction. The results are given for a high flux (500 photons per subaperture) and a loop gain of 0.5 and 0.7.

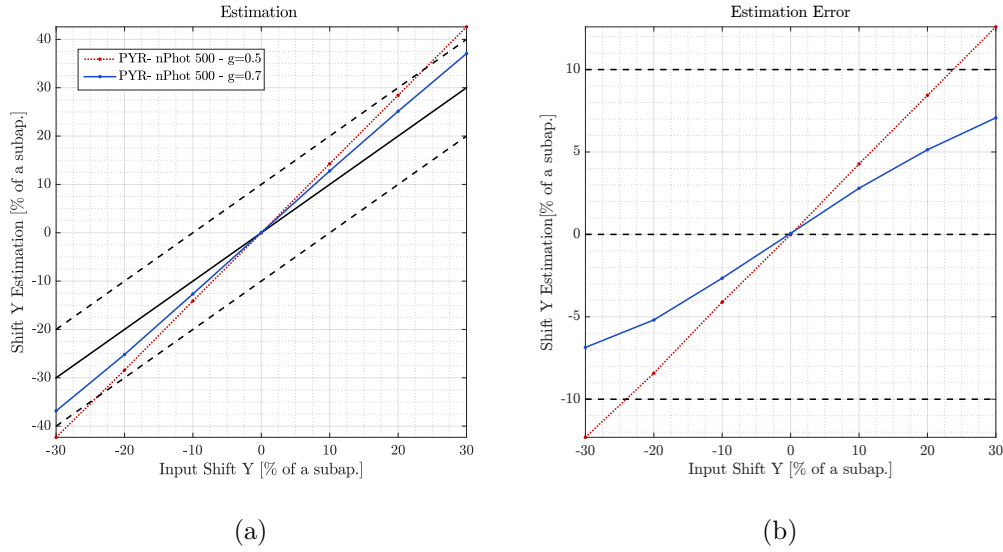
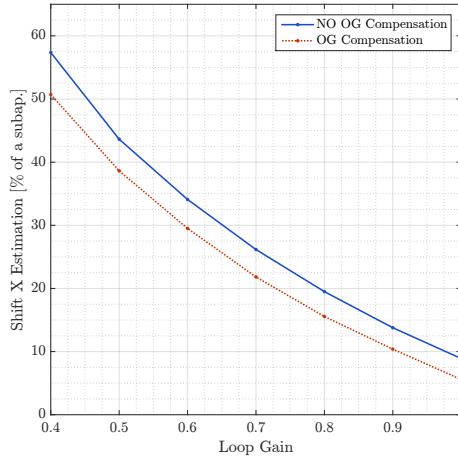


Figure 4.34. – Estimation (a) and corresponding error (b) corresponding to a ramp of shift Y using a PWFS in a Frozen Flow configuration with a wind speed of 10 m/s in the X direction. The results are given for a high flux (500 photons per subaperture) and a loop gain of 0.5 and 0.7.

This is once again in line with the observations made with the SH-WFS: by reducing the contribution of the temporal error, the bias due to the spatio-temporal correlations between $\phi_{k-2}^{res\ temporal}$ and the $\delta\phi_k^{res}$ is reduced and we notice that the estimation of the other parameters is also improved. However, the bias on the shift parameter is higher than for a SH-WFS under the same observing conditions. It appears then that estimating the interaction matrix from the telemetry data with a PWFS will be more complex than with a SH-WFS in high flux configuration.

4.4.2. Impact of the loop gain

We now consider the extreme case of strong wind with high flux for a centered system and we investigate the bias on the estimation of the shift X, as a function of the loop gain similarly to what was done for the SH-WFS (see 4.3.3.1). However, in the case of the PWFS, we also consider the impact of the optical gains compensation. Figure 4.35 displays the results corresponding to the shift X estimation for various loop gains, with and without optical gains compensation.



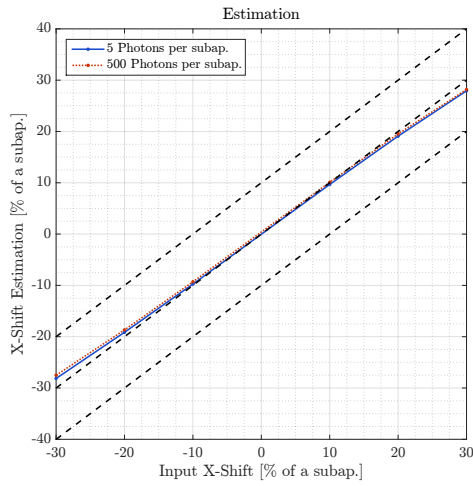
(a)

Figure 4.35. – Estimation Error of the shift X corresponding to a non mis-registered case with Frozen Flow in the X direction and wind speed of 30 m/s. The cases with gain higher than 1 were diverging.

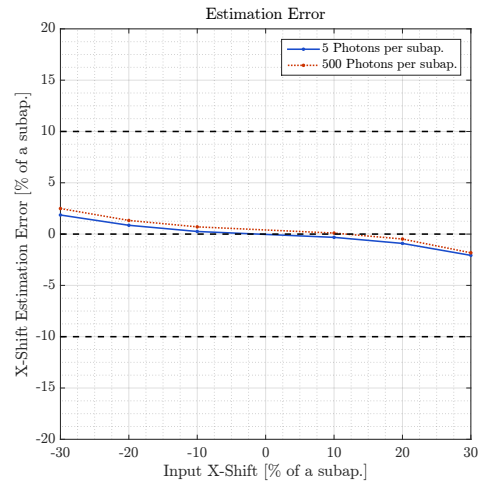
This figure shows that compensating the optical gains allows to reduce the impact of the bias due to the shifts. This corresponds in fact to getting closer to the hypothesis of a perfect WFS. However, the loop gain appears to be more crucial to reduce the effect of the spatio temporal/correlations in the estimation of the interaction matrix. In this extreme case (high flux and strong wind), it appears that contrarily to the SH-WFS the bias due to the spatio temporal correlations remains quite high and is reduced to 5% of a subaperture in the best case ($g=1$ with optical gains compensation). A possible explanation for this result is that the noise propagation for a PWFS is smaller than for a SH-WFS. The resulting contribution of the noise in the composition of the δc_k remains smaller with respect to $\phi_{k-2}^{res\ temporal}$. The PWFS appears to be more sensitive to the effects of the spatio-temporal correlations between $\phi_{k-2}^{res\ temporal}$ and $\delta\phi_k^{res}$.

4.4.3. Limit cases

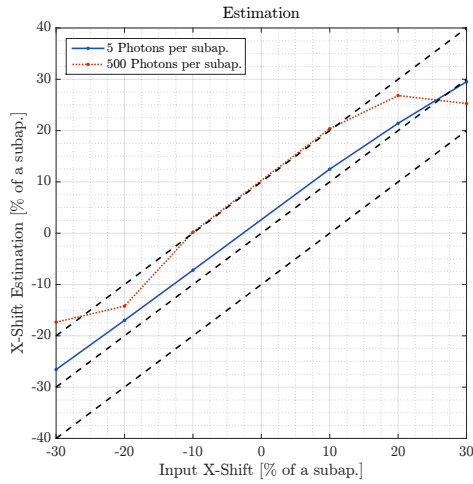
In this section we consider the limit cases considered with the SH-WFS with a slow wind of 5 m/s and 30 m/s respectively in a low and high noise regime. The estimation of the shift X in a Frozen Flow configuration is given in 4.36. These results are consistent with the trend identified with a SH-WFS: the high noise regime appears to be poorly sensitive to the wind speed while the low noise regime exhibits an important bias especially in a strong wind configuration.



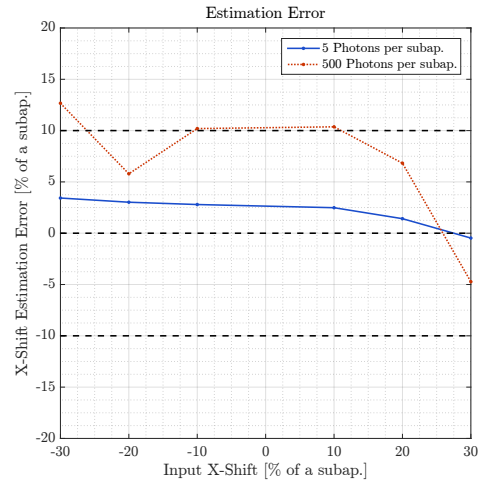
(a) Frozen Flow 5 m/s



(b) Frozen Flow 5 m/s



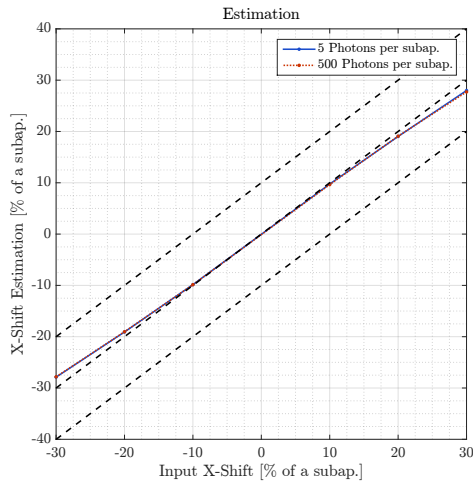
(c) Frozen Flow 30 m/s



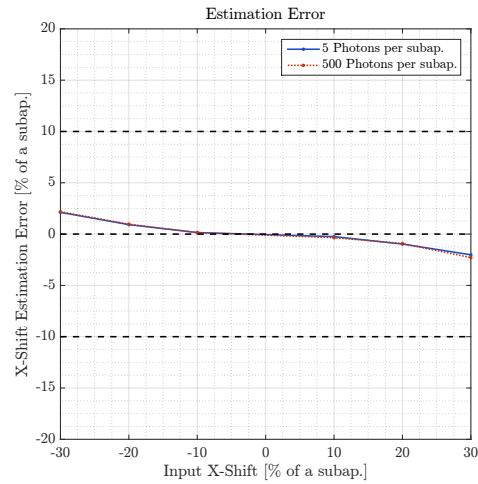
(d) Frozen Flow 30 m/s

Figure 4.36. – Estimation (a) and corresponding error (b) corresponding to a ramp of shift X using a PWFS in a Frozen Flow configuration with a wind speed of 5 and 30 m/s in the X direction. The results are given for a high flux (500 photons per subaperture) and a loop gain of 0.3 and 0.7 with compensation of the OG.

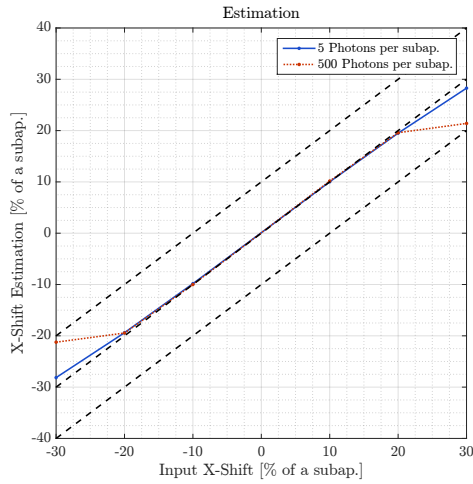
The estimation of the shift X in a Boiling configuration is given in 4.37 and shows that the bias disappears in the estimation of the parameter, as a consequence of the compensation of the structures due to the opposite wind directions (see Figure 4.15)



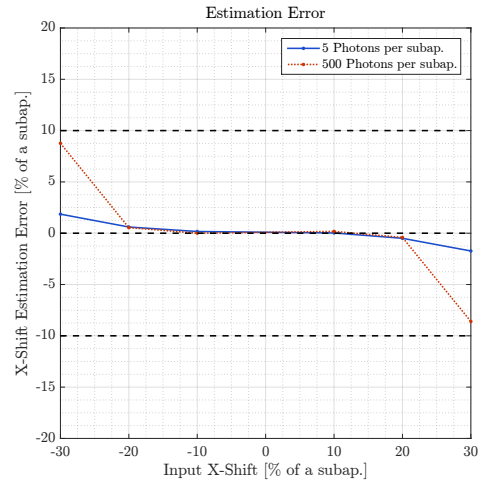
(a) Boiling 5 m/s



(b) Boiling 5 m/s



(c) Boiling 30 m/s



(d) Boiling 30 m/s

Figure 4.37. – Estimation (a) and corresponding error (b) corresponding to a ramp of shift X using a PWFS in a Boiling configuration with a wind speed of 5 and 30 m/s in the X direction. The results are given for a high flux (500 photons per subaperture) and a loop gain of 0.3 and 0.7 with compensation of the OG.

Overall, the results presented in the case of a Pyramid WFS are in agreement with the behavior identified with the SH-WFS. In the case of the PWFS, the hypothesis of a perfect WFS is also challenged and contributes to reducing the accuracy of the estimation of the parameters. By linearizing the PWFS using a compensation of its optical gains, we manage to slightly improve the accuracy of the algorithm. However the most critical factor to accurately identify the parameters remains related to the minimization of the temporal error. The domain of validity of the method appears then to be smaller working with a PWFS than with a SH-WFS especially in high flux conditions which is the typical operating point of PWFS AO systems.

4.5. Discussion

This section has presented numerous results, exploring the limits of the observing conditions. It is important to keep in mind that we considered **the worst cases of application**, as a pure Frozen Flow with one layer and a constant wind speed in time and direction remains quite unrealistic. Similarly, a wind-speed of 30 m/s would more likely force the telescope to close the dome (typically, at the VLT, this limit is fixed at 18 m/s). However, by considering these extreme cases we were able to identify the limitations of the method and to understand the physics behind the estimation of the parameters.

Table 4.6 gives a summary of the accuracy achieved with the method for the different observing conditions in the case of a Frozen Flow, working with a SH-WFS. The estimation of the parameters corresponds to a realistic case in the sense that the gains of the loop are optimized to maximize the AO performance and not the mis-registration parameters identification.

We define a high accuracy **HA** when the parameter estimation error is lower than 5% of a subaperture for a shift and lower than 0.28° in the case of a rotation. We define a good accuracy **GA** when the parameter estimation error is lower than 10% of a subaperture for a shift and lower than 0.56° in the case of a rotation. We define a low accuracy **LA** when the parameter estimation error is higher than 10% of a subaperture for a shift and higher than 0.56° in the case of a rotation.

	Slow wind	Intermediate wind	Strong wind
Low Flux	HA	HA	HA
Intermediate Flux	HA	HA	GA
High Flux	HA	GA	GA

Table 4.6. – Summary of the accuracy of the estimated mis-registration parameters in a Frozen Flow configuration with SH-WFS.

Similarly, Table 4.7 gives a summary of the accuracy achieved in the case of a Frozen Flow, working with a Pyramid WFS.

	Slow wind	Intermediate wind	Strong wind
Low Flux	HA	HA	HA
Intermediate Flux	HA	HA	LA
High Flux	GA	GA	LA

Table 4.7. – Summary of the accuracy of the estimated mis-registration parameters in a Frozen Flow configuration with Pyramid WFS.

The summaries of the accuracy achieved in the case of a Boiling atmosphere are given in Table 4.8 for a SH-WFS and in Table 4.9 for a PWFS. The intermediate levels of noise and wind speeds were not investigated for the Boiling configuration.

	Slow wind	Strong wind
Low Flux	HA	HA
High Flux	HA	HA

Table 4.8. – Summary of the accuracy of the estimated mis-registration parameters in a Boiling configuration with SH-WFS.

	Slow wind	Strong wind
Low Flux	HA	HA
High Flux	HA	GA

Table 4.9. – Summary of the accuracy of the estimated mis-registration parameters in a Boiling configuration with Pyramid WFS.

Depending on the observing conditions and accuracy requirements, this method will thus be suited to provide an online tracking of the parameters. To be optimal in terms of accuracy, it requires to minimize the temporal error of the system by adjusting the gains of the loop. However, these gains have to be optimized with respect to the whole error budget and might not always be optimal for the mis-registration identification.

This section was focused on analyzing the method that is currently the baseline for the AO instruments of the AOF: tracking the mis-registration parameters using only closed loop data, without adding any disturbance to the loop. This method is particularly attractive since it offers a way to auto-calibrate the AO loop during the operations. We presented a thorough analysis of the method to understand the validity of its hypothesis and the physics that underpin the estimation of the interaction matrix. We established that the signals of interest used to estimate the interaction matrix are composed of three main terms corresponding to the temporal error, the noise propagation in the AO loop and the calibration errors.

When the temporal error is dominating, we put in evidence the strong spatio-temporal correlations between the signal of interest and the disturbance. The signature of these correlations in the estimated interaction matrices takes the form of replicas of the signal of an actuator. This signal appears to be located at a different position in the pupil depending on the wind speed and direction. In the situation where these undesired signals overlap with the signals of interest, they impact the estimation of the mis-registration parameters by creating structures in the estimated interaction matrix. The presence of such structures in the interaction matrix creates a bias on the estimation of the shift corresponding to the wind direction. In addition, these structures appear to create a differentiated scaling for the interaction matrix signals depending on the wind speed and direction.

We have demonstrated that the amplitude of these structures depends on the level of correction of the temporal error and thus on the value of the loop gain. By minimizing the temporal error, the impact on the parameter estimation can be reduced.

In addition, we generalized this calibration strategy to the case of the Pyramid WFS. We retrieved the behaviors identified with the SH-WFS. The PWFS appears to be more sensitive to the effects of the spatio-temporal correlations. To reduce these effects, we put in evidence the necessity to optimize both the optical gains of the PWFS and the AO loop gain with respect to the temporal error.

Conclusion and Perspectives

Conclusion

The first part of this manuscript presented the context of my research: the Large Adaptive Telescopes. I introduced the principle of adaptive optics, showing how the key components of an AO system interact with each other through the interaction matrix of the system. In particular, I have focused on the specificities of the Pyramid WFS to present the operational complexity of this sensor. In terms of operation, I highlighted the necessity to maintain an accurate AO calibration during the scientific observations, illustrating the dramatic impact of the mis-registrations on the scientific path. This point will be particularly critical for the future and existing Large Adaptive Telescopes as the unprecedented distance between DM and WFS may lead to frequent evolution of the mis-registrations. To overcome this technical challenge, we propose to consider a pseudo synthetic calibration where the interaction matrix is generated in a synthetic model that requires experimental inputs to tune the mis-registration parameters of the model. This approach has the advantage of providing noise-free interaction matrices that require only a few parameters to be updated. The feasibility of such methods, coupled with the complexity of the pyramid WFS defined the research question addressed in this thesis.

The second chapter was dedicated to the development of a pseudo synthetic model for the LBT AO system FLAO. The work was focused on the modelling of the three key-elements of the AO system, (i) the Adaptive Secondary Mirror, (ii) the Pyramid WFS and (iii) the modeling of the mis-registrations in the simulator. Two different strategies have been presented to identify the mis-registrations from experimental data. The first one is based on the minimization of the quadratic norm between experimental and synthetic signals, optimizing a single parameter at a time. The second one is based on the projection of an experimental interaction matrix on a set of sensitivity matrices which allows to get an estimation of all the parameters at the same time. The development of the model included a sensitivity analysis to the mis-registrations to identify the accuracy required for the identification of the parameters. I presented the extensive numerical validation achieved in the simulator that allowed to proceed to the experimental validation of the model. At the LBT, the synthetic reconstructor provided a slightly better AO performance than an experimental interaction matrix measured at the telescope with fiber. This last option is the baseline for AO-assisted operations at the LBT. This demonstrated the high accuracy of the model. As a complement, I developed a second model using synthetic influence functions for the DM model instead of experimental ones. This provides a higher flexibility for the modelling of the mis-registrations and speeds up the mis-registrations identification procedures. The experimental validation of this second model remains however to be investigated.

To tune the parameters of the model, I had access to a high SNR interaction matrix measured at telescope. This will not be the case for the future large adaptive telescopes. The scope of chapter 3 was then to investigate a first procedure to provide an online tracking of the mis-registrations parameters. This can be achieved by applying well selected signals on the DM during the operations and retrieving their signatures in the WFS signals to extract the corresponding mis-registration parameters. This strategy appears to be robust to the different observing conditions. To optimize the method and minimize the impact on science, I demonstrated that by using a Principal Component Analysis (PCA), we could identify the most sensitive modes to a given mis-registration. Using a combination of a few of these PCA modes, I could provide an accurate tracking of the parameters even when the parameters were evolving dynamically during the operations. This demonstrated that a whole interaction matrix is not required to estimate accurately the mis-registration parameters. This is consistent with the fact that we could control up to 500 modes at the LBT using the synthetic reconstructor while the experimental interaction matrix used to tune the model contained only 400 modes. However, the impact on the scientific path of this invasive approach must be carefully evaluated. The choice of the signals selected to identify the mis-registrations must result of a trade-off that is system-dependent: typically by defining the accuracy required, the spatial and temporal characteristics of the perturbation allowed on the scientific path and the time allocated for the acquisition of the signals.

In chapter 4, I presented an alternative strategy that is based on the estimation of a noisy interaction matrix using telemetry data to extract the mis-registration parameters. I carried out a thorough analysis of the underlying physics behind the reconstruction of the interaction matrix. This allowed me to understand the composition of the signals of interest and predict the domain of validity and limitations of the method. Challenging the validity of the hypothesis defining different types of observing conditions, I could retrieve the expected trend in the estimation of the parameters. In particular, the estimation of the parameters appears to be jeopardized when the loop is dominated by a high temporal error. In this situation, spatio-temporal correlations between signal of interest and disturbance on the measurement impact the reconstruction of the noisy interaction matrix. The effect takes the form of replicas of actuators signals in the interaction matrix. When these structures overlap with the signals of interest, they bias the estimation of the parameters and lower the accuracy of the estimation. When the composition of the signals is dominated by an uncorrelated noise, the reconstruction of the interaction becomes unbiased and the estimation of the mis-registration parameters is improved. Finally, the application of the method with a Pyramid WFS exhibits the same trends but since the PWFS is impacted by its non-linearities, it appears to be more sensitive to the effects of spatio-temporal correlations. To reduce the impact, we put in evidence the necessity to optimize both optical gains of the PWFS and loop gain of the loop with respect to the temporal error.

Perspectives

Regarding the first part of the work presented in chapter 2, in terms of perspective, an interesting feature that would improve the accuracy of a synthetic model would be to consider a hybrid model for the influence functions of the DM, fitting mathematical functions to reproduce experimental measurements of the influence functions. The flexibility provided by a set of synthetic influence functions appears indeed to optimize the modelling of the mis-registrations and speed-up the identification procedures. A comparison of performance considering the three types of DM modelling strategies (measured, synthetic and hybrid influence functions) would allow to optimize the future modelling of the AO systems of the future large adaptive telescopes, especially in terms of tuning of the model. In addition, having models that take in consideration the ageing of the DM influence functions would allow to optimize the accuracy of the model.

Further, we could consider the addition of other types of mis-registrations in the model (typically the distortions or more complex transformations) to provide a more thorough modelling of the behavior of the real system. Considering the architecture of the identification algorithm, this would require only to model these transformations in the simulator and to generate the corresponding sensitivity matrices. However, if these different transformations exhibit large couplings with the other parameters, some research may be needed to orthogonalize the different sensitivity matrices.

In terms of tracking of the parameters during the operation, the main perspective would be to experimentally validate both invasive (chapter 3) and non invasive methods (chapter 4) presented in this manuscript. The purpose of these experimental validations would be to reproduce the trend identified in the simulator.

The most attractive strategy presented in this manuscript is the non-invasive approach since it has no impact on the scientific path. From the thorough analysis of the method, I identified potential improvements of the method. We could for instance add priors to the computation of the interaction matrix retrieved from the telemetry data. This would allow to take in consideration the spatio-temporal correlations that jeopardize the estimation of the matrix and thus the estimation of the mis-registration parameters to make it more robust to the different observing conditions. Some research to optimize the post-processing of the interaction matrices retrieved using closed-loop data could also improve the accuracy of the parameters estimation. Other algorithms could also be developed that do not require the intermediate step of estimating the interaction matrix.

Within the framework of my PhD, my research was focused on the mis-registration tracking with a pseudo-synthetic model in the case of the PWFS. This issue depends mostly on the geometry and the linearity of the AO system (number and size of the subapertures of the WFS, DM geometry). Taking the case of the ELT, an interesting perspective would be to add other effects that could be instruments or telescope-related (PWFS optical gains tracking and compensation, wind-shake, fragmentation effect, phasing residuals, Non Common Path Aberrations). Some of these issues are currently being actively investigated for the ELT-AO instruments and different strategies have already been identified to master these operational challenges. The

coupling of all these different effects will have to be evaluated and a thorough understanding of wave-front reconstruction with PWFS will be required to achieve an optimized system identification strategy. This will provide a realistic estimation of the AO performance of the future Large Adaptive Telescope and identify the validity and potential limitations of these methods. Such developments will also benefit the scientific instruments as it will have to be integrated in a performance prediction tool to optimize the scientific return of the future Large Adaptive Telescopes.

6. Résumé Long

6.1. Introduction et Contexte

L'observation d'objets astronomiques depuis le sol fait face à un défi majeur: les aberrations optiques introduites par la turbulence atmosphérique. Ce phénomène affecte grandement la qualité des observations et nécessite d'équiper les télescopes terrestres de systèmes d'Optique Adaptative (OA) pour corriger les aberrations de front d'onde en temps réel et retrouver ainsi la résolution spatiale du télescope.

6.1.1. L'Optique Adaptative

6.1.1.1. Principe

Un système d'OA se compose de 3 éléments principaux: un Analyseur de Surface d'Onde (ASO) qui mesure des signaux reliés à la phase incidente, un ordinateur à temps réel (RTC en anglais) qui calcule les commandes correspondantes à appliquer sur l'élément correcteur de la boucle: un miroir déformable (DM en anglais). Un schéma d'un système d'Optique Adaptative est donné dans la section 1.2.1. Dans la majeure partie des cas, un système d'OA est utilisée en boucle de rétro-action à une fréquence au moins dix fois plus haute que la fréquence d'évolution typique de la turbulence (typiquement 1 kHz). Cette technologie est maintenant largement diffusée sur les télescopes grands champs et sera indispensable pour les instruments des futurs télescopes géants (ELT en anglais) dont les diamètres atteindront 39 m. Cependant, pour déterminer quelle surface appliquer sur le DM en fonction d'une mesure donnée de l'ASO, la boucle d'OA doit être parfaitement étalonnée avant les opérations.

6.1.1.2. Étalonnage d'un système d'OA

L'étalonnage d'un système d'OA consiste à étalonner comment la déformation du miroir obtenue en activant chaque actionneur¹ est vue dans l'espace de l'ASO. Cette information est stockée dans une matrice d'interaction D :

$$D = M_{WFS} \cdot M_{DM} \quad (6.1)$$

où M_{WFS} représente le modèle de mesure de l'ASO et M_{DM} les déformations du DM (les fonctions d'influences du miroir). Cette **matrice d'interaction** est ensuite inversée pour calculer le **reconstructeur** R du système qui est injecté dans le RTC pour calculer les commandes à appliquer sur le DM en fonction des mesures de l'ASO.

1. On appelle cette déformation la fonction d'influence de l'actionneur.

Si la relation opto-géométrique du système DM-ASO évolue durant les opérations², la matrice d'interaction n'est plus représentative de l'état de l'alignement du système. On parle de *mis-registration* en anglais. En présence de telles *mis-registrations*, dans le meilleur des cas les performances du système d'OA sont impactées et dans le pire des cas, la boucle devient instable. Cet effet est illustré Figure 6.1a qui donne les performances d'un système d'OA en fonction d'une translation du DM vis à vis de l'ASO. On peut modéliser ces *mis-registrations* grâce à un vecteur de paramètres α qui décrit les transformations relatives entre DM et ASO. On peut donc ré-écrire l'équation 6.1 en faisant apparaître la dépendance en α :

$$D_{\alpha} = M_{\text{WFS}} \cdot M_{\text{DM}_{\alpha}} \quad (6.2)$$

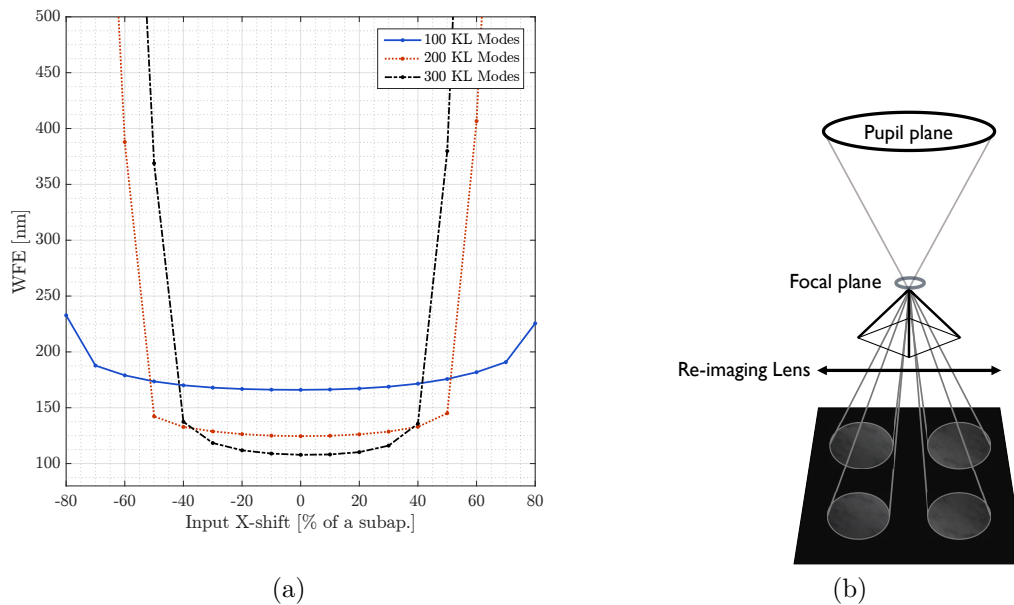


Figure 6.1. – **a)** Impact d'une translation sur les performances de l'OA (WFE = Erreur de Front d'Onde) pour différent nombre de modes KL contrôlés dans le reconstruteur. **b)** Schéma représentatif de l'ASO Pyramide.

La Figure 6.1a indique qu'il est nécessaire de maintenir une haute précision de l'étalonnage du système d'OA pour assurer le bon déroulement des observations scientifiques. Une règle bien connue est de maintenir cette précision en dessous d'une translation de 10% d'une sous-ouverture (Dessenne 1998) mais ce résultat dépend du nombre et type de modes contrôlés dans le reconstruteur.

2. Translation, rotation, grossissement ou autre anamorphoses plus complexes.

6.1.2. Le contexte des futurs grands télescopes adaptatifs

Les futurs ELT seront des télescopes adaptatifs³. L'échelle et la complexité de ces géants imposeront de nouvelles contraintes en terme d'étalonnage qui n'ont jamais été traitées auparavant. Tout d'abord, la question se pose sur la durée nécessaire pour étalonner un système équipé d'un DM de 5000 actionneurs, vraisemblablement sans source d'étalonnage externe. Plus critique encore, durant les observations, la grande distance séparant le DM et les instruments pourra affecter régulièrement la relation opto-géométrique entre le DM et l'ASO (sous l'effet de la gravité), impactant ainsi les performances de correction. Il faudra alors compenser ces erreurs d'étalonnages pendant les observations tout en minimisant l'impact sur ces dernières.

D'autre part, tous les instruments de première lumière de l'ELT ont prévu d'utiliser un ASO de type Pyramide pour leur mode à une seule étoile guide. Un schéma représentatif de ce type d'analyseur est donné Figure 6.1b. Cet ASO permet de gagner en sensibilité (par rapport à l'ASO de type Shack-Hartmann) au prix d'une plus grande complexité opérationnelle. L'ASO Pyramide a en effet la particularité d'avoir des gains optiques: une sensibilité modale qui dépend de la phase résiduelle vue par l'ASO (et donc du niveau de correction de l'OA, du seeing ou bien des erreurs d'étalonnage). Il devient donc crucial de développer ou d'optimiser les procédures d'étalonnage pour les rendre plus adaptées à ces nouvelles conditions d'utilisation et maximiser le temps disponible pour les observations scientifiques. Un premier défi se pose alors: comment étalonner rapidement le système sans source d'étalonnage? La seconde difficulté réside alors dans la mise à jour régulière de la matrice d'interaction pour des systèmes à grand nombre de degrés de liberté.

Pour répondre à cette nouvelle problématique, deux principales stratégies d'étalonnage ont été identifiées par la communauté. La première consiste à faire une mesure sur ciel de la matrice d'interaction et la seconde se base sur des modèles pseudo-synthétiques qui permettent de reproduire le système réel dans un simulateur et de calculer numériquement la matrice d'interaction du système. Cette seconde approche apparaît plus adaptée au cas des futurs ELT car elle nécessite uniquement l'identification de quelques paramètres pour mettre à jour toute la matrice d'interaction. Cette stratégie est actuellement utilisée au Very Large Telescope (VLT) pour des systèmes équipés d'ASO Shack-Hartmann.

Cette thèse a pour but de proposer des optimisations et nouvelles stratégies d'étalonnage prenant en compte les nombreuses contraintes des systèmes d'OA des futurs ELT, en particulier la complexité de l'ASO Pyramide. La première étape a consisté à étudier la faisabilité de l'approche pseudo-synthétique avec ASO Pyramide en prenant le cas du Large Binocular Telescope qui est équipé d'un miroir secondaire adaptatif. Le développement et la validation d'un tel modèle sont présentés dans la section 6.2. La seconde étape a consisté à optimiser le suivi des paramètres du modèle durant les observations avec l'objectif de minimiser l'impact sur la voie scientifique. Au cours de cette thèse, deux approches ont été considérées, une **approche perturbatrice** (section 6.3) et une **approche non-perturbatrice** (section 6.4).

3. Le DM sera situé dans le télescope, à des dizaines de mètres des instruments scientifiques et avec des optiques mobiles entre les deux.

6.2. Modélisation de système d'OA avec ASO Pyramide: le cas du Large Binocular Telescope

6.2.1. Développement du modèle et principaux objectifs

Le Large Binocular Telescope est un télescope équipé de deux miroirs primaires de 8.4 mètres de diamètre qui peuvent être combinés pour faire de l'interférométrie ou bien utilisés indépendamment. Chaque télescope est équipé de son propre système d'OA FLAO⁴ avec miroir secondaire adaptatif: l'Adaptive Secondary Mirror (ASM). L'analyse de front d'onde est effectuée avec un ASO Pyramide localisé après le focus du télescope. Le but de cette étude est de développer un modèle pseudo-synthétique de FLAO dans l'outil de simulation OOMAO qui permette de calculer des matrices d'interactions synthétiques qui puissent être utilisées pour fermer la boucle du système d'OA du LBT. Le modèle se compose de deux éléments principaux:

- **Le modèle de l'ASM** qui consiste à définir les fonctions d'influences du miroir qui permettent de reproduire la base modale du système. Dans notre cas, nous avons utilisé des mesures des fonctions d'influences effectuées sur site grâce à un interféromètre. D'autres concepts ont été étudiés au cours de la thèse en basant le modèle de miroir sur des fonctions d'influences synthétiques mais n'ont pu être testés au télescope. Le modèle de l'ASM permet d'ajuster les paramètres de rotation et de grossissement du modèle.
- **Le modèle d'ASO Pyramide** qui consiste à reproduire l'ASO de FLAO en définissant le masque de phase correspondant. Les paramètres du masque du modèle ont été ajustés pour reproduire au mieux la carte d'illumination expérimentale de l'ASO et obtenir des pupilles de 30 pixels de diamètre dont les centres sont séparés de 36 pixels. Le modèle est monochromatique et utilise la longueur d'onde centrale de l'ASO expérimental (750 nm) et la modulation Tip/Tilt ($3 \lambda/D$) du modèle a été considérée comme nominale. L'ajustement de la position des pupilles du modèle permet d'ajuster le paramètre de translation du modèle.

Les paramètres de *mis-registrations* du modèle ont été ajustés grâce à une matrice d'interaction complète ($N=400$ Modes de KL), mesurée sur site avec un rétro-rélecteur, et qui a servi de référence au modèle. Pour cette étude, la procédure pour identifier les paramètres du modèle est présentée dans la Figure 6.2 et consiste à minimiser le RMS résiduel χ_N entre les N signaux de référence (matrice d'interaction expérimentale D_α) et les signaux provenant du modèle synthétique D_α^* en ajustant un paramètre de mis-registration α_i à la fois. La procédure pour ajuster les paramètres du modèle dans la suite de la thèse a été optimisée pour permettre d'identifier tous les paramètres du modèle simultanément grâce à des matrices de sensibilités (voir section 2.5).

4. FLAO a maintenant été remplacé par un nouveau système, SOUL qui est en phase de mise en service.

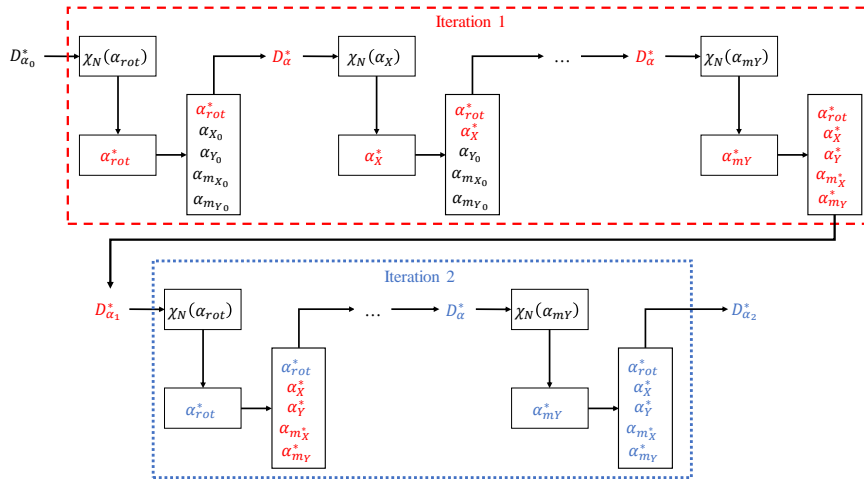


Figure 6.2. – Principe de l’algorithme itératif d’identification des paramètres de *mis-registrations* α_i à partir d’une matrice de référence expérimentale D_{α}^* et de matrices synthétiques D_{α}^* .

La Figure 6.3 résume le développement et l’ajustement du modèle en indiquant quels éléments sont de nature expérimentale ou synthétique.

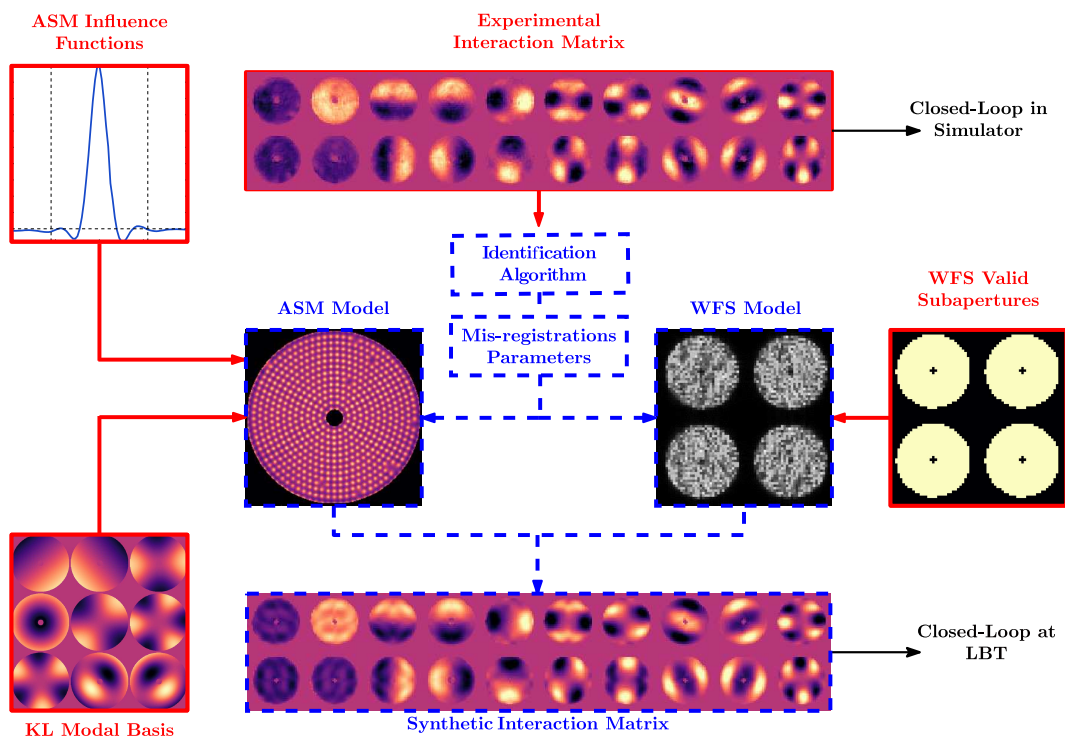


Figure 6.3. – Schéma représentatif du développement du modèle Pseudo-Synthétique de FLAO. Les lignes rouges correspondent aux données expérimentales et les lignes pointillées bleues aux données générées par le modèle.

6.2.2. Validation du modèle

Comme indiqué sur la Figure 6.3, le modèle a été validé en deux étapes. La première consiste à injecter le reconstruteur calculé à partir de la matrice d'interaction expérimentale dans le simulateur pour fermer la boucle du modèle synthétique. Cette expérience consiste donc à effectuer l'opposé du but initial mais si les deux reconstruteurs (synthétique et expérimental) offrent les mêmes performances de correction d'OA dans le simulateur, cela signifie que le modèle est représentatif du système réel. La Figure 6.4a montre que les deux reconstruteurs offrent en effet les mêmes niveaux de correction. Une analyse plus détaillée (en faisant varier les paramètres de mis-registation du modèle) a montré que les performances optimales étaient bien obtenues pour les paramètres identifiés par la procédure d'estimation présentée Figure 6.2.

Une fois cette première validation effectuée, la seconde étape consiste à effectuer la même comparaison au télescope. Pour cela, nous avons eu accès au télescope pour faire des tests de jour en simulant des cycles de turbulence grâce à des commandes envoyées sur l'ASM. La comparaison de performance entre reconstruteur pseudo-synthétique et expérimental est donnée Figure 6.4b et montre que les deux reconstruteurs offrent le même niveau de correction.

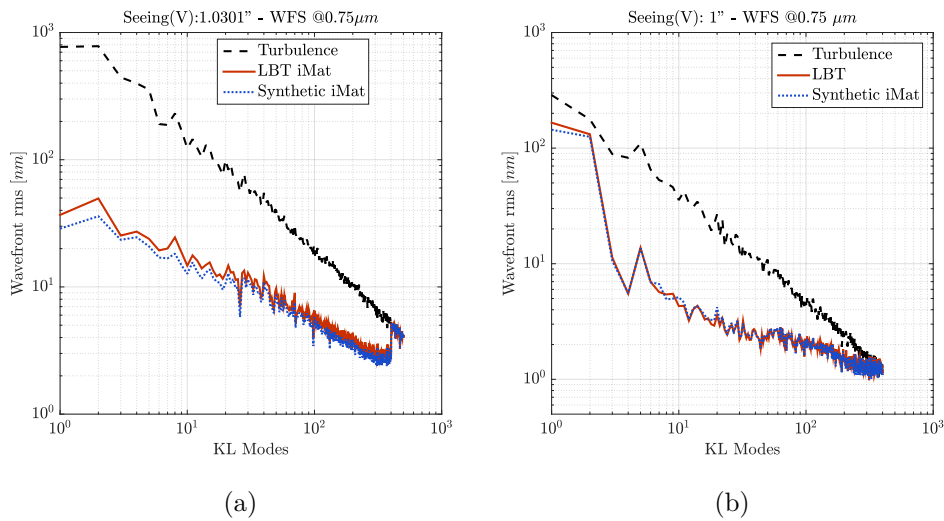


Figure 6.4. – (a): Densités Spectrales de Puissances modales obtenues avec les reconstruteurs synthétique et expérimental dans le simulateur. (b) DSP modale obtenues avec les reconstruteurs synthétique et expérimental au LBT en simulant une turbulence sur l'ASM.

D'autre part, la haute précision du modèle a permis de contrôler jusqu'à 500 modes dans le reconstruteur et d'obtenir des performances stables en boucle fermée. Les Fonctions d'Étalement du Point (FEP) obtenue avec les différents reconstruteurs en bande H avec l'instrument LUCI sont illustrées Figure 6.5.

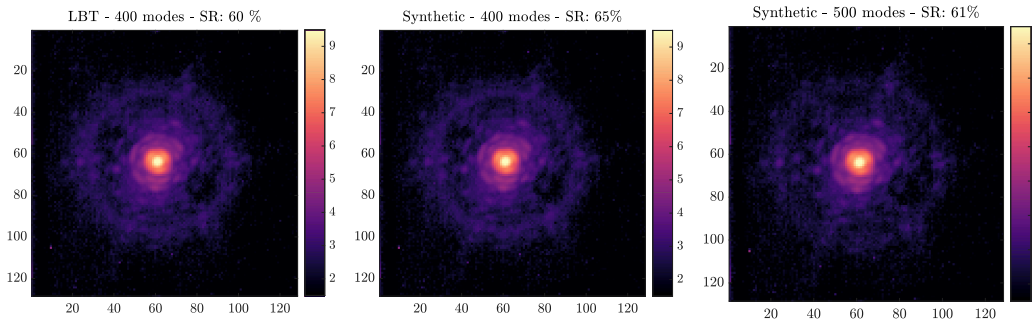


Figure 6.5. – FEP (en échelle logarithmique) obtenues en simulant une turbulence sur l’ASM dans le cas d’un reconstituteur expérimental (gauche) et synthétique pour 400 modes (centre) et 500 modes (droite). Images obtenues avec l’instrument LUCI du LBT (bande H). SR correspond au critère de qualité de l’image: 100% correspond à une image limitée par la diffraction.

Ce travail valide donc l’approche pseudo-synthétique pour l’ASO Pyramide et a donné lieu à une publication dans le journal MNRAS (voir section 2.3). Cette étude a montré que la précision des paramètres du modèle était un élément crucial pour le bon fonctionnement de la méthode. Nous disposons alors d’une matrice d’interaction complète pour identifier les paramètres du modèle ce qui ne sera sûrement pas le cas des instruments de l’ELT. Il est donc nécessaire de développer de nouvelles méthodes d’identification de ces paramètres, si possible en minimisant l’impact sur les observations. Cette problématique a été traitée durant la seconde partie de ma thèse en considérant deux stratégies: une approche perturbatrice (voir section 6.3) qui consiste à envoyer des signaux à faible amplitude sur le DM et une approche non-perturbatrice qui consiste à utiliser les données de boucle fermée (voir section 6.4).

6.3. Identification des paramètres du modèle sur ciel: l’approche perturbatrice

Cette approche consiste à moduler des signaux de faibles amplitudes sur le DM durant les observations afin d’identifier les paramètres dans les mesures de l’ASO, de la même manière qu’un étalonnage sur ciel. Dans notre cas, nous proposons de minimiser le nombre de signaux nécessaires pour minimiser l’impact sur la voie scientifique. Pour cela, nous utilisons une approche basée sur une Analyse en Composante Principale (PCA en anglais) de matrices de sensibilités afin de déterminer les signaux pour lesquels le système ASO-DM est le plus sensible à une mis-registation donnée et ainsi minimiser le nombre de signaux nécessaires. Des exemples de tels signaux sont donnés Figure 6.6.

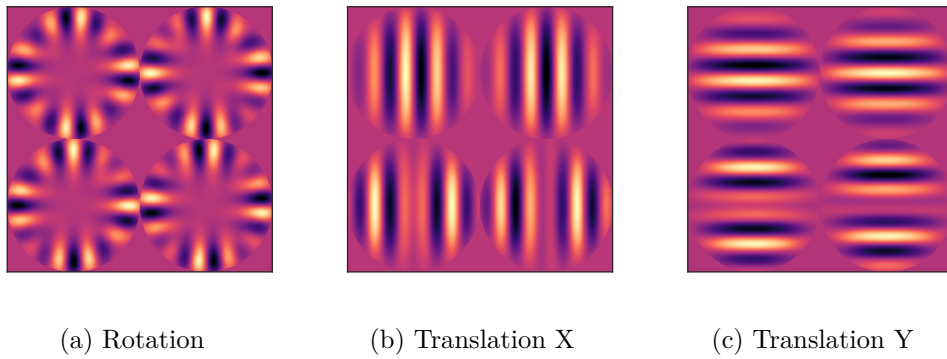


Figure 6.6. – 4 modes les plus sensibles pour différents types de *mis-registrations* obtenus grâce à la PCA des matrices de sensibilité.

En utilisant de faibles amplitudes (10 et 20 nm RMS), nous avons montré qu'il était possible de suivre les paramètres du modèle qui évoluent dynamiquement avec une précision bien en dessous des spécifications requises (translation de 10% d'une sous-ouverture et translation équivalente en bord de pupille pour la rotation). Les résultats sont présentés dans la Figure 6.7 qui donne l'estimation des paramètres en comparaison avec la vraie valeur des paramètres.

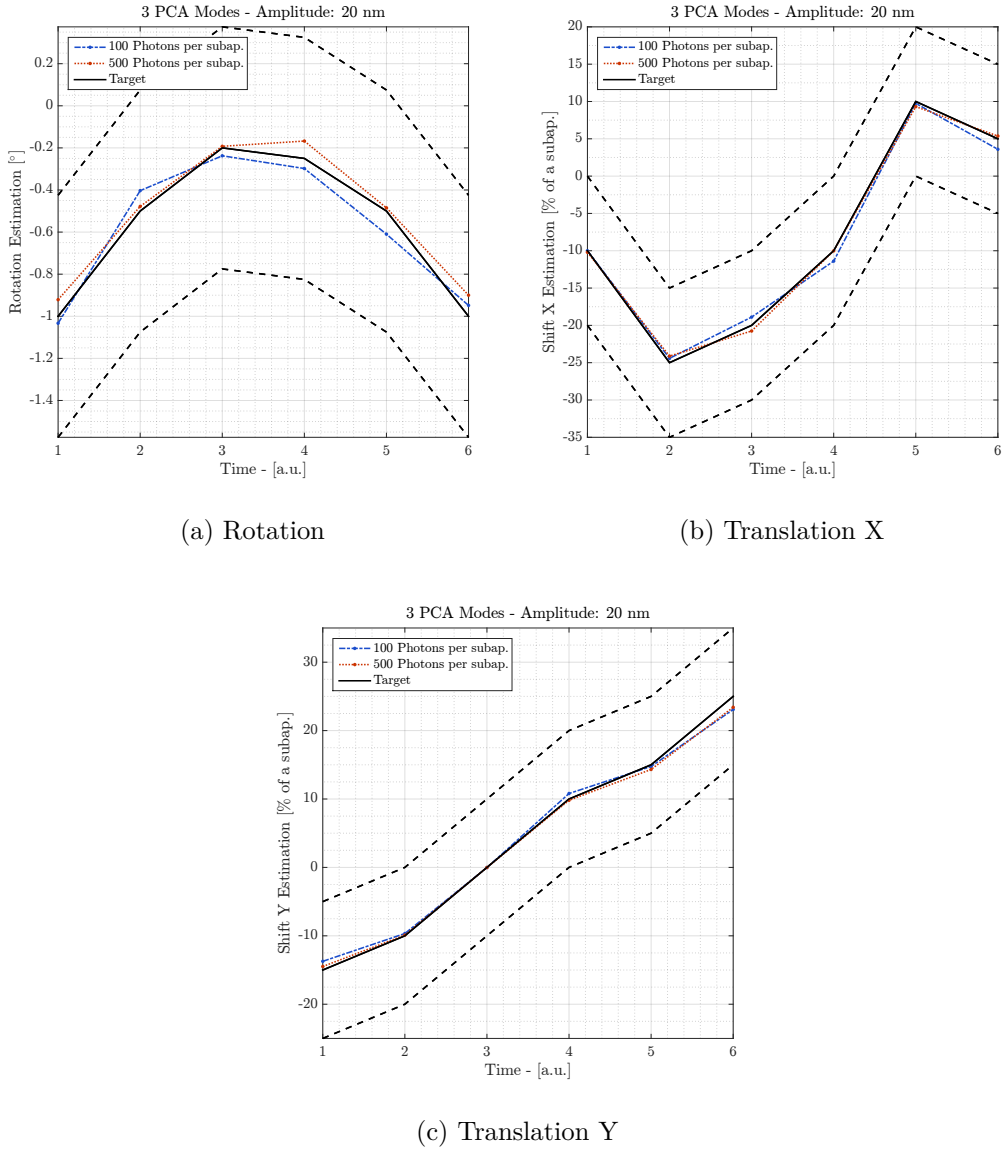


Figure 6.7. – Estimation dynamique des *mis-registrations* en fonction du nombre d'itérations en utilisant 3 modes PCA. A chaque itération, les *mis-registrations* sont modifiées. Le cas présenté correspond à une amplitude de 20 nm RMS et 20 mesures *push-pull* pour chaque mode. Les lignes noires pointillées correspondent aux niveaux d'erreur maximales pour être dans les spécifications.

La question de l'impact sur la voie scientifique se pose alors, bien que cet effet soit dépendant du système considéré et du type d'observation. Pour donner une illustration, nous proposons de considérer l'application d'un mode PCA sur une Fonction d'Étalement du Point à la limite de diffraction. La Figure 6.8 montre que cet effet est négligeable comme en atteste la valeur maximale de la FEP résiduelle.

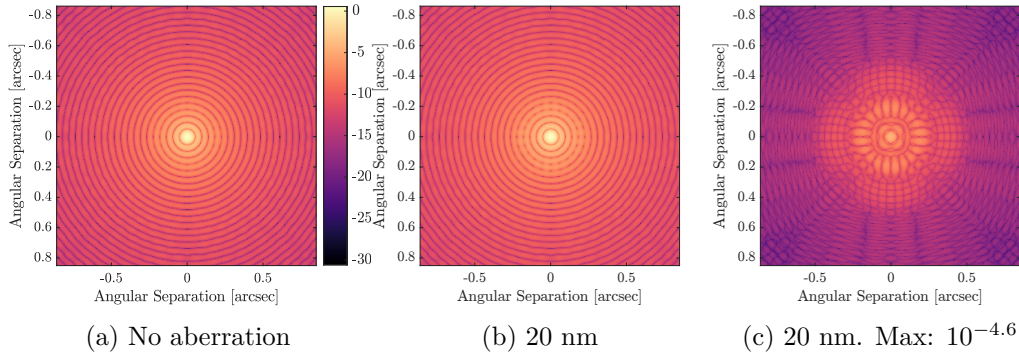


Figure 6.8. – FEP en bande H, limitée par la diffraction (a) (échelle logarithmique) et avec une amplitude de 20 nm RMS du mode PCA le plus sensible à la rotation (b). (c) FEP résiduelle (échelle logarithmique).

Le suivi des paramètres grâce à cette approche perturbatrice apparaît donc comme très précise (erreur inférieure à quelques pour-cents d’une sous-ouverture, et moins de 0.3° pour la rotation) et des études plus approfondies ont montré qu’elle était très robuste face aux différentes conditions d’observation. De plus, l’impact sur la science est négligeable dans la plupart des cas. Cependant, pour un application de type haut contraste, la signature du signal dans la FEP pourrait être problématique. Dans ce cas là, l’utilisation de méthodes non-perturbatrices pourrait être une alternative.

6.4. Identification des paramètres du modèle sur ciel: l’approche non-perturbatrice

Cette approche, plus séduisante, consiste à identifier les paramètres pendant les observations, sans introduire de perturbation. Cette stratégie est actuellement utilisée au VLT avec un ASO Shack-Hartmann mais nécessite une étude plus approfondie dans le cas de l’ASO Pyramide. L’idée de cette méthode est de retrouver une estimation de la matrice d’interaction du système D_α^* à partir des données de boucle fermée. Cette matrice n’a cependant pas un rapport signal à bruit suffisant pour être utilisée comme étalonnage du système mais elle permet l’identification des paramètres pour le modèle en utilisant l’algorithme présenté section 2.5. Mon travail s’est concentré sur l’analyse détaillée de cette stratégie pour identifier le domaine de validité et éventuelles limitations. En pratique, en analysant les équations de boucle fermée d’un système d’OA, on obtient que les incréments de mesure de l’ASO δy_k et les incréments de commandes δc_k à l’instant k sont reliés par la matrice d’interaction D_α :

$$\delta y_k = -D_\alpha \cdot \delta c_k + \delta z_k \quad (6.3)$$

où δz_k est un terme de perturbation sur la mesure qui contient la propagation des incréments de la phase turbulente dans l’espace ASO $M_{\text{WFS}} \cdot \delta \phi_k^{\text{turb}}$ et le bruit de mesure de l’ASO $\delta \eta_k$:

$$\delta z_k = M_{\text{WFS}} \cdot \delta \phi_k^{\text{turb}} + \delta \eta_k \quad (6.4)$$

A partir de l'équation 6.3, on peut montrer que la matrice d'interaction D_α peut être estimée par D_α^* :

$$D_\alpha^* = -(C_{\delta y, \delta c}) \cdot (C_{\delta c, \delta c})^\dagger \quad (6.5)$$

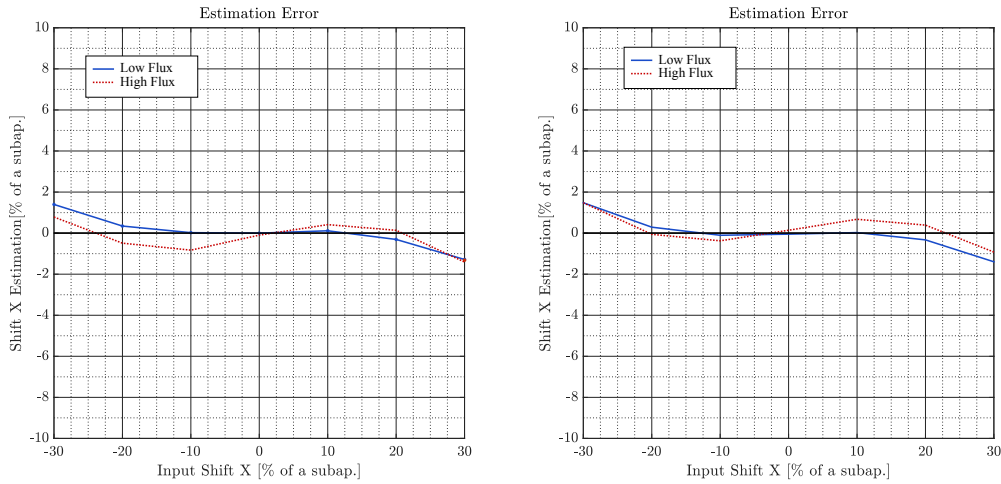
où $C_{\delta y, \delta c}$ et $C_{\delta c, \delta c}$ sont les matrices de covariances estimées avec N incréments:

$$C_{\delta y, \delta c} = \frac{\sum_{k=1}^{k=N} (\delta y_k \cdot \delta c_k^T)}{N} \quad C_{\delta c, \delta c} = \frac{\sum_{k=1}^{k=N} (\delta c_k \cdot \delta c_k^T)}{N} \quad (6.6)$$

Cette expression est cependant obtenue en faisant l'hypothèse que (i) les δc_k et δz_k sont indépendants et que (ii) l'ASO est parfait (sans variation de gains). En analysant la composition des incréments de commandes δc_k , j'ai pu mettre en évidence que :

- L'hypothèse (i) sera discutable dans le cas d'un régime fort flux avec une erreur temporelle importante (typiquement dans des conditions de fort vent avec une direction privilégiée).
- Le bruit agira comme un signal d'intérêt car étant décorrélé d'une trame à l'autre.

De nombreuses simulations ont été effectuées en faisant varier les conditions d'observations: régimes de bruit et profils d'atmosphère (type *Frozen Flow*⁵ et type bouillonnant) pour différentes vitesses de vent. En considérant d'abord un système avec ASO Shack-Hartmann (pour être au plus proche de (ii)), des simulations ont permis de mettre en évidence que dans des conditions de *Frozen Flow* et régime fort flux, **l'identification des paramètres de translation est biaisée**. Ce biais est d'ailleurs **corrélé à la vitesse et direction du vent** considérée. Lorsque l'on considère un régime dominé par le bruit, ce biais disparaît (voir Figure 6.9).



(a) Frozen Flow +10 m/s

(b) Frozen Flow -10m/s

Figure 6.9. – Erreur sur l'estimation d'une translation en X pour une atmosphère de type *Frozen Flow* avec un vent de 10 m/s dans la direction X. Les résultats sont donnés pour un ASO de type Shack-Hartmann dans un régime à bas flux (10 photons par sous-ouverture) et fort flux (500 photons par sous-ouverture).

5. Des écrans de phase fixes qui avancent dans une direction privilégiée.

L'origine de ce biais a pu être expliquée en étudiant la reconstruction de la matrice d'interaction en explorant des vitesses de vent non réalistes, de manière à atteindre le cas où deux trames successives sont totalement décorrélées⁶ (voir Figure 6.10). Les corrélations spatio-temporelles ont pour effet de créer des structures qui correspondent à **des répliques des signaux d'actionneurs** dans la matrice d'interaction estimée. Lorsque ces répliques se superposent avec le vrai signal de l'actionneur, l'estimation des paramètres est impactée.

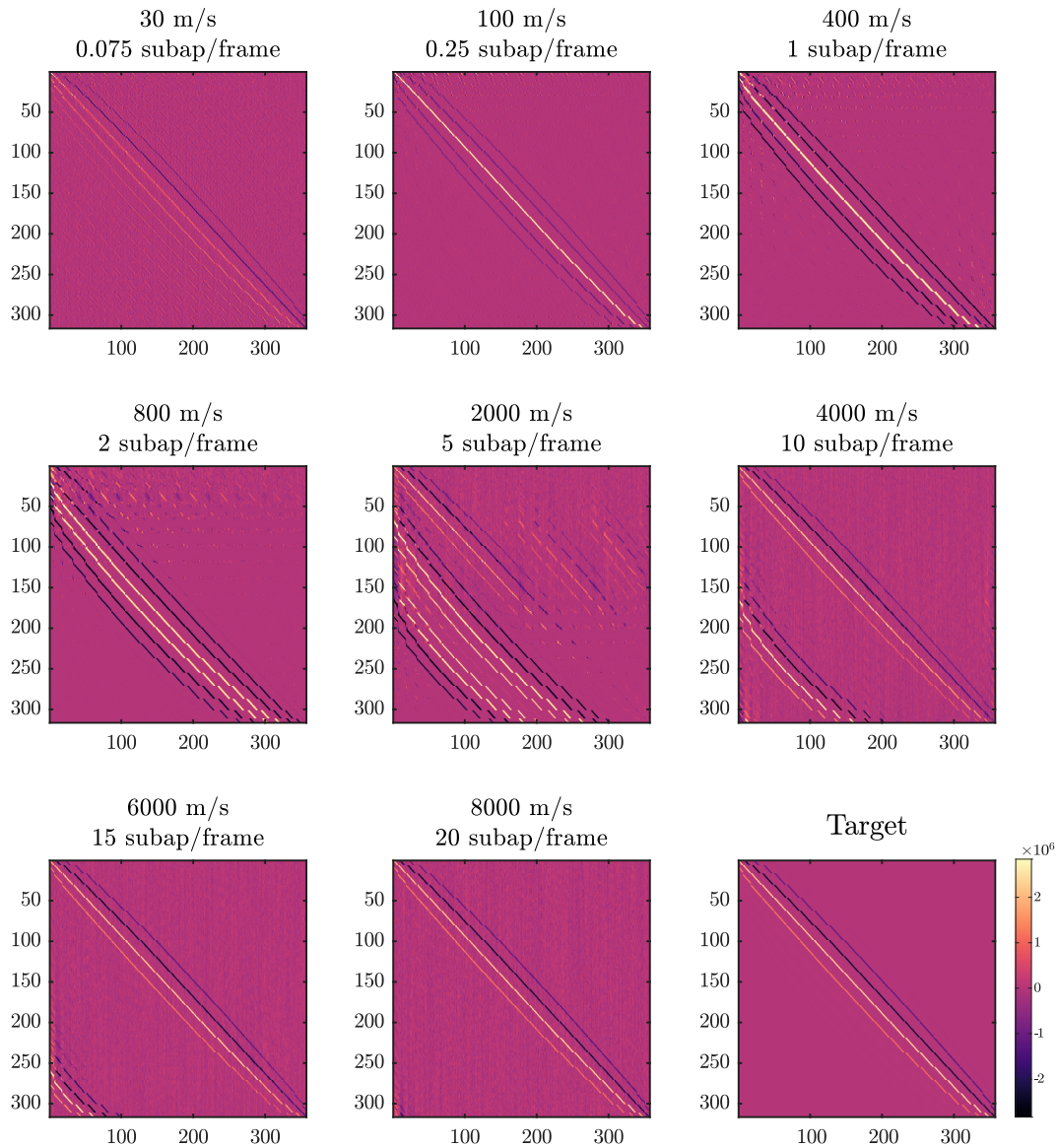


Figure 6.10. – Matrices d'interaction estimées (Signal en X uniquement) pour différentes valeurs de vent. La matrice d'interaction vraie est donnée dans le coin bas-droite.

D'autre part, nous avons mis en évidence que la valeur du biais dépend de la valeur du gain choisie pour l'intégrateur. La bande passante du système, et donc la correction de l'erreur temporelle, est directement liée à l'apparition de ces structures. En

6. Dans ce cas là, une turbulence de très faible amplitude est considérée pour rester dans le régime de linéarité de l'ASO.

minimisant l'erreur temporelle, il est possible de minimiser ce biais sur l'estimation des paramètres comme illustré Figure 6.11. Cependant, ce point de fonctionnement sera optimal pour l'identification des paramètres mais ne le sera pas nécessairement du point de vue de la performance de l'OA.

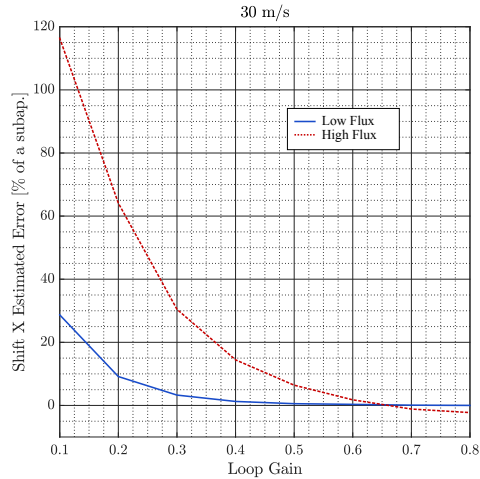


Figure 6.11. – Estimation de la translation en X en fonction du gain de boucle pour une atmosphère de type *Frozen Flow* avec un vent de 30 m/s dans la direction X. Les résultats sont donnés pour un ASO de type Shack-Hartmann dans un régime à bas flux (10 photons par sous-ouverture) et fort flux (500 photons par sous-ouverture).

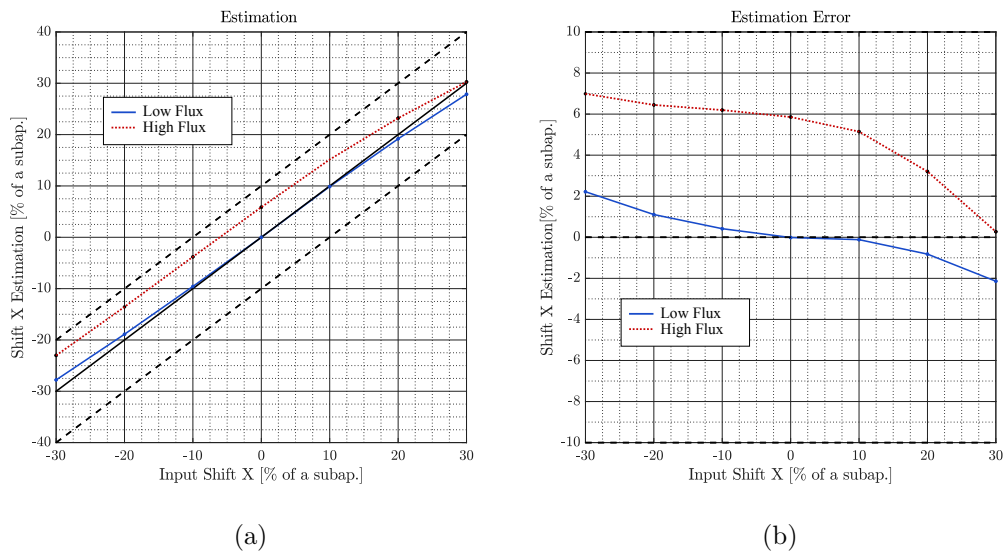


Figure 6.12. – Estimation (a) et Erreur d'estimation (b) d'une translation en X pour une atmosphère de type *Frozen Flow* avec un vent de 10 m/s dans la direction X. Les résultats sont donnés pour un ASO de type Pyramide dans un régime à bas flux (10 photons par sous-ouverture) et fort flux (500 photons par sous-ouverture).

Enfin, en appliquant les mêmes cas avec un ASO Pyramide, nous avons retrouvé les tendances identifiées dans le cas de l'ASO Shack-Hartmann avec un biais plus important (voir Figure 6.12). La compensation des gains optiques durant les opérations permet alors de réduire légèrement ce biais mais le facteur clé pour identifier au mieux les paramètres reste la minimisation de l'erreur temporelle en optimisant le gain de boucle (voir Figure 6.13).

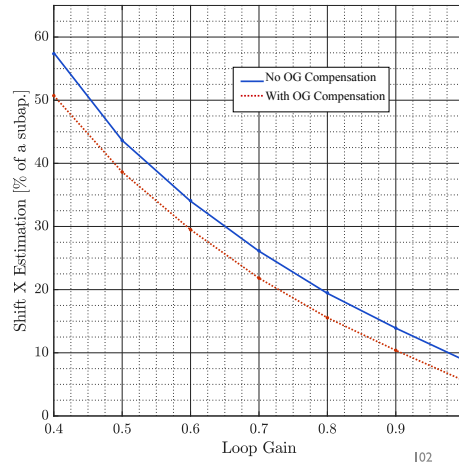


Figure 6.13. – Estimation de la translation en X en fonction du gain de boucle pour une atmosphère de type *Frozen Flow* avec un vent de 30 m/s dans la direction X. Les résultats sont donnés pour un ASO de type Pyramide avec et sans compensation des gains optiques.

Cette étude a permis de mieux caractériser la physique de cette méthode non perturbatrice pour mettre en évidence ses limites d'applications dans un cas où la turbulence est de type *Frozen Flow* avec fort vent et dans un régime de fort flux. Il est cependant peu réaliste que la direction et la vitesse du vent reste constante sur d'aussi longues séquences (de l'ordre de la minute). On peut donc espérer avoir une meilleure estimations des paramètres de *mis-registration* avec des données réelles. Comme perspective, cette méthode pourrait être optimisée en ajoutant des *a priori* sur la vitesse et la direction du vent et ainsi débiaiser l'algorithme d'identification des paramètres.

Appendix

A. AO Modelling of the High Order Test-Bench

The High Order Test-bench (HOT) has recently been refurbished (1.3x oversampling of DM by WFS, spectral and spatial filters, improved calibration methods) to optimize the PWFS performance. HOT now corrects for up to 600 K-L modes providing diffraction limited performance at optical wavelengths in good seeing conditions. In this section, we present the adaptation of the AO model developed for the LBT AO systems to the HOT AO systems.

The High Order Test-Bench

The optical design of the test bench is given in Figure A.1. The design of the WFS unit is almost identical as the FLAO system (see Figure 1.28) with an achromatic double PWFS (DP) and a Tip/Tilt Mirror (TTM) in charge of the PWFS modulation. The WFS camera is an Andor L3CCD. The bench is equipped with two corrective devices, a Low Order ALPAO DM 52 in charge of the Tip/Tilt correction and a High Order Boston Micro-Machine (BMM) DM with 1024 by 1024 actuators. Upstream of the deformable mirrors, a turbulence generator allows to simulate turbulence phase screens. A diagram providing the distances between the different optical elements of the bench is given in Figure A.2.

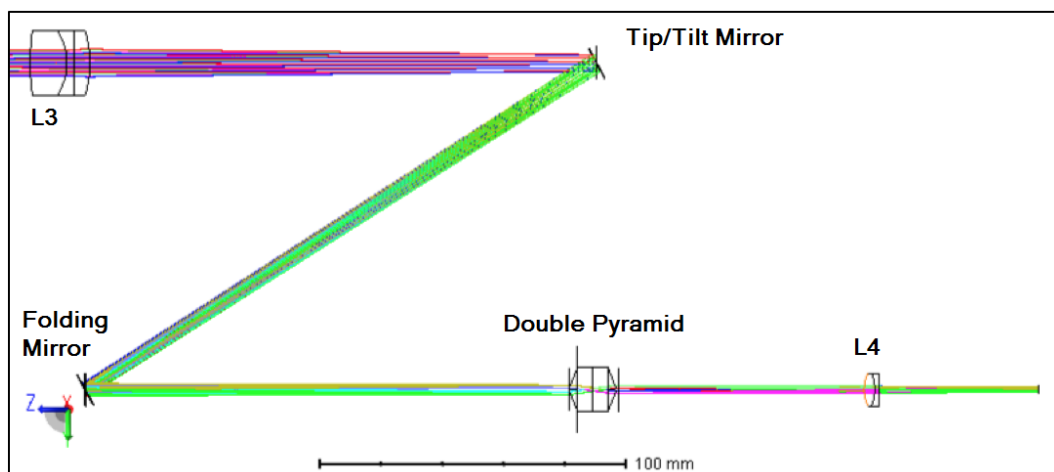


Figure A.1. – Optical layout of the WFS unit of HOT. The lens L3 is used to focus the light on the top of the Double Pyramid and the lens L4 is in charge of re-imaging the PWFS pupils on the Andor camera detector.

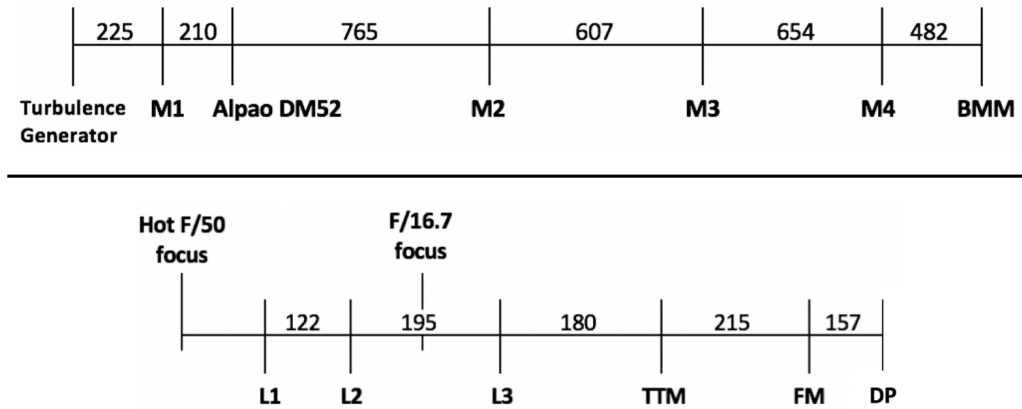


Figure A.2. – Distances between the different HOTA optical elements.

In addition, we provide a picture of the PWFS prism and BMM are given in Figure A.3.

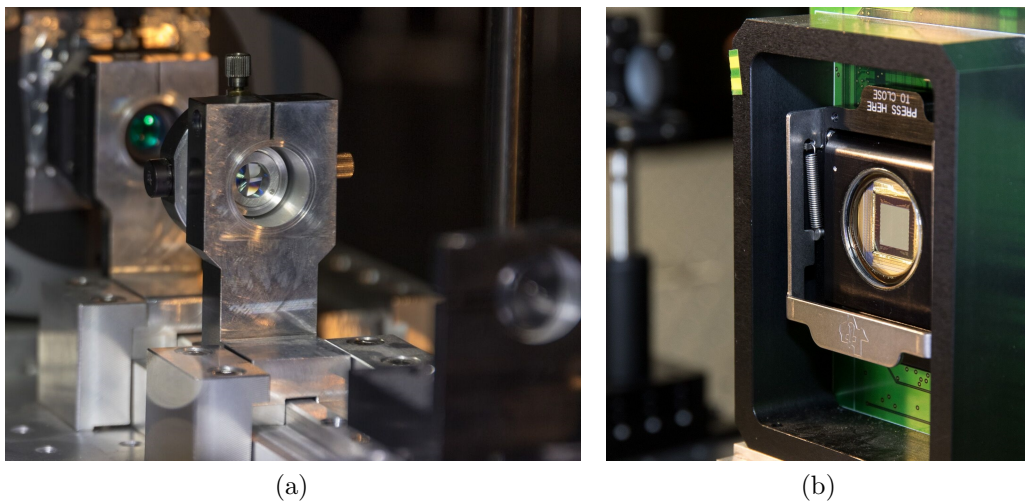


Figure A.3. – HOT PWFS Pyramid (left) and BMM (right). Courtesy of N. Cerpa and M. Kasper.

Modelling of the AO System

The summary of the model is given in Figure A.4.

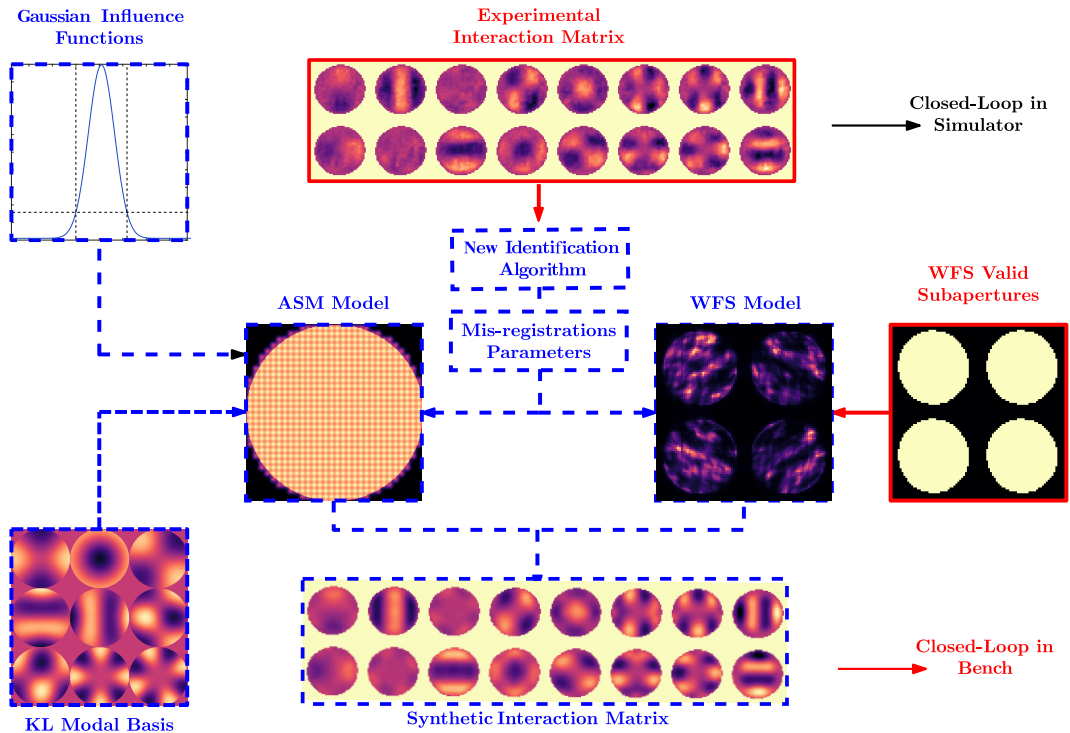


Figure A.4. – Summary of the development of the Pseudo-Synthetic model of the HOT AO systems in the simulator. The **solid red lines** correspond to the experimental inputs and the **dashed blue lines** to the model components and outputs.

The modelling of the PWFS was almost identical as for the LBT experiment (see chapter 2). However, we see in Figure A.4 that by contrast with the LBT model, no experimental measurements of the BMM influence functions or modal basis were available. The model was then based on purely synthetic Gaussian Influence Functions characterized by a mechanical coupling of 15% and taking the theoretical actuators coordinates given in the documentation of the BMM. The mis-registration identification was achieved using the new mis-registration algorithm presented in section 2.5.

Experimental Validation

This study is still preliminary as no extensive analysis of the model has been carried out. In particular, at the time of the study, the calibration of the test-bench was often evolving (typically the position and definition of the PWFS pupils following a DM replacement). However, using a rough tuning of the parameters, we could obtain stable closed loop performance controlling 100 KL modes. As a metric of performance, we provide the PWFS closed-loop pupils and corresponding slopes RMS.

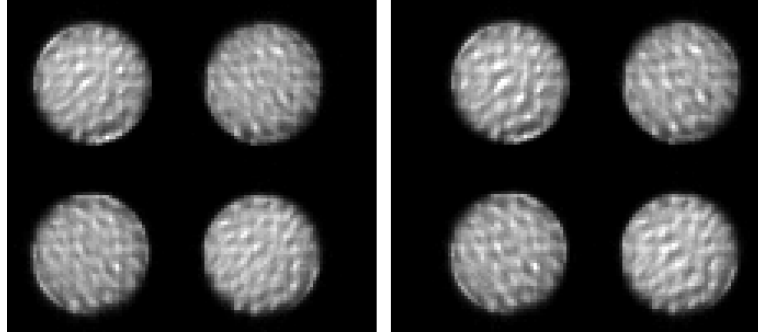


Figure A.5. – Closed-loop pupils of the HOT PWFS simulating the phase screens with the turbulence simulator. The left image corresponds to the interaction matrix experimentally measured with fiber (slopes RMS=0.0955 a.u.) and the right image corresponds to the interaction matrix generated from the synthetic model (slopes RMS=0.1073 a.u.)

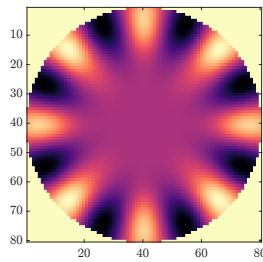
Using a larger number of modes, the loop was diverging, exhibiting characteristic patterns of residual mis-registrations. A fine tuning of the model would be required to provide a high accuracy calibration but we are confident that this preliminary model can easily be upgraded to reproduce accurately the real system. Since the second part of my PhD research was focused on the analysis of the mis-registration identification strategy, we did not investigate this model any further.

B. Complementary Analysis of the PCA Modes

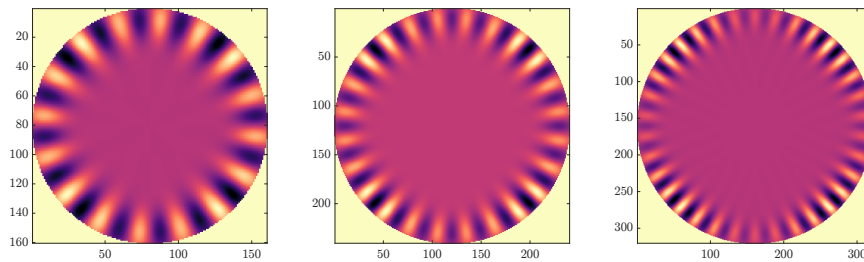
In this section, we present the impact of the AO systems properties on the computation of the PCA modes (see section 3.3.2). We consider a SH-WFS to speed up the computation of the sensitivity matrices $\delta\mathbf{D}_{\alpha_0}(\varepsilon_i)$ corresponding to the mis-registration ε_i .

Impact of the number of subapertures

We consider an AO systems composed of a SH-WFS with different numbers of subapertures with a Cartesian DM in a Fried geometry. The following Figures provide the most sensitive mode to each type of mis-registration.

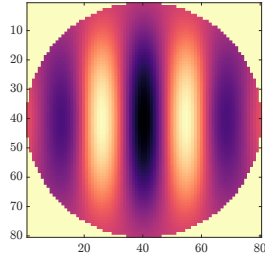


(a) 10×10 subapertures

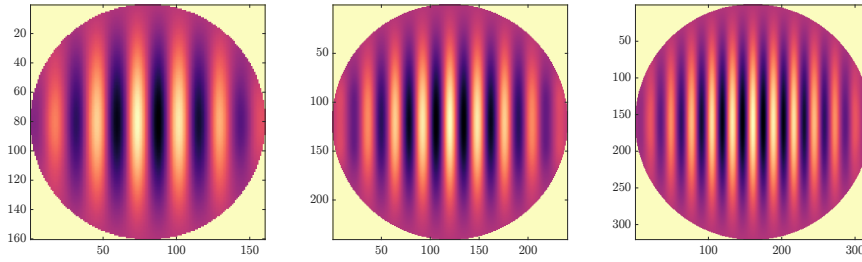


(b) 20×20 subapertures (c) 30×30 subapertures (d) 40×40 subapertures

Figure B.1. – PCA modes corresponding to the rotation for AO systems with different number of subapertures.

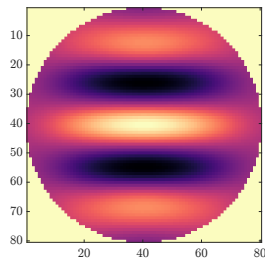


(a) 10×10 subapertures

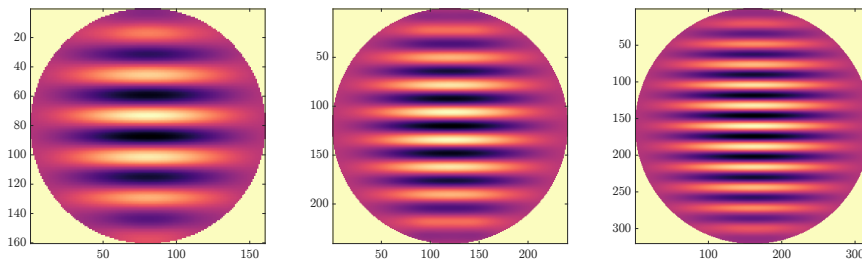


(b) 20×20 subapertures (c) 30×30 subapertures (d) 40×40 subapertures

Figure B.2. – PCA modes corresponding to the shift X for AO systems with different number of subapertures.

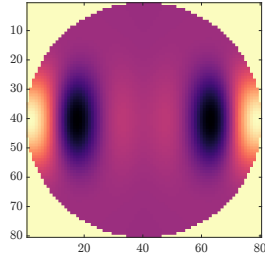


(a) 10×10 subapertures

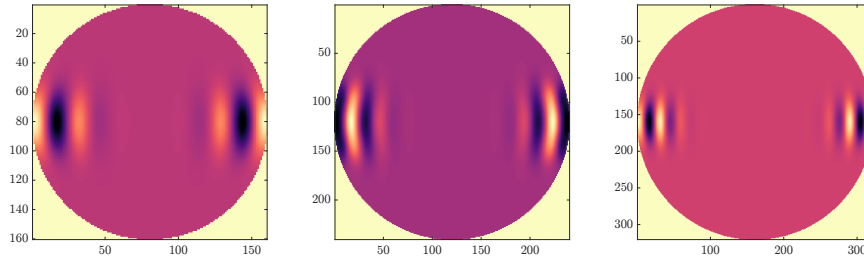


(b) 20×20 subapertures (c) 30×30 subapertures (d) 40×40 subapertures

Figure B.3. – PCA modes corresponding to the shift Y for AO systems with different number of subapertures.

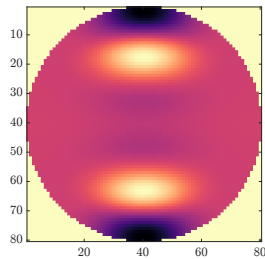


(a) 10×10 subapertures

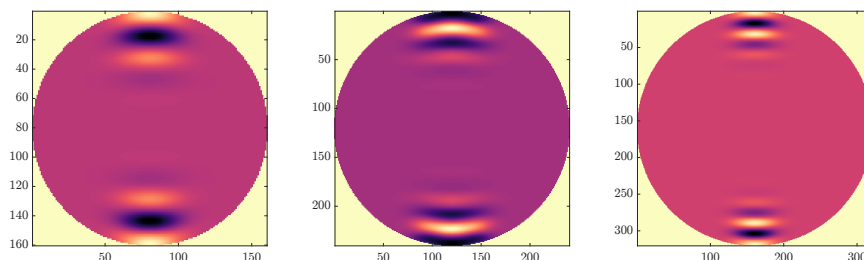


(b) 20×20 subapertures (c) 30×30 subapertures (d) 40×40 subapertures

Figure B.4. – PCA modes corresponding to the magnification X for AO systems with different number of subapertures.



(a) 10×10 subapertures



(b) 20×20 subapertures (c) 30×30 subapertures (d) 40×40 subapertures

Figure B.5. – PCA modes corresponding to the magnification Y for AO systems with different number of subapertures.

Figures B.1, B.2, B.3, B.4 and B.5 illustrate the impact of the number of subapertures on the computation of the PCA modes. For a High Order system (large number

of subapertures), the spatial frequencies of the most sensitive modes becomes larger than for a Low Order System (small number of subapertures).

Impact of the Influence Functions mechanical coupling

In this section we are interested in characterizing the impact of the influence function mechanical coupling on the computation of the PCA modes. We consider a 20 by 20 subapertures system with a Cartesian DM in the Fried geometry.

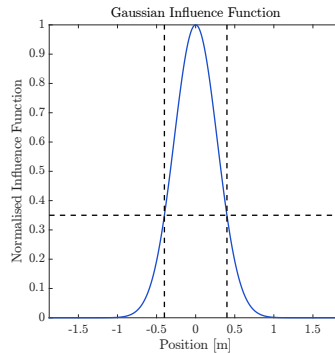
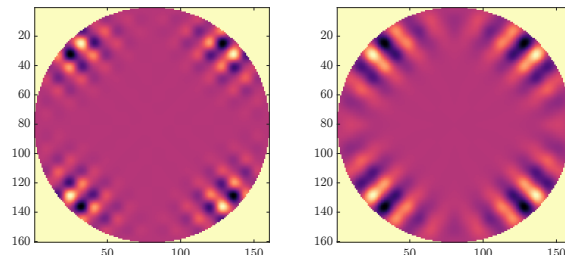
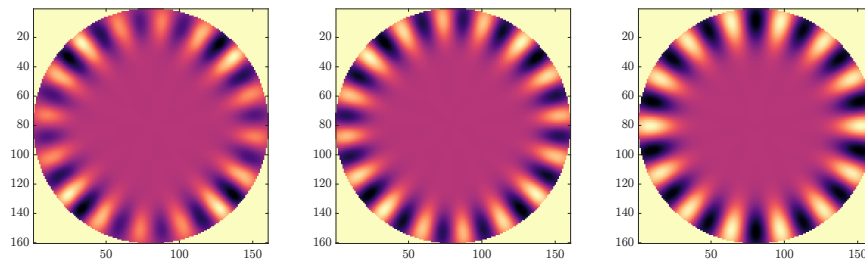


Figure B.6. – 1D section of a Gaussian influence function with a mechanical coupling of 45%



(a) 10 % Coupling

(b) 20 % Coupling

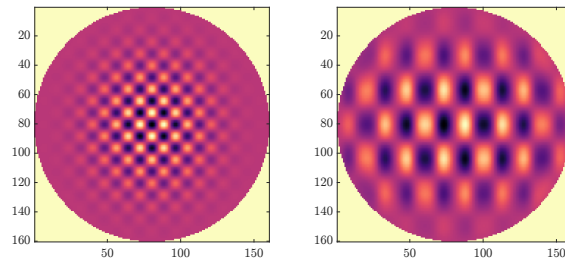


(c) 30 % Coupling

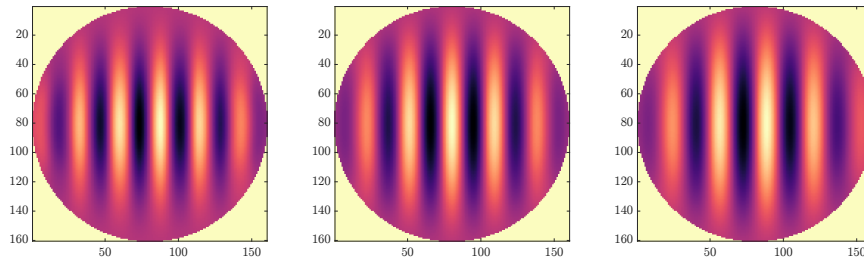
(d) 40 % Coupling

(e) 50 % Coupling

Figure B.7. – PCA modes corresponding to the rotation for AO systems with different mechanical couplings.

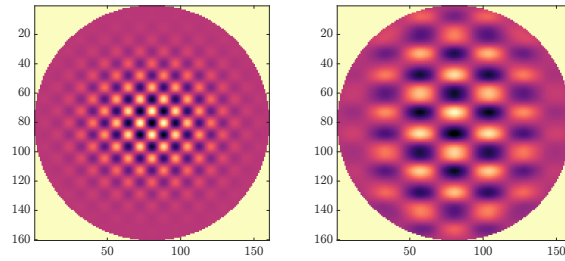


(a) 10 % Coupling (b) 20 % Coupling

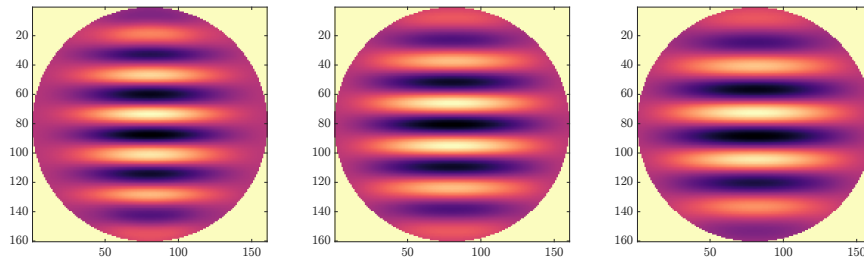


(c) 30 % Coupling (d) 40 % Coupling (e) 50 % Coupling

Figure B.8. – PCA modes corresponding to the shift X for AO systems with different mechanical couplings.



(a) 10 % Coupling (b) 20 % Coupling



(c) 30 % Coupling (d) 40 % Coupling (e) 50 % Coupling

Figure B.9. – PCA modes corresponding to the shift Y for AO systems with different mechanical couplings.

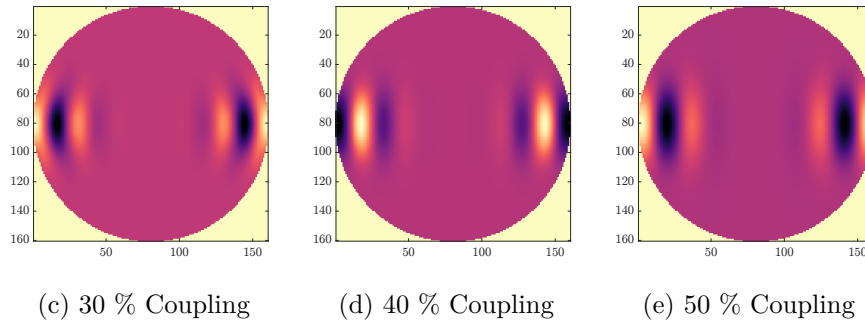
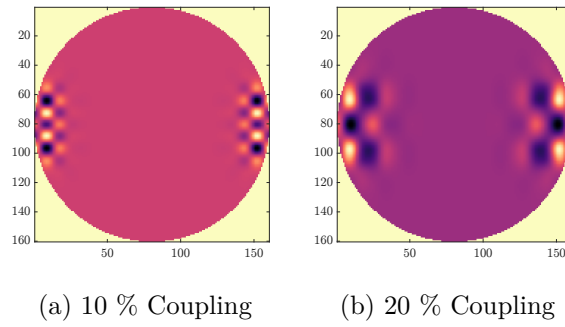


Figure B.10. – PCA modes corresponding to the magnification X for AO systems with different mechanical couplings.

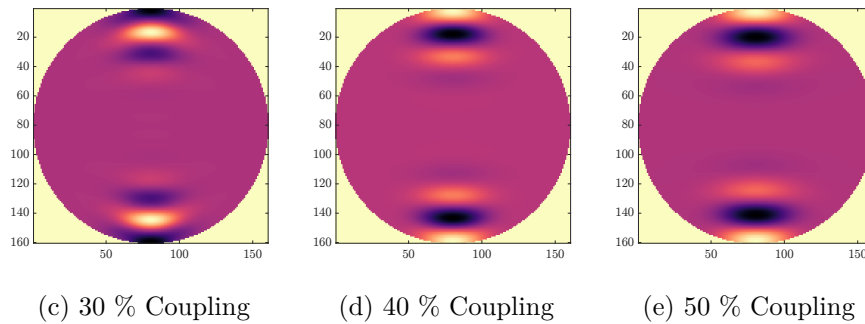
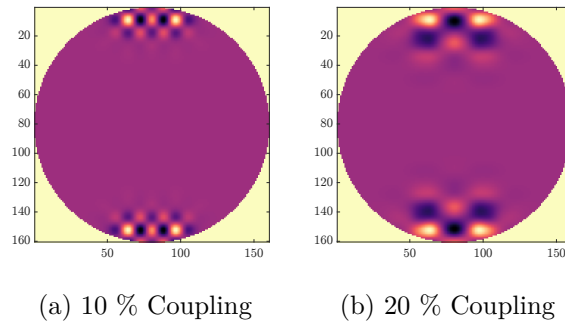


Figure B.11. – PCA modes corresponding to the magnification Y for AO systems with different mechanical couplings.

Figures B.7, B.8, B.9, B.10 and B.11 illustrate the impact of the influence function

mechanical coupling on the computation of the PCA modes. For a large mechanical couplings the spatial frequencies of the most sensitive modes becomes larger than for a small mechanical coupling.

**C. AO4ELT5 Conference Proceeding:
Overview of the AO Calibration
Strategies in the ELT context.**

Overview of the AO calibration strategies in the ELT context

Cedric T. Heritier^{a,b,c,d}, Thierry Fusco^b, Benoit Neichel^a, Simone Esposito^c, Sylvain Oberti^d, Carlos Correia^a, Jean-François Sauvage^b, Charlotte Bond^e, Olivier Fauvarque^a, Enrico Pinna^c, Guido Agapito^c, Alfio Puglisi^c, Johann Kolb^d, Pierre-Yves Madec^d, and Clémentine Bechet^f

^a Aix Marseille Université, CNRS, LAM (Laboratoire d'Astrophysique de Marseille) UMR 7326, 13388, Marseille, France

^bONERA, DOTA, Unité HRA, 29 avenue de la division Leclerc, 92322 Chatillon, France

^cINAF - Osservatorio Astrofisico di Arcetri Largo E. Fermi 5, 50125 Firenze, Italy

^dEuropean Southern Observatory, Karl-Schwarzschild-str-2, 85748 Garching, Germany

^eInstitute for Astronomy, University of Hawaii, 640 N. Aohoku Place, Hilo, HI 96720

^fPontificia Universidad Católica, Av Libertador Bernardo O'Higgins 340, Santiago, Chile

ABSTRACT

The scientific potential of the ELT will rely on the performance of its AO systems that will require to be perfectly calibrated before and during the operations. The actual design of the ELT will provide a constraining environment for the calibration and new strategies have to be developed to overcome these constraints. This will be particularly true concerning the Interaction Matrix of the system with no calibration source upward M4 and moving elements in the telescope. After a brief presentation of the ELT specificities for the calibration, this communication focuses on the different strategies that have already been developed to get/measure the Interaction Matrix of the system, either based on synthetic models or using on-sky measurements. First tests of these methods have been done using numerical simulations for a simple AO system and a proposition for a calibration strategy of the ELT will be presented.

Keywords: Adaptive Optics, Calibration, Interaction Matrix, ELT, On-Sky Interaction Matrix, Pseudo-Synthetic Interaction Matrix

1. INTRODUCTION

Within a decade, the new generation of Extremely Large Telescopes (ELT) will make a breakthrough in the ground based Astronomy. The scientific potential of these giants relies on challenging new Adaptive Optics (AO) systems, integrated inside the telescope itself, and providing images to all the instrumentation downstream. The complexity of these instruments leads to new problematics, especially concerning the calibration of the Interaction Matrix (IM), the link between the Wave Front Sensor (WFS) measurements and the Deformable Mirror (DM) actuators. The registration between the WFS and the DM may evolve dynamically with the telescope environment, making the calibration detuned, and resulting in a loss of the AO system performance. These telescopes will also provide a new and constraining environment with no direct access to intermediate focal plane in front of the DM and thus no external calibration source.

In this context, accelerating the calibration procedures or performing it on sky, if possible during the AO correction itself, becomes necessary.¹ Some strategies have already been developed and are currently tested/validated on current 8m telescope facilities such as the AOF^{2,3} at the VLT and FLAO⁴⁻⁶ at the LBT. A first idea consists in computing a theoretical model of the IM and update it during the operation by identifying key parameters, either on-sky or directly using AO closed-loop data.⁷⁻⁹ A second idea is to acquire the IM directly on-sky. In this communication, we focus on some of these calibration strategies to evaluate their feasibility on an ELT, putting light on their drawbacks, advantages or limits and offering eventual optimization.

Further author information: E-mail: cedric.heritier@lam.fr/ heritier@arcetri.astro.it/cheritie@eso.org

2. CONTEXT

2.1 Calibration of an AO system

The good behavior of any AO system relies on two main calibration phases: the construction of its Interaction Matrix (IM) and the calibration of the Non Common Path Aberrations (NCPA). Figure 1a illustrates where these calibrations phases take place in a classical AO system.

To build the IM, the most common way consists in poking on each actuator of the DM (or apply a modal basis for a modal IM) and record the corresponding WFS signals. By inverting this matrix, one gets a reconstruction matrix (often called "Reconstructor") that is used to compute the commands to apply on the DM for a given WFS measurement. This experimental process ensures to take into account any misregistration lying between the DM and the WFS. The term misregistration stands here for any shift, rotation of the DM actuators with respect to the WFS subapertures or any higher order of pupil distortion.

The accuracy of the IM is crucial as the system is extremely sensitive to any drift in the calibration (especially for high order systems) and it will consistently impact the AO system performance. Defining the quality of such an object is then not easy to do (SNR? Conditioning number? Eigenvalues spectrum?) as it mostly depends on the characteristics of the system. So far, the best way to evaluate the quality of an IM is to try using it in closed loop and study the effectiveness of the correction.

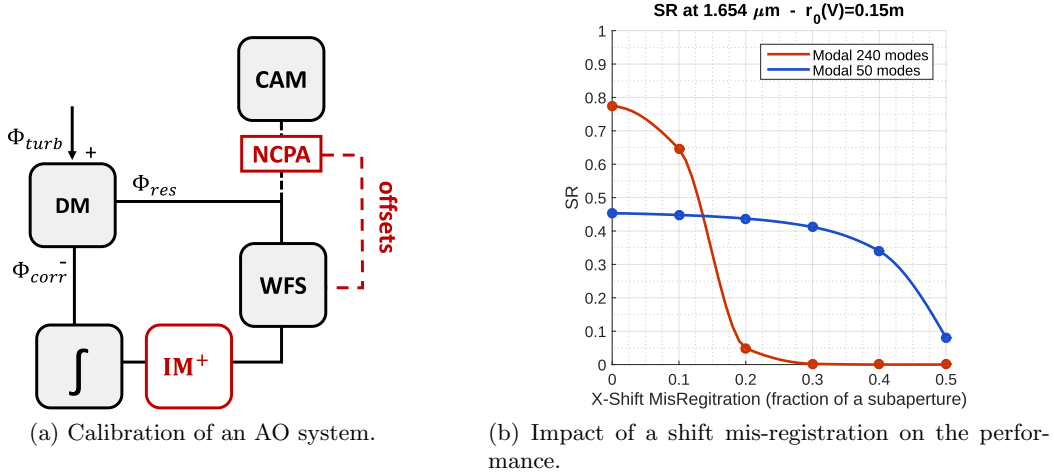


Figure 1: Calibration of an AO System (a) and (b) sensibility to an horizontal shift for two IM controlling 50 and 240 modes.

The sensibility to misregistrations depends mostly on the geometry of the DM but also on the number of modes controlled in the IM. Figure 1b shows the impact of a shift of the DM actuators for a classical AO system defined in Table 1. This plot shows that a high order system provides better AO performance but will be extremely sensitive to any misregistration while a low-order system maintains its performance despite high misregistration values. Therefore, a trade-off has to be made on the number of modes to control and the sensibility to misregistrations.

2.2 AO calibration in the ELT context

In the ELT case, the situation will be completely different as the DM will be located in the telescope itself, few tens of meters away from the WFS so that the registration between the WFS and the DM may evolve dynamically with the telescope. This specificity already provides a new constraining environment as it will require frequent updates of the IM, and this even during the operations. Moreover, there won't be any direct access to an intermediate focal plane in front of the DM, and thus no external calibration source to calibrate initially the system.

The number of actuators of the DM will drastically increase (around 5000 actuators), increasing the calibration time. The DM will also have a different geometry than the Fried’s one with 6 petals composed of around 860 actuators and organised in bricks.¹⁰

Therefore, new methods and optimization of the calibration procedures have to be developed accounting for ELT specificities: complex models of both DM and WFS, fast calibration necessary with no or low impact on the operations, large number of actuators and moving elements in the system. So far, different strategies have been identified and remain to be investigated to meet with the ELT requirements or speed up the measurements:

- **On-Sky IM:** We measure the interaction matrix on-sky, finding a way to get rid of the turbulence effects and speed up the calibration procedures (Fast push-pull?,¹ using Hadamard matrix to speed up the process?^{11,12} Modulation/Demodulation?⁴⁻⁶).
- **Synthetic IM:** We build a model of the AO system and we generate an IM from it.¹
- **Pseudo-Synthetic IM:** We build a synthetic IM and we measure some key-parameters on-sky to estimate the registration of the system and update the IM during the operation.^{2,3,7-9}

The next sections will focus on some of these new strategies that are being tested on numerical simulations of a classical AO system with Pyramid WFS.

2.3 Numerical Simulation Tool

The simulations presented in this paper were done using the OOMAO tool that stands for Object Orient Matlab Adaptive Optics.¹³ The properties of the system defined in these simulations are given in Table 1 but it mostly consists in a Single Conjugate Adaptive Optics (SCAO) system with Natural Guide Star (NGS) for an 8-m class telescope and Pyramid WFS. This reduced size system was chosen to speed up the simulation and simulations on an ELT-size telescope will be done once the best strategy and its implementation will be defined.

Atmosphere	Wavelength	0.55 μm	WFS	Subapertures	16x16
	r_0	15 cm		Modulation	$3\lambda/D$
	L_0	30 cm		Detector RON	0.1 e-
	Cn^2 profile	3 layers		Detector Photon Noise	On
Telescope	Diameter	8 m	DM	Controlled Actuators	241
	Central Obstruction	None		Pitch	0.5 m
	Resolution	128 pix		Influence Functions	Gaussian
Science	Wavelength	H(1.65 μm)	Loop	Mechanical Coupling	30%
	Magnitude	10		Frequency	500 Hz
NGS	Wavelength	I(0.79 μm)	Delay	2 frames	
	Magnitude	8	Nominal Performance	70% SR	

Table 1: Numerical Simulations Parameters

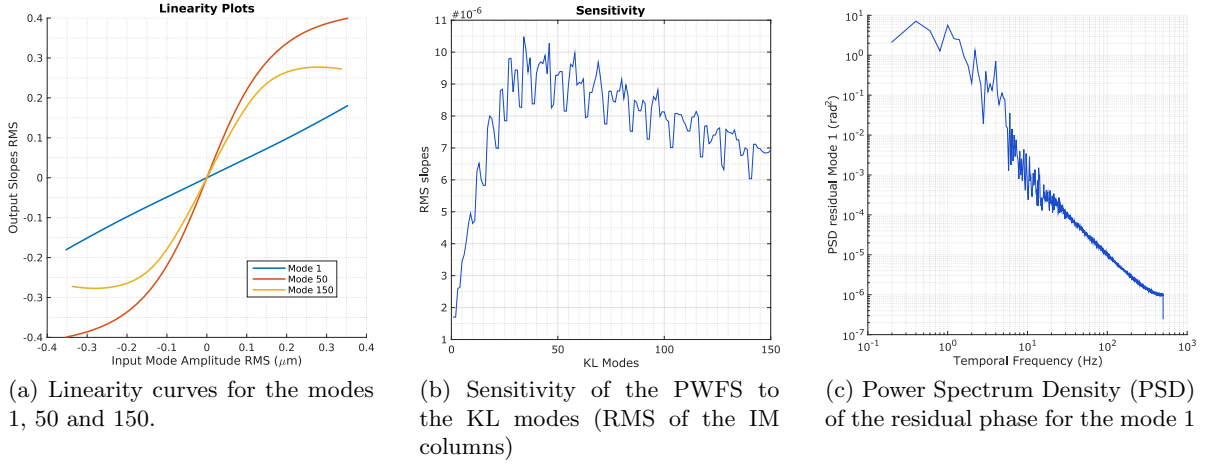
The modal basis used here consists in 150 Karhunen-Loève modes generated from Zernikes polynomial, diagonalizing the turbulence covariance matrix of the Zernikes.¹⁴ The linearity and sensibility plots to these modes are given in Figure 2 with the residual PSD of the loop for the mode 1.

3. ON-SKY INTERACTION MATRIX

3.1 Description of the method

The on-sky calibration faces one major challenge: the impact of the turbulence on the WFS measurements. One way to get rid of it consists in using a periodic modulation signal of the modal basis applied on the DM that is then demodulated in the Fourier space. This method allows even to calibrate several modes at the same time to reduce the calibration time.

A crucial point is that the periodic signals must be injected in a closed loop providing already a good correction such as the sum of the injected signals and the phase residuals remain in the linearity range of the WFS. To do so, as illustrated in Figure 3, the loop is closed using the best reconstructor R available for the system (inverting



the IM_{lab} that would be measured in lab using an optical calibration source) to be in the optimal conditions (lowest residuals and best correction of the modes introduced). Once the correction is sufficient and the residuals low enough we start modulating the modes:

- One mode \mathbf{m} is modulated at a given frequency (or several modes at several frequencies) using a periodic signal on the DM, the corresponding slopes and command are saved to be sent to a demodulation tool.
- A first demodulation process is achieved on the commands signals (or directly on the DM positions if available) to identify the phase delay Φ of the signal (due to the integration time and the command computation) and the amplitude a_0 of the corresponding mode seen by the WFS. The amplitude injected could indeed be different from the one seen by the WFS.
- A second demodulation is achieved on each pixel of the slopes maps to retrieve the module value of each pixel and its initial sign (phase δ or $\delta + \pi$) providing the slopes vector s_0 corresponding to the actuation of the mode \mathbf{m} .
- Each column of the IM is built by normalizing the slopes vector s_0 with the amplitude a_0 .

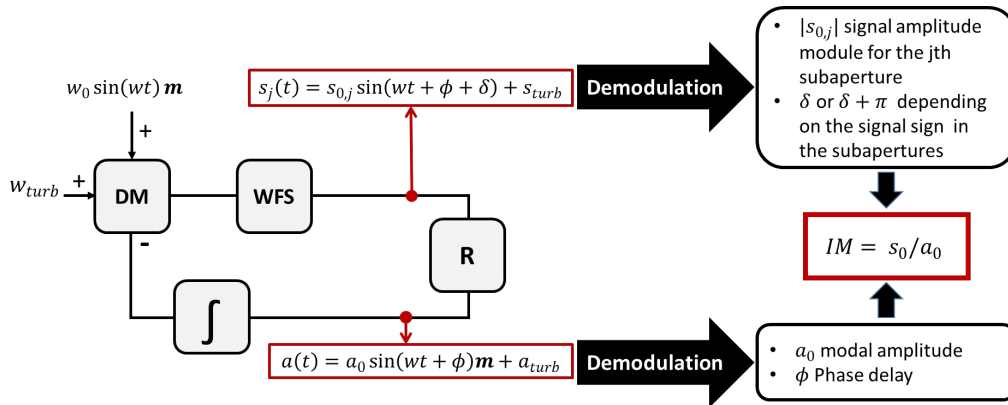
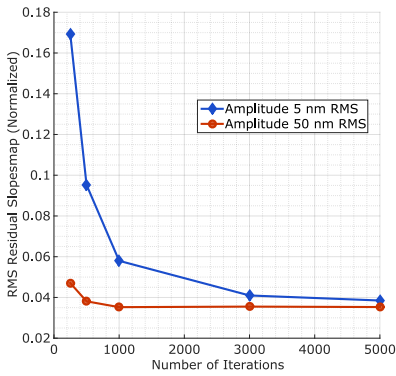


Figure 3: On-Sky IM measurement using periodic signals.

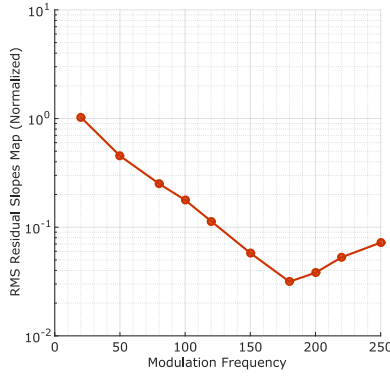
3.2 Trade-off study for the parameters

The goal is to get the best SNR with the lowest impact on science and for the shortest calibration time. Therefore, a trade-off study has to be done for the parameters of the modulation signal. The current study follows an analysis that was done at the LBT.⁶

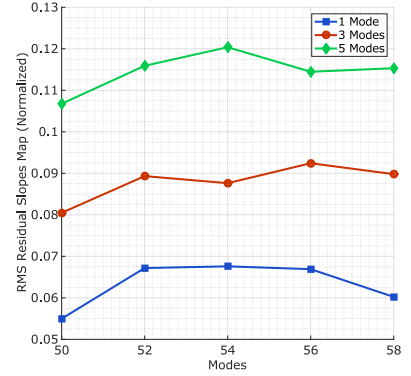
- **Amplitude:** If the goal is to record the IM during the observations, the amplitude of the injected signal must be as small as possible to minimize the effects on the operations but large enough to ensure a good SNR of the measurements, without saturating the WFS. Moreover, for a Pyramid WFS, as the sensibility and the linearity is not the same for all the modes, it is necessary to adapt the modes amplitude and flatten the sensibility curve of the WFS (see Figure 2).



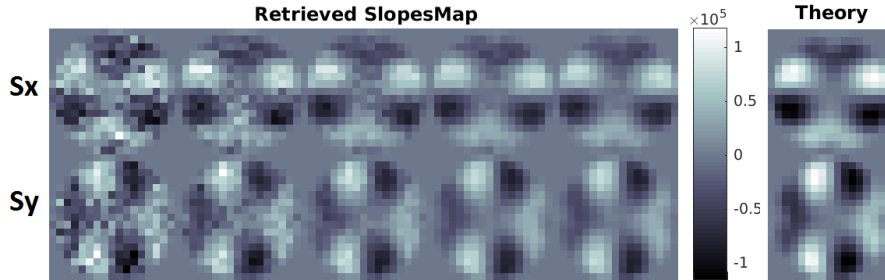
(a) Error on the Slopes Maps retrieved on-sky for different lengths of modulation signals. Results are given for two amplitudes, 5 nm RMS and 50 nm RMS.



(b) Error on the Slopes Maps retrieved on-sky for different modulation frequency. Results are given for 500 iterations.



(c) Error on the Slopes Maps retrieved on-sky when modulating 1 mode (5×500 iterations), 3 modes (3×500 iterations) and 5 modes (500 iterations) at the same time. (5 nm RMS amplitude)



(d) Slopes Map estimation for 250,500,1000,3000 and 5000 iterations with a mode amplitude of 5 nm

Figure 4: Trade-off study for the modulation signal parameters.

Nevertheless, if a dedicated calibration phase (with no observation at the same time) is scheduled to get the IM, the choice for the amplitude can be as large as possible, staying in the linear range of the WFS.

- **Sampling** The number of measurement points necessary to get a good SNR has to be investigated as the goal is to minimize the calibration time. In our case, we tested several values and we study the quality of the reconstruction for a given mode. The errors on the slopes maps reconstruction are presented in Figure 4a modulating modes at 200 Hz. It seems then necessary to use long modulation signals when applying a small amplitudes but signals can be shorter if using a higher amplitude.

- **Frequency Modulating** at high frequencies should give more interesting results as it makes the identification easier in the Fourier spectrum because most of the energy of the turbulence is in the low order frequencies (see Figure 2c). Studying the rejection transfer functions is also an important input because modulating a mode at a frequency that would be either filtered or amplified by the closed loop will disturb the measurements. Moreover, some experimental results⁶ showed the presence of "bad" frequencies and aliasing effects related to other frequencies of the system that need to be investigated ahead of the calibration phase to select a range of "good" frequencies. Figure 4b shows that, in our case, the optimal frequency seems to be between 160 and 200 Hz.
- **Multiplexing** Modulating several signals at different frequencies to lower the calibration time requires to have a perfectly orthogonal basis in the DM space as any cross-talking between the modes will affect the quality of the IM retrieved on-sky. Moreover, there is a price at applying several modes at the same time on the DM as it will have a higher impact the operations. A plot showing the effect of modulating several modes at the same time is given in Figure 4d and shows that it also has an impact on the estimation of the slopes maps but allows to reduce the calibration time.

3.3 Validation of the method

To validate the method, we apply it for the ideal case: the loop is closed using the IM_{lab} that is synthetically measured (no noise) with a system perfectly aligned (no misregistration). The list of the parameters chosen in this case is given in Table 2 (some of them were chosen to speed up the simulations) and the results displayed in Figure 5.

Mode Amplitude	50 nm RMS	Number of Modes	150
Number of iterations/cycle	500	Sampling Frequency	1000 Hz
Multiplexing	5 modes	Modulation frequency	200-202-204-206-208 Hz
Misregistrations	None	WFS Camera Noise	On

Table 2: Modulation Signals Parameters

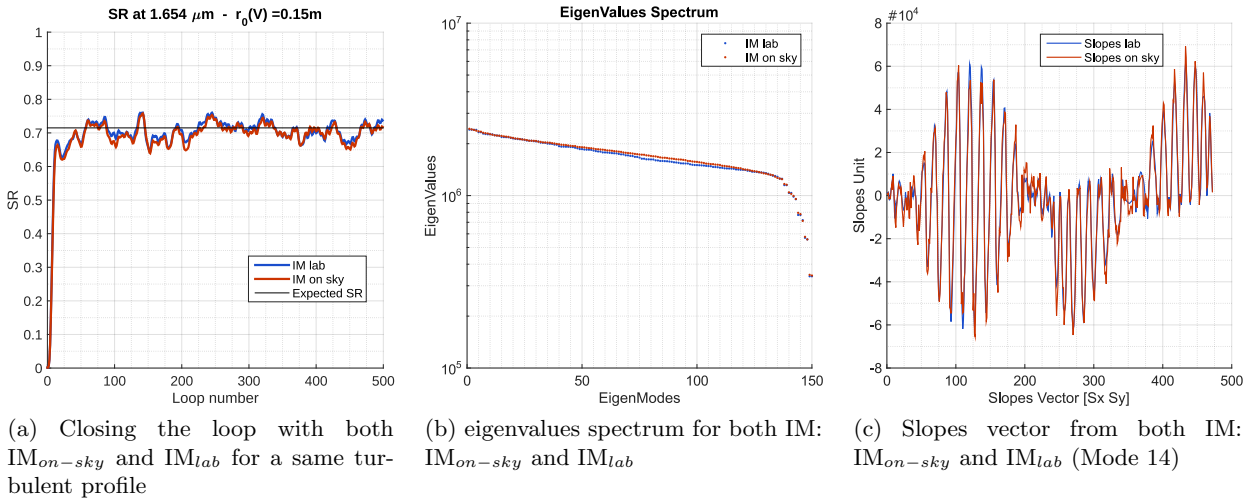


Figure 5: Validation of the on-sky calibration method using modulation signals

An explicit comparison of both IM, IM_{on-sky} and IM_{lab} , is given in the plot of Figure 5a: for a same turbulent profile, the corrections are (almost) exactly the same, confirming the good quality of the IM retrieved on sky.

Figure 5b and 5c give a more detailed comparison with the eigenvalues spectrums and a slopes vector (*e.g.* one row of the IM concatenating the slopes in X and Y). These two plots are also a criteria to confirm the good quality of the $IM_{on\ sky}$ with only small differences that are negligible and will not affect the effectiveness of the corrections.

3.4 Test of the method with Large Mis-Registrations

As presented in 2.2, the AO systems of the ELT could be subject to large misregistrations. In that case, can we catch up the nominal performance of the system using the on-sky calibration?

Based on the plot given in Figure 1b, the idea is to apply a static misregistration (X-shift of 25% of a subaperture) that maintains correct performance (approx. 60% SR) and then start applying the method. Two IM from the lab are generated:

- IM_{lab}^0 : acquired with no noise and when the system was perfectly aligned.
- $IM_{lab}^{shifted}$: acquired with no noise and when the system is shifted of 25% of a subaperture.

Using the same values for the modulation parameters as in Table 2, the method is applied when the system is shifted. The IM used to closed the loop is IM_{lab}^0 which does not correspond to the actual alignment of the system but provides a sufficient correction to start modulating the modes.

The results are presented in Figure 6. We see an improvement in the correction: the $IM_{on\ sky}$ catches up pretty well with the performance of the $IM_{lab}^{shifted}$ that represents the best IM available for the system (as if the shift was measured before the calibration phase). This shows that if the loop can be closed partially, using an IM that does not fit perfectly with the alignment of the system, it seems possible to apply the method and provide an on-sky IM that takes into account the misregistrations of the system.

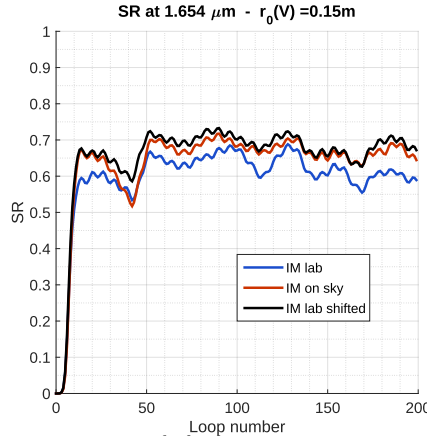


Figure 6: Closing the loop with IM_{lab}^0 , $IM_{lab}^{shifted}$ and $IM_{on\ sky}$ for a same turbulence profile. The

In that case, only 150 modes were retrieved, but an eventual idea would be to close the loop with a low or medium order IM, less sensitive to misregistration (see Figure 1b) and then modulates higher order modes. That way, one could build a high order IM. However, depending on the amplitude, it would maybe require to send commands to the DM to correct the modes injected as the Reconstructor would not "see" the high order modes modulated and would not be able to send the commands to correct it.

4. PSEUDO-SYNTHETIC INTERACTION MATRIX

The methods presented here were developed at ESO for the AOF and were based on two ambitious ideas: generate the IM from synthetic models of the system or from closed-loop data to make the AO system free of this calibration phase.

4.1 Synthetic or Pseudo-Synthetic Interaction Matrix?

Theoretically, building a synthetic IM has a lot of advantages: it is noise-free and it can be generated during the day, saving time for the operations. It requires to have perfect models of both WFS and DM, but also that the registration of the system does not evolve between the IM generation and the operation. In some cases, the response of the WFS will also depends on the seeing conditions (optical gains with a Pyramid,) and are ,therefore, unpredictable. Using only synthetic IM is then doable for an AO system⁶ with really stable alignment but seems complex on a ELT.

What can be done is to generate a synthetic IM from models fed with experimental measurements of misregistration parameters. The IM obtained is then Pseudo-Synthetic (PSIM) and can be easily updated during the operation (accounting for a good estimation of the misregistration parameters during the operations). However, working with synthetic IM, even PSIM, requires to have extremely accurate and sensitive models for both DM and WFS which will not be easy to do for the ELT.

4.2 Interaction Matrix from closed loop data

The other idea is to re-compute the IM during the operation using only closed loop data, that would take into account the actual registration of the system. This would have the advantage of tracking the registration state of the system without having any impact on the operation. The method is described in several documents^{2,8} and is illustrated in Figure 7: it requires to have a first IM (measured or synthetic) to invert and close the loop, at least partially, and start saving the interesting signals: DM residual commands and WFS residual slopes.

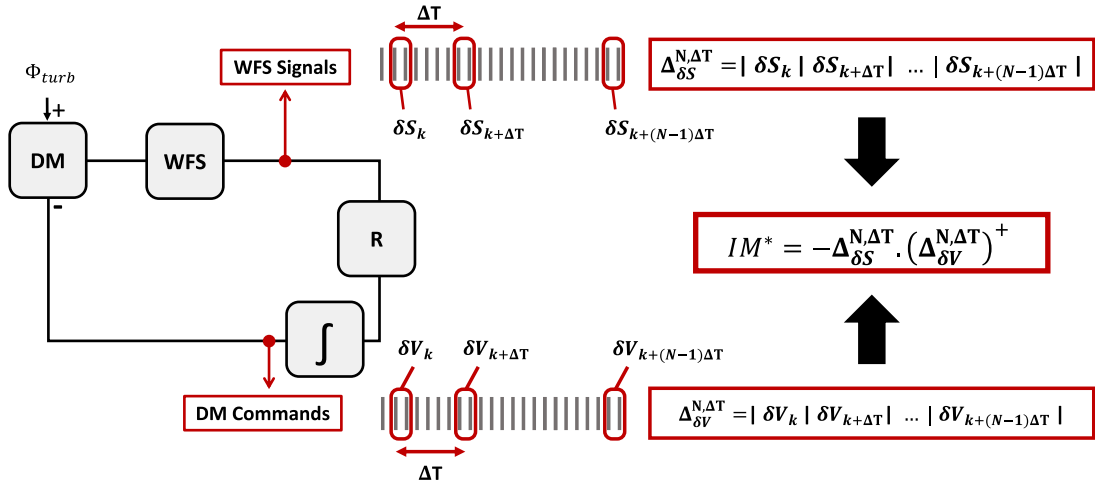


Figure 7: Estimation of the IM using closed loop data

The AO closed-loop equation is:

$$S_k = -IM(p) \cdot V_k + M_{WFS} \cdot \Phi_k + z_k \quad (1)$$

Where S is the WFS measurement, V the corresponding DM commands, $IM(p)$ the interaction matrix corresponding to the registration parameter p , M_{WFS} the propagation and sensing model, Φ the turbulence and z the noise associated to the measurement, and k the loop number.

Defining

$$e_k = M_{WFS} \cdot \Phi_k + z_k \quad (2)$$

If we consider $\delta S_k = S_{k+1} - S_k$:

$$\delta S_k = -IM(p) \cdot \delta V_k + \delta e_k \quad (3)$$

If we get rid of δe_k we can get an estimation of the IM:

$$IM(p) = -\delta S_k / \delta V_k \quad (4)$$

To get rid of the noise, the idea is to average the δe_k with a large number N of measurements (typically 40 000 frames) and de-correlate them by selecting only the δS_k and δV_k one every ΔT , ΔT being the step parameter that has to be determined to maximize the SNR of the IM studying the correlation of both buffers $\Delta_{\delta S}$ and $\Delta_{\delta V}$:

$$\Delta_{\delta S}^{N,\Delta T} = |\delta S_k| |\delta S_{k+\Delta T}| \dots |\delta S_{k+(N-1)\Delta T}| \quad (5)$$

$$\Delta_{\delta V}^{N,\Delta T} = |\delta V_k| |\delta V_{k+\Delta T}| \dots |\delta V_{k+(N-1)\Delta T}| \quad (6)$$

An estimation of the IM of the system is then:

$$IM^* = -\Delta_{\delta S}^{N,\Delta T} . (\Delta_{\delta V}^{N,\Delta T})^+ \quad (7)$$

Where $^+$ stands for the pseudo-inverse. First tests at the AOF² show that it is indeed possible to retrieve an IM but it is really noisy and has a too low SNR to close the loop. Nevertheless, this noisy IM could provide enough information to estimate some misregistration parameters.(see 4.3)

4.3 Misregistration identification

In the frame of this study, the main question is : can we track the registration of the system using only closed loop-data? That way, it would be possible to update the synthetic models during the operations with no impact on science.

One idea to do that is to use the noisy IM retrieved using the closed loop data and project it on a catalog of "sensibility" IM.² This makes the hypothesis that an IM can be expressed as a linear combination of IM_0 (synthetic for a system perfectly aligned) and sensibility matrix δIM (built from the difference between IM_0 and synthetic IM recorded in presence of one type of misregistration):

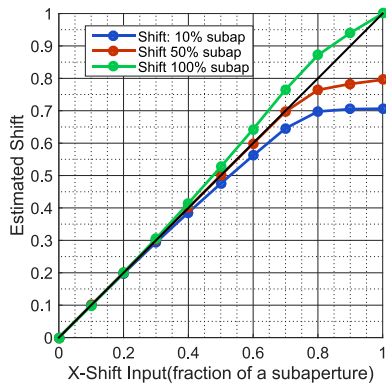
$$\delta IM_\alpha = IM_\alpha - IM_0 \quad (8)$$

with α standing for shift, rotation or magnification.

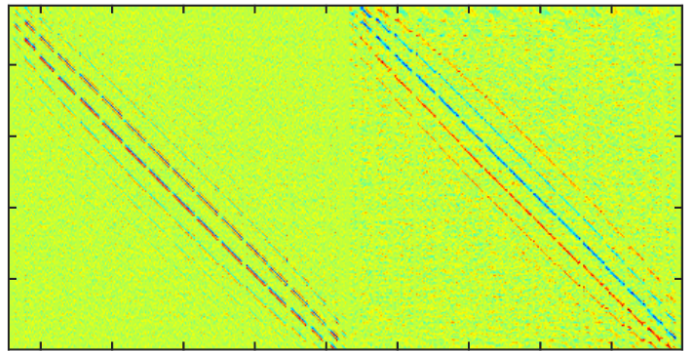
That way, any IM^* can be expressed:

$$IM^* = \alpha_0 IM_0 + \alpha_x \delta IM_x + \alpha_y \delta IM_y + \alpha_{rot} \delta IM_{rot} + \alpha_{magn} \delta IM_{magn} \quad (9)$$

The orthogonality of the δIM_α is ensured by the normalization of IM_0 that gives the scaling factor α_0 . The misregistration parameters $\alpha_x, \alpha_y, \alpha_{rot}$ and α_{magn} can be obtained by projecting the IM^* on the sensibility matrix.



(a) Sensibility of the misregistration identification process



(b) Noisy zonal IM (DM Actuators \times WFS slopes) retrieved from closed-loop data (40 000 frames with $\Delta T=5$)

Figure 8: Using closed loop data to track the misregistration of the system

To validate this process of identification and study its sensitivity, first tests have been done by generating 10 synthetic IM (noise-free) with an X shift starting from 0% to a full subaperture with a step of 10%. These IM are then projected on 3 different δIM built with a different shift in X: 10%, 50% and 100% of a subaperture. The result is displayed in 8a and shows the linear regime for the identification. In Figure 8b is displayed an exemple of Noisy IM that was retrieved using 40 000 iterations and a step ΔT of 5. The identification of misregistrations from such a noisy IM is still on-going work.

5. A CALIBRATION STRATEGY FOR THE ELT

The goal is here to present a first calibration strategy for the ELT, taking in consideration the actual methods studied in this paper to overcome the ELT constraints. The strategy is illustrated in Figure 9.

Without any calibration source, the first IM of the system would be generated synthetically from models and using an M4 like SLM (Spatial Light Modulator DM with a large number of actuators) during the AIT phase. This synthetic IM would be used during the first commissioning night to get a measurement of the IM on-sky that would take into account any difference with the model.

This measurement of the IM would then feed the models of the WFS and DM to generate a first PSIM. The PSIM would be used to start the operations and would be regularly updated using the misregistration identifications provided by the closed loop data. In case of performance drop we could imagine a calibration night during which the IM is acquired on-sky again to update the models and start using a PSIM again.

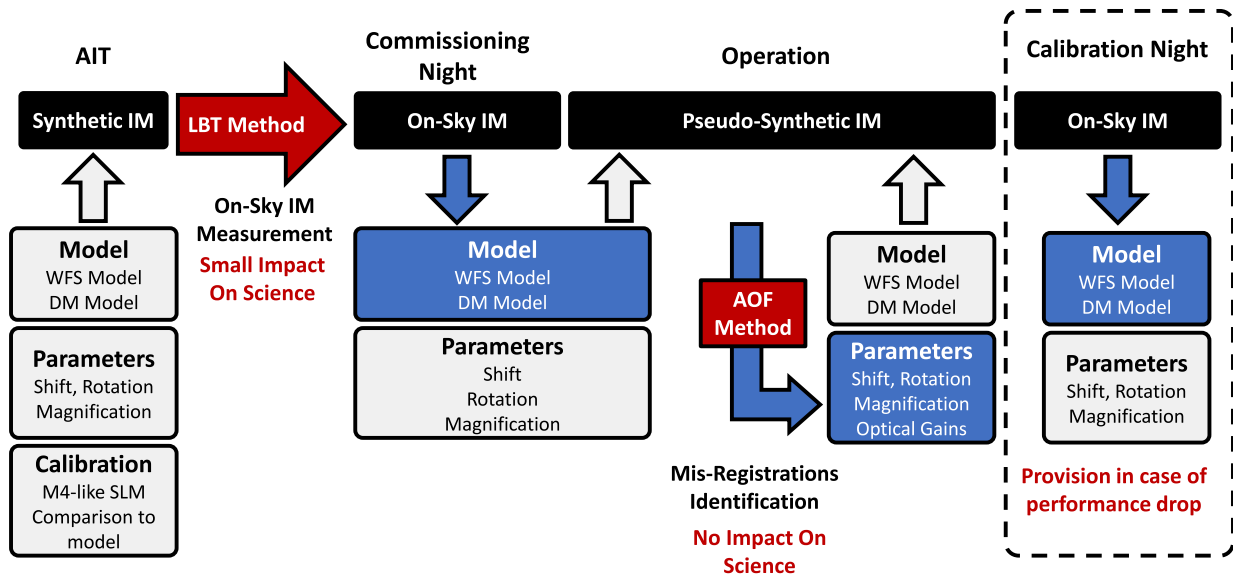


Figure 9: Proposal for a calibration strategy for the ELT

6. CONCLUSION AND PERSPECTIVES

In this communication, we have presented the context of the AO calibration for the first generation of ELT instruments, pointing out the main challenges that need to be overcome to benefit from the full potential of the telescope.

The first method investigated using an on-sky IM has been validated in simulations, and provided interesting results even using large misregistration but only using a medium-order AO system. Using it for a high order system with large misregistrations remains to be investigated as it may need a long calibration time. Optimization of the method are still on-going work.

The second method based on PSIM seems to be ideal for an ELT as it has no impact on science and generate noise-free IM but it relies on complex models with fast and accurate misregistrations identification. Although accurate misregistrations identifications were achieved at the AOF using closed loop data, this wasn't achieved yet using our numerical simulations with Pyramid WFS. Moreover, as the Pyramid WFS model will be extremely complex for the ELT, a thorough study is necessary to reach the precision necessary to use it and generate PSIM. This method remains then to be investigated, also because the amplitude of the misregistrations will be much larger and will evolve regularly with the telescope (based on an ESO internal study for the first generations of instruments of the ELT).

In any case, a fast and accurate identification of the misregistrations is necessary. If this can be done using closed loop data, it will provide an impact-free identification, ideal for a PSIM-based calibration. If not, what could be done is to use the on-sky calibration method of modulation/demodulation process using either specific patterns or modes to identify misregistrations but this remains to be investigated.

ACKNOWLEDGMENTS

This project has received funding from the European Union's Horizon 2020 research and innovation programme under grant agreement No 730890. This material reflects only the authors views and the Commission is not liable for any use that may be made of the information contained therein.

REFERENCES

- [1] Oberti, S., Quirós-Pacheco, F., Esposito, S., Muradore, R., Arsenault, R., Fedrigo, E., Kasper, M., Kolb, J., Marchetti, E., Riccardi, A., et al., "Large DM AO systems: synthetic IM or calibration on sky?," in [*Proc. SPIE*], **6272**, 627220 (2006).
- [2] Kolb, J., Madec, P.-Y., Louarn, M. L., Muller, N., and Béchet, C., "Calibration strategy of the AOF," in [*Proc. of SPIE Vol*], **8447**, 84472D-1 (2012).
- [3] Kolb, J., "Review of ao calibrations, or how to best educate your AO system," in [*SPIE Astronomical Telescopes+ Instrumentation*], 99090K-99090K, International Society for Optics and Photonics (2016).
- [4] Pieralli, F., Puglisi, A., Quirós-Pacheco, F., and Esposito, S., "Sinusoidal calibration technique for Large Binocular Telescope system," *Adaptive Optics Systems N. Norbert Hubin and EM Claire and and PL Wizinowich and eds* **7015**, 70153A (2008).
- [5] Esposito, S., Tubbs, R., Puglisi, A., Oberti, S., Tozzi, A., Xompero, M., and Zanotti, D., "High SNR measurement of interaction matrix on-sky and in lab," *Proc.SPIE* **6272**, 6272 – 6272 – 8 (2006).
- [6] Pinna, E., Quirós-Pacheco, F., Riccardi, A., Briguglio, R., Puglisi, A., Busoni, L., Arcidiacono, C., Argomedo, J., Xompero, M., Marchetti, E., et al., "First on-sky calibration of a high order adaptive optics system," in [*Proc. SPIE*], **8447**, 84472B (2012).
- [7] Kolb, J., Muller, N., Aller-Carpentier, E., Andrade, P., and Girard, J., "What can be retrieved from adaptive optics real-time data?," in [*Proc. of SPIE Vol*], **8447**, 84475U-1 (2012).
- [8] Béchet, C., Kolb, J., Madec, P.-Y., Tallon, M., and Thiébaud, E., "Identification of system misregistrations during ao-corrected observations," (2011).
- [9] Béchet, C., Tallon, M., and Thiébaud, E., "Optimization of adaptive optics correction during observations: Algorithms and system parameters identification in closed-loop," in [*SPIE Astronomical Telescopes+ Instrumentation*], 84472C-84472C, International Society for Optics and Photonics (2012).
- [10] Vernet, E., Cayrel, M., Hubin, N., Mueller, M., Biasi, R., Gallieni, D., and Tintori, M., "Specifications and design of the E-ELT M4 adaptive unit," in [*Adaptive Optics Systems III*], **8447** (2012).
- [11] Kasper, M., Fedrigo, E., Looze, D. P., Bonnet, H., Ivanescu, L., and Oberti, S., "Fast calibration of high-order adaptive optics systems," *JOSA A* **21**(6), 1004-1008 (2004).
- [12] Meimon, S., Fusco, T., and Petit, C., "An optimized calibration strategy for high order adaptive optics systems: the slope-oriented Hadamard actuation," in [*1st AO4ELT conference-Adaptive Optics for Extremely Large Telescopes*], 07009, EDP Sciences (2010).
- [13] Conan, R., Correia, C., et al., "Object-oriented Matlab adaptive optics toolbox," SPIE (2014).
- [14] Roddier, N., "Atmospheric wavefront simulation using Zernike polynomials," *Optical Engineering* **29**(10), 1174-1180 (1990).

**D. SPIE Conference Proceeding:
Analysis of AO modelling for
Pseuo-Synthetic Interaction Matrix
at the LBT.**

Analysis of AO modeling for pseudo-synthetic interaction matrix at the LBT

Cedric T. Heritier^{a,b,c,d}, Simone Esposito^c, Thierry Fusco^{b,a}, Benoit Neichel^a, Sylvain Oberti^d, Guido Agapito^c, Alfio Puglisi^c, Enrico Pinna^c, Carlos Correia^a, Jean-François Sauvage^b, Pierre-Yves Madec^d, Johann Kolb^d, and Fernando Quiros-Pacheco^e

^a Aix Marseille Univ, CNRS, CNES, LAM, Marseille, France

^bONERA, DOTA, Unité HRA, 29 avenue de la division Leclerc, 92322 Chatillon, France

^cINAF - Osservatorio Astrofisico di Arcetri Largo E. Fermi 5, 50125 Firenze, Italy

^dEuropean Southern Observatory, Karl-Schwarzschild-str-2, 85748 Garching, Germany

^eGMTO Corporation, 465 N. Halstead, Suite 250, Pasadena, CA 91107 USA

ABSTRACT

The performance of an Adaptive Optics (AO) System relies on the accuracy of its Interaction Matrix which defines the opto-geometrical link between the Deformable Mirror (DM) and the Wave Front Sensor (WFS). Any mis-registrations (relative shifts, rotation, magnification or higher order pupil distortion) will strongly impact the performance, especially for high orders AO systems. Adaptive Telescopes provide a constraining environment for the AO calibration with large number of actuators DM, located inside the telescope with often no access to a calibration source and with a high accuracy required. The future Extremely Large Telescope (ELT) will take these constraints to another level with a longer calibration time required, no artificial calibration source and most of all, frequent updates of the calibration during the operation. To overcome these constraints, new calibration strategies have to be developed either doing it on-sky or working with synthetic models. The most promising approach seems to be the Pseudo-Synthetic Calibration. The principle is to generate the Interaction Matrix of the system in simulator, injecting the correct model alignment parameters identified from on-sky Measurements. It is currently the baseline for the Adaptive Optics Facility (AOF) at the Very Large Telescope (VLT) working with a Shack-Hartmann WFS but it remains to be investigated in the case of the Pyramid WFS.

Keywords: Adaptive Optics, Calibration, Interaction Matrix, ELT, On-Sky Interaction Matrix, Pseudo-Synthetic Interaction Matrix

1. INTRODUCTION

The good behavior of any AO system relies on the quality of its calibration. Defining accurately the link between each actuator of the DM and the corresponding WFS subapertures is indeed necessary to produce the surface that corresponds to the optical aberrations measured by the WFS. This information is stocked in the Interaction Matrix of the system which concatenates the WFS signals corresponding to a set of calibration patterns, chosen to span the entire space of the DM. The calibration is however only valid at the time of the measurement and if the system registration evolves during the operation, the system performance will be impacted. Updating the calibration becomes then necessary.

The particular design of the adaptive telescopes provides a constraining environment for the AO calibration: The DM has usually a large number of actuators to provide a high order AO correction to the instruments and is located inside the telescope, far away from the WFS and often with no access to a calibration source. These two features establish two major constraints as it can take a long time to calibrate the system, taking in consideration that the ASM/WFS registration may evolve faster in time than for a post-focal AO system and requiring thus regular updates of the corresponding calibration. In the case of a high order AO system, the sensitivity to such mis-registrations becomes critical and a high accuracy calibration is necessary.

The future Extremely Large Telescope (ELT) will push these constraints to another level with a larger number

Further author information: E-mail: cedric.heritier@lam.fr / heritier@arcetri.astro.it / cheritie@eso.org

of actuator (4356) and a larger distance between WFS and DM. Updating the calibration regularly during the operation will then be required as the size and weight of the telescope will create larger mechanical constraints and thus lead to misalignments of diverse optical systems, resulting in mis-registrations between the DM and the WFS.

To overcome these constraints, new strategies have been investigated, by speeding up the measurement^{1,2} or changing the way to estimate the interaction matrix, working on synthetic models³ or measuring it on-sky.^{4,5}

The on-sky approach consists in measuring experimentally the interaction matrix, finding a way to get rid of the turbulence effects. This approach ensures to have a direct calibration of the system registration at the time of the measurement but can become demanding in terms of telescope time for large number of actuators systems and is thus not suited for regular updates. The sensitivity to the seeing conditions is still to be investigated, especially for a Pyramid WFS, and if such a calibration is done during the operations, the impact on science has to be quantified. The two main on-sky strategies consists in using a fast push-pull measurement to freeze the turbulence or to multiplex signals on the DM and retrieve their signature in the WFS space using a demodulation process.⁶

The synthetic approach consists in reproducing the behavior of the AO systems in simulator to generate synthetically the interaction matrix of the system, injecting mis-registrations parameters to replicate the registration of the real system. That way, a fast update of the calibration becomes easy and fast to achieve. It relies only on a good estimation of the mis-registrations parameters. Therefore, the community has been converging toward this pseudo-synthetic approach that takes advantage of both strategies: The calibration data are generated from a simulator to provide fast updates and the model mis-registrations parameters measured using on-sky data/measurements. The principle of the pseudo synthetic approach is summarized in Figure 1

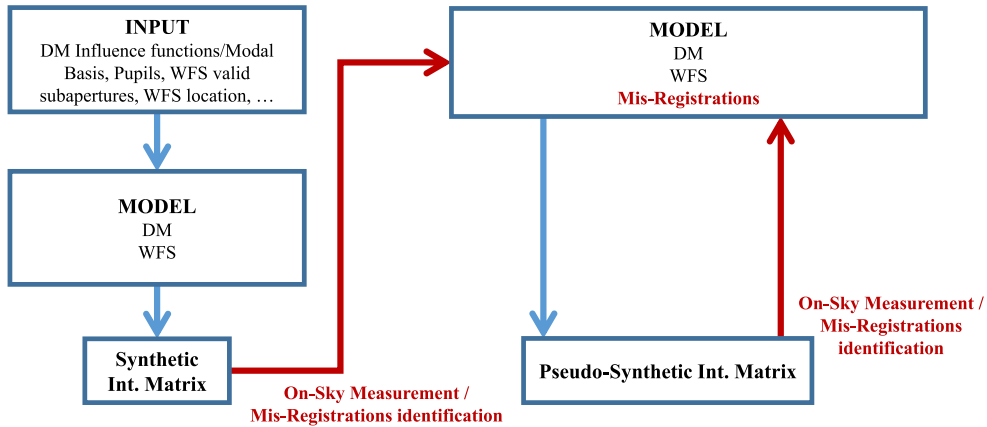


Figure 1: Pseudo-Synthetic Calibration: Experimental data/measurements are required to update a synthetic model and generate a Pseudo-Synthetic Interaction Matrix that is regularly updated using experimental inputs.

In terms of state of the art, modeling efficiently an AO system to generate calibration data for the telescope has been demonstrated on various systems, at the Very Large Telescope³ or at the Large Binocular Telescope.⁴ To track the mis-registrations during the operation, some methods have also been validated using either telemetry data⁷ or WFS signals.⁸

Focusing on the calibration of the AOF, the Pseudo Synthetic approach is currently the baseline for all the AO modes, using a Shack Hartmann WFS. In practice, the Interaction Matrix is updated every 5 minutes, using telemetry data to retrieve the mis-registrations parameters.³

The purpose of this study is to analyze the feasibility of the pseudo-synthetic approach in the case of a Pyramid WFS, more complex than a SH-WFS with a modal linearity and sensitivity that depends on the seeing conditions. This communication focuses on the development of a model of the LBT-FLAO system⁹ described

in section 2. Section 3 describes the model alignment procedure. The analysis and validation of the model in simulator is developed in section 4.

2. MODELLING OF THE FLAO SYSTEMS

To provide an efficient synthetic based calibration, two key-elements are necessary: an accurate simulator and the good values for the mis-registrations parameters. In our case, we developed our model in the OOMAO simulator,¹⁰ a full end to end AO simulator. To reproduce accurately the behavior of FLAO, we focused on the two key-elements of the AO system: the ASM and Pyramid WFS.

The ASM model is composed of 663 actuators (+ 9 broken actuators) disposed in circular concentric rings with a 30 cm radial pitch. We take the influence functions measurements from interferometer as a direct input to take in consideration all the features of the real system. The commands producing the KL modes on the ASM are also used in the simulator to generate the corresponding modes.

The Pyramid WFS is designed to reproduce the geometry of the FLAO WFS, producing pupils of 30 pixels with centers separated of 36 pixels, using a modulation of $3 \lambda/D$ and the central wavelength for the wavefront sensing at 750 nm. We impose the valid subapertures map to the model and set its position to maximize the light in the corresponding subapertures. We also normalize the WFS signals to be in line with a double pass measurement using a retro-reflector and adjust the WFS slopes signs to match with the WFS location according to the side of the telescope.

Finally, to retrieve the good registration between ASM and WFS, we used the current interaction matrix used at the telescope as a reference to identify **5 mis-registrations parameters**: shifts α_x and α_y , rotation α_{rot} and magnifications α_{mx} and α_{my} . We define α as the mis-registrations vector :

$$\alpha \triangleq \{\alpha_x, \alpha_y, \alpha_{rot}, \alpha_{mx}, \alpha_{my}\} \quad (1)$$

In practice, we interpolated the ASM influence functions measurements to apply the desired rotation and magnification and we shifted the pyramid pupils to provide a sub-pixel sensitivity.

At the LBT, the baseline for the AO mode is to control 400 KL modes. We reproduced the corresponding calibration procedure to compute the interaction matrix, using a standard SVD to get the command matrix without truncating any mode. The generation of the Interaction Matrix is achieved around the zero-point of the Pyramid WFS to avoid any non-linear effect. A summary of the model definition, indicating the inputs from the telescope and the outputs of the model is given in Figure 2.

3. ASM/WFS MIS-REGISTRATIONS CALIBRATION

3.1 Model Alignment Procedure

The main challenge of the synthetic calibration is to reproduce the registration between the ASM and Pyramid models to match with the real system. To do so, we extract these parameters from the current interaction matrix used at the telescope. The difficulty here is that these parameters are strongly correlated and we need to define an iterative procedure to get the correct estimation of the parameters.

We define σ_j as the Root Mean Square Error (RMSE) between the synthetic WFS measurement $Y^*(\alpha)$ in the configuration α and the reference WFS measurement Y of the mode j :

$$\sigma_j = RMSE(Y_j, Y_j^*(\alpha)) = \sqrt{\frac{1}{N_S} \sum_{n=1}^{N_S} |Y_j - Y_j^*(\alpha)|^2} \quad (2)$$

where N_S is the number of WFS slopes.

The alignment procedure consisted in minimizing the quadratic norm of $\sigma_N = \{\sigma_i\}_{i=1,2,\dots,N}$ adjusting α and eventually playing on the number of modes N :

$$\chi_N(\alpha) = arg_{min} \|\sigma_N\|_2 \quad (3)$$

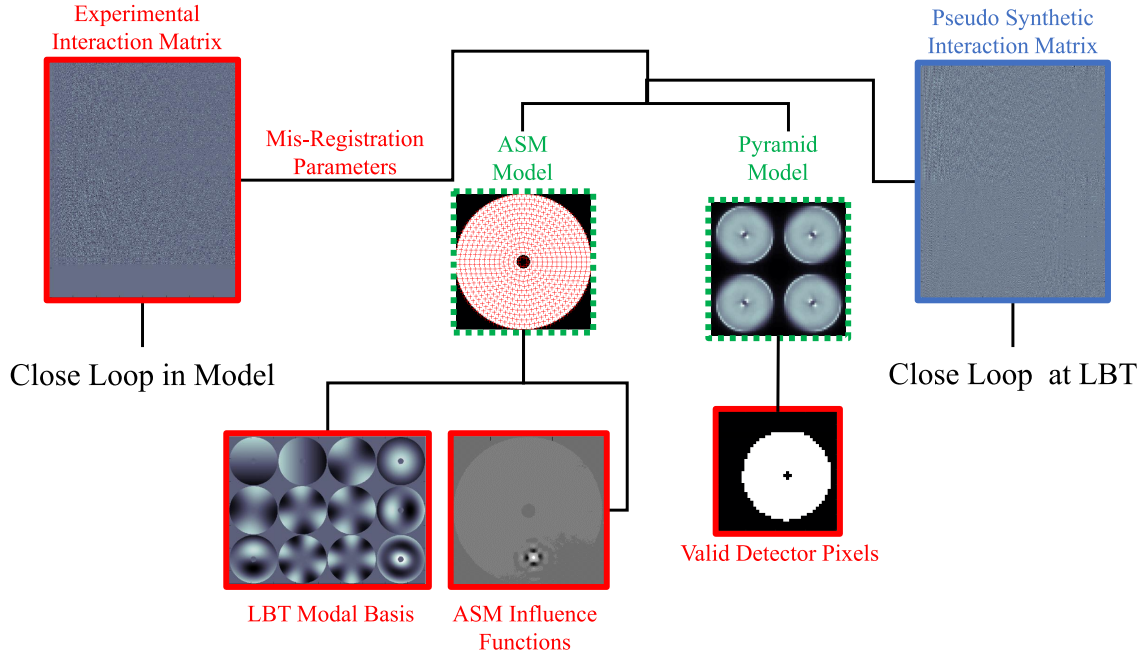


Figure 2: Summary of the model definition. Red lines represent the experimental inputs and green lines the synthetic data.

We make the assumption that the optimal value for the mis-registrations parameters is the iterative minimization of χ_{400} using all the reference signals available. In practice, the shifts and rotation are the most critical parameters to adjust (See Figure 12). Therefore the iterative procedure consisted in setting these parameters first and then adjust the magnification. Two steps were enough to converge to a satisfying estimation of the mis-registrations parameters. The last estimation for each parameter is given in Figure 3. As a final step, we tune the amplitude of the KL modes to minimize the RMS of the residual slopes with respect to the reference Interaction Matrix.

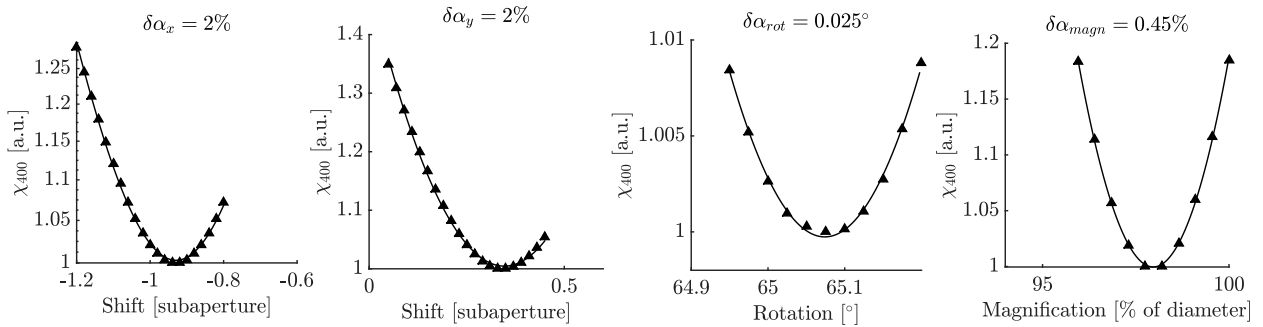


Figure 3: Last estimation of the mis-registrations parameters.

3.2 Impact of the numbers of reference signals on the parameters estimation

A pseudo-synthetic calibration requires to regularly update the mis-registrations parameters that could evolve during the operations. One possible approach consists in dithering signals on the DM to retrieve their signatures

in the WFS space and the corresponding mis-registrations parameters. However, the type and number of signals required is still to be investigated as no clear optimization has been identified yet. In our case, we only have KL modes signals to consider and we could study the impact of the number of modes necessary to align our model.

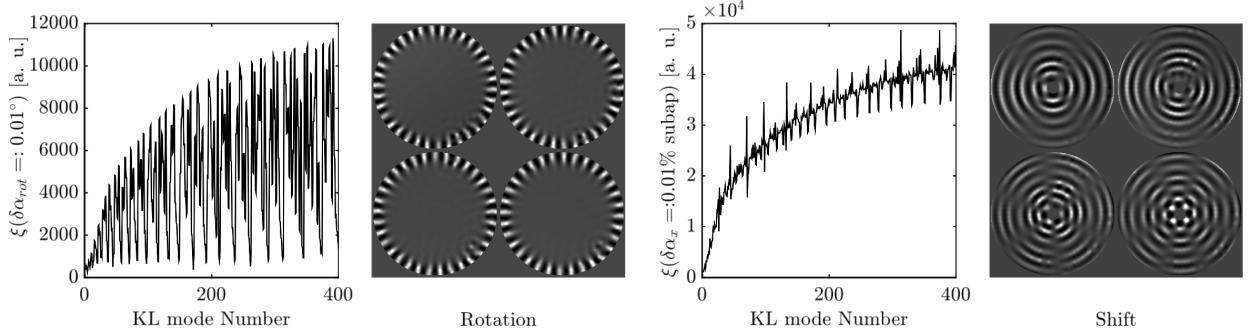


Figure 4: Sensitivity of the KL modes to a rotation (Left) and a shift (Right) displaying the modes with the highest sensitivity.

The first step consists in sorting the KL modes by their sensitivity to a given mis-registration. We define $\xi_j(\alpha_i)$ the sensitivity of the mode j to a mis-registration α_i as the RMSE of the WFS slopes for a step $\delta\alpha_i$:

$$\xi_j(\delta\alpha_i) \triangleq RMSE(Y_j(\alpha_i), Y_j(\alpha_i + \delta\alpha_i)) \quad (4)$$

Figure 4 shows that, globally, the sensitivity to a shift increases with the spatial frequency (and thus with the number of the mode) while this evolution is more complex for a rotation. Since the modes mostly have a circular symmetry, this plot can evolve when considering higher values of rotation such as 10, 30 or 45 degrees but we make the assumption that our working point is close enough not to consider these values. In the following of the paper, the modes are ordered according to their sensitivity to the studied mis-registration.

The second step is to quantify the error on the estimation of the parameters as a function of the number of modes N used to minimize χ_N . This work is still on going and we show here only preliminary results for the estimation of the rotation (see Figure 5). This seems to show that the number of modes necessary can be reduced to less than 10 modes. Studying other specific patterns could also provide a gain in speed and SNR but remains to be investigated.

4. MODEL ANALYSIS

4.1 Numerical Validation

4.1.1 Direct Comparison of WFS Signals

The first step consists in comparing the synthetic WFS signals with the experimental ones. This is provided in Figure 6 which shows that both interaction matrices are almost identical, validating the good quality of the model. We can notice however that second order features are missing from the synthetic model signals: in the experimental data, a few subapertures seem to be less illuminated than others, especially close to the central the experimental measurement as evolving a lot between two experimental Interaction Matrices. This is well illustrated in Figure 7. These are thus not reproduced in the simulator as we consider a perfect illumination of the pyramid and taken into account these features in the model is still to be investigated. However, this should not be problematic as the most important feature remains the ASM/WFS registration.

As an additional information, Figure 8 shows that both model and real system have a similar sensitivity to the KL modes and the same stability with a similar conditioning number and similar eigen Values spectra. The residual differences between both curves can be explained by the fact that the synthetic Interaction Matrix is noise-free, we can then expect that the knee of the eigen values distribution for a higher eigen mode number, which is clearly visible on the plot.

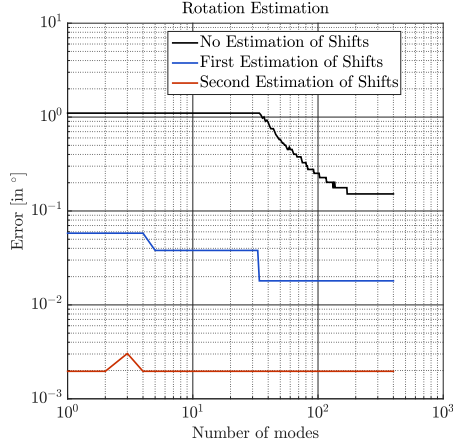


Figure 5: Error on the estimation of the rotation as a function of the number of reference signals used for the identification. In that case the reference is a synthetic Interaction Matrix. The results are given for each step of the alignment procedure: between two estimations of the rotation, both values of shifts are updated.

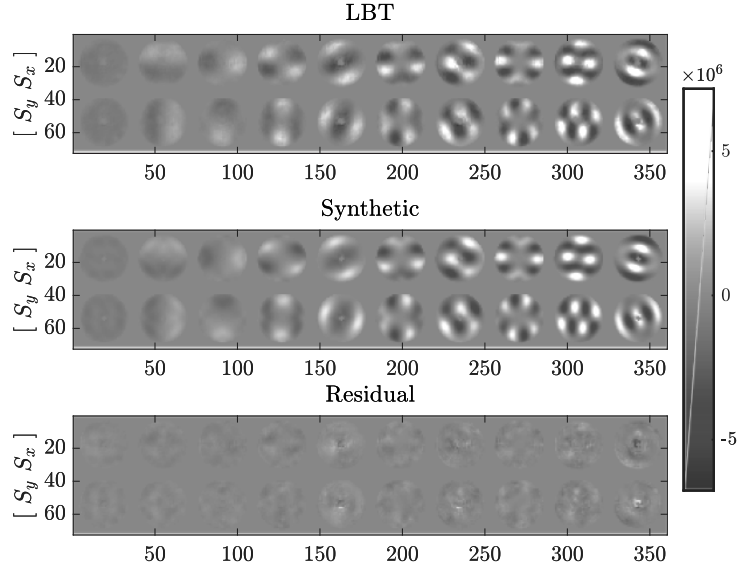


Figure 6: Comparison between synthetic and experimental WFS Slopes Maps for the uneven KL modes from 1 to 19.

4.1.2 Closed Loop Performance in Simulator

Estimating the quality of a synthetic Interaction Matrix can be complex as this object relies essentially on experimental measurements and on the registration between WFS and DM. Therefore the easiest way consists in testing it in closed loop on the real system to evaluate the AO performance. The first milestone of this work was then to efficiently close the loop of the simulator using the experimental Interaction Matrix from LBT.

This is basically the opposite of our initial goal but it provides already a first indication of the model quality: if an experimental Interaction Matrix can be used to close the loop in simulator, the model should be representative enough of the real system. Figure 9 displays the performance for the same turbulent phase screens with and without aliasing (projecting the turbulence on the modal basis controlled by the DM). We can still see small

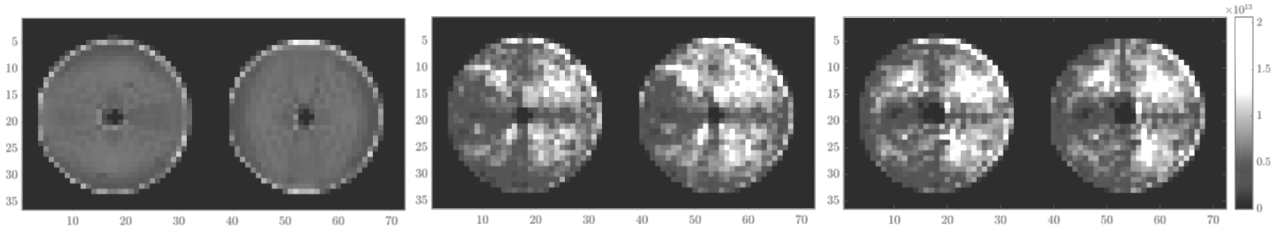


Figure 7: Variance Map of the WFS Slopes over the 400 KL modes using a synthetic Interaction Matrix (Left) and an experimental one from 2016 (Center) and 2017 (Right). In the synthetic case, the ring on the border of the pupil is due to the interpolation errors of the Influence Functions measurements.

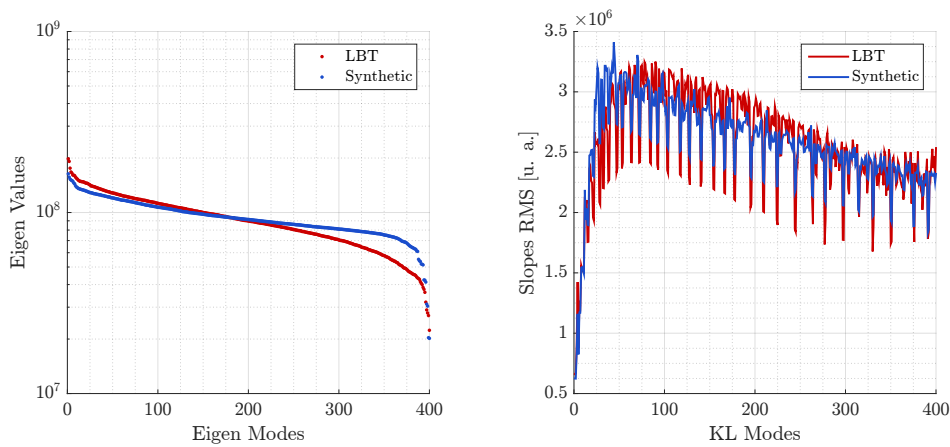


Figure 8: Left: Eigen Values Spectra: Conditioning numbers are 8.1 in the synthetic case and 8.85 in the experimental case. Right: Slopes RMS of both Interaction Matrix for the 400 KL modes showing that the sensitivity of the Pyramid WFS is well reproduced in the simulator.

differences in the performance but globally the correction is equivalent which validates the model quality and pushes to consider the final step of the model validation: an experimental test at the LBT.

4.2 Sensitivity to Mis-Registrations

4.2.1 Characterization of a Mis-Registration,

In presence of large amplitude mis-registrations, some specific moving patterns can be visible displaying the DM actuator position/force map. Here we want to detect the smallest mis-registration possible with respect to the reference Interaction Matrix, effect that would not be visible using the ASM positions. Such signature can however be identified in the residual phase screens that are accessible in simulator.

To be able to isolate this small effect, one needs to consider the error budget that is defined as the sum of all the relevant contributors (fitting, aliasing, temporal error, noise, calibration error and model) to the residual phase variance $\sigma_{\Phi_{res}}^2$:

$$\begin{aligned} \sigma_{\Phi_{res}}^2 = & \sigma_{\Phi_{fitting}}^2 + \sigma_{\Phi_{aliasing}}^2 + \sigma_{\Phi_{temporal}}^2 \\ & + \sigma_{\Phi_{noise}}^2 + \sigma_{\Phi_{calib}}^2 + \sigma_{\Phi_{model}}^2 \end{aligned} \quad (5)$$

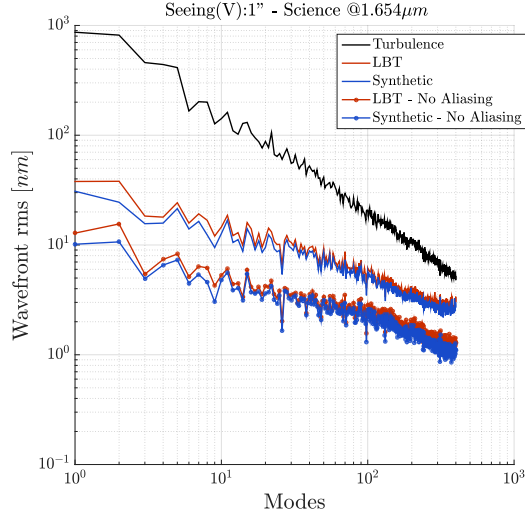


Figure 9: Comparison of Closed Loop performance in simulator. The correction is almost identical and confirms the good quality of the synthetic model and its alignment.

We are only interested in $\sigma_{\Phi_{model}}^2$ and we can cancel out some terms of the error budget: $\sigma_{\Phi_{noise}}^2$ can be disabled and the turbulence phase can be projected on the modal basis controlled by the ASM to get rid of the fitting and aliasing effects. Moreover, for the purpose of the model alignment, it can be interesting to close the loop of the model on a static phase screen getting rid of the temporal delay and any effect related to the wind direction. That way, in presence of eventual mis-registrations between the model and the reference Interaction Matrix, some specific moving patterns are visible in the residual phase screen. These patterns are a direct signature of the mis-registration type as illustrated in Figure 10 where we can clearly see how the correction is mis-applied.

In the case of a shift, one will see fringes moving in the direction of the corresponding shift. Superposing the actuators coordinates and the corresponding average patterns shows that both are extremely correlated. This makes sense as a shift will impact all the subapertures equally. However, in the case of a rotation, the residual phase screens displays a rotating pattern that corresponds to a mode controlled in the Interaction Matrix. These modes correspond actually to the most sensitive modes identified in Figure 4.

These features could be useful for the model alignment purpose. Once that the mis-registrations parameters are correctly set, the patterns disappear and second order model errors, already identified in Figure 7, become visible. The corresponding impact on the closed loop (see Figure 11) is a second order effects and will not impact the performance. This however confirms the good alignment of the model.

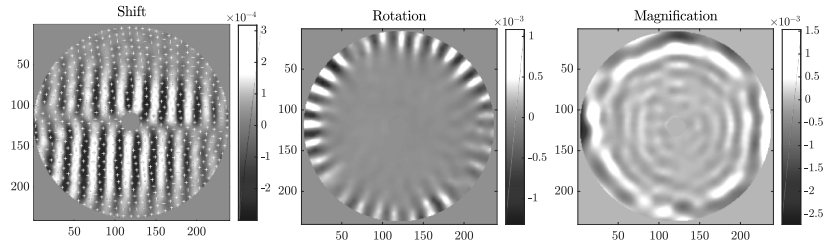


Figure 10: Typical patterns of the residual phase (in rad) closing the loop on a static phase screen for different types of mis-registrations. Left: shift of 20 % of a subaperture superposing the actuators coordinates, Middle: Rotation of 0.5° , Right: magnification of 98 % of the pupil.

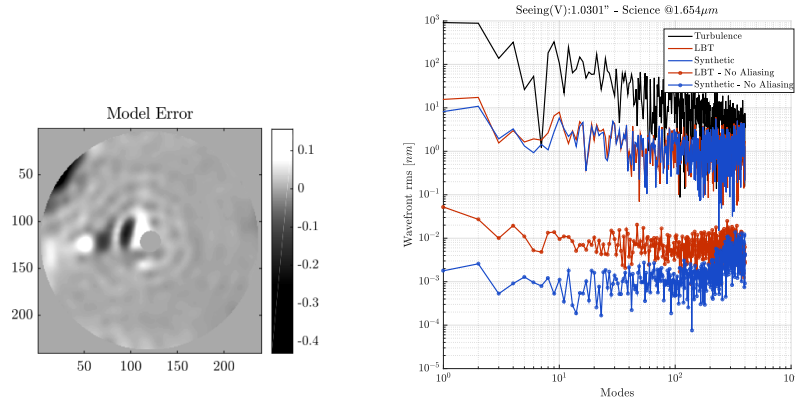


Figure 11: Left: Residual Phase Screen closing the loop on a static pattern with the experimental Interaction Matrix in the simulator. The patterns visible correspond to the model errors identified in Figure 7. Right: Corresponding Modal PSD showing that these errors are negligible and that the model is correctly aligned.

4.2.2 Impact on the performance

For an AO system with Shack Hartmann WFS, the common rule is not to exceed an mis-registration of 10 % of a subaperture. This result has to be taken carefully as the sensitivity to a mis-registration will depend on the DM geometry and on the number and type of modes controlled in the Interaction Matrix. Using our model of Pyramid WFS and ASM with circular geometry, we could simulate the impact of each type of mis-registrations in terms of Strehl Ratio. The results are presented in Figure 12 and show that the rotation and the shift are the most critical parameters while the impact of a magnification becomes problematic when controlling a high number of modes only.

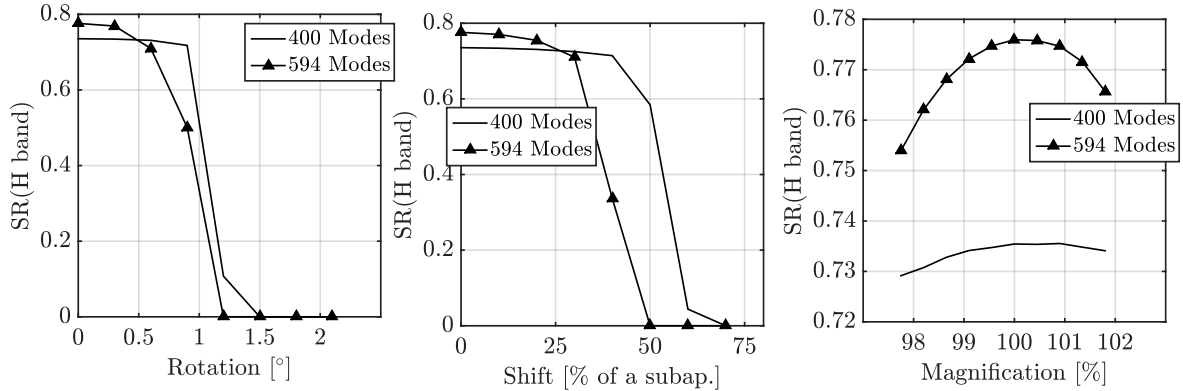


Figure 12: Impact of mis-registrations on the performance in simulation. Results are given for two configurations, controlling 400 and the maximum number, 594 modes.

5. CONCLUSION AND PERSPECTIVES

We could develop a synthetic model of the LBT AO system, focusing on the ASM and Pyramid WFS. We could identify the ingredients required from the telescope: Modal basis, ASM influence functions, WFS geometry and valid subapertures and the key elements : the mis-registrations parameters. Concerning this last element, we established an iterative alignment procedure to calibrate the mis-registrations between the ASM and the WFS using WFS signals.

The synthetic model has then been intensely validated against experimental data in simulator. The first milestone of this study was to close the AO loop in simulator using the experimental Interaction Matrix, and obtain equivalent AO correction, confirming the good quality of the model.

Moreover, we could study the sensitivity of the KL modes to the different types of mis-registrations and quantify the impact on the performance for a system in the LBT configuration. We are also currently studying the cost of reducing the number of reference signals on the estimation of the mis-registrations parameters. Preliminary results show that only a few well-chosen signals can be enough to align the model.

The model seems now ready to be tested on the real system for experimental validation. This should be possible using day-time test at LBT, controlling the telescope in remote. If possible, we will also study experimentally the sensitivity of the model to mis-registrations errors. Another interesting test would be to retrieve a few calibration signals on-sky and try to align the model from it. This would be complimentary to the analysis of number of modes required as it will provide information on the SNR of the on-sky signals required to get a satisfying estimation of the mis-registrations parameters.

ACKNOWLEDGMENT

This project has received funding from the European Union's Horizon 2020 research and innovation programme under grant agreement No 730890. This material reflects only the authors views and the Commission is not liable for any use that may be made of the information contained therein.

REFERENCES

- [1] Kasper, M., Fedrigo, E., Looze, D. P., Bonnet, H., Ivanescu, L., and Oberti, S., "Fast calibration of high-order adaptive optics systems," *JOSA A* **21**(6), 1004–1008 (2004).
- [2] Meimon, S., Petit, C., and Fusco, T., "Optimized calibration strategy for high order adaptive optics systems in closed-loop: the slope-oriented hadamard actuation," *Opt. Express* **23**, 27134–27144 (Oct 2015).
- [3] Kolb, J., Madec, P.-Y., Louarn, M. L., Muller, N., and Béchet, C., "Calibration strategy of the AOF," in [*Proc. of SPIE Vol.*], **8447**, 84472D–1 (2012).
- [4] Pinna, E., Quirós-Pacheco, F., Riccardi, A., Briguglio, R., Puglisi, A., Busoni, L., Arcidiacono, C., Argomedo, J., Xompero, M., Marchetti, E., et al., "First on-sky calibration of a high order adaptive optics system," in [*Proc. SPIE*], **8447**, 84472B (2012).
- [5] Kellerer, A., Vidal, F., Gendron, E., Hubert, Z., Perret, D., and Rousset, G., "Deformable mirrors for open-loop adaptive optics," in [*Adaptive Optics Systems III*], **8447**, 844765, International Society for Optics and Photonics (2012).
- [6] Oberti, S., Quirós-Pacheco, F., Esposito, S., Muradore, R., Arsenault, R., Fedrigo, E., Kasper, M., Kolb, J., Marchetti, E., Riccardi, A., et al., "Large DM AO systems: synthetic IM or calibration on sky?," in [*Proc. SPIE*], **6272**, 627220 (2006).
- [7] Béchet, C., Kolb, J., Madec, P.-Y., Tallon, M., and Thiébaud, E., "Identification of system misregistrations during AO-corrected observations," *AO4ELT II Conference* (2011).
- [8] Neichel, B., Parisot, A., Petit, C., Fusco, T., and Rigaut, F., "Identification and calibration of the interaction matrix parameters for ao and mcao systems," in [*Proc. SPIE*], **8447**, 84475N (2012).
- [9] Esposito, S., Riccardi, A., Fini, L., Puglisi, A. T., Pinna, E., Xompero, M., Briguglio, R., Quirós-Pacheco, F., Stefanini, P., Guerra, J. C., et al., "First light AO (FLAO) system for LBT: final integration, acceptance test in europe, and preliminary on-sky commissioning results," in [*Adaptive Optics Systems II*], **7736**, 773609, International Society for Optics and Photonics (2010).
- [10] Conan, R., Correia, C., et al., "Object-oriented Matlab adaptive optics toolbox," SPIE (2014).

Bibliography

- [All+08] Emmanuel Aller-Carpentier et al. “High order test bench for extreme adaptive optics system optimization”. In: *Adaptive Optics Systems*. Vol. 7015. International Society for Optics and Photonics. 2008, 70153Z (cit. on p. 90).
- [Ars+06] R Arsenault et al. “A deformable secondary mirror for the VLT”. In: *Advances in Adaptive Optics II*. Vol. 6272. International Society for Optics and Photonics. 2006, p. 62720V (cit. on pp. 37, 38, 54).
- [Ars+08] R Arsenault et al. “ESO adaptive optics facility”. In: vol. 7015. 2008, pp. 7015–7015 (cit. on pp. 47, 53).
- [AWG06] François Assémat et al. “Method for simulating infinitely long and non stationary phase screens with optimized memory storage”. In: *Optics express* 14.3 (2006), pp. 988–999 (cit. on pp. 23, 139).
- [Bab53] Horace W Babcock. “The possibility of compensating astronomical seeing”. In: *Publications of the Astronomical Society of the Pacific* 65.386 (1953), pp. 229–236 (cit. on pp. 16, 23).
- [Bac+10] R Bacon et al. “The MUSE second-generation VLT instrument”. In: *Ground-based and Airborne Instrumentation for Astronomy III*. Vol. 7735. International Society for Optics and Photonics. 2010, p. 773508 (cit. on p. 53).
- [Béc+11] C Béchet et al. “Identification of system misregistrations during AO-corrected observations”. In: *AO4ELT II Conference* (2011) (cit. on p. 50).
- [BTT12] C Béchet et al. “Optimization of adaptive optics correction during observations: Algorithms and system parameters identification in closed-loop”. In: *SPIE Astronomical Telescopes+ Instrumentation*. International Society for Optics and Photonics. 2012, pp. 84472C–84472C (cit. on pp. 54, 133–135).
- [Bia+10] R Biasi et al. “Contactless thin adaptive mirror technology: past, present, and future”. In: *Adaptive Optics Systems II*. Vol. 7736. International Society for Optics and Photonics. 2010, 77362B (cit. on p. 37).
- [Bia+12] R Biasi et al. “VLT deformable secondary mirror: integration and electromechanical tests results”. In: *Adaptive Optics Systems III*. Vol. 8447. International Society for Optics and Photonics. 2012, 84472G (cit. on p. 38).
- [Bon+18a] CZ Bond et al. “Fourier wavefront reconstruction with a pyramid wavefront sensor”. In: *Adaptive Optics Systems VI*. Vol. 10703. International Society for Optics and Photonics. 2018, p. 107034M (cit. on p. 33).
- [Bon+18b] CZ Bond et al. “Optimized calibration of the adaptive optics system on the lam pyramid bench”. In: *Adaptive Optics for Extremely Large Telescopes* (2018) (cit. on pp. 28, 35).

- [Boy18] C Boyer. “Adaptive optics program at TMT”. In: *Adaptive Optics Systems VI*. Vol. 10703. International Society for Optics and Photonics. 2018, 107030Y (cit. on p. 47).
- [BMR90] C Boyer et al. “Adaptive optics: interaction matrix measurements and real time control algorithms for the COME-ON project”. In: *Adaptive Optics and Optical Structures*. Vol. 1271. International Society for Optics and Photonics. 1990, pp. 63–82 (cit. on p. 39).
- [Bra+16] Bernhard R Brandl et al. “Status of the mid-infrared E-ELT imager and spectrograph METIS”. In: *Ground-based and Airborne Instrumentation for Astronomy VI*. Vol. 9908. International Society for Optics and Photonics. 2016, p. 990820 (cit. on pp. 28, 56).
- [Cha+ep] V Chambouleyron et al. “Pyramid WFS optical gains compensation using a convolutional model”. In: (in prep) (cit. on pp. 28, 35, 99, 105, 167).
- [CMM10] Alessandro Chiuso et al. “Dynamic calibration of adaptive optics systems: A system identification approach”. In: *IEEE Transactions on Control Systems Technology* 18.3 (2010), pp. 705–713 (cit. on p. 50).
- [Cir+18] M Cirasuolo et al. “The ELT in 2017: The year of the Primary Mirror”. In: *The Messenger* 171 (2018), pp. 20–23 (cit. on p. 56).
- [Clé+16] Yann Clénet et al. “Joint MICADO-MAORY SCAO mode: specifications, prototyping, simulations and preliminary design”. In: *Adaptive Optics Systems V*. Vol. 9909. International Society for Optics and Photonics. 2016, 99090A (cit. on pp. 28, 56).
- [Cle14] Christophe Clergeon. “Etude d’un analyseur de surface d’onde haute sensibilité pour l’optique adaptative extrême”. PhD thesis. Observatoire de Paris, 2014 (cit. on p. 31).
- [Clo+13] Laird M Close et al. “Diffraction-limited Visible Light Images of Orion Trapezium Cluster with the Magellan Adaptive Secondary Adaptive Optics System (MagAO)”. In: *The Astrophysical Journal* 774.2 (2013), p. 94 (cit. on pp. 27, 47).
- [Con94] Jean-Marc Conan. “Etude de la correction partielle en optique adaptative”. PhD thesis. Paris 11, 1994 (cit. on pp. 22, 23).
- [C+14] R Conan et al. “Object-oriented Matlab adaptive optics toolbox”. In: SPIE. 2014 (cit. on pp. 18, 22, 23).
- [Cor+10] SA Cornelissen et al. “MEMS deformable mirrors for astronomical adaptive optics”. In: *Adaptive Optics Systems II*. Vol. 7736. International Society for Optics and Photonics. 2010, p. 77362D (cit. on p. 37).
- [Cor+14] C Correia et al. “Static and predictive tomographic reconstruction for wide-field multi-object adaptive optics systems”. In: *JOSA A* 31.1 (2014), pp. 101–113 (cit. on p. 44).
- [Deo+18a] V Deo et al. “A modal approach to optical gain compensation for the pyramid wavefront sensor”. In: *Adaptive Optics Systems VI*. Vol. 10703. International Society for Optics and Photonics. 2018, p. 1070320 (cit. on pp. 28, 34, 35, 99, 100, 105).

- [Deo+18b] V Deo et al. “Assessing and mitigating alignment defects of the pyramid wavefront sensor: a translation insensitive control method”. In: *Astronomy & Astrophysics* 619 (2018), A56 (cit. on p. 31).
- [Deo+19] V Deo et al. “A telescope-ready approach for modal compensation of pyramid wavefront sensor optical gain.” In: (2019) (cit. on pp. 28, 35, 104).
- [Des98] Caroline Dessenne. “Commande modale et prédictive en optique adaptative”. PhD thesis. Paris 7, 1998 (cit. on p. 183).
- [DMR98] Caroline Dessenne et al. “Optimization of a predictive controller for closed-loop adaptive optics”. In: *Applied optics* 37.21 (1998), pp. 4623–4633 (cit. on p. 46).
- [Dio+16] E Diolaiti et al. “MAORY: adaptive optics module for the E-ELT”. In: *Adaptive Optics Systems V*. Vol. 9909. International Society for Optics and Photonics. 2016, p. 99092D (cit. on p. 57).
- [EA01] S Esposito et al. “Pyramid wavefront sensor behavior in partial correction adaptive optic systems”. In: *Astronomy & Astrophysics* 369.2 (2001), pp. L9–L12 (cit. on pp. 27, 32, 33).
- [Esp+06] S Esposito et al. “High SNR measurement of interaction matrix on-sky and in lab”. In: *Proc.SPIE* 6272 (2006), pp. 6272–6272. DOI: [10.1117/12.673514](https://doi.org/10.1117/12.673514) (cit. on p. 48).
- [Esp+10a] S Esposito et al. “First light AO (FLAO) system for LBT: final integration, acceptance test in Europe, and preliminary on-sky commissioning results”. In: *Adaptive Optics Systems II*. Vol. 7736. International Society for Optics and Photonics. 2010, p. 773609 (cit. on p. 38).
- [Esp+10b] S Esposito et al. “Laboratory characterization and performance of the high-order adaptive optics system for the Large Binocular Telescope”. In: *Applied Optics* 49.31 (2010), G174–G189 (cit. on pp. 51, 52, 59).
- [Esp+12] S Esposito et al. “Natural guide star adaptive optics systems at LBT: FLAO commissioning and science operations status”. In: *Adaptive Optics Systems III*. Vol. 8447. International Society for Optics and Photonics. 2012, 84470U (cit. on p. 27).
- [Esp+13] S Esposito et al. “LBT observations of the HR 8799 planetary system-First detection of HR 8799e in H band”. In: *Astronomy & Astrophysics* 549 (2013), A52 (cit. on p. 52).
- [Esp+15] S Esposito et al. “Non common path aberration correction with non linear WFSs”. In: *Adaptive Optics for Extremely Large Telescopes 4–Conference Proceedings*. Vol. 1. 1. 2015 (cit. on pp. 28, 35, 99).
- [Fau17] Olivier Fauvarque. “Optimisation des analyseurs de front d’onde à filtrage optique de Fourier”. PhD thesis. Aix-Marseille, 2017 (cit. on pp. 29, 33).
- [Fau+16] Olivier Fauvarque et al. “General formalism for Fourier-based wave front sensing”. In: *Optica* 3.12 (2016), pp. 1440–1452 (cit. on p. 35).

- [Fau+17] Olivier Fauvarque et al. “General formalism for Fourier-based wave front sensing: application to the pyramid wave front sensors”. In: *Journal of Astronomical Telescopes, Instruments, and Systems* 3.1 (2017), p. 019001 (cit. on pp. 28, 29).
- [Fau+19] Olivier Fauvarque et al. “Kernel formalism applied to Fourier-based wavefront sensing in presence of residual phases”. In: *JOSA A* 36.7 (2019), pp. 1241–1251 (cit. on pp. 28, 35, 105, 167).
- [Fea+11] Philippe Feautrier et al. “Ocam with ccd220, the fastest and most sensitive camera to date for ao wavefront sensing”. In: *Publications of the Astronomical Society of the Pacific* 123.901 (2011), p. 263 (cit. on pp. 28, 52).
- [Fri77] David L Fried. “Least-square fitting a wave-front distortion estimate to an array of phase-difference measurements”. In: *JOSA* 67.3 (1977), pp. 370–375 (cit. on pp. 36, 45).
- [Fri65] DL Fried. “Statistics of a geometric representation of wavefront distortion”. In: *JoSA* 55.11 (1965), pp. 1427–1435 (cit. on pp. 16, 20).
- [Fus+01] T Fusco et al. “Optimal wave-front reconstruction strategies for multiconjugate adaptive optics”. In: *JOSA A* 18.10 (2001), pp. 2527–2538 (cit. on p. 39).
- [Gen95] Eric Gendron. “Optimisation de la commande modale en optique adaptative: applications à l’astronomie”. PhD thesis. 1995 (cit. on pp. 40, 62, 63, 139).
- [GL94] Eric Gendron et al. “Astronomical adaptive optics. 1: Modal control optimization”. In: *Astronomy and Astrophysics* 291 (1994), pp. 337–347 (cit. on p. 44).
- [Gil05] Luc Gilles. “Closed-loop stability and performance analysis of least-squares and minimum-variance control algorithms for multiconjugate adaptive optics”. In: *Applied Optics* 44.6 (2005), pp. 993–1002 (cit. on p. 39).
- [GS07] Roberto Gilmozzi et al. “The European Extremely large telescope (E-ELT)”. In: *The Messenger* (2007) (cit. on pp. 17, 47, 55).
- [Har00] J Hartmann. “notes about the construction and adjustment of spectrographs”. In: *Zeitschrift für Instrumentenkunde* 20 (1900), p. 47 (cit. on p. 25).
- [Heg+85] E Keith Hege et al. “Multiple mirror telescope as a phased array telescope”. In: *Applied optics* 24.16 (1985), pp. 2565–2576 (cit. on p. 16).
- [Hei+18] Jochen Heidt et al. “Commissioning of the adaptive optics supported LUCI instruments at the Large Binocular telescope: results”. In: vol. 10702. 2018, pp. 10702–10702 (cit. on p. 59).
- [Her+ep] C T Heritier et al. “Online Identification of key-parameters for synthetic-based calibrations with Pyramid WFS”. In: *Monthly Notices of the Royal Astronomical Society* (in prep) (cit. on p. 18).

- [Her+18] C T Heritier et al. “A new calibration strategy for adaptive telescopes with pyramid WFS”. In: *Monthly Notices of the Royal Astronomical Society* (2018) (cit. on pp. 18, 59).
- [Hin+10] Philip M Hinz et al. “The GMT adaptive optics system”. In: *Adaptive Optics Systems II*. Vol. 7736. International Society for Optics and Photonics. 2010, p. 77360C (cit. on p. 47).
- [Joh06] Matt Johns. “The giant magellan telescope (GMT)”. In: *Ground-based and Airborne Telescopes*. Vol. 6267. International Society for Optics and Photonics. 2006, p. 626729 (cit. on p. 47).
- [Jov+15] N Jovanovic et al. “The Subaru coronagraphic extreme adaptive optics system: enabling high-contrast imaging on solar-system scales”. In: *Publications of the Astronomical Society of the Pacific* 127.955 (2015), p. 890 (cit. on p. 27).
- [Kas+04] M Kasper et al. “Fast calibration of high-order adaptive optics systems”. In: *JOSA A* 21.6 (2004), pp. 1004–1008 (cit. on p. 44).
- [Kel+12] A Kellerer et al. “Deformable mirrors for open-loop adaptive optics”. In: *Adaptive Optics Systems III*. Vol. 8447. International Society for Optics and Photonics. 2012, p. 844765 (cit. on p. 48).
- [Kol+12a] J Kolb et al. “Calibration strategy of the AOF”. In: *Proc. of SPIE Vol. Vol. 8447*. 2012, pp. 84472D–1 (cit. on pp. 48, 50, 54, 91, 133).
- [Kol+12b] J Kolb et al. “What can be retrieved from adaptive optics real-time data?”. In: *Proc. of SPIE Vol. Vol. 8447*. 2012, 84475U–1 (cit. on p. 48).
- [KVL08] Visa Korkiakoski et al. “Improving the performance of a pyramid wavefront sensor with modal sensitivity compensation”. In: *Applied optics* 47.1 (2008), pp. 79–87 (cit. on pp. 28, 34, 35, 99).
- [Kul+06] Caroline Kulcsár et al. “Optimal control, observers and integrators in adaptive optics”. In: *Optics express* 14.17 (2006), pp. 7464–7476 (cit. on p. 44).
- [Lei+12] Jarron M Leisenring et al. “On-sky operations and performance of LMIR-cam at the Large Binocular Telescope”. In: *Ground-based and Airborne Instrumentation for Astronomy IV*. Vol. 8446. International Society for Optics and Photonics. 2012, 84464F (cit. on p. 52).
- [Mad12] P-Y Madec. “Overview of deformable mirror technologies for adaptive optics and astronomy”. In: *Adaptive Optics Systems III*. Vol. 8447. International Society for Optics and Photonics. 2012, p. 844705 (cit. on pp. 36, 37, 47).
- [Mai+15] A-L Maire et al. “The LEECH Exoplanet Imaging Survey. Further constraints on the planet architecture of the HR 8799 system”. In: *Astronomy & Astrophysics* 576 (2015), A133 (cit. on pp. 52, 53).
- [Mar63] Donald W Marquardt. “An algorithm for least-squares estimation of non-linear parameters”. In: *Journal of the society for Industrial and Applied Mathematics* 11.2 (1963), pp. 431–441 (cit. on p. 50).

- [MA96] HM Martin et al. “Steps toward optical fabrication of an adaptive secondary mirror”. In: *European Southern Observatory Conference and Workshop Proceedings*. Vol. 54. 1996, p. 401 (cit. on p. 47).
- [MPF15] S Meimon et al. “Optimized calibration strategy for high order adaptive optics systems in closed-loop: the slope-oriented Hadamard actuation”. In: *Opt. Express* 23.21 (Oct. 2015), pp. 27134–27144. DOI: [10.1364/OE.23.027134](https://doi.org/10.1364/OE.23.027134) (cit. on p. 45).
- [Mye+08] Richard M Myers et al. “CANARY: the on-sky NGS/LGS MOAO demonstrator for EAGLE”. In: *Adaptive Optics Systems*. Vol. 7015. International Society for Optics and Photonics. 2008, 70150E (cit. on p. 48).
- [Nei+12] B Neichel et al. “Identification and calibration of the interaction matrix parameters for AO and MCAO systems”. In: *Proc. SPIE*. Vol. 8447. 2012, 84475N (cit. on p. 50).
- [Nei+16] B Neichel et al. “The adaptive optics modes for HARMONI: from Classical to Laser Assisted Tomographic AO”. In: *Adaptive Optics Systems V*. Vol. 9909. International Society for Optics and Photonics. 2016, p. 990909 (cit. on pp. 28, 56).
- [NMF85] Jerry E Nelson et al. “The design of the Keck Observatory and Telescope”. In: (1985) (cit. on p. 16).
- [Nol76] Robert J Noll. “Zernike polynomials and atmospheric turbulence”. In: *JOsA* 66.3 (1976), pp. 207–211 (cit. on p. 21).
- [Obe+04] S Oberti et al. “Calibration of a curvature sensor/bimorph mirror AO system: interaction matrix measurement on MACAO systems”. In: *Advancements in Adaptive Optics*. Vol. 5490. International Society for Optics and Photonics. 2004, pp. 139–151 (cit. on pp. 44, 45, 104).
- [Obe+06] S Oberti et al. “Large DM AO systems: synthetic IM or calibration on sky?” In: *Advances in Adaptive Optics II*. Vol. 6272. International Society for Optics and Photonics. 2006, p. 627220 (cit. on pp. 47, 48, 50, 104).
- [Obe+18] S Oberti et al. “The AO in AOF”. In: vol. 10703. 2018, p. 20 (cit. on p. 54).
- [Pau+10] Jérôme Paufigue et al. “GRAAL: a seeing enhancer for the NIR wide-field imager Hawk-I”. In: *Adaptive Optics Systems II*. Vol. 7736. International Society for Optics and Photonics. 2010, 77361P (cit. on p. 53).
- [Pea01] Karl Pearson. “Principal components analysis”. In: *The London, Edinburgh, and Dublin Philosophical Magazine and Journal of Science* 6.2 (1901), p. 559 (cit. on p. 107).
- [Pet+08] Cyril Petit et al. “First laboratory validation of vibration filtering with LQG control law for adaptive optics”. In: *Optics Express* 16.1 (2008), pp. 87–97 (cit. on p. 44).
- [Pie+08] F Pieralli et al. “Sinusoidal calibration technique for Large Binocular Telescope system”. In: *Adaptive Optics Systems N. Norbert Hubin and EM Claire and and PL Wizinowich and eds* 7015 (2008), 70153A (cit. on pp. 48, 104).

- [Pin+12] E Pinna et al. “First on-sky calibration of a high order adaptive optics system”. In: *Proc. SPIE*. Vol. 8447. 2012, 84472B (cit. on pp. 48, 50, 104).
- [Pin+14] E Pinna et al. “Design and numerical simulations of the GMT Natural Guide star WFS”. In: *Adaptive Optics Systems IV*. Vol. 9148. International Society for Optics and Photonics. 2014, p. 91482M (cit. on p. 28).
- [Pin+16] E Pinna et al. “SOUL: the Single conjugated adaptive Optics Upgrade for LBT”. In: *Adaptive Optics Systems V*. Vol. 9909. International Society for Optics and Photonics. 2016, p. 99093V (cit. on pp. 51, 52).
- [Pir+04] Jean-Francois Pirard et al. “HAWK-I: A new wide-field 1-to 2.5- μm imager for the VLT”. In: *Ground-based Instrumentation for Astronomy*. Vol. 5492. International Society for Optics and Photonics. 2004, pp. 1763–1772 (cit. on p. 53).
- [Rag96] Roberto Ragazzoni. “Pupil plane wavefront sensing with an oscillating prism”. In: *Journal of modern optics* 43.2 (1996), pp. 289–293 (cit. on pp. 17, 27, 28, 31, 32).
- [RF99] Roberto Ragazzoni et al. “Sensitivity of a pyramidic wave front sensor in closed loop adaptive optics”. In: *Astronomy and Astrophysics* 350 (1999), pp. L23–L26 (cit. on pp. 27, 33).
- [Ric+03] A Riccardi et al. “Adaptive secondary mirrors for the Large Binocular Telescope”. In: *Adaptive Optical System Technologies II*. Vol. 4839. International Society for Optics and Photonics. 2003, pp. 721–733 (cit. on p. 59).
- [Ric+10] A Riccardi et al. “The adaptive secondary mirror for the Large Binocular Telescope: optical acceptance test and preliminary on-sky commissioning results”. In: *Proc. SPIE*. Vol. 7736. 2010, p. 77362C (cit. on pp. 37, 38, 47).
- [Rod99] François Roddier. *Adaptive optics in astronomy*. Cambridge university press, 1999 (cit. on pp. 20, 36, 44).
- [Rou+90] G Rousset et al. “First diffraction-limited astronomical images with adaptive optics”. In: *Astronomy and Astrophysics* 230 (1990), pp. L29–L32 (cit. on pp. 16, 23, 27).
- [SDB94] P Salinari et al. “A study of an adaptive secondary mirror”. In: *European Southern Observatory Conference and Workshop Proceedings*. Vol. 48. 1994, p. 247 (cit. on p. 47).
- [Sau+10] J-F Sauvage et al. “SAXO, the eXtreme Adaptive Optics System of SPHERE: overview and calibration procedure”. In: *Adaptive Optics Systems II*. Vol. 7736. International Society for Optics and Photonics. 2010, 77360F (cit. on p. 37).
- [Sha71] Roland V Shack. “Production and use of a lecticular Hartmann screen”. In: *J. Opt. Soc. Am.* 61 (1971), pp. 656–661 (cit. on p. 25).
- [Ske+14] Andrew J Skemer et al. “High contrast imaging at the LBT: the LEECH exoplanet imaging survey”. In: *Adaptive Optics Systems IV*. Vol. 9148. International Society for Optics and Photonics. 2014, p. 91480L (cit. on p. 52).

- [Skr+10] MF Skrutskie et al. “The Large Binocular Telescope mid-infrared camera (LMIRcam): final design and status”. In: *Ground-based and Airborne Instrumentation for Astronomy III*. Vol. 7735. International Society for Optics and Photonics. 2010, 77353H (cit. on p. 52).
- [Str+12] S Ströbele et al. “GALACSI system design and analysis”. In: *Adaptive Optics Systems III*. Vol. 8447. International Society for Optics and Photonics. 2012, p. 844737 (cit. on p. 53).
- [Str+06] S Stroebele et al. “The ESO adaptive optics facility”. In: *Advances in Adaptive Optics II*. Vol. 6272. International Society for Optics and Photonics. 2006, 62720B (cit. on p. 53).
- [Tay38] Geoffrey Ingram Taylor. “The spectrum of turbulence”. In: *Proceedings of the Royal Society of London. Series A-Mathematical and Physical Sciences* 164.919 (1938), pp. 476–490 (cit. on p. 23).
- [Toz+08] A Tozzi et al. “The double pyramid wavefront sensor for LBT”. In: *Adaptive Optics Systems*. Vol. 7015. International Society for Optics and Photonics. 2008, p. 701558 (cit. on p. 52).
- [Vér+15] Jean-Pierre Véran et al. “Pyramid versus Shack-Hartmann: trade study results for the NFIRAOS NGS WFS”. In: *Adaptive Optics for Extremely Large Telescopes 4—Conference Proceedings*. Vol. 1. 1. 2015 (cit. on p. 28).
- [Vér04] Christophe Vérinaud. “On the nature of the measurements provided by a pyramid wave-front sensor”. In: *Optics Communications* 233.1-3 (2004), pp. 27–38 (cit. on pp. 27, 31, 33, 99).
- [Ver+14] Elise Vernet et al. “On the way to build the M4 Unit for the E-ELT”. In: *Adaptive Optics Systems IV*. Vol. 9148. International Society for Optics and Photonics. 2014, p. 914824 (cit. on p. 56).
- [Ver+12] E Vernet et al. “Specifications and design of the E-ELT M4 adaptive unit”. In: *Adaptive Optics Systems III*. Vol. 8447. 2012 (cit. on pp. 37, 38, 47, 56).
- [Vio+16] V Viotto et al. “Expected gain in the pyramid wavefront sensor with limited Strehl ratio”. In: *Astronomy & Astrophysics* 593 (2016), A100 (cit. on p. 35).
- [Wal83] EP Wallner. “Optimal wave-front correction using slope measurements”. In: *JOSA* 73.12 (1983), pp. 1771–1776 (cit. on p. 39).
- [Wil+03] F Wildi et al. “First light of the 6.5-m MMT adaptive optics system”. In: vol. 5169. 2003, pp. 5169–5169 - 9 (cit. on p. 47).
- [WB04] F Wildi et al. “Determining the interaction matrix using starlight”. In: *Advancements in Adaptive Optics*. Vol. 5490. International Society for Optics and Photonics. 2004, pp. 164–174 (cit. on p. 48).
- [Zer34] Frits Zernike. “Diffraction theory of the knife-edge test and its improved form, the phase-contrast method”. In: *Monthly Notices of the Royal Astronomical Society* 94 (1934), pp. 377–384 (cit. on p. 21).

List of Figures

1.1	2D representation of the 16 first Zernike Polynomials (a) and decomposition of the turbulence variance on the 400 first Zernike polynomials (b).	22
1.2	Temporal PSD of the first (a) and 300 th Zernike Polynomial (b). The red curves correspond to the theoretical PSD determined in J.-M. Conan 1994. We considered a wind-speed of 15 m/s and an 8-meter telescope.	23
1.3	Principle of an Adaptive Optics System.	24
1.4	Linearity curve of a WFS characterized by a sensitivity of 1. It exhibits the linear regime (within the two dotted lines) and the saturation of the WFS outside of the linear regime (absolute amplitude > 40 nm RMS).	25
1.5	Principle of the Shack Hartmann WFS: the movements of the spots on the detector indicate the presence of local Tip/Tilt at the level of the lenslet array.	26
1.6	SH-WFS measurements corresponding to a non-aberrated wave-front (left) and with aberrations (right).	27
1.7	Wave Front Error (WFE) as function of the number of photons per subaperture for a PWFS and a SH WFS.	28
1.8	Layout of the Pyramid WFS.	29
1.9	Illustration of the concept of Fourier Filtering optical System (courtesy of O. Fauvarque, taken from Fauvarque et al. 2017)	29
1.10	Illustration of the argument of the mask m (a) of a classical Pyramid WFS and corresponding Pyramid Pupils (b) when I_P is circular with a central obstruction.	30
1.11	Definition of the PWFS Pupils I_i (a) and Quadrants I_{Q_i} (b)	31
1.12	Illustration of the Pyramid Pupils for different modulations.	32
1.13	Illustration of the PWFS signals corresponding to a Tip (a), a Tilt (b) and a Focus (c) aberration for a modulation of $3\lambda/D$	32
1.14	Sensitivity Curves of the PWFS with respect to the KL Modal Basis (see section 1.5.2). The results are given for different modulation radius.	33
1.15	Linearity curves for different modulation radius for different KL modes (see section 1.5.2).	33
1.16	Illustration of the impact of residual phase on the push pull measurement of the KL mode 20 (see section 1.5.2) using a Pyramid WFS.	34
1.17	Illustration of the Optical Gains of the PWFS as a function of the Fried Parameter r_0 . This plot reproduces the results presented in Deo et al. 2018a.	35
1.18	Illustration of an AO system in the Fried Geometry.	36
1.19	Image of the DSM indicating the main components of the mirror. Image taken from Biasi et al. 2012	38
1.20	Position of the ASM actuators with respect to the FLAO WFS subapertures.	38

1.21	Illustration of the Zernike Polynomials (Left) and KL modes (Right) defined for an atmosphere characterized with $r_0 = 11cm$	41
1.22	Chronogram of an AO system characterized by a total of 2 frames delay. T represents the duration of a frame.	42
1.23	Block diagram of a Closed Loop Adaptive System where $G(f)$ is the open loop transfer function.	42
1.24	Rejection Transfer Function of an AO loop running at 1 kHz for different loop gains. Left: Theoretical, Right: End-to-end simulation.	43
1.25	(a) Wave-Front Error as a function of the input X-Shift for the different number of modes considered. (b) H-Band PSF (log-scale) versus shift X mis-registration for different numbers of modes controlled in the interaction matrix. The sub-images are 0.5" across.	46
1.26	Pseudo Synthetic Calibration: Experimental inputs (solid black lines) are injected into the synthetic model (dashed blue lines) to reproduce the registration of the real system. The pseudo-synthetic interaction matrix (dotted red lines) is then regularly updated during the operation tracking the mis-registration parameters.	49
1.27	Optical Layout of the LBT taken from http://oldweb.lbto.org . The Front-bent focus is not displayed in this representation.	51
1.28	Optical Layout of the FLAO system WFS, taken from Esposito et al. 2010b.	51
1.29	L' Band image of the HR8799 multiple planet system using the LMIR-Cam. Image taken from Maire et al. 2015.	53
1.30	Layout of the Adaptive Optics Facility at the UT 4 of the VLT. Image taken from https://www.eso.org	53
1.31	Comparison of the observation of the globular cluster NGC 6388 with the instrument MUSE in wide-field mode without Adaptive Optics (Left) and the MUSE narrow field mode (7.5" square) with Adaptive Optics (Right). Image taken from the ESO Press Release https://www.eso.org/public/germany/news/eso1824/	55
1.32	Optical Design of the ELT (taken from Cirasuolo et al. 2018).	56
1.33	Illustration of a petal of the M4 mirror. Taken from Elise Vernet et al. 2014	56
2.1	Variance map of the influence functions of the ASM measured with an interferometer. We can notice the 9 inactive actuators.	60
2.2	Illustration of the different mis-registration types. The initial DM actuators position is indicated before (black crosses) and after (red crosses) application of the mis-registration.	61
2.3	Sensitivity in Wave Front Error to the different mis-registrations for a synthetic model of the FLAO system controlling 400 modes.	62
2.4	Influence Function from the ASM measured with an interferometer showing the overshoot due to the imposed definition of the influence function.	64

2.5	Top-left quarter of an influence function input to the model from an experimental measurement of influence function. It exhibits numerical edge-effects due to the interpolation of the experimental data to apply a rotation to the DM model.	64
2.6	Gaussian Influence Function with a mechanical coupling of 35%, 1D section (a) and 2D representation (b). Same influence function after applying an exaggerated anamorphosis of 120 % of the diameter for $\theta=45^\circ$ (c).	66
2.7	Argument of the optical mask m_4 of the perfect Pyramid WFS. Each face has an angle of $\alpha = \frac{\pi}{2}$	67
2.8	Optical Mask and pupils of the Pyramid WFS Model in presence of an (exaggerated) imperfection.	67
2.9	Definition of the pyramid model parameters d_{WFS} and D_{WFS}	68
2.10	Definition of the Pyramid Pupils I_i (a) and Pyramid Quadrants I_{Q_i} (b)	68
2.11	Left: Sum of the four quadrants I_{4Q} and selection of the valid subapertures $m_{I_{4Q}}$ (white dots). Right: Detector mask $m_{detector}$ for the slopes computation	69
2.12	Adjusting the parameter θ of the model to displace the pyramid pupils on the detector plane (a). Sum of the four quadrants of the pyramid model compared to the position of $m_{I_{4Q}}^{exp}$ (white dots) without adjusting θ (b) and after adjusting θ (c).	70
2.13	Iterative minimization of the criteria χ_N by playing on a single parameter at a time. \mathbf{D}_α^* corresponds to the interaction matrix computed in the model after identifying the mis-registration parameters α	71
2.14	Summary of the development of the Pseudo-Synthetic model of the LBT in the simulator. The solid red lines correspond to the experimental inputs and the dashed blue lines to the model components and outputs.	72
2.15	Summary of the development of the Pseudo-Synthetic model of the LBT in the simulator. The solid red lines correspond to the experimental inputs and the dashed blue lines to the model components and outputs. The model parameters were identified using the algorithm presented in section 2.5.	85
2.16	(a) Residual variance between the experimental and synthetic modal basis for the different mechanical coupling of the influence functions. The values are ordered in decreasing order. (b) Illustration of the cross-matrix $\mathbf{B}_{synth}^T \cdot \mathbf{B}_{exp}$ in the case of 45% mechanical coupling showing that the matrix is well diagonal.	86
2.17	Illustration of the 4 worst modes reproduced by the model. Each sub-figure provides the experimental mode (left), synthetic (center) and residual (right).	87
2.18	Comparison of simulated closed loop modal PSD using both interaction matrices, synthetic and experimental. The model was developed using fully synthetic influence functions.	88
2.19	Comparison of 2D slopes maps $[S_x S_y]$ for the KL modes 3,10,100 and 400. From Top to bottom: Experimental, Fully Synthetic Model, Synthetic Model with Experimental Influence Functions.	89

2.20	Closed loop performance using the experimental reconstructor in the simulator and playing around the convergence value of the mis-registration parameters.	90
2.21	Iterative estimation of the scaling parameter γ^* and mis-registration parameters α^* from the interaction matrix \mathbf{D}_α	92
2.22	Linearity Curves of the identification algorithm for $\alpha = \alpha_{rot}$ (a), $\alpha = \alpha_X$ (b), $\alpha = \alpha_{mX}$ (c) and $\alpha = \alpha_{mX} = \alpha_{mY}$ (d) in a 30x30 Cartesian Geometry (solid blue), ASM Geometry (dashed red) and 20x20 Cartesian Geometry (dotted black).	95
2.23	Coupling of the parameters with the rotation. The results are the same for both shifts and for both magnifications. The horizontal black dashed lines give the maximum error that can be accepted (see Figure 2.3).	96
2.24	Coupling of the parameters with the shift X. The algorithm does not exhibit any coupling with the rotation and shift Y parameters. The horizontal black dashed lines give the maximum error that can be accepted (see Figure 2.3).	97
2.25	Coupling of the parameters with the magnification. The results are the same for both shifts. The horizontal black dashed lines give the maximum error that can be accepted (see Figure 2.3).	98
2.26	Iterative estimation of large values of mis-registrations updating the meta-sensitivity matrix $\mathbf{\Lambda}_{\alpha^*}$ after each estimation of the parameter α^*	99
2.27	Diagonal coefficients of the matrix \mathbf{G}_{r_0} for different value of r_0 in the visible.	100
2.28	Comparison of the estimation of the shift X for interaction matrices impacted by optical gains variations.	100
3.1	Identification of the model mis-registration parameters from reference signals. The estimated interaction matrix can be reduced to only given number of modes N	103
3.2	4 most sensitive modes to a given mis-registration derived from the PCA of $\delta\mathbf{D}_{\alpha_0}(\varepsilon_i)$	108
3.3	WFS measurement [Sx Sy] corresponding to the 4 most sensitive modes to a given mis-registration derived from the PCA of $\delta\mathbf{D}_{\alpha_0}(\varepsilon_i)$	109
3.4	9 Less sensitive modes to a given mis-registration derived from the PCA of $\delta\mathbf{D}_{\alpha_0}(\varepsilon_i)$	109
3.5	Eigen Values distribution of the sensitivity matrices $\delta\mathbf{D}_{\alpha_0}(\varepsilon_i)$	110
3.6	Cumulative variance corresponding to the different mis-registrations. Around 100 modes are required to explain 90% of the variance in all cases.	110
3.7	Estimation error for a ramp of mis-registration. The results are given for interaction matrices reduced to the 1 st , 10 th , 100 th and 200 th most sensitive modes for each type of mis-registration.	111
3.8	Sensitivity criteria ξ_{RMS} corresponding to various modal basis. The results are given for a rotation of 0.25, 0.75 and 1.25 °	112
3.9	Sensitivity criteria ξ_{RMS} corresponding to various modal basis. The results are given for a shift X of 10, 30 and 50 % of a subaperture.	113

3.10	Sensitivity criteria ξ_{RMS} corresponding to various modal basis. The results are given for a magnification X of 100.25, 100.75 and 101.25% of the diameter.	114
3.11	Estimation Error for the Rotation (a) and the Shift X (b). The estimation using 2 (solid blue) and 10 modes PCA (dotted red) is given and can be compared to the estimation using the full interaction matrix (black dashed)	115
3.12	Top: H Band PSF (log scale) when no mode is applied (a) and applying a 10 nm RMS mode corresponding to most sensitive PCA mode to the shift X. Bottom: Residual H-Band PSF (log scale) for the most sensitive PCA modes of the different types of mis-registrations.	116
3.13	Top: H Band PSF (log scale) and applying different amplitudes for the most sensitive PCA mode to the rotation. Bottom: Corresponding residual H-Band PSF (log scale).	117
3.14	WFS signals $[S_X S_Y]$ retrieved averaging 20 push/pull measurements for different levels of noise η and different amplitudes a . The signal corresponds to the PCA mode most sensitive to the shift X.	119
3.15	Slopes RMS corresponding to the most sensitive PCA mode to the shift X as a function of the number of measurements averaged.	120
3.16	Illustration of the different modal basis, 30 PCA Modes (a) and 3 PCA Modes (b), used to retrieve the mis-registration parameters	120
3.17	Estimation Error corresponding to a shift X of 20% of a subaperture as a function of the number of measurement averaged. This case corresponds to a full interaction interaction matrix (300 KL Modes). The dashed black lines correspond to our specification in terms of accuracy.	121
3.18	Estimation Error corresponding to a shift X of 20% of a subaperture retrieving 30 PCA Modes on-sky. The dashed black lines correspond to our specification in terms of accuracy.	121
3.19	Estimation Error corresponding to a shift X of 20% of a subaperture retrieving 3 PCA Modes on-sky. The dashed black lines correspond to our specification in terms of accuracy	122
3.20	Estimation Error corresponding to a shift X of 20% of a subaperture retrieving 3 PCA modes on sky. In the first case (a) we consider the most sensitive modes for each type of mis-registration and in the second case (b), we consider the 100 th PCA modes for each mis-registration. The dashed black lines correspond to our specification in terms of accuracy	123
3.21	Estimation corresponding to a shift X using 30 PCA modes. The results are given for different wind speed considering an amplitude a of 10 nm (left) and 20 nm RMS (right) and for different levels of noise (from the top to the bottom). We consider $N = 20$ measurements are averaged per mode. The dashed black lines correspond to our specification in terms of accuracy	124
3.22	Estimation (left) and corresponding Error (right) of a ramp of rotation using 30 PCA modes. The results are given for different level of noise η and amplitude of push-pull a . In this case, we consider $N= 20$ measurements for each mode. The dashed black lines correspond to our specification in terms of accuracy	125

3.23	Estimation (left) and corresponding Error (right) of a ramp of rotation using 3 PCA modes. The results are given for different level of noise $\boldsymbol{\eta}$ and amplitude of push-pull a . In this case, we consider $N=20$ measurements for each mode. The dashed black lines correspond to our specification in terms of accuracy	126
3.24	Estimation (left) and corresponding Error (right) of a ramp of shift Y using 30 PCA modes. The results are given for different level of noise $\boldsymbol{\eta}$ and amplitude of push-pull a . In this case, we consider $N=20$ measurements for each mode. The dashed black lines correspond to our specification in terms of accuracy	127
3.25	Estimation (left) and corresponding Error (right) of a ramp of shift Y using 3 PCA modes. The results are given for different level of noise $\boldsymbol{\eta}$ and amplitude of push-pull a . In this case, we consider $N=20$ measurements for each mode. The dashed black lines correspond to our specification in terms of accuracy	128
3.26	Estimation (left) and corresponding Error (right) of a ramp of shift Y using 30 PCA modes. The results are given for different level of noise $\boldsymbol{\eta}$ and amplitude of push-pull a . In this case, we consider $N=20$ measurements for each mode. The dashed black lines correspond to our specification in terms of accuracy	129
3.27	Estimation (left) and corresponding Error (right) of a ramp of shift Y using 3 PCA modes. The results are given for different level of noise $\boldsymbol{\eta}$ and amplitude of push-pull a . In this case, we consider $N=20$ measurements for each mode. The dashed black lines correspond to our specification in terms of accuracy	130
3.28	Dynamic estimation of the mis-registration parameters as a function of the time using an amplitude a 20 nm RMS. In this case, we consider $N=20$ measurements for each mode. The dashed black lines correspond to our specification in terms of accuracy	131
4.1	Modal gains of a SH-WFS for an r_0 of 15 and 20 cm in the visible. The curves are flat and close to 1 in both cases. The difference between the two curves is due to the different level of residual during the on-sky calibration.	139
4.2	Relative error with respect to the convergence value for the estimation of a shift Y in a nominal case (slow boiling with low flux).	140
4.3	Rotation Estimation (a) and Estimation Error (b) as a function of the input rotation for a Frozen Flow of 10 m/s for different levels of noise.	141
4.4	Shift X Estimation (a) and Estimation Error (b) as a function of the input shift X for a Frozen Flow of 10 m/s for different levels of noise.	141
4.5	Shift Y Estimation (a) and Estimation Error (b) as a function of the input shift Y for a Frozen Flow of 10 m/s for different levels of noise.	142
4.6	First Estimation of the scaling factor γ as a function of the input mis-registration in a Frozen Flow configuration with a wind of 10 m/s for different levels of noise.	143
4.7	Estimation Error of the shift X parameter for a Frozen Flow configuration with a wind of 10 m/s in the X (a) and -X direction (b)	144

4.8	Definition of the different configurations identified to characterize the estimation of the interaction matrix using telemetry data. FF stands for Frozen Flow.	145
4.9	Estimation of the mis-registration parameters as a function of the number of signals used to estimate the interaction matrix from closed loop data in the case of a Frozen Flow turbulence with slow and strong wind for a low and high flux.	146
4.10	Estimation of the mis-registration parameters as a function of the number of signals used to estimate the interaction matrix from closed loop data in the case of a Boiling turbulence with slow and strong wind for a low and high flux.	147
4.11	Interaction matrix signal corresponding to the actuator 100 for a Frozen Flow (a) and a Boiling (b) atmosphere in the case of a slow wind and a low flux.	148
4.12	Interaction matrix signal corresponding to the actuator 100 for a Frozen Flow (a) and a Boiling (b) atmosphere in the case of a fast wind and a low flux.	149
4.13	Interaction matrix signal corresponding to the actuator 100 for a Frozen Flow (a) and a Boiling (b) atmosphere in the case of a slow wind and a high flux.	150
4.14	Interaction matrix signal corresponding to the actuator 100 for a Frozen Flow (a) and a Boiling (b) atmosphere in the case of a fast wind and a high flux.	151
4.15	1D signal of the estimated interaction matrices signals with no mis-registration, corresponding to the actuator 100 for a high flux regime and different configurations of atmosphere (top). 1D signals of noise-free interaction matrices for different shift X (bottom). We retrieve the same symmetry in the estimated signals with a Frozen Flow as in the mis-registered matrices.	152
4.16	Difference of estimation between an algorithm using a global scaling γ or a different scaling γ_X in X and γ_Y in Y.	154
4.17	Estimation Error of the Shift Y as a function of the number of frames considered. The results are given for a Frozen Flow (a) and a Boiling configuration (b) with different wind speeds and levels of noise.	155
4.18	Wave Front Error (WFE) as a function of the loop gain for a Frozen Flow configuration and a wind of 30 m/s.	156
4.19	Estimated interaction matrices (slopes X only) in the case of a Frozen Flow of 30 m/s using different loop gains for a high flux (500 Photons per subapertures).	157
4.20	Shift X estimation in a Frozen Flow configuration with a wind speed of 30 m/s and -30 m/s. We show the estimation for different fluxes (in number of photons per subaperture) as a function of the loop gain.	158
4.21	Shift X estimation in a Frozen Flow configuration with a wind speed of 5 m/s and 15 m/s. We show the estimation for different fluxes (in number of photons per subaperture) as a function of the loop gain.	158

4.22	(a) Wave Front Error (WFE) as a function of the wind speed (in subapertures per frames). (b) Shift X Estimation as a function of the wind speed (in subapertures per frames). For this specific case, we do not normalize the parameters estimation with the scaling parameter identified by the algorithm.	160
4.23	Estimated interaction matrices (slopes X only) for different wind speeds using 20 000 frames.	161
4.24	WFE as a function of the loop gain for a slow (a) and fast Frozen Flow (b). We present the results for different levels of flux.	162
4.25	Rotation estimation (left) and corresponding estimation error (right) as a function of the input rotation in $^{\circ}$. The results are given for a wind of 5 m/s (top) and 30 m/s (bottom). The dashed lines are the rotation value that corresponds to a shift of 10% of a subaperture for an actuator located on the border of the pupil.	163
4.26	Shift Y estimation (left) and corresponding estimation error (right) as a function of the input shift Y % of a subaperture. The results are given for a slow (top) and fast (bottom) Frozen Flow, corresponding to a wind speed of respectively 5 m/s and 30 m/s.	164
4.27	Shift X estimation (left) and corresponding estimation error (right) as a function of the input shift X % of a subaperture. The results are given for a slow (top) and fast (bottom) Frozen Flow, corresponding to a wind speed of respectively 5 m/s and 30 m/s.	165
4.28	Shift X estimation (left) and corresponding estimation error (right) as a function of the input shift X % of a subaperture. The results are given for a slow (top) and fast (bottom) Boiling, corresponding to a wind speed of respectively 5 m/s and 30 m/s.	166
4.29	Estimation (a) and corresponding error (b) corresponding to a ramp of rotation using a PWFS in a Frozen Flow configuration with a wind speed of 10 m/s in the X direction.	168
4.30	Estimation (a) and corresponding error (b) corresponding to a ramp of shift X using a PWFS in a Frozen Flow configuration with a wind speed of 10 m/s in the X direction.	168
4.31	Estimation (a) and corresponding error (b) corresponding to a ramp of shift Y using a PWFS in a Frozen Flow configuration with a wind speed of 10 m/s in the X direction.	169
4.32	Estimation (a) and corresponding error (b) corresponding to a ramp of rotation using a PWFS in a Frozen Flow configuration with a wind speed of 10 m/s in the X direction. The results are given for a high flux (500 photons per subaperture) and a loop gain of 0.5 and 0.7.	170
4.33	Estimation (a) and corresponding error (b) corresponding to a ramp of shift X using a PWFS in a Frozen Flow configuration with a wind speed of 10 m/s in the X direction. The results are given for a high flux (500 photons per subaperture) and a loop gain of 0.5 and 0.7.	170
4.34	Estimation (a) and corresponding error (b) corresponding to a ramp of shift Y using a PWFS in a Frozen Flow configuration with a wind speed of 10 m/s in the X direction. The results are given for a high flux (500 photons per subaperture) and a loop gain of 0.5 and 0.7.	171

4.35	Estimation Error of the shift X corresponding to a non mis-registered case with Frozen Flow in the X direction and wind speed of 30 m/s. The cases with gain higher than 1 were diverging.	172
4.36	Estimation (a) and corresponding error (b) corresponding to a ramp of shift X using a PWFS in a Frozen Flow configuration with a wind speed of 5 and 30 m/s in the X direction. The results are given for a high flux (500 photons per subaperture) and a loop gain of 0.3 and 0.7 with compensation of the OG.	173
4.37	Estimation (a) and corresponding error (b) corresponding to a ramp of shift X using a PWFS in a Boiling configuration with a wind speed of 5 and 30 m/s in the X direction. The results are given for a high flux (500 photons per subaperture) and a loop gain of 0.3 and 0.7 with compensation of the OG.	174
6.1	a) Impact d'une translation sur les performances de l'OA (WFE = Erreur de Front d'Onde) pour différent nombre de modes KL contrôlés dans le reconstruteur. b) Schéma représentatif de l'ASO Pyramide.	183
6.2	Principe de l'algorithme itératif d'identification des paramètres de <i>mis-registrations</i> α_i à partir d'une matrice de référence expérimentale \mathbf{D}_α et de matrices synthétiques \mathbf{D}_α^*	186
6.3	Schéma représentatif du développement du modèle Pseudo-Synthétique de FLAO. Les lignes rouges correspondent aux données expérimentales et les lignes pointillées bleues aux données générées par le modèle.	186
6.4	(a): Densités Spectrales de Puissances modales obtenues avec les reconstruteurs synthétique et expérimental dans le simulateur. (b) DSP modale obtenues avec les reconstruteurs synthétique et expérimental au LBT en simulant une turbulence sur l'ASM.	187
6.5	FEP (en échelle logarithmique) obtenues en simulant une turbulence sur l'ASM dans le cas d'un reconstruteur expérimental (gauche) et synthétique pour 400 modes (centre) et 500 modes (droite). Images obtenues avec l'instrument LUCI du LBT (bande H). SR correspond au critère de qualité de l'image: 100% correspond à une image limitée par la diffraction.	188
6.6	4 modes les plus sensibles pour différents types de <i>mis-registrations</i> obtenus grâce à la PCA des matrices de sensibilité.	189
6.7	Estimation dynamique des <i>mis-registrations</i> en fonction du nombre d'itérations en utilisant 3 modes PCA. A chaque itération, les <i>mis-registrations</i> sont modifiées. Le cas présenté correspond à une amplitude de 20 nm RMS et 20 mesures <i>push-pull</i> pour chaque mode. Les lignes noires pointillées correspondent aux niveaux d'erreur maximales pour être dans les spécifications.	190
6.8	FEP en bande H, limitée par la diffraction (a) (échelle logarithmique) et avec une amplitude de 20 nm RMS du mode PCA le plus sensible à la rotation (b). (c) FEP résiduelle (échelle logarithmique).	191

6.9	Erreur sur l'estimation d'une translation en X pour une atmosphère de type <i>Frozen Flow</i> avec un vent de 10 m/s dans la direction X. Les résultats sont donnés pour un ASO de type Shack-Hartmann dans un régime à bas flux (10 photons par sous-ouverture) et fort flux (500 photons par sous-ouverture).	192
6.10	Matrices d'interaction estimées (Signal en X uniquement) pour différentes valeurs de vent. La matrice d'interaction vraie est donnée dans le coin bas-droite.	193
6.11	Estimation de la translation en X en fonction du gain de boucle pour une atmosphère de type <i>Frozen Flow</i> avec un vent de 30 m/s dans la direction X. Les résultats sont donnés pour un ASO de type Shack-Hartmann dans un régime à bas flux (10 photons par sous-ouverture) et fort flux (500 photons par sous-ouverture).	194
6.12	Estimation (a) et Erreur d'estimation (b) d'une translation en X pour une atmosphère de type <i>Frozen Flow</i> avec un vent de 10 m/s dans la direction X. Les résultats sont donnés pour un ASO de type Pyramide dans un régime à bas flux (10 photons par sous-ouverture) et fort flux (500 photons par sous-ouverture).	194
6.13	Estimation de la translation en X en fonction du gain de boucle pour une atmosphère de type <i>Frozen Flow</i> avec un vent de 30 m/s dans la direction X. Les résultats sont donnés pour un ASO de type Pyramide avec et sans compensation des gains optiques.	195
A.1	Optical layout of the WFS unit of HOT. The lens L3 is used to focus the light on the top of the Double Pyramid and the lens L4 is in charge of re-imaging the PWFS pupils on the Andor camera detector.	197
A.2	Distances between the different HOT optical elements.	198
A.3	HOT PWFS Pyramid (left) and BMM (right). Courtesy of N. Cerpa and M. Kasper.	198
A.4	Summary of the development of the Pseudo-Synthetic model of the HOT AO systems in the simulator. The solid red lines correspond to the experimental inputs and the dashed blue lines to the model components and outputs.	199
A.5	Closed-loop pupils of the HOT PWFS simulating the phase screens with the turbulence simulator. The left image corresponds to the interaction matrix experimentally measured with fiber (slopes RMS=0.0955 a.u.) and the right image corresponds to the interaction matrix generated from the synthetic model (slopes RMS=0.1073 a.u.)	200
B.1	PCA modes corresponding to the rotation for AO systems with different number of subapertures.	201
B.2	PCA modes corresponding to the shift X for AO systems with different number of subapertures.	202
B.3	PCA modes corresponding to the shift Y for AO systems with different number of subapertures.	202
B.4	PCA modes corresponding to the magnification X for AO systems with different number of subapertures.	203

B.5	PCA modes corresponding to the magnification Y for AO systems with different number of subapertures.	203
B.6	1D section of a Gaussian influence function with a mechanical coupling of 45%	204
B.7	PCA modes corresponding to the rotation for AO systems with different mechanical couplings.	204
B.8	PCA modes corresponding to the shift X for AO systems with different mechanical couplings.	205
B.9	PCA modes corresponding to the shift Y for AO systems with different mechanical couplings.	205
B.10	PCA modes corresponding to the magnification X for AO systems with different mechanical couplings.	206
B.11	PCA modes corresponding to the magnification Y for AO systems with different mechanical couplings.	206

List of Tables

1.1	Comparison of the main differences between the ASM, DSM and M4. . .	57
1.2	Comparison of the main different Wave-Front Sensing and Calibration Strategies for the LBT, AOF and ELT instruments.	58
2.1	Mis-registration parameters estimation from the new identification algorithm. The values for the shifts are in fraction of a subaperture and the values for the magnifications in percentage of diameter.	87
2.2	Definition of the three AO Systems considered to characterized the linearity of the identification algorithm	93
3.1	Numerical Simulations parameters for the chapter 3	105
3.2	Total number of averaged push pull Measurements required to reach convergence ($< 1\%$ of a subaperture) for the mis-registration estimation of a shift X in all the conditions of noise investigated (10,100,500 and 1000 photons per subaperture per frame).	123
4.1	Numerical Simulations parameters for the sections 4.2 and 4.3	140
4.2	Scaling factors $[\gamma_X, \gamma_Y]$ for a wind speed of 5 m/s.	152
4.3	Scaling factors $[\gamma_X, \gamma_Y]$ for a wind speed of 30 m/s.	153
4.4	Definition of the different configurations identified to characterize the estimation of the interaction matrix using telemetry data. FF stands for Frozen Flow.	162
4.5	Numerical Simulations parameters for the section 4.4	167
4.6	Summary of the accuracy of the estimated mis-registration parameters in a Frozen Flow configuration with SH-WFS.	175
4.7	Summary of the accuracy of the estimated mis-registration parameters in a Frozen Flow configuration with Pyramid WFS.	175
4.8	Summary of the accuracy of the estimated mis-registration parameters in a Boiling configuration with SH-WFS.	176
4.9	Summary of the accuracy of the estimated mis-registration parameters in a Boiling configuration with Pyramid WFS.	176